

RADIATION DOSIMETRY STUDIES FOR SYNCHROTRON RADIATION BEAMLINES

By
PRASANTA KUMAR SAHANI
Enrollment No. PHYS03201204004

Raja Ramanna Centre for Advanced Technology, Indore

A thesis submitted to the
Board of Studies in Physical Sciences
In partial fulfillment of requirements
for the Degree of
DOCTOR OF PHILOSOPHY
of
HOMI BHABHA NATIONAL INSTITUTE

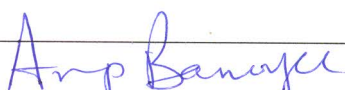
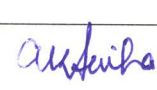
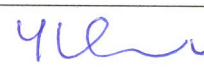
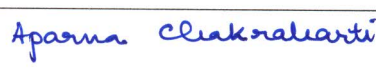

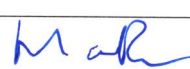
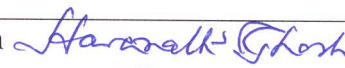



August, 2018

Homi Bhabha National Institute¹

Recommendations of the Viva Voce Committee

As members of the Viva Voce Committee, we certify that we have read the dissertation prepared by Prasanta Kumar Sahani entitled "Radiation dosimetry studies for synchrotron radiation beamlines" and recommend that it may be accepted as fulfilling the thesis requirement for the award of Degree of Doctor of Philosophy.


Chairman – Dr. Arup Banerjee		Date: 31/05/2019.
Guide / Convener – Dr. A. K. Sinha		Date: 31/05/2019
Examiner – Dr. Y. S. Mayya		Date: 31/05/19
Member 1- Dr. A. Chakrabarti		Date: 31.05.2019
Member 2- Dr. Vinit Kumar		Date: 31.05.2019
Member 3- Dr. M. P. Singh		Date: 31.05.2019
Member 4- Dr. Haranath Ghosh		Date: 31.05.2019
Member 5- Dr. Sataya Bulusu		Date: 31.05.2019

Final approval and acceptance of this thesis is contingent upon the candidate's submission of the final copies of the thesis to HBNI.

I/We hereby certify that I/we have read this thesis prepared under my/our direction and recommend that it may be accepted as fulfilling the thesis requirement.

Date: 31/05/2019

Place: RRCAT, Indore


Dr. A. K. Sinha
Guide

¹ This page is to be included only for final submission after successful completion of viva voce.

STATEMENT BY AUTHOR

This dissertation has been submitted in partial fulfillment of requirements for an advanced degree at Homi Bhabha National Institute (HBNI) and is deposited in the Library to be made available to borrowers under rules of the HBNI.

Brief quotations from this dissertation are allowable without special permission, provided that accurate acknowledgement of source is made. Requests for permission for extended quotation from or reproduction of this manuscript in whole or in part may be granted by the Competent Authority of HBNI when in his or her judgment the proposed use of the material is in the interests of scholarship. In all other instances, however, permission must be obtained from the author.

Prasanta Kumar Sahani

Prasanta Kumar Sahani

DECLARATION

I, hereby declare that the investigation presented in the thesis has been carried out by me. The work is original and has not been submitted earlier as a whole or in part for a degree / diploma at this or any other Institution / University.

Prasanta Kumar Sahani

Prasanta Kumar Sahani

List of Publications arising from the thesis

Journal

1. Simulation of absorbed dose rate due to synchrotron radiation and shielding thickness for radiation safety at Indus-2 using FLUKA, **P. K. Sahani**, G. Haridas and P. K. Sarkar, Indian Journal of Pure and Applied Physics **50**, pp. 818-820 (2012).
2. Gas bremsstrahlung studies for medium energy electron storage rings using FLUKA Monte Carlo code, **P. K. Sahani**, Haridas G., A. K. Sinha and P. R. Hannurkar, Radiation Physics and Chemistry **119**, pp. 51–54 (2016).
3. Interaction of electrons with residual gas molecules and its effect on gas bremsstrahlung radiation in electron storage rings, **P. K. Sahani**, G. Haridas, A. K. Sinha, K.V.A.N.P.S. Kumar and T. A. Puntambekar, Radiation Physics and Chemistry **156**, pp. 252–258 (2019).
4. Application of XANES in gamma dosimetry, **P. K. Sahani**, A. K. Sinha, G. Haridas, M. N. Singh and T. A. Puntambekar, Applied Radiation and Isotopes **149**, pp. 48–51 (2019).

Conferences

1. Evaluation of radiological conditions in the experimental hutch of SEXAFS beam line of Indus-2 due to introduction of a photon beam shutter, **P. K. Sahani**, M. K. Nayak, Haridas G., T. Bandyopadhyay and P R Hannurkar, DAE-BRNS Indian Particle Accelerator Conference (InPAC-2013), 19-22 November 2013, VECC, Kolkata.
2. Radiation safety studies at synchrotron radiation beam lines of Indus-2, **P. K. Sahani**, Haridas G., A. K. Sinha, T. Bandyopadhyay and P. R. Hannurkar, 8th

International Workshop on Radiation Safety at Synchrotron Radiation Sources (RadSynch-2015), 3-5 June 2015, DESY, Hamburg, Germany.

3. Design and optimization of gas bremsstrahlung stop for insertion device beamline on Indus-2, **P. K. Sahani**, A. K. Das, Haridas G., A. K. Sinha, B. N. Rajasekhar, T. A. Puntambekar, and N.K.Sahoo, 20th National Symposium on Radiation Physics (NSRP-20), 28-30 October 2015, Mangalore University, Mangalore.
4. Radiation shielding for undulator beamline in Indus-2 synchrotron radiation source, **P. K. Sahani**, A. K. Das, Haridas G., A. K. Sinha, B. N. Rajasekhar, T. A. Puntambekar and N K Sahoo, 9th International Workshop on Radiation Safety at Synchrotron Radiation Sources (RadSynch-2017), 19-22 April 2017, NSRRC, Taiwan.
5. Effect of residual gas molecules on gas bremsstrahlung dose rate in Indus-2, **P. K. Sahani**, A. K. Sinha, K.V.A.N.P.S. Kumar and T. A. Puntambekar, DAE-BRNS Indian Particle Accelerator Conference (InPAC-2018), 9-12 January 2018, RRCAT, Indore
6. Effect on CaSO₄:Dy TL Material on Exposure to High Dose, **P. K. Sahani**, Haridas G., A. K. Sinha, and T. A. Puntambekar, IARP International Conference (IARPIC-2018), 16-20 January 2018, BARC, Mumbai.
7. Synchrotron beamline for radiation physics research, **P. K. Sahani**, Haridas G., A. K. Sinha and T. A. Puntambekar, 21st National Symposium on Radiation Physics (NSRP-21), 5-7 March 2018, RRCAT, Indore.

Others

1. Experimental investigation of synchrotron and bremsstrahlung hazards at Lithography beam line of Indus-2 SRS, M. K. Nayak, **P. K. Sahani**, M. Khare, T. K. Sahu, P. Haridas, V. Dev, S. Dashora, V. Dhamgaye, G. Haridas and P. K. Sarkar, Indian Journal of Pure and Applied Physics **50**, pp. 829-831 (2012).
2. Radiation safety aspects of the operation of first three synchrotron beamlines of Indus-2, M. K. Nayak, Haridas G. Nair, A. K. Bakshi, **P.K. Sahani**, S. Singh, S. Khan, D. Verma, V. Dev, T. K. Sahu, M. Khare, V. Kumar, T. Bandyopadhyay, R. M. Tripathi and D. N. Sharma, Radiation Protection Dosimetry **164** (3), pp. 187–193 (2015).

Prasanta Kumar Sahani

Prasanta Kumar Sahani

I dedicate this thesis to

My Parents

ACKNOWLEDGEMENTS

The success of any research study requires a lot of guidance and assistance from many people and I am extremely privileged to have got this all along the path. Foremost, I would like to express my sincere gratitude to my supervisor Dr. A. K. Sinha for his excellent guidance, valuable advice, continuous support and encouragement in the course of work. The elaborate technical discussions with him have not only increased my understanding of the subject but also motivated to explore in depth. I would like to express special gratitude to my technology advisor Dr. Haridas G. for his extraordinary support throughout the research work. His patience, enthusiasm, immense knowledge and motivation have smoothed my research path.

I sincerely thank Dr. P. A. Naik, Director, RRCAT for his support and encouragement in the study. I would like to thank Dr. K. S. Pradeepkumar, Director, Health Safety & Environment Group (BARC) and Shri A. C. Thakurta, Director, Electron Accelerator Group (RRCAT) for their wholehearted support. My thanks are also due to Shri T. A. Puntambekar, Head, BDCSD (RRCAT), Dr. T. Bandyopadhyay, Head, ARSS (BARC), Shri G. Singh, Ex-Head, IOAPDD (RRCAT), Dr. P. K. Sarkar, Ex-Head, HPD (BARC), Dr. A. K. Bakshi, Head, PMSS (BARC) and Shri K. K. Thakkar, Ex-Officer-in-Charge, HPU (RRCAT) for their valuable suggestions and support. I would like to thank the members of the Doctoral Committee, HBNI (RRCAT) for their critical reviews and valuable suggestions. Heartfelt thanks are also due to my friends and colleagues at RRCAT for providing me technical and moral support. Last but not the least, I would like to thank my family members especially wife (Madhumita) and sons (Swastik & Shaurya) for providing encouragement and support throughout this journey. Finally I thank the Almighty for making my ambition true and success.

CONTENTS

	Page No.
SUMMARY	I
LIST OF FIGURES	III
LIST OF TABLES	X
CHAPTER 1 INTRODUCTION	1
1.1 Synchrotron radiation source	2
<i>1.1.1 Synchrotron radiation beamline</i>	6
1.2 Radiation environment in synchrotron radiation facility	8
<i>1.2.1 Bremsstrahlung radiation</i>	8
<i>1.2.2 Synchrotron radiation</i>	14
<i>1.2.3 Photo-neutrons</i>	20
<i>1.2.4 Electromagnetic cascade</i>	22
1.3 Dosimetry at synchrotron radiation beamlines	24
<i>1.3.1 Gas Bremsstrahlung radiation dosimetry</i>	25
<i>1.3.2 Synchrotron radiation dosimetry</i>	28
<i>1.3.3 Photo-neutron dosimetry</i>	29
1.4 Radiation shielding studies for synchrotron radiation beamlines	30
1.5 Radiation dosimetry at Indus synchrotron facility	32
<i>1.5.1 Personnel dosimetry in Indus Synchrotron facility</i>	34
1.6 Summary and thesis motivations	38
CHAPTER 2 MATERIALS AND METHODS	42
2.1 Introduction	42
2.2 Monte Carlo simulation techniques	42
<i>2.2.1 Radiation transport in Monte Carlo</i>	45

2.2.2	<i>FLUKA Monte Carlo code</i>	48
2.3	Thermoluminescence dosimetry	50
2.3.1	<i>Principle of Thermoluminescence</i>	50
2.3.2	<i>Theory of thermoluminescence</i>	52
2.3.3	<i>Thermoluminescence materials for dosimetry</i>	54
2.3.4	<i>Thermoluminescence in CaSO₄:Dy</i>	56
2.4	X-ray diffraction (XRD)	58
2.4.1	<i>ADXRD beamline in Indus-2</i>	60
2.5	X-Ray Absorption Near Edge Structure Spectroscopy	61
CHAPTER 3 GAS BREMSSTRAHLUNG RADIATION DOSIMETRY STUDIES		64
3.1	Introduction	64
3.2	Benchmarking studies on simulation of gas bremsstrahlung radiation using FLUKA	67
3.3	Simulation of gas bremsstrahlung dose for medium energy electron storage rings	72
3.3.1	<i>Comparison with experimental data</i>	74
3.3.2	<i>Application of the study for Indus-2</i>	75
3.4	Effect of residual gas molecules on gas bremsstrahlung radiation	79
3.4.1	<i>Residual gas composition in electron storage rings</i>	79
3.4.2	<i>Comparison with experimental data</i>	93
3.5	Summary and conclusion	95
CHAPTER 4 SYNCHROTRON RADIATION DOSIMETRY STUDIES		97
4.1	Introduction	97
4.2	Evaluation of synchrotron radiation dose in Indus-2	99
4.2.1	<i>Synchrotron radiation spectrum in Indus-2</i>	100

4.2.2	<i>Absorbed dose rate due to direct synchrotron radiation</i>	100
4.2.3	<i>Absorbed dose rate due to scattered synchrotron radiation</i>	104
4.2.4	<i>Evaluation of shielding thickness</i>	107
4.3	Response of personnel dosimetry device to synchrotron radiation	109
4.3.1	<i>Simulation for energy response of the TLD badge</i>	110
4.3.2	<i>Experimental verification</i>	112
4.3.3	<i>Theoretical calculation for energy response</i>	113
4.3.4	<i>Discussion of the results</i>	115
4.4	Estimation of high dose in CaSO ₄ :Dy TL materials using XANES spectroscopy	120
4.5	Design of primary standard for dosimetry at synchrotron beamlines in Indus-2	125
4.5.1	<i>Working principle of FAIC</i>	127
4.5.2	<i>Design parameters of FAIC for Indus-2 synchrotron beamlines</i>	131
4.6	Summary and conclusion	134
	CHAPTER 5 RADIATION SHIELDING STUDIES ON SYNCHROTRON BEAMLINES IN INDUS-2	137
5.1	Introduction	137
5.2	Radiation shielding studies for SEXAFS beamline (Bending magnet beamline)	140
5.2.1	<i>Dose equivalent rate due to channeled electrons</i>	142
5.2.2	<i>Gas bremsstrahlung dose evaluation</i>	143
5.2.3	<i>Discussion of the results</i>	144
5.3	Radiation shielding studies for AMOS beamline (Insertion device beamline)	146
5.3.1	<i>Gas bremsstrahlung dose rate in beamline hutch</i>	147
5.3.2	<i>Photo-neutron dose rate in beamline hutch</i>	153

5.3.3	<i>Synchrotron radiation dose rate in beamline hutch</i>	155
5.4	Summary and conclusion	157
CHAPTER 6 DESIGN OF SYNCHROTRON RADIATION BEAMLINE FOR RADIATION PHYSICS RESEARCH		159
6.1	Introduction	159
6.2	Optics for hard x-ray synchrotron beamline	161
6.3	Ray tracing calculations	165
6.4	Optics design calculation for radiation physics beamline	167
6.5	Summary and conclusion	176
CHAPTER 7 SUMMARY AND CONCLUSIONS		177
REFERENCES		182
APPENDICES		200
<i>A. Indus synchrotron radiation source</i>		200
<i>B. Radiation quantities and units</i>		215

SUMMARY

The radiation environment in synchrotron beamlines is dominated by gas bremsstrahlung radiation (BR), produced by inelastic scattering of high energy electrons with residual gas molecules inside the vacuum chamber of storage ring. The gas BR channel to beamline along with synchrotron radiation and produce scattered photons and photo-neutrons on interaction with the beamline components. Thus the radiation scenario is complex because of the mixed radiation field of photons and neutrons with broad spectral range and sharp angular distribution. The thesis is focused on the studies of these radiation components and to optimize the radiation shielding for synchrotron beamlines. The spectral behavior, angular distribution and depth dose profile of the gas BR in electron storage rings are studied in the energy range 1 - 3 GeV using FLUKA Monte Carlo code. From the study, an optimized emission angle of 0.1 mrad is established for scoring dose due to gas BR. The effect of residual gas composition (in vacuum chamber) on energy distribution, angular distribution and absorbed dose rate of gas BR is also investigated. From the studies, empirical relations for gas bremsstrahlung dose have been proposed. The proposed empirical relations show better agreement to the reported experimental data than the existing empirical relations. The simulation techniques are then applied for radiation shielding evaluation of the bending magnet and undulator based beamlines on Indus-2 synchrotron source. Absorbed dose due to direct and the scattered synchrotron radiation in beamlines are studied. Investigation on energy response of thermoluminescence (TL) detectors ($\text{CaSO}_4:\text{Dy}$ and $\text{LiF}:\text{Mg,Ti}$) used in dosimetry of synchrotron beam is reported. The effect of dosimeter material thickness and metal filters used in personnel dosimetry applications are discussed. From the study, it is

concluded that LiF:Mg,Ti TL material shows better flat response than CaSO₄:Dy and therefore seems to be a better TL material for dosimetry in synchrotron beamlines in comparison to CaSO₄:Dy based dosimeters. Effect of high gamma ray dose on CaSO₄:Dy TL dosimeter is studied using X-ray Absorption Near Edge Structure (XANES) spectroscopy which gives direct evidence of Dy³⁺ to Dy²⁺ transition on gamma ray irradiation and confirms Nambi's redox model. Also, linear increase in the area under the white line of XANES spectra with increasing dose has been observed for high dose up to 1 kGy which suggests XANES technique for evaluation of high dose from CaSO₄:Dy TL dosimeter, where the conventional TL dosimetry technique fails. The design aspects of a free air ionization chamber for application as a standard for dosimetry in synchrotron beamlines and for calibration of conventional dosimeters have been described. The design of a synchrotron beamline for carrying out radiation physics and safety research in the low energy region is also reported in the thesis.

LIST OF FIGURES

CHAPTER-1

1.1	Schematic layout of a storage ring showing synchrotron emission from a dipole (BM) and an insertion device (ID)	4
1.2	Schematic layout of a synchrotron beamline	7
1.3	Generation of bremsstrahlung radiation	9
1.4	Schematic diagram of a beamline showing channeling of gas bremsstrahlung radiation from storage ring	12
1.5	Radiation pattern from (a) non-relativistic and (b) relativistic charged particle under centripetal acceleration	15
1.6	Spectral distribution of synchrotron radiation from a bending magnet	17
1.7	Radiation pattern from bending magnet, wiggler and undulator	19
1.8	Electromagnetic cascade and the corresponding depth dose in medium	23
1.9	Relative response of TLD badge	35

CHAPTER-2

2.1	Simple algorithm on Monte Carlo approach	47
2.2	Mechanism of thermoluminescence	51
2.3	Glow curve patterns for CaSO ₄ :Dy and LiF:Mg,Ti	54
2.4	Nambi's redox model for thermoluminescence in CaSO ₄ :Dy	57
2.5	Stoebe's model for thermoluminescence in CaSO ₄ :Dy	58
2.6	Schematic showing diffraction of X-ray radiation from a crystal	59
2.7	Experimental station having (a) diffractometer with NaI(Tl) detector and (b) image plate (Mar 345 area detector)	61

2.8	Typical X-ray absorption spectrum	62
2.9	Experimental set up for XAS measurement at synchrotron beamline	63
CHAPTER-3		
3.1	Geometry used in FLUKA simulation for benchmark study	67
3.2	Gas bremsstrahlung spectrum from 7 GeV positron beam for $L = 15$ m	69
3.3	Depth dose profile inside tissue phantom for scoring radius 0.02 and 0.4 cm	69
3.4	Effect of suppression of multiple scattering on depth dose profile	70
3.5	Effect of multiple scattering on radial dose distribution in tissue phantom	70
3.6	Angular distribution of the gas bremsstrahlung radiation	72
3.7	Absorbed dose rate as a function of $L/d(L+d)$ for 1 to 3 GeV electron beam [normalized to 300 mA ($1.875 \times 10^{18} \text{ e}^-/\text{s}$)]	73
3.8	Gas bremsstrahlung spectrum as a function of straight section length	76
3.9	Gas bremsstrahlung photon fluence as a function of straight section length	76
3.10	Absorbed dose rate as a function of distance from straight section ($E_0 = 2.5 \text{ GeV}$, $I = 300 \text{ mA}$)	77
3.11	Comparison of simulated data and the proposed empirical relation to that of Ferrari et.al. (1993)	78
3.12	Composition of residual gases in Indus-2, NSRRC and ILSF storage rings in comparison with air	80
3.13	Gas bremsstrahlung spectrum for (a) 1 GeV, (b) 2 GeV and (c) 3	84

	GeV electrons from 1 m straight section for different gas compositions	
3.14	Gas bremsstrahlung spectrum $k(dN/dK)$ as a function of k/E for (a) 1 GeV, (b) 2 GeV and (c) 3 GeV electron	86
3.15	(a) Gas bremsstrahlung spectrum and (b) photon fluence from 3 GeV electron beam as a function of straight section length.	87
3.16	Gas bremsstrahlung photon fluence due to 1, 2 and 3 GeV electron beam from 1 m straight section as a function of $Z_{eff} * A$.	88
3.17	Angular distribution of gas bremsstrahlung photons from different gaseous compositions in 1 m straight section for (a) 1 GeV, (b) 2 GeV and (c) 3 GeV electrons	90
3.18	Absorbed dose rate as a function of $L/d(L+d)$ for different gas composition due to (a) 1 GeV, (b) 2 GeV and (c) 3 GeV electrons	92
3.19	Gas bremsstrahlung spectra in ADONE and NSRRC storage ring for actual gas composition	93
CHAPTER-4		
4.1	Schematic layout of a synchrotron beamline at Indus-2 showing various hutch compartments and optical elements housed in these compartments	98
4.2	Synchrotron radiation spectrum in Indus-2 (300 mA at 2.5 GeV)	100
4.3	Geometry used in the simulation study	101
4.4	Depth dose profile in water phantom due to direct synchrotron radiation	101
4.5	Photograph (a) and the schematic diagram (b) of the experimental	105

	set-up	
4.6	Angular distribution of scattered synchrotron radiation from Aluminium, Copper and Tantalum targets	106
4.7	Surface dose rate in water phantom with respect to lead thickness	108
4.8	Schematic of the TLD badge	109
4.9	Simulation geometry of the TLD badge generated using FLAIR.	111
4.10	Experimental set up at BL-4 (Indus-2)	113
4.11	Relative response of CaSO ₄ and LiF with and without self attenuation correction for synchrotron produced low energy photons	114
4.12	Relative energy response of CaSO ₄ :Dy and LiF:Mg,Ti TL discs under metal (D1), Perspex (D2) and open window (D3)	115
4.13	Disc ratio D3/D1, D2/D1 and D3/D2 for CaSO ₄ :Dy and LiF:Mg,Ti discs	117
4.14	Disc ratio D3/D1, D2/D1 and D3/D2 for CaSO ₄ :Dy and LiF:Mg,Ti discs	118
4.15	XANES spectra of reference standard (Dy ₂ O ₃) and CaSO ₄ :Dy samples	121
4.16	Relative XANES spectra of CaSO ₄ :Dy with respect to standard Dy ₂ O ₃	122
4.17	Relative areas under XANES spectra as function of absorbed dose	123
4.18	XRD pattern of CaSO ₄ :Dy samples	125
4.19	Photon flux and the air dose rate as a function of energy of synchrotron radiation from Indus-2 bending magnet	126
4.20	Schematic layout of parallel plate type FAIC	128

4.21	Charge collection efficiency exposure rate range 1 mR/s to 100 R/s at different applied potential	134
-------------	--	-----

CHAPTER-5

5.1	Schematic layout of the front end for the synchrotron beamline in Indus-2	138
5.2	Schematic layout of SEXAFS beamline	141
5.3	Geometry used for bremsstrahlung photon and photo-neutron dose estimation	142
5.4	Solid bremsstrahlung spectrum generated from mirror due to 2.5 GeV electrons.	144
5.5	Photo-neutron spectrum inside water phantom	145
5.6	Geometry used for estimation of unshielded gas bremsstrahlung dose	148
5.7	(a) Gas bremsstrahlung spectrum and (b) the depth dose inside tissue phantom	149
5.8	Geometry used for bremsstrahlung dose evaluation in 0^0 and 90^0 from the mirror	150
5.9	Scattered gas bremsstrahlung spectra from mirror in 0 and 90-degree direction	150
5.10	Depth dose profile inside tissue phantom in (a) 0^0 and (b) 90^0	151
5.11	Geometry used for bremsstrahlung dose evaluation outside hutch	152
5.12	Optimized gas bremsstrahlung stop	153
5.13	Spatial distribution of photon and neutron dose equivalent rate around the beamline	154
5.14	Synchrotron spectrum from undulator (U1) for 200 mA at 2.5 GeV	156

5.15	Depth dose profile inside tissue phantom due to direct synchrotron beam	156
5.16:	Spatial distribution of synchrotron dose equivalent rate around the beamline	157
CHAPTER-6		
6.1	Beamline components in Reflectivity beamline (BL-3) of Indus-2	160
6.2	Meridional and sagittal focusing using a toroidal mirror	164
6.3	X-ray transmission curve for 200 μm thick beryllium window	168
6.4	Optical layout of the beamline showing photon beam tracing in focused mode	169
6.5	Proposed layout of the synchrotron beamline	170
6.6	Reflectivity of rhodium, gold and platinum coated mirror	171
6.7	Footprint of synchrotron beam at (a) source, (b) mirror surface, (c) slit-2 after mirror and (d) sample position	174
6.8	Spectral distribution at source point, mirror and image spot at experimental station	175
APPENDIX-A		
A.1	Schematic layout of Indus synchrotron facility showing Microtron, Booster, Indus-1 and Indus-2 synchrotron sources	201
A.2	Synchrotron spectra from bending magnet in Indus-1 and Indus-2 storage ring	202
A.3	Schematic diagram of Indus-2 DBA (Double Bend Achromat) lattice	203
A.4	Photograph of the Indus-2 storage ring (a) RF cavities section (b) Frontend of bending magnet beamline from the ring.	204

A.5	Design beam loss scenario for Indus-2 storage ring	207
A.6	Radiation safety pathway for Indus synchrotron facility	210
A.7	Cross-section of Indus-2 shielded tunnel showing the reference points (A, B, C & D) used for shielding calculation	211

LIST OF TABLES

CHAPTER-1

1.1	Design parameters of six synchrotron radiation sources	5
1.2	Degree of importance of radiation hazards in synchrotron beamlines	24

CHAPTER-2

2.1	Comparison of MCNPX, GEANT4 and FLUKA MC code	43
2.2	Comparison of important characteristics of the TL materials	55

CHAPTER-3

3.1	Optimised parameters for studying gas bremsstrahlung radiation	71
3.2	Comparison of simulated gas bremsstrahlung dose with experiments	75
3.3	Composition of residual gas in electron storage rings (in comparison with air)	80
3.4	Effective atomic number of residual gas and gas mixtures	81
3.5	Comparison of calculated and experimental gas bremsstrahlung dose	94

CHAPTER-4

4.1	Specifications of detector used for direct synchrotron dose measurement	102
4.2	Comparison of the simulated and experimental results	103
4.3	Specifications of FLUKE-451B ion chamber	104
4.4	Composition of materials used in simulation study	112
4.5	Calculated flux attenuation factors for the filters of the badge	119
4.6	Comparison between the actual and the estimated dose	124
4.7	Major elements of FAIC	128
4.8	Parameters of FAIC for Indus-2 synchrotron beamlines	133

CHAPTER-5

5.1	Estimated dose rate at the experimental hutch	145
5.2	Gas bremsstrahlung (BR) and photo-neutron dose rate in the beamline	155

CHAPTER-6

6.1	Electron beam parameters used in ray tracing calculations	168
6.2	Beamline acceptance and optical design parameters	171
6.3	Design parameters of the cylindrical mirror	172
6.4	Source and image beam properties	175

APPENDIX - A

A.1	Major parameters of Indus-1 and Indus-2 synchrotron sources	202
A.2	Indus-2 synchrotron beamlines and their utilisation	204
A.3	Estimated dose rate due to induced activity in Indus-2	208
A.4	Dose per year at the reference points based on design beam loss scenario	212

Chapter 1

Introduction

Synchrotron radiation sources (SRS) are advanced light sources capable of providing intense photons called as synchrotron radiation. These sources are powerful tool for scientific studies such as elastic and inelastic scattering, x-ray absorption spectroscopy, resonant reflectivity, photoelectron spectroscopy, x-ray fluorescence, imaging, etc. Thus these facilities are in great demand by the scientific community worldwide. This demand is in terms of extracting scientific data on materials through various experiments in relatively short time, up to the lowest possible detection limit and achieving high signal to noise ratio which otherwise is impossible with conventional x-ray sources or laboratory sources.

SRS provides photon intensity of the order of 10^{16} photons/s/mrad²/mm²/0.1% Bandwidth whereas that of conventional x-ray sources is 10^8 photons/s/mrad²/mm²/0.1% Bandwidth only. Advanced SRS like Free Electron Laser (FEL) facilities are able to achieve enhanced photon intensity typically up to 10^{20} photons/s/mrad²/mm²/0.1% Bandwidth. In these facilities high energy electrons (\sim GeV) are allowed to move under the influence of transverse magnetic fields for the generation of synchrotron radiation, which is in the relatively low energy regime (up to tens of keV). Bremsstrahlung x-rays (whose energy extends up to the energy of electron) are also generated due to the interaction of the electrons with structural materials of the accelerator and gas molecules in the vacuum chamber. Both the radiations are highly directional. Synchrotron

radiation is used for carrying out various experiments whereas bremsstrahlung x-rays are unwarranted and pose a major radiation hazard in the facility, in addition to the synchrotron radiation. The radiation environment in synchrotron facilities is quite complex due to the presence of synchrotron radiation, bremsstrahlung radiation and their secondary radiations, posing a challenge to radiation protection in these facilities. Besides, the radiation environment is facility specific and has strong dependency on parameters like beam energy, vacuum condition and structural components of the accelerator facility. Safe operation of such facilities requires proper identification of radiation hazards and its accurate quantification for mitigating them effectively. The chapter describes the characteristics of SRS, properties of synchrotron radiation, radiation environment in beamlines and the challenges faced in radiation dosimetry. The aim of the present work reported in the thesis and the probable outcome are also summarized at the end of the chapter.

1.1 Synchrotron radiation source

Synchrotron radiation sources (SRS) or synchrotron light sources are high energy electron accelerators producing intense photon beam in the energy range from infrared to hard x-ray [1-3]. The SRS produced photon beam can be $\sim 10^{11}$ times more intense than conventional laboratory x-ray sources [4]. Ultra high intensity, low divergence and energy tunability have made these sources demanding in the field of materials science, bioscience, environmental science and industrial applications. These light sources are unique tools to study structural, physical and chemical properties of materials like crystal structures, magnetic properties, local structural environment, elemental composition, oxidation state, bond length, etc. through various spectroscopic techniques like x-ray diffraction, photoelectron spectroscopy, photo-absorption spectroscopy, x-ray fluorescence, etc [5-7]. In addition, coherent time structure of synchrotron radiation (\sim picosecond pulses separated by nanosecond) allows time resolved studies of physical

and chemical properties. The polarization property of synchrotron photons has been utilized to study the magnetism including magnetic circular dichroism [5-8].

Synchrotron radiation was first observed in a 70 MeV synchrotron at General Electric Research Laboratory, New York on 24th April 1947. Later on synchrotron radiation was observed in many high energy electron storage rings but the radiation was considered as parasitic energy loss. These facilities are called as first generation SRS. Later on, storage rings completely dedicated for utilization of synchrotron radiation, generated only from dipole magnets were developed and are called as the second generation SRS. Subsequently advanced storage rings were designed using periodic magnetic elements called as the insertion devices for increasing the photon flux. These facilities are called as the third generation SRS, where the intensity of synchrotron radiation is many order higher than the second generation sources. Down the time line, with technological improvements, higher intense synchrotron sources based on Free Electron Laser (FEL) came up, which are called as the fourth generation light sources. These fourth generation light sources can cover a broad range from vacuum ultra violet (VUV) to hard x-rays with intensity 5 - 6 orders higher than the previous generation light sources and also provide pulsed beam (~ picosecond) with high degree of coherence [5-8].

Synchrotron radiation source comprises of an injector linac (or a microtron), booster synchrotron and a storage ring. High energy electrons (~ MeV) from the injector linac (or microtron) are fed to the booster synchrotron, where it attains desired energy (~ GeV) and finally these electron-bunches are injected to the storage ring. The storage ring is configured as a periodic arrangement of magnetic elements like dipoles, quadrupoles, sextupoles etc. forming a lattice (or unit cell). The lattice is repeated to form the closed ring of appropriate circumference. The dipole magnets in the storage ring play a major role by providing radial acceleration and thereby maintaining the

electrons in a closed orbit. Under the influence of transverse magnetic field of dipole magnets, the relativistic electrons move in circular path and emit synchrotron radiation tangentially to the circular path. Besides dipole magnets, intense synchrotron radiation is also produced with the help of insertion devices, where the electrons are allowed to move in a sinusoidal path under the influence of the periodic arrangement of permanent magnets. The radiated power loss by the electrons in the form of synchrotron radiation is compensated by the energy provided through radiofrequency (RF) cavities placed in the storage ring. As a result the energy of electrons is maintained at a constant value in the ring and radius of closed orbit is maintained. The production of synchrotron radiation from electrons passing through a dipole and an insertion device in a synchrotron storage ring is schematically shown in figure 1.1.

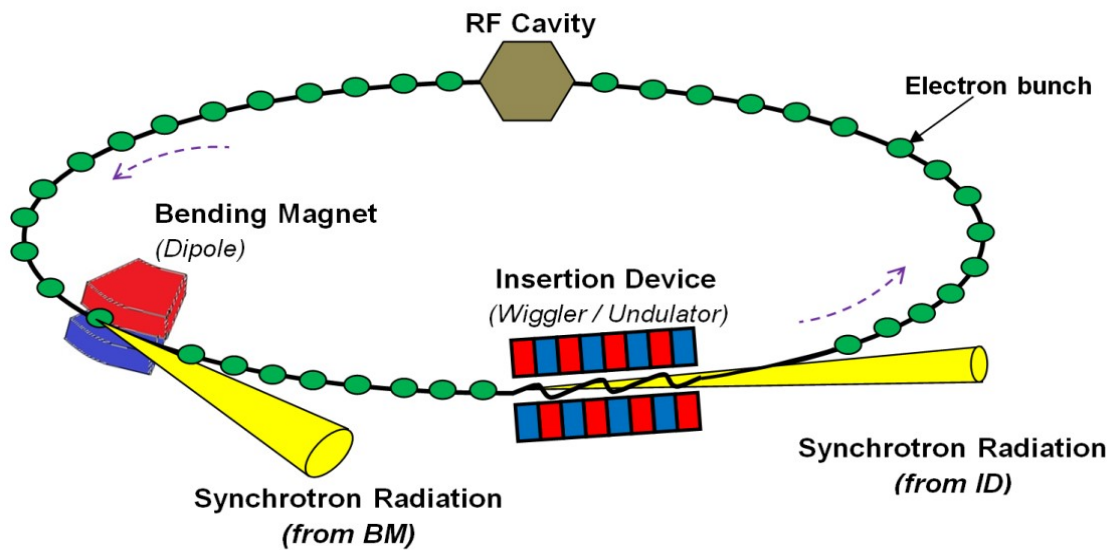


Figure 1.1: Schematic layout of a storage ring showing synchrotron emission from a dipole (BM) and an insertion device (ID) (not to scale)

As per classical electromagnetic theory, an accelerated charged particle will emit energy in the form of electromagnetic radiation. The radiated power from the charged particle is calculated using Larmor's equation as given below [5].

$$P_{rd} = \left(\frac{dE}{dt} \right)_{rad} = \frac{q^2}{6\pi\epsilon_0 c^3} a^2 \quad \text{----- (1.1)}$$

Here P , E , q , a , c respectively represent power loss, energy, charge, acceleration of charged particle and velocity of light in vacuum. From equation (1.1), the radiated power is proportional to the square of the acceleration. Thus the radiated power loss by light charged particle (electron) is $\sim 10^6$ times higher than heavy charged particle (proton) of the same energy and therefore, high energy electron (or positron) storage rings are best suited for synchrotron light sources. A comparison table for design parameters of six synchrotron radiation sources is given in table 1.1 [9-13].

Table 1.1: Design parameters of six synchrotron radiation sources

Parameter	ALS (USA)	Indus-2 (India)	NLSLS-II (USA)	SSRL (USA)	APS (USA)	SPring-8 (Japan)
Beam Energy (GeV)	1.9	2.5	3.0	3.0	7.0	8.0
Stored Current (mA)	500	300	500	500	100	100
Stored Particles ($\times 10^{12}$)	1.6	1.1	8.2	2.4	2.3	3.0
Ring Circumference (m)	197	172.3	792	234	1104	1496
Beam emittance, ϵ_x	2.0	58.1	0.55	10.0	3.1	3.4
(nm-rad) ϵ_y	0.04	5.81	0.008	0.014	0.04	0.0068
Design Lifetime ^s (hrs)	8	24	~ 3	20	54	150
Wiggler ID Field, B (T)	2.1	5	3.5	2	1	1
ID E_c (keV)= $0.665BE^2$	5	21	21	12	33	43

^s**Note:** Beam lifetime is usually defined as the time during which the stored beam current decays to $1/e$ of its initial value, assuming a pure exponential decay of stored beam. Abbreviations used in the table are listed below.

[**ALS:** Advance Light Source, Lawrence Berkeley National Laboratory, Berkley, USA; **Indus-2:** Indus-2 synchrotron facility, Raja Ramanna Centre for Advanced Technology (RRCAT), India; **NSLS-II:** National Synchrotron Light Source II, Brookhaven National Laboratory, USA; **SSRL:** Stanford Synchrotron Radiation Laboratory, Stanford Linear Accelerator Center (SLAC), USA; **APS:** Advance Photon Source, Argonne National Laboratory, USA; **SPRING-8:** Super Photon ring 8, RIKEN, Japan]

The properties of synchrotron radiation like broad spectral range, high intensity, high collimation, polarization and pulsed nature immensely attract scientific community. Therefore dedicated beamlines are designed and developed on SRS for utilization of the synchrotron radiation. The details of the synchrotron beamline will be discussed in the following section.

1.1.1 Synchrotron radiation beamline

A synchrotron beamline is an arrangement of optical elements like mirrors, monochromators, slits, filters etc. to transport synchrotron beam from the source point to the sample at the experimental station, typically 10 to 50 m from the source point. The synchrotron beam is tailored to the experimental requirements like beam size, photon flux, energy, polarization, etc. in the beamline. Each synchrotron radiation facility has many synchrotron beamlines and each beamline is designed depending on the experimental requirement. For application of soft x-ray photons, the complete beamline is maintained under vacuum condition, whereas in hard x-ray beamlines the samples can be kept at atmospheric condition in air. The schematic layout of a typical beamline is shown in figure-1.2.

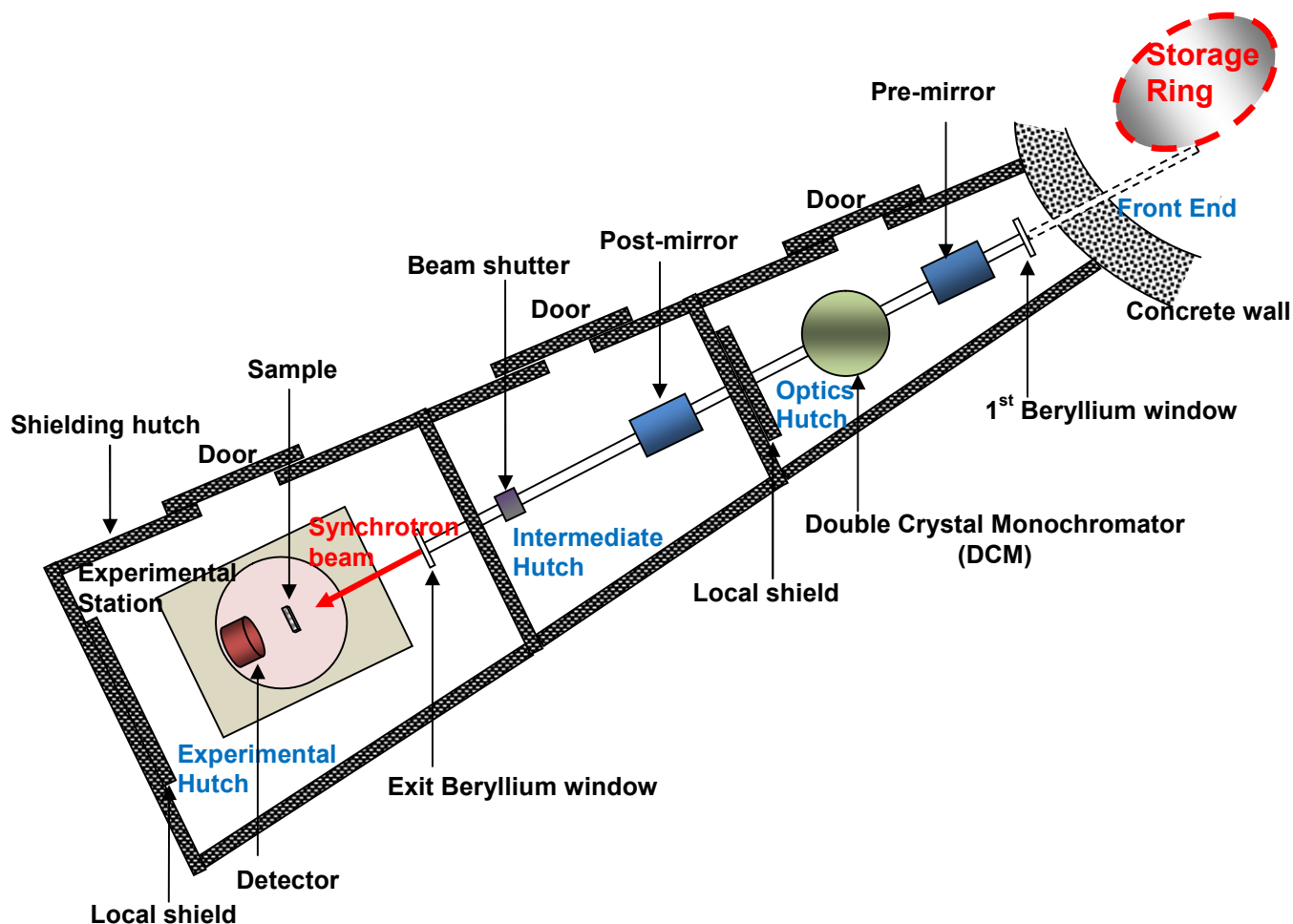


Figure 1.2: Schematic layout of a synchrotron beamline (not to scale)

For any synchrotron beamline, front end acts as the interface between the storage ring and the beam line. The front end has various safety and beam defining components like fast closing shutter, water cooled shutter, safety shutter, collimator, fixed mask etc. The safety shutter is made up of a thick densimet block and acts as a radiation stopper. In hard x-ray beamlines, the front end is connected to the beamline through water cooled beryllium window (typically 200 μm thick) placed at the end of the front end. The entire beamline is housed in a shielded hutch. The beamline hutch is usually divided into three sections; the optics hutch, the intermediate hutch and the experimental hutch. The optics hutch which joins the front end of the beamline

primarily comprises of major optical components like pre-mirror, Double Crystal Monochromator (DCM) etc. The collimated, monochromatic beam from the DCM enters the intermediate hutch where the beam is focused to the experimental station using post-mirror. The final and most important part of the beamline is the experimental hutch, where the synchrotron radiation/hard x-ray beam comes in air and incident on samples placed on a sample stage. The operation of the beamline is controlled from a control room, outside the experimental hutch. However, it may be noted that the beamline configuration mentioned above is typical and may change depending upon the requirement of the experiment. Because of high radiation hazard, all the beamline components are enclosed inside the shielded hutch. The details of the radiation environment in synchrotron beamlines will be discussed in the following section.

1.2 Radiation environment in synchrotron radiation facility

In electron storage rings, relativistic electrons are allowed to circulate in vacuum envelope maintained at ultra high vacuum ($\sim n$ Torr). During circulation, electron beam gets diverted from orbital path due to a) elastic collision between electron and residual gas molecules (Touschek scattering) (b) inelastic electron-gas collision (bremsstrahlung) and (c) intra-beam electron-electron collisions resulting in electron beam loss [14-15]. The interaction of electron beam with structural materials (and/or gas molecules) in vacuum chamber result in the production of bremsstrahlung radiation, electrons, positrons and photoneutrons through electromagnetic cascade process [16]. In addition to the synchrotron radiation, the bremsstrahlung x-ray dominates the radiation environment in synchrotron beamlines. The types of radiation encountered in synchrotron beamlines and their properties are discussed in the following section.

1.2.1 Bremsstrahlung radiation

As per classical electromagnetic theory, an accelerated charge will emit electromagnetic radiation. Therefore the electron on interaction with the atomic nucleus gets accelerated due to

coulomb interaction and emits out electromagnetic radiation, called as bremsstrahlung radiation. The process is also known as free–free emission since the radiation corresponds to transitions between unbound states of the electron in the field of the nucleus [17]. The process of bremsstrahlung emission is shown in the figure 1.3.

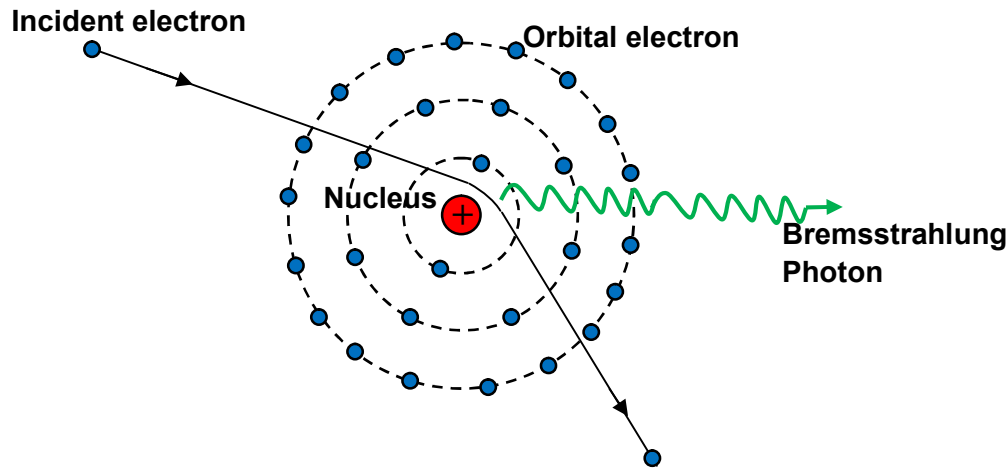


Figure 1.3: Generation of bremsstrahlung radiation

Bremsstrahlung radiation is also treated as the radiative energy loss by charged particles and is the dominant mechanism of energy loss by high energy electrons, interacting with materials. The radiative energy loss by electrons per unit length in the medium is mathematically given by following expression [18].

$$-\left(\frac{dE}{dx}\right)_{rad} = \frac{NEZ(Z+1)e^4}{137m_0^2c^4} \left(4 \ln \frac{2E}{m_0c^2} - \frac{4}{3}\right) \quad \text{----- (1.2)}$$

Here N = Number density of absorber atoms, Z = Atomic number of the absorber atom, m_0 = rest mass of electron, e = charge of electron, c = velocity of light, E = Kinetic energy of electron.

In case of Indus-2 (2.5 GeV electron synchrotron), the first term inside the bracket of equation (1.2), is nearly 36 ($\gg 4/3$) and thus the radiative loss scales approximately as Z^2 and $ELnE$. So the bremsstrahlung yield will be higher for high energy electrons and in high atomic number

materials. Depending upon the density of interacting medium, the bremsstrahlung can be classified in two categories, solid bremsstrahlung and gas bremsstrahlung.

1.2.1.1 Solid bremsstrahlung

Solid bremsstrahlung radiation is generated by the interaction of energetic electrons with solid materials like metallic vacuum pipes and other structural materials in the storage ring. As a conservative approach in radiation protection, solid bremsstrahlung dose rate is calculated assuming the interaction medium to be high atomic number and thick target, producing maximum yield of bremsstrahlung photons. The thickness of the target (x), in this case is much higher than the radiation length (X_0). Radiation length is the mean thickness of material in which a high energy electron loses $(1/e)$ of its energy through bremsstrahlung process. Thus the fractional energy loss by high energy electrons in a medium can be given by the following expression [19-21].

$$\left(\frac{dE}{dx}\right)_{rad} = -\frac{E}{X_0} \quad \Rightarrow \quad E(x) = E_0 e^{-x/X_0} \quad \text{----- (1.3)}$$

Here E_0 is the incident electron energy. The bremsstrahlung energy spectrum is extended up to the incident electron energy (E_0). The bremsstrahlung spectrum in the forward direction (0°) falls off as $\sim k^{-2}$, where k is the photon energy and falls off at a faster rate at higher angles. Hence the spectral intensity of bremsstrahlung radiation depends on energy of the electron, atomic number, thickness of the target and also on the angle of observation. The bremsstrahlung photon intensity initially increases with increasing target thickness until the self-absorption modifies this increase to a broad maximum, followed by an exponential fall at larger thicknesses [19]. The intensity of bremsstrahlung radiation peaks in forward direction for incident electron energies, $E_0 > 1.5$ MeV. The harder radiation (most energetic photons) is emitted in the forward direction and the radiation becomes softer at higher angles. The angular distribution becomes sharper with

increase in incident electron energy. The characteristic angle of bremsstrahlung is given by the following empirical relation [19].

$$\theta_{1/2}(\text{degree}) \approx \frac{100}{E_0(\text{MeV})} \quad \text{----- (1.4)}$$

Here $\theta_{1/2}$ = angular width of the forward lobe of bremsstrahlung at half intensity.

The normalized total photon differential yield per incident electron is given by the following empirical relation [21].

$$\frac{1}{E_0} \frac{dN}{d\Omega} = 4.76E_0 \exp(-\theta^{0.6}) + 1.08 \exp\left(-\frac{\theta}{72}\right) \text{ Photons } sr^{-1} \text{ GeV}^{-1} \text{ electron}^{-1} \quad \text{----- (1.5)}$$

Here θ = angle of observation (degree). From equation (1.5), first term reflects sharp fall of intensity at smaller angles and the second term shows slow variation at wider angles. The first term is due to the high energy photons, confined to smaller angles and the second term represents a slow fall because of the low energy photons. From the above relation, it is clear that the bremsstrahlung dose will also have a strong angular dependence. Swanson has suggested three rules of thumb for estimation of bremsstrahlung absorbed dose rate at one meter from a high Z thick target, normalized to incident electron beam power and are listed below [19].

$$\left. \begin{array}{l} \text{a) } \theta = 0^\circ, E_0 < 20 \text{ MeV:} \quad \dot{D}(\text{Gyh}^{-1} \text{kW}^{-1} \text{m}^2) \approx 20 E_0^2 \\ \text{b) } \theta = 0^\circ, E_0 > 20 \text{ MeV:} \quad \dot{D}(\text{Gyh}^{-1} \text{kW}^{-1} \text{m}^2) \approx 300 E_0 \\ \text{c) } \theta = 90^\circ, E_0 > 100 \text{ MeV:} \quad \dot{D}(\text{Gyh}^{-1} \text{kW}^{-1} \text{m}^2) \approx 50 \end{array} \right\} \text{----- (1.6)}$$

Where \dot{D} = Absorbed dose rate and E_0 = Incident electron energy (MeV).

Recent study on bremsstrahlung dose rate from thick targets for electron energies 450 MeV to 3 GeV has reported overestimation in dose calculation using equation (1.6-b) [22]. Thus the

bremsstrahlung dose has a strong dependency on target material, target thickness and also on the angle of observation.

1.2.1.2 Gas bremsstrahlung

As discussed earlier, relativistic electrons are circulated inside the storage ring to produce synchrotron radiation. The storage rings are maintained at ultra high vacuum (nTorr) to reduce electron beam loss due to scattering with gas molecules in the vacuum chamber. Inelastic scattering of electrons with residual gas molecules will produce bremsstrahlung radiation, called as gas bremsstrahlung. The gas bremsstrahlung radiation has a broad spectrum ranging up to the energy of primary electron beam. These photons channel to beamline along with the synchrotron radiation and pose radiation hazard to beamline users [23-24]. These high energy photons as compared to synchrotron photons (\sim keV) require special attention for their mitigation especially in the case of insertion device beamlines. Hence gas bremsstrahlung is treated as major radiation hazard in synchrotron beamlines. Schematic layout of a beamline showing the channeling of gas bremsstrahlung radiation into the beamline is given in figure 1.4.

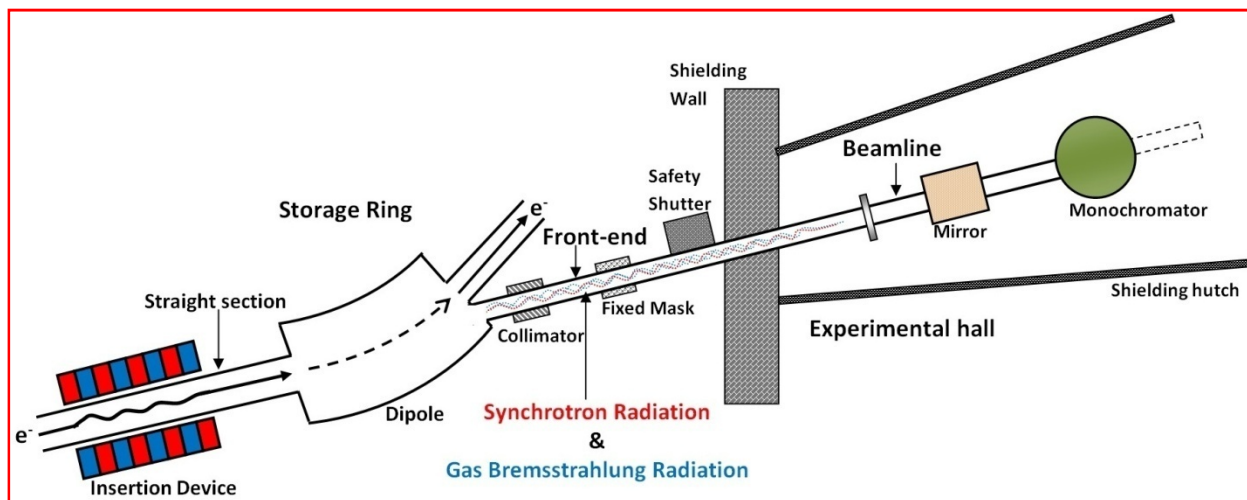


Figure 1.4: Schematic diagram of a beamline showing channeling of gas bremsstrahlung radiation from storage ring (not to scale)

Since the density of residual gas molecules is very small compared to thick solid targets, the gas bremsstrahlung radiation can be treated as thin target bremsstrahlung and is emitted out in a very narrow cone (\sim mrad). Although the number of residual gas molecules is very small, the production of gas bremsstrahlung is significant due to the millions of turns taken by the electrons per second through the vacuum pipe. Similar to solid bremsstrahlung radiation, the gas bremsstrahlung also has a broad spectrum ranging up to the primary electron energy. Because of strong angular distribution, broad energy range and mixed with intense synchrotron radiation, gas bremsstrahlung radiation poses challenges in detection and measurement.

The probability of an electron with energy E_0 to produce a photon of energy between k and $k+dk$ while interacting with an atom of atomic number Z , is given by the following expression [23]

$$\Phi_k dk = 4\alpha r_e^2 Z(Z+1) \frac{dk}{k} f(\nu, z) \quad \text{----- (1.7)}$$

Where,

$$f(\nu, z) = \left(\nu^2 - \frac{4\nu}{3} + \frac{4}{3} \right) \ln \left(\frac{183}{Z^{1/3}} \right) + \frac{1}{9} (1-\nu) \quad \text{----- (1.8)}$$

And $\alpha =$ Fine structure constant ($1/137$), $r_e =$ Classical radius of electron (2.82×10^{-13} cm) are constants and $\nu = k/E_0$ is the normalized energy of the emitted photon.

The gas bremsstrahlung production has strong atomic number dependence of $Z(Z+1)$, the same as in the case of solid bremsstrahlung (see equation (1.2)). Rossi suggested an analytical formula to calculate the gas bremsstrahlung spectrum from air and as per the formula, the number of photons with energy k and $k+dk$ produced by an electron with energy E_0 passing through an air thickness of 1 g cm^{-2} is given by [25]

$$k \frac{dN}{dk} = 4\alpha r_e^2 \left(\frac{2N_A}{A} \right) Z(Z+1) f(\nu, z) \quad \text{----- (1.9)}$$

Here N_A = Avogadro's number (6.023×10^{23}), A = molecular mass of air (28.9 g mole^{-1}) and Z = effective atomic number of air (7.23). The multiplier 2 accounts for the fact that over 99% of air is made of diatomic molecules.

1.2.2 Synchrotron radiation

Synchrotron radiation is also a source of high radiation hazard in synchrotron beamlines because of its high intensity and broad spectral range. The major properties of synchrotron radiation from bending magnet and insertion devices [5-8], which play crucial role in dosimetry, are discussed below.

1.2.2.1 Properties of synchrotron radiation from bending magnet

a) **High intensity:** Synchrotron radiation intensity or flux is many orders higher than conventional x-ray sources and thus reduces experimental time significantly. Usually flux is the unit used to quantify intensity of x-ray photons however, synchrotron community uses special term "Brightness or Brilliance" as a measure of the intensity of synchrotron radiation. Spectral flux and brilliance are defined as follows.

$$Flux = \frac{(\text{photons/s}) \text{ per } mrad(H) \text{ acceptance}}{0.1\% \text{ bandwidth}}$$

$$Brilliance = \frac{Flux}{[mrad]^2 \times [mm]^2}$$

Where $(mm)^2$ and $(mrad)^2$ represents transverse area and divergence of the source particles (i.e. electron bunch) respectively. Smaller bunch size or the angular divergence of the electron beam, more will be the intensity of the synchrotron radiation. The order of brilliance of x-ray tubes, bending magnet, insertion device and FEL synchrotron sources are of the order of 10^8 , 10^{12} , 10^{16} , $10^{20} \text{ photons/s/mrad}^2/\text{mm}^2/0.1\% \text{ BW}$ [3,6].

b) High collimation: The emission pattern of synchrotron radiation can be understood from the theory of radiation emission by accelerated charged particles and its relativistic transformation. The emission patterns of radiation by non-relativistic and relativistic charged particles undergoing centripetal acceleration are shown below.

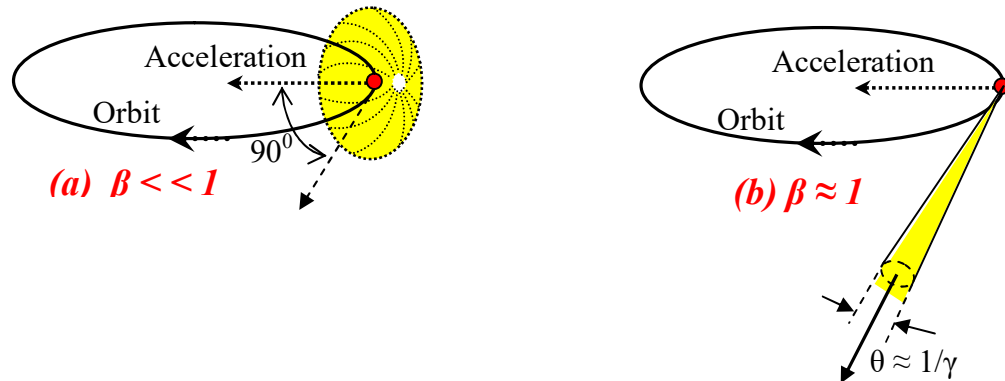


Figure 1.5: Radiation pattern from (a) non-relativistic and (b) relativistic charged particle under centripetal acceleration

The radiation emitted by accelerated charged particle moving at velocity, $v \ll c$, is similar to that of an oscillating dipole radiation which has maximum intensity in the direction perpendicular to the acceleration vector and no emission along the direction of acceleration. The emission pattern is independent of velocity of charged particle. However in the case of relativistic charged particle ($v \approx c$), the emission pattern gets transformed to a narrow cone in the direction of motion of the charged particle. The vertical opening angle depends on the velocity of charged particle as follows [5].

$$\theta \approx \frac{1}{\gamma} \quad \text{----- (1.10)}$$

Where the relativistic factor, $\gamma = \frac{1}{\sqrt{1-\beta^2}}$ & $\beta = v/c$

Because of this narrow emission angle, synchrotron facilities provide high intense photon beam on very small area of experimental sample. In the case of bending magnet radiation, a fan of synchrotron beam is produced in horizontal direction as the electrons produce radiation cone tangentially at each point of its curved path. Whereas, in insertion device based sources, both horizontal and vertical collimations are retained.

c) Broad and continuous spectrum: Spectral range of synchrotron radiation usually extends from infrared to hard x-ray and thus provides selection of energy as per the experimental requirement using monochromators and filters. The spectral distribution of bending magnet source is a continuous function and can be characterized by the critical wavelength (λ_c), which divides the spectrum into two parts of equal radiated power. The corresponding energy is called as critical energy (E_c) and mathematically expressed as [6,7]

$$E_c(\text{keV}) = 2.218 \frac{E_0[\text{GeV}]^3}{\rho[\text{m}]} = 0.665 \times E_0[\text{GeV}]^2 \times B[\text{T}] \quad \text{----- (1.11)}$$

Here E , B and ρ represent energy of electron beam, magnetic field of bending magnet and bending radius of electron beam respectively.

Due to very small emission cone ($\theta \approx \gamma^{-1}$) of radiation in tangential direction, an observer in laboratory frame sees a pulse of light for a short duration ($\Delta t \propto \gamma^{-3}$) as the electron passes by. Thus the frequency of these light pulses will be same as the electron revolution frequency and in frequency domain, the spectral distribution (i.e. Fourier transformation of Δt) becomes broad and continuous [6,7]. The spectral distribution [8] of bending magnet radiation in the horizontal plane can be expressed as

$$N(x) = 1.33 \times 10^{13} E_0[\text{GeV}]^2 \times I[\text{A}] \times x^2 K_{2/3}^2(x/2) \frac{(\text{photons/s})}{(\text{mrad})^2 (0.1\% \text{BW})} \quad \text{----- (1.12)}$$

Where $x = E/E_c$ and $K_{2/3}(x/2)$ is modified Bessel function.

The universal curve for spectral distribution of synchrotron radiation from a bending magnet as a function of E/E_c is shown below [26]. The energy dependencies of the two regions (shown in the curve) are approximate.

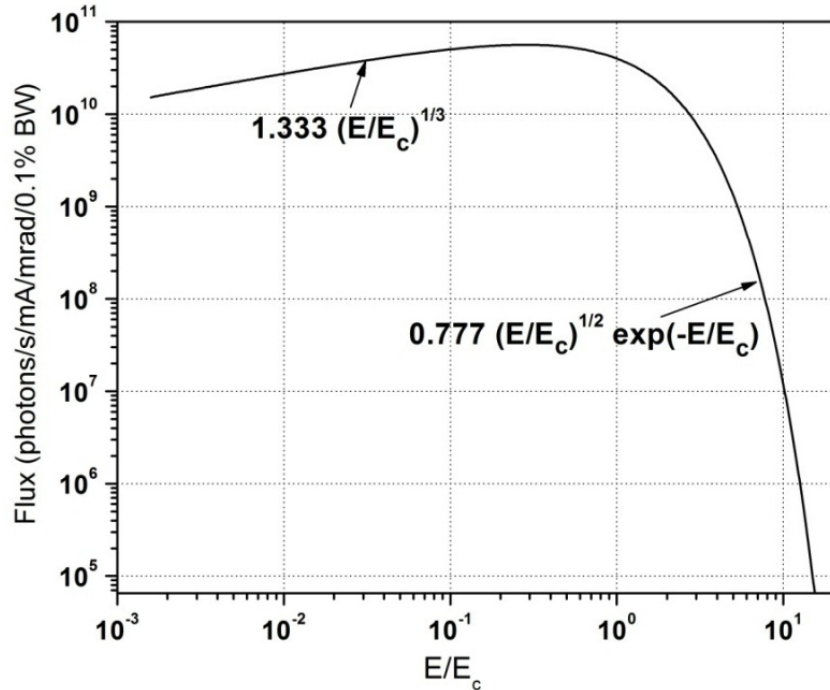


Figure 1.6: Spectral distribution of synchrotron radiation from a bending magnet

d) Polarization: In spatial distribution, synchrotron radiation from bending magnet is linearly polarized in the orbit plane whereas, elliptically polarized in above and below the orbit plane and thus provides useful tool to study magnetic behavior of experimental samples.

e) Pulsed time structure: Since the longitudinal electron bunch size and separation between two bunches are tunable, it provides flexibility in changing the pulse structure of synchrotron radiation for studying time evolution phenomena in samples. Small light pulses of picoseconds duration separated by nanosecond interval are very useful for time resolved experiments. The electron bunch length decides the synchrotron beam ON time and the bunch separation decides the OFF time.

1.2.2.2 Properties of synchrotron radiation from insertion devices

Insertion device (ID) is an array of periodic permanent magnets with alternating magnetic fields, used to enhance the brilliance of the synchrotron beam by several orders of magnitude as compared to that of bending magnet radiation. Electrons while passing through the alternating magnetic field oscillate in horizontal plane and emit synchrotron radiation. Thus these multiple deflections of electron increase the intensity of synchrotron radiation as compared to the bending magnet source. The energy range and intensity of synchrotron beam can be customized by varying the magnetic field through the movement of the upper and lower jaws (containing magnetic poles). The insertion devices are of two kinds, wigglers and undulators, characterized by its deflection parameter (K), given by the expression [6,7]

$$K = \frac{e}{2\pi m_e c} \lambda_u B = 0.934 \lambda_u [cm] \times B [T] \quad \text{----- (1.13)}$$

Here λ_u represents the period length of magnetic element. Physically, the deflection parameter signifies the maximum angular deflection of the electron beam. The deflection parameter for wiggler is $K \gg 1$, while that of undulator is $K \sim 1$.

Because of higher magnetic field in wiggler, the electron follows a curved trajectory with a smaller radius of curvature in comparison to dipole magnet. Thus the critical energy and spectral range of synchrotron radiation beam gets extended towards higher energies. Because of larger emission angle, the synchrotron photons emitted at different poles do not interfere and the net intensity increases only by a factor of $2N$ (where N stands for number of periods). However in the case of undulator, the emission angle is very small (because of weaker magnetic field) resulting in interference effect and the net intensity increases by a factor of N^2 and the spectral behavior is quasi-monoenergetic with peaks called as harmonics. The fundamental wavelength of radiation observed at an angle θ with respect to the axis of the undulator is given as [5-7].

$$\lambda = \frac{\lambda_u}{2\gamma^2} \left[1 + \frac{K^2}{2} + \gamma^2 \theta^2 \right] \quad \text{----- (1.14)}$$

In addition to the fundamental wavelength, higher harmonics of shorter wavelengths ($\lambda_n = \lambda/n$) are emitted. However on the axis ($\theta = 0$) only odd harmonics are emitted. The number and intensity of harmonics increase with K . Since K linearly depends upon magnetic field strength, energy of emission can be customized by varying the distance between upper and lower jaw of undulator. The high collimation (in vertical and horizontal directions) and the constructive interference effect increase the brightness of radiation from undulator. Pattern of radiation emission from different sources [adopted from Ref [5]] is shown in figure 1.7.

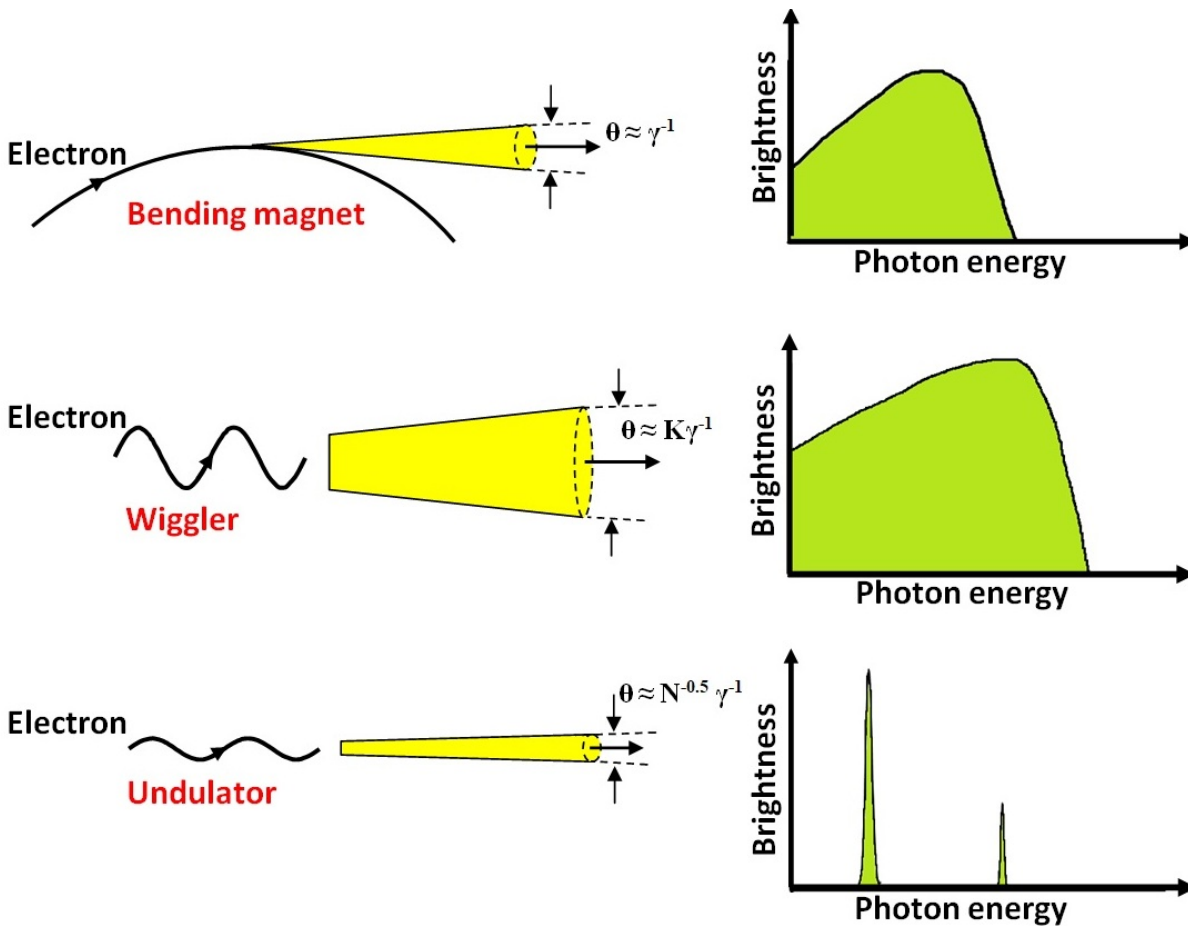


Figure 1.7: Radiation pattern from bending magnet, wiggler and undulator

1.2.3 Photo-neutrons

After bremsstrahlung radiation, the next major contributor to the radiation dose in high energy electron storage ring is photo-neutron. Photo-neutrons are produced as a result of interaction of bremsstrahlung radiation (high-energy photons) with accelerator structures. Since the energy of the bremsstrahlung photons is extended up to the incident electron energy and is well above the threshold for neutron production in interacting medium, neutrons are ejected out from the nucleus. Even very high energy bremsstrahlung photons (hundreds of MeV or higher) open up channels for (γ, n) , $(\gamma, 2n)$, (γ, np) etc. reactions. Electrons with energy higher than threshold energy for neutron production, on direct interaction with nucleus can also produce neutrons via virtual photon reactions. The photo-neutron processes dominate over the electro-neutron production because of 100 to 200 times higher cross section. The expression for neutron yield per incident electron of energy E_0 in terms of photon differential track length is given as follows [19].

$$Y(E_0) = \frac{N_A \rho}{A} \int_{k_{th}}^{E_0} \sigma_n(k) \frac{dL}{dk}(E_0, k) dk \quad \text{----- (1.15)}$$

Here $\sigma_n(k)$ is photo-neutron cross-section from (γ, n) , $(\gamma, 2n)$, (γ, np) reactions. $\frac{dL}{dk}$ is the photon differential track length distribution representing the total track length of all photons having an energy in the interval k and $k+dk$ and ρ is the density of the medium.

Three major photo-neutron production mechanisms based on the photon energy are giant resonance, quasi-deuteron effect and photo-pion decay. The processes are briefly described below.

1.2.3.1 Giant resonance mechanism

Photons with energy between neutron production threshold and ~ 30 MeV produce neutrons

primarily through 'giant photonuclear resonance', where the electric field of the photon transfers its energy to the nucleus and induces an oscillation between group of protons and the group of neutrons. The giant resonance cross-section has a large maximum at photon energies ~ 20 - 23 MeV for light nuclei and 13 - 18 MeV for medium and heavy nuclei. For $A > 40$, the width of resonance peak is approximately given by [19]

$$k_0(\text{MeV}) = 80A^{-1/3} \quad \text{----- (1.16)}$$

The integrated cross-section from threshold to 30 MeV can be expressed as,

$$\sigma = \int_{E_{th}}^{30\text{MeV}} \sigma_n(k) dk \sim \frac{NZ}{A} \quad \text{----- (1.17)}$$

Where $\sigma_n(k)$ is the photo-neutron cross-section as a function of photon energy and $N = A - Z$. The neutron spectrum from the giant resonance process has two components. The first one arises from the absorption of the photon to form a compound excited nucleus, which gives an isotropic evaporation spectrum (similar to fission neutron spectrum) with an average neutron energy of 1 - 2 MeV approximately. The second component is the direct emission neutrons with energy above 3 - 4 MeV. In the spectrum, nearly 86% neutrons are evaporation neutrons whereas, the direct emission accounts for only $\sim 14\%$ in case of medium to high Z materials.

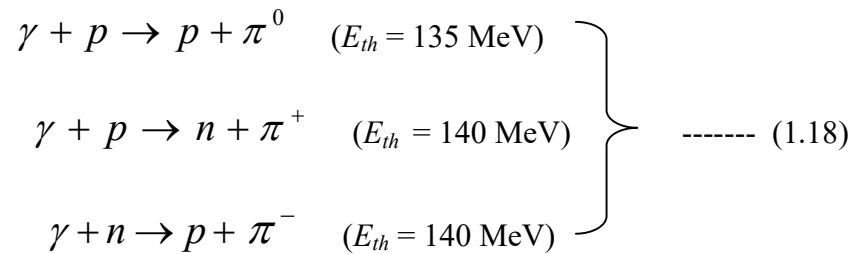
1.2.3.2 Quasi-Deuteron Effect

Photon in the energy range 30 - 300 MeV produce neutrons through quasi-deuteron effect, where the photon interacts with a neutron-proton pair rather than the entire nucleus unlike giant resonance mechanism. The wavelength of photon (~ 30 MeV) closely matches with the average inter-nucleon distance and the photon interacts with pairs of nucleons. Because of the non-zero electric dipole moment, only neutron-proton pair interacts with the incident photon and thus this interaction is termed as quasi-deuteron effect. The cross-section reduces with further increase in

photon energy. The cross-section for this process is an order of magnitude less than the giant resonance peak. The contribution of this effect to the neutron spectrum is to add a high-energy tail to the giant resonance spectrum. The energy of neutrons from quasi-deuteron effect may go up to half of the incident electron energy, above which only negligible neutrons may be present.

1.2.3.3 Photo-Pion effect

The photo-pion production starts at photon energy about 140 MeV, rest mass energy of pion. The photo-pion cross-section has a number of resonance peaks within ~ 1.1 GeV. The gamma-nucleon reactions responsible for pion production are [20]



The neutrons produced via photo-pion effect are more energetic than giant resonance neutrons, but their number is only a fraction of the giant resonance neutrons.

1.2.4 Electromagnetic cascade

The complex radiation field encountered in any high energy electron accelerator is the manifestation of electromagnetic (EM) cascade. Interaction of high energy electrons with any of the accelerator components will generate bremsstrahlung photons and these photons will produce electron and positron pairs through pair production. These interactions go on multiplying with the depth in medium and result in a cascade or shower of electrons, positrons and photons within the absorber medium. The number of particles in the cascade approximately doubles at each step until the electron energy falls below the critical energy (E_c) and the electron preferably undergoes collision. Similarly when the energy of bremsstrahlung photons within the cascade

reduces to a low value where the cross-section for pair production is comparable with that of Compton scattering, the shower development stops and the particles exponentially attenuate due to Compton scattering and photoelectric absorption. Therefore the depth dose profile has a build up at initial depth followed by exponential fall. The schematic representation of EM shower generation and the corresponding depth dose profile are shown in figure-1.8.

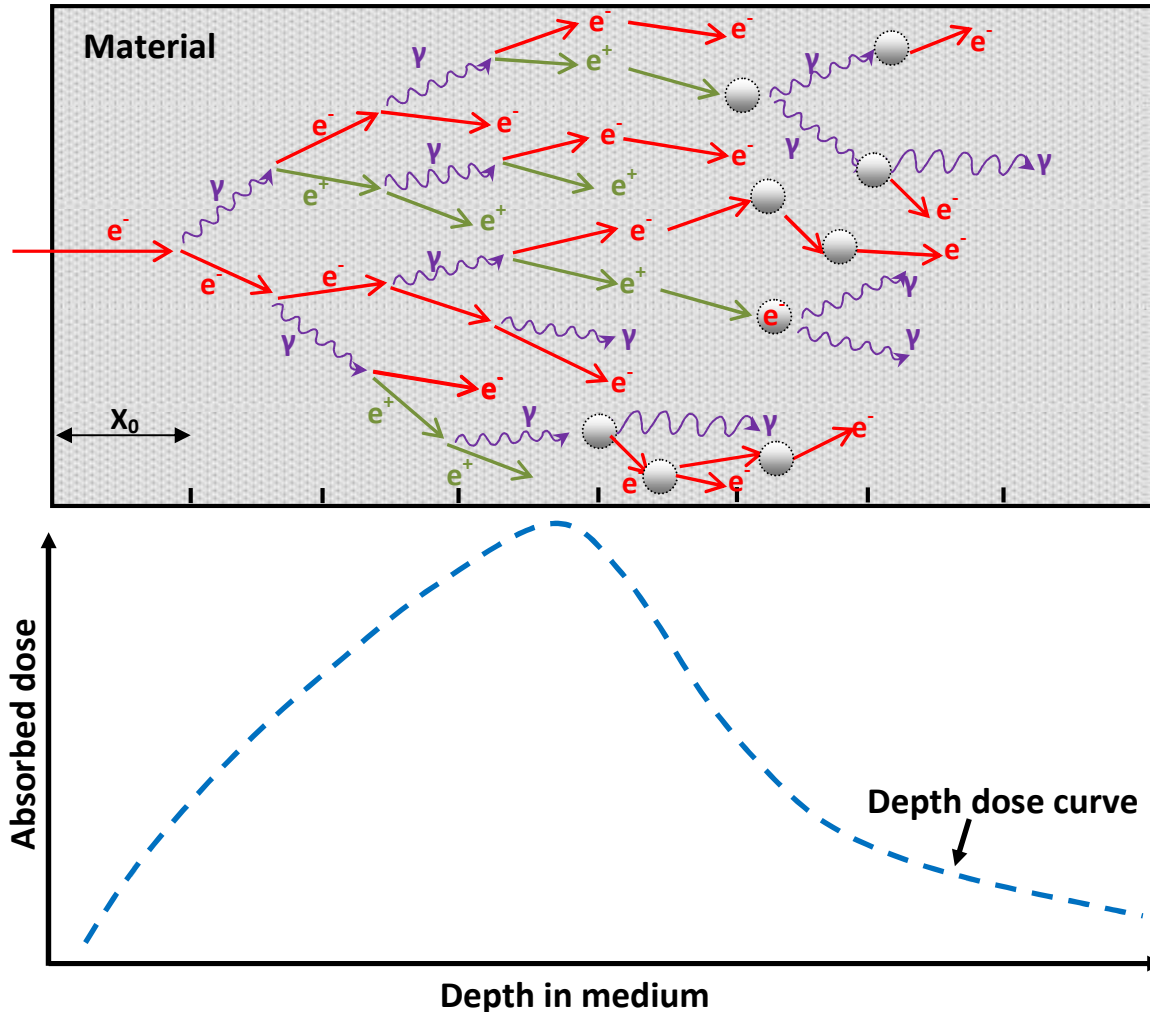


Figure 1.8: Electromagnetic cascade and the corresponding depth dose in medium.

Electromagnetic shower in copper and lead generated by 1 GeV electrons was experimentally studied where the authors have measured the energy absorption in thin absorbers using LiF thermoluminescence dosimeters (TLD-700) [27]. In the forward direction (in the direction of the

electron beam), the absorbed dose in the exposed material increases initially up to a certain depth and then decreases. This dose build up effect has been studied extensively in the past and dose maximum in tissue phantom (dose equivalent index) was evaluated. The dose equivalent index is the maximum dose in 30 cm water (or tissue) phantom and can be assigned as the dose to the exposed human body [19-20].

The radiation environment in synchrotron beamline is therefore very complex due to mixed radiation field with broad energy spectrum and sharp angular distribution. The radiation environment is also dependent on the operating condition of storage ring as well as the beamline. In shielding point of view, the radiation hazards in synchrotron beamlines can be classified as mention in the table 1.2 below.

Table 1.2: Degree of importance of radiation hazards in synchrotron beamlines

Type of beamline	Gas bremsstrahlung	Synchrotron	Photo-neutrons
<i>Bending magnet</i>	Minor	Major	Minor
<i>Insertion device</i>			
<i>Undulator</i>	Major	Minor	Major
<i>Wiggler</i>	Major	Major	Major

Note: ‘Minor’ represents the case where that particular hazard is not potentially dangerous and can be mitigated with minor efforts.

1.3 Dosimetry at synchrotron radiation beamlines

Gas bremsstrahlung is considered as the primary radiation hazard in synchrotron beamlines because of its high energy nature. The gas bremsstrahlung photons on interaction with the beamline components produce scattered photons and photo-neutrons. In insertion device beamlines, the gas bremsstrahlung dominates radiation hazards whereas, the radiation environment in bending magnet beamlines is dominated by synchrotron radiation. Primary and scattered synchrotron radiations from beamline components are also potential source of radiation

hazard. Thus the radiation scenario in a synchrotron beamline is complex because of mixed radiation field of photons and neutrons with broad spectral range and sharp angular distribution. Radiation dosimetry in such radiation environment is very challenging due to limitations in conventional detector system in terms of energy response (up to few MeV), angular dependency and interference between the radiation types [24]. Therefore Monte Carlo packages like FLUKA, EGS, MCNP, etc. have been extensively used for quantifying the radiation environment in synchrotron beamlines of APS, NSLS-II, SPring-8, CLS, ILSF, SSRF, etc. synchrotron facilities. Radiation dosimetry studies performed at various synchrotron facilities are discussed in the following subsections.

1.3.1 Gas bremsstrahlung radiation dosimetry

The gas bremsstrahlung radiation dose in high energy electron storage ring was initially reported by Rindi in 1982. Using equation (1.7), the suggested theoretical expression for the number of photons of energy between k and $k+dk$ emitted per second per unit path length by electrons with beam current I (in e/s) inside a storage ring at pressure P (Torr) and temperature T (K) is given below [23].

$$\Phi_k dk = 8.21 \times 10^{-11} Z(Z+1)P \left(\frac{273}{T} \right) I \frac{dk}{k} f(v, z) \quad (cm^{-1} s^{-1}) \quad \text{-----} \quad (1.19)$$

The theoretical expression was compared with the measured gas bremsstrahlung spectrum at ADONE storage ring [28] and found to have good agreement except at very high energy due to poor resolution of the spectrometer. From equation (1.19), the energy spectrum was found to have $1/k$ dependency for a large range of k and extended up to the energy of the primary electrons.

Many researchers have studied the properties of gas bremsstrahlung like energy spectrum, angular distribution and corresponding dose rate in high energy storage rings. Most of reported

studies have used Monte Carlo simulation techniques to quantify the gas bremsstrahlung radiation. The reported experimental studies have highlighted the measurement issues due to factors like broad energy range, narrow emission angle of gas bremsstrahlung radiation and also due to the interference of accompanying intense synchrotron radiation.

The gas bremsstrahlung radiation was found to be highly forward-peaked with a characteristic emission angle (angle at which the intensity becomes $1/e$ of the maximum intensity) given as follows [30].

$$\theta_c = \frac{m_0 c^2}{E_0} = \frac{1}{\gamma + 1} \rightarrow \frac{1}{\gamma} \quad \text{for } \gamma \gg 1 \quad \text{----- (1.20)}$$

Rindi has also reported the measurement of gas bremsstrahlung dose in 1.5 GeV ADONE storage ring using LiF thermoluminescent dosimeter (TLD-100), with Co-60 calibration [23]. The measurement of gas bremsstrahlung spectrum and depth dose profile inside 30 cm water phantom in 2.5 GeV storage ring (Photon factory) using scintillation counter has been reported by S. Ban et al in 1987 [29]. Later on in 1989, the authors have extended the work using theoretical estimation of gas bremsstrahlung intensity, absorbed dose and shielding requirement for storage rings up to 10 GeV [30]. In 1990, a semi-empirical relation for estimating absorbed dose rate due to gas bremsstrahlung from storage ring was generated using EGS4 electron-photon Monte Carlo Code by Tromba and Rindi and is given below [31].

$$\dot{D}[\text{Gy/h}] = 1.7 \times 10^{-16} E_0^{2.43} \frac{P}{P_{atm}} I L \left(\frac{10 + \frac{L}{2}}{r} \right)^2 \quad \text{----- (1.21)}$$

Here E_0 = Electron energy (MeV), P = Pressure of the ring (Torr), P_{atm} = Atmospheric Pressure (= 760 Torr), I = Beam current (electrons/sec), L = length of straight section (m) and r = distance from the centre of the straight section (m).

The proposed equation (1.21) was based on data generated for primary electron energies ranging from 500 MeV to 10 GeV passing through air target at atmospheric pressure using EGS4 Monte Carlo code. In this study, the angular distribution of gas bremsstrahlung photons showed large broadening due to multiple scattering of electron with air molecules at atmospheric pressure. But in actual case, the number of molecules at ultra high vacuum condition is very less as compared to air at atmospheric pressure. Therefore Ferrari et al. in 1993, modified the empirical relation by artificially suppressing the multiple Moller scattering effects in air (at atmospheric pressure) using FLUKA Monte Carlo code. The empirical relation was established by simulation carried out for electron energy ranging between 100 MeV to 1 GeV and straight section lengths of 1 to 50 m. The suggested empirical expressions for fluence rate and absorbed dose rate are given below [32].

$$\Phi[cm^{-2}s^{-1}] = 1.9 \times 10^{-18} \left(\frac{E_0}{m_0 c^2} \right)^2 \frac{L}{d(L+d)} I \frac{P}{P_0} \quad \text{----- (1.22)}$$

$$\dot{D}[Gy/h] = 2.5 \times 10^{-27} \left(\frac{E_0}{m_0 c^2} \right)^{2.67} \frac{L}{d(L+d)} I \frac{P}{P_0} \quad \text{----- (1.23)}$$

Where d is the distance of the reference point from the end of the straight section (m).

In most of the simulation studies, characteristics of gas bremsstrahlung radiation were evaluated with air target (at atmospheric pressure) as a representative of vacuum chamber in storage ring and the results were normalized to the actual pressure (nTorr) in vacuum chamber. In real scenario, the composition of residual gas inside vacuum chamber at ultra high vacuum (UHV) condition is significantly different from atmospheric air composition. The composition of atmospheric air is dominated by nitrogen whereas, the residual gas inside vacuum chamber is dominated by hydrogen and gases containing carbon. In past, few simulation studies attempted to generate gas bremsstrahlung radiation in National Synchrotron Radiation Research Center,

Taiwan (NSRRC) storage ring and Iranian Light Source Facility, Tehran (ILSF) storage ring for the residual gas composition using FLUKA Monte Carlo code [33,34]. The studies were focused to evaluate radiation shielding due to gas bremsstrahlung in the respective storage rings. However dependency of gas bremsstrahlung dose on residual gas composition has not been established for actual vacuum conditions of different storage rings.

1.3.2 Synchrotron radiation dosimetry

Radiation dosimetry for synchrotron radiation needs special considerations due to its high intensity and low energy spectrum from few keV to about 100 keV. In hard x-ray beamlines, samples are exposed to synchrotron beam in air, and hence there exists a potential radiation hazard due to primary and scattered radiation around the sample location. The photons in keV energy range are highly absorbing and can result in very high skin dose on exposure to direct synchrotron beam. Photoelectric effect being the most dominant mechanism of interaction, most of the passive detectors shows strong energy response depending on its atomic number and energy of the incident photon. Energy and dose response of various radiation detectors like LiF based thermoluminescence materials, MOSFET detector and radiochromic films have been studied using synchrotron radiation [35-39]. These studies emphasized on the requirement of correction factor for accurate dose measurement depending on the energy and intensity of radiation in synchrotron beamlines. In addition, TL efficiency, energy attenuation co-efficient, light (TL) attenuation coefficients are also important factors in synchrotron dosimetry [36,37]. The observed variations in the degree of supralinearity, dose response curves, glow curve patterns in various dosimeters like LiF:Mg,Ti, Li₂B₄O₇:Cu, BeO and CaSO₄:Tm with incident photon energy have emphasized on the requirement for characterization of dosimetry devices in synchrotron radiation [38,39]. Thus the calibration of dosimeters through a primary standard device like free air ionization chamber [40,41] for low energy photons is essential for dosimetry

at synchrotron beamlines. Various standard laboratories like BIPM, NIST, PTB, NPL, ENEA etc. have established free air ionization chambers (FAIC) for calibration of dosimetry systems at low energy photons in the range 10-50 keV. These are particularly useful for calibration of secondary standard detectors used in dosimetry at medical diagnosis and radiotherapy facilities. Studies for radiation dosimetry at synchrotron facilities using FAIC are very rare. However a few researchers have tried to measure air kerma using free air ionization chamber at synchrotron beamlines [41-45]. Absolute air kerma measurement using a free air ionization chamber at beamline of ELETTRA synchrotron source has been reported in literature [41]. Various designs of FAICs have been established by several standard laboratories for low energy x-ray dosimetry but the most commonly used ones are parallel plate type. Synchrotron facility, SPring-8 has designed a parallel plate FAIC as an intensity monitor for synchrotron radiation up to 150 keV [42]. Depending on the energy and intensity of the radiation field, FAICs have been designed to cater radiation dosimetry studies in synchrotron facilities.

1.3.3 Photo-neutron dosimetry

The photo-neutron generation in synchrotron beamline has been studied using Monte Carlo codes, EGS4, MARS and FLUKA at beamlines of synchrotron sources like APS, SSRL, NSRRC, etc. Relative yield of neutrons and neutron dose from lead, copper, iron, tungsten and aluminum targets due to gas bremsstrahlung have been studied for 0.5 to 10 GeV electrons [46]. From the study, neutron yield has been found to be proportional to the $Z^{0.8}$, where Z is the atomic number of target. The authors have also pointed out that the relation may not be very general for other materials as the observed neutron yield from silicon target (commonly found in mirrors and monochromators) was only half of that from an aluminum target. The authors also proposed a simple scaling method for estimation of neutron yield and dose in synchrotron beamlines from gas bremsstrahlung radiation with the approximations like neutron yield from

high Z thick target and fluence to dose conversion factors for giant resonance neutrons only [46]. The study has also highlighted the dependence of photo-neutron yield on target (beamline components) diameter, angular divergence of gas bremsstrahlung photons, which can vary from facility to facility. Few measurements were reported on photo-neutron dose at undulator beamlines in NSRRC, SPring-8, APS synchrotron light sources [33,47-49]. Gas bremsstrahlung and associated photoneutrons in synchrotron beamlines of SPring-8 (8 GeV, 100 mA) synchrotron radiation facility were studied using EGS-4 code [47,48]. The complexities in quantification of photo-neutron dose have strongly motivated many researchers for independent evaluation of photo-neutron dose in synchrotron beamlines and have been reported in literatures [48-51].

1.4 Radiation shielding evaluation for synchrotron radiation beamlines

Depending on the beamline components and storage ring parameters, radiation shielding of the beamline needs to be evaluated. The intensity, spectral behavior and angular distribution of scattered radiation varies from beamline to beamline depending on the radiation source (bending magnet or insertion device), usable energy spectrum (white, pink or monochromatic) and the beamline optical design. Thus large numbers of independent studies have been performed to evaluate the radiation environment and respective shielding requirements for bending magnet and insertion device beamlines in synchrotron facilities like APS, NSLS-II, SPring-8, CLS, ILSF, etc. For synchrotron beamline shielding design applications, dedicated analytical codes like PHOTON and STAC8 have been developed to evaluate synchrotron radiation energy spectrum, its scattering effects due to different optical elements and shielding parameters [52-54]. A comparison study on the analytical codes (STAC8, PHOTON) and Monte Carlo codes (FLUKA, EGS4) used in shielding calculations due to synchrotron radiation in bending magnet and wiggler beamlines was reported by Liu et al [55]. From the study, STAC8 code was found to

have good agreement with FLUKA code in calculating synchrotron spectrum for bending magnet beamline at SSRL (3 GeV, 500 mA storage ring), while an underestimation was observed at high energy part of the spectrum calculated using PHOTON code. Also from the study, the calculated dose equivalent due to scattered synchrotron from silicon mirror showed a good agreement between FLUKA and EGS4, whereas STAC8 overestimated the dose by a factor of 2 to 5 and PHOTON underestimated [55]. The gas bremsstrahlung stop for undulator beamlines of 7 GeV electron synchrotron at Advanced Photon Source (APS) was evaluated using FLUKA Monte Carlo code [51]. Based on the study, 18 cm thick tungsten bremsstrahlung shield followed by 15 cm polyethylene neutron shield has been suggested. Empirical relations for surface dose rate as a function of electron beam energy (0.5 GeV to 10 GeV) due to scattered gas bremsstrahlung radiation in the angular range 145 to 180 degree in lead, copper, tungsten, silicon and aluminium targets have been reported using EGS4 Monte Carlo code [46,56]. Energy distribution of back scattered gas bremsstrahlung photons (produced by 3 GeV electrons) from lead target was found to be within 10 MeV. Radiation safety design on account of primary/scattered synchrotron radiation generated from optical elements of insertion device beamlines at various synchrotron facilities has been studied by many researchers using PHOTON code [57,58]. The angular distribution of scattered synchrotron radiation from scatterer and the effect of ground shine (scattered synchrotron radiation by a concrete floor of the beamline hutch) in SPring-8 (8 GeV, 100 mA) and X-ray Free electron laser (XFEL: 8 GeV electron Linac, 30 nA) were also evaluated using EGS-4 and STAC8 code [59,60]. The shielding requirement for various insertion device based beamlines at Canadian Light Source (2.9 GeV, 500 mA) due to secondary gas bremsstrahlung radiation generated by beam shutter (Copper), silicon crystal and gas bremsstrahlung stop (Lead) etc. were evaluated using EGS-4 code [60-64]. In these simulation

studies, shielding evaluation was performed by scoring radiation dose in water phantoms placed around the hutch wall. Similarly radiation shielding calculations for the synchrotron beamlines at National Synchrotron Light Source (NSLS)-II (3 GeV, 500 mA) were studied using EGS4 and STAC8 computer programs assuming 3 cm thick copper and 0.1 cm aluminum as potential scatterer for bremsstrahlung and synchrotron radiation [66]. Radiation levels and corresponding shielding requirement for experimental hutch due to gas bremsstrahlung and synchrotron radiation at 14.35 GeV Free electron laser facility (Linac Coherent Light Source- LCLS) was evaluated using FLUKA Monte-Carlo code [67]. FLUKA code was also used in evaluation of the shielding requirement for gas bremsstrahlung and synchrotron radiation in beamlines hutches of NSLS-II, Stanford Synchrotron Radiation Light source (SSRL), Iranian Light Source Facility (ILSF), Shanghai Synchrotron Radiation Facility (SSRF) etc. [68-72].

From these studies, it is clear that the radiation scenario in synchrotron beamlines are very specific to the facility as it depends on operating condition of storage ring as well as the beamline components. The primary radiation has a strong dependency on the storage ring parameters whereas, the secondary and scattered radiation are strongly dependent on the beamline components. Monte Carlo codes like EGS-4, PHOTON, FLUKA, etc. have been very useful for the shielding evaluation of the synchrotron beamlines worldwide. Independent evaluation of radiation shielding is essential for mitigating the primary and scattered radiation in every synchrotron beamline.

1.5 Radiation dosimetry at Indus synchrotron facility

Radiation monitoring and mitigation are essential requirements for running a radiation facility. Several studies have been performed in past to assess the impact of high energy radiation on dose rates indicated by radiation monitoring systems in Indus synchrotron facility [73-77]. The detail description on Indus synchrotron facility is given in Appendix-A. Underestimation of the dose by

a factor of 2-4 due to the high-energy bremsstrahlung photon radiation by conventional radiation monitors in Indus-1 storage ring (0.45 GeV, 100 mA) was highlighted by Haridas et al. based on depth dose measurements [73,74]. Studies on dose build up in water phantom for Indus-1 and Indus-2 (2.5 GeV, 300 mA) electron synchrotrons were also reported in order to evaluate the dose received by accidentally trapped radiation worker inside the storage ring area [75]. The authors also highlighted the requirement of proper build up medium for absorbed dose measurement using bare detectors like thermoluminescent dosimeter (TLD) or thin walled ion chamber during accidental beam loss at Indus-1 and Indus-2 storage rings. Measurement of direct and transmitted bremsstrahlung spectrum in energy range 300 keV to 12 MeV was measured using 50.8 mm x 50.8 mm BGO detector to study the spectral degradation on account of hybrid shielding around Indus-1 storage ring. From the study, the average energy of the transmitted bremsstrahlung spectrum was found to be 3.3 MeV and hence no build up medium is required for radiation monitoring outside the shielding wall. However build up medium is essential for dosimetry of unshielded high energy radiations in the storage ring area [76]. Bremsstrahlung dose in storage ring area due to accidental beam loss in Indus-1 was also experimentally measured using indigenously developed 17 cc cylindrical ion chamber with 5 mm perspex wall and found to be 5.69 mGy/event [77].

Besides area radiation monitoring, personnel dosimetry is another essential part of radiation safety program for any radiation facility. Thermoluminescent materials have been extensively used worldwide for personnel monitoring because of their wide dose range, stable response in varying environmental conditions, reusability, low fading and low cost. In Indus facility, personnel monitoring of radiation workers is carried out using $\text{CaSO}_4:\text{Dy}$ based thermoluminescence dosimeter (TLD) badge.

1.5.1 Personnel dosimetry in Indus synchrotron facility

CaSO₄:Dy based thermoluminescence dosimeter (TLD) badge is the standard personnel dosimeter being used all over India in radiation facilities like nuclear reactors, radiation processing facilities and accelerator facilities for monitoring photon and beta dose. This badge contains three CaSO₄:Dy PTFE (Teflon) thermoluminescence (TL) discs (diameter-13 mm and thickness-0.8 mm) as the radiation detectors. The TL discs are prepared from a homogeneous mixture of CaSO₄:Dy phosphor powder mixed with Teflon resin in a weight ratio of 1:3. The presence of dopant (Dysprosium) at 0.05 mol % in CaSO₄ makes the phosphor highly efficient for dosimetry applications. CaSO₄:Dy being a high atomic number material is nearly 40 times more sensitive for Co-60 gamma rays than most commonly used LiF based TL phosphors [78].

1.5.1.1 Energy response of the TLD badge

CaSO₄:Dy being a high atomic number material, shows strong energy dependence (over response) at low photon energies below 120 keV, due to dominance of photoelectric absorption [79-81]. To compensate this over response, metal filters are often used for dosimetry applications. The energy response of CaSO₄:Dy was studied with various combinations of metal filters like aluminium, stainless steel, copper, cadmium, tin and lead [81]. From the study, single high Z metal filter was found showing poor energy compensation due to its K-absorption edge and thus pointed out that better photon energy compensation can be achieved with filter combination of a high Z and a low Z material, (low Z material nearer to the TL disc). Based on these important aspects, the filter combination of presently used TLD badge for personnel monitoring in India was first reported by Vohra et al. in 1980 [78]. This badge was made up of three CaSO₄:Dy TL disc fixed on an aluminum card. The card was placed inside a plastic enclosure such that the TL discs were placed under different filters [metal (Cu+Al) filter, Perspex filter and open window (no filter)] from both front and backside. Three TL discs loaded

on the aluminium card are placed inside the plastic cassette. The metal and perspex filter combinations helps in discrimination of x-ray, gamma ray and beta particles in mixed radiation field. Beta response was studied with ^{90}Sr - ^{90}Y ($E_{\text{max}} = 2.27 \text{ MeV}$), ^{32}P ($E_{\text{max}} = 1.71 \text{ MeV}$) and ^{204}Tl ($E_{\text{max}} = 0.77 \text{ MeV}$) radioactive sources and photon energy response was studied with Philips ^{60}Co teletherapy machine, laboratory radium source (for gamma exposure) and Siemens deep-therapy x-ray machine (for x-ray exposure). The photon energy dependence of this TLD badge was studied in the energy range from 30 keV to 1.25 MeV. With the help of metal filter (Combination of copper and aluminium), energy response was modified, with a 65% over-response at about 60 keV and a 25% under-response at 30 keV, compared to a flat response at energies above 200 keV. Response of the TLD badge (Adopted from Ref.[78]) is shown in figure 1.9.

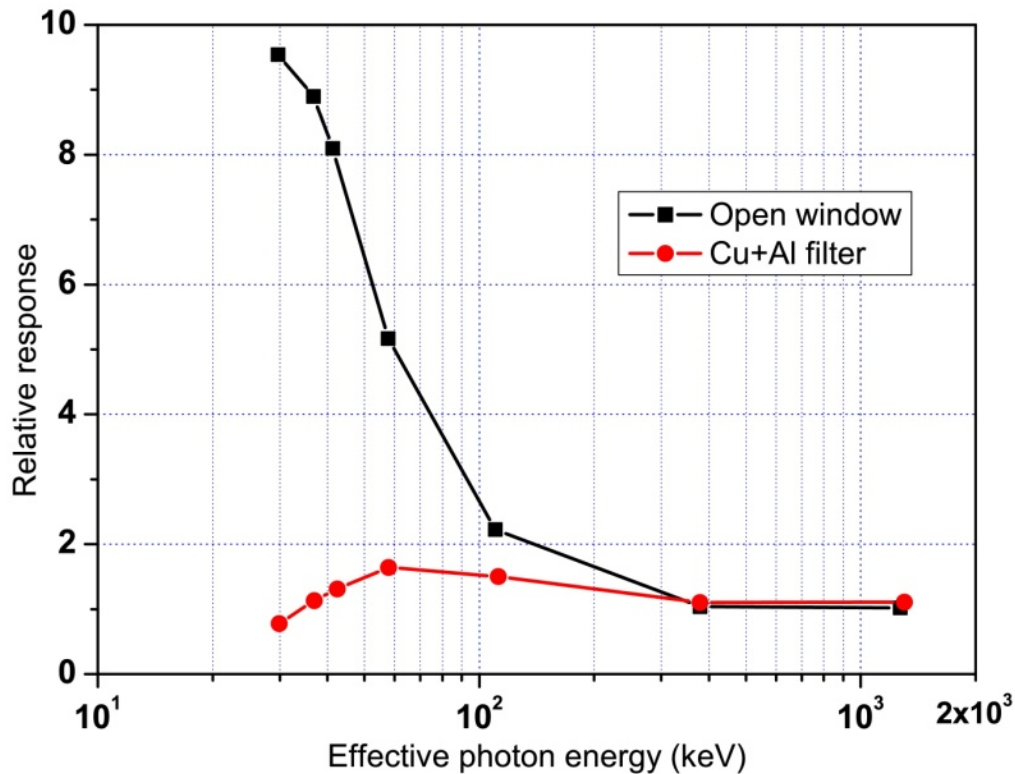


Figure 1.9: Relative response of TLD badge

Later on several algorithms have been proposed to extend energy response of the badge especially for low energy photons down to 17 keV [82-85]. Extensive studies in past have shown that LiF:Mg,Ti TL material ($Z_{\text{eff}} = 8.14$) was found to have better energy response than CaSO₄:Dy ($Z_{\text{eff}} = 15.3$) because of its tissue equivalence. The energy response of the CaSO₄:Dy and LiF:Mg,Ti TL materials has been studied in the x-ray regime of 7 to 35 keV by many researchers [86-89]. However the response of the TLD badge has not been subjected to studies below 30 keV.

Response of this TLD badge to high energy photon beams encountered at various medical Linacs up to 24 MV (effective photon energy ~ 9 MeV) is available in literature. Increase in response of the disc (under metal filter) with increase in photon energy was observed due to the energy deposited by the secondary electrons produced from the metal filter. Whereas, the decrease in response of the discs (bare and under Perspex filter) were observed with increase in photon beam energy due to the lack of build-up medium [90]. This study showed that the uncertainty in dose estimation using TLD badge has been found to be within 30% for photon of energy up to 15 MV (effective photon energy ~ 6 MeV) and beyond 15 MV, suggested for using suitable correction factor based on ratio of absorbed dose in TL disc under different filters. The energy of bremsstrahlung photons in the experimental hall of Indus-1 (450 MeV) synchrotron facility was measured experimentally using the TLD badge and estimated to be in the range of 1 - 4 MeV by using ratio of discs under metal and perspex filters [91]. Similarly study on the response of this TLD badge to high energy electron beam up to 18 MeV revealed that the disc under metal filter showed higher response than discs (bare and Perspex filter) and also the response of disc under metal filter was found to decrease with increase in the energy of the electron beam [92]. The studies highlighted the complexity in dose estimation using present TLD badge in high energy

synchrotron facilities like Indus-1 and Indus-2 because of the mixed radiation environment of high energy photons ($E \geq 15\text{-}20$ MeV) and high-energy electrons having energy of order of hundreds of MeV [92,93].

1.5.1.2 Dose response of TLD badge

In TL dosimetry, absorbed dose is estimated from the TL glow curve i.e. TL intensity as a function of temperature. The integrated counts under the glow curve are converted to the absorbed dose using calibration factor obtained by exposing to the doses with the standard radioactive source like Co-60. The $\text{CaSO}_4\text{:Dy}$ disc (in Teflon matrix) is having dose linearity up to 30 Gy and beyond 30 Gy, it shows supralinearity followed by saturation [94,95]. Because of low energy and high intensity synchrotron radiation, very high dose of the order of kGy/h is encountered in direct exposure to synchrotron radiation. Therefore in high dose exposure condition, the supralinearity and/or the saturation effects can lead to over or underestimation of actual dose. Study on effect of high dose on glow curve pattern of $\text{CaSO}_4\text{:Dy}$ disc has shown minimum variations in the glow curves for doses less than 1 Gy (with a single peak at $\sim 222^\circ\text{C}$), however wide variations in the shapes of glow curves were observed in dose range 1 to 1000 Gy, due to nonlinear growth and shift of high temperature shoulder [96]. Estimation of correct dose in the supralinear region (> 30 Gy) was also attempted but with limited success [97]. Moreover the TL fading increases with increase in dose and has been found to be $\sim 9\%$ for dose ~ 1 kGy in $\text{CaSO}_4\text{:Dy}$ disc after one month [98], is also detrimental factor in high dose estimation using conventional TL dosimetry technique. Thus the estimation of high dose using $\text{CaSO}_4\text{:Dy}$ through conventional TL technique is prone to errors due to many nonlinear effects and needs special investigations to overcome these challenges.

1.6 Summary and thesis motivations

The radiation scenario in synchrotron radiation sources is complex due to the presence of radiations with different characteristics as mentioned below.

- i) Broad spectral energy range of bremsstrahlung photons up to primary particle energy
- ii) High energy photo neutrons
- iii) Intense synchrotron radiation
- iv) Narrow angular distribution of gas bremsstrahlung and synchrotron radiation
- v) Pulsed nature of radiation
- vi) Mixed radiation environment (photons, neutrons, electrons, positrons)

The dosimetry of these radiations with conventional detection systems is challenging. Underestimation of dose from high energy radiation due to lack of proper dose build up inside detector medium also makes the measurement inaccurate. Intense synchrotron beam with broad spectral range (up to few tens of keV) and high energy gas bremsstrahlung radiation channeling into the beam line, complicate the radiation dosimetry. In addition, there is a wide variation in dose level of these radiations. Dose rate in scattered bremsstrahlung radiation can be as low as $\mu\text{Gy/h}$ whereas, the dose rate in direct synchrotron radiation may be in the range of kGy/h . So both sensitivity and the dynamic range of dosimetry devices have to be considered for accurate dosimetry in synchrotron beamlines. The complexity is further enhanced when these radiation interact with beamline components, producing scattered radiation. Therefore the estimation of dose becomes difficult due to uncertainty in the path of radiation and the geometry of the scatterer. In the past, several attempts have been made to address these issues, but the successes have only been partial. Moreover the magnitude of radiation is quite different for different facilities even with same energy and beam current because of the variations in vacuum condition,

structural components etc. The requirement of energy response correction in detectors is essential for proper estimation of dose especially in synchrotron energy range. Issue of high dose dosimetry using TL technique also needs special attention, as dose encountered in synchrotron beamlines is of the order of kGy, where conventional dosimetry techniques fail to measure dose accurately. The available empirical relation for determination of gas bremsstrahlung dose is limited for storage ring up to 1 GeV only. Besides the effect of the residual gases (inside vacuum chamber) on gas bremsstrahlung radiation dose are important and needs detail investigation. It is also felt from literature survey that there is no standardized radiation dosimetry system existing today for the kind of radiation environment in synchrotron beamlines. Energy response of the existing personnel dosimetry system in Indus-2 is established for energy range 30 keV to 3 MeV, whereas the energy of synchrotron beam regularly used in Indus-2 beamlines is lower than 30 keV.

Therefore it is strongly felt that significant amount of experimental and simulation studies are required to generate data for understanding radiation environment, addressing radiation dosimetry issues and radiation shielding schemes for synchrotron beamlines in 3rd generation light sources. The aim of the present work is given as follows:

1. To study the effect of residual gas composition of storage ring on gas bremsstrahlung dose and bring out a suitable relation to estimate dose rate accurately.
2. To study the energy response of conventional TL dosimeters in synchrotron radiation especially in the energy range <30 keV for accurate dose estimation. Also a primary standard detector needs to be designed for absolute dosimetry at synchrotron beamlines and calibration of various dosimeters.

3. To look for an alternative method to TL technique for estimation of high dose from CaSO₄:Dy dosimeters.
4. To quantify radiation dose in Indus-2 synchrotron beamlines and apply them for radiation shielding of the beamlines. Also a dedicated synchrotron beamline is required to address the gray areas in radiation safety research studies on ozone generation, Linear Energy Transfer (LET) for low energy photon, radiobiology, radiation damage of materials etc.

The thesis is organized in seven chapters and the contents of the chapters are briefly discussed below.

Chapter 1: Synchrotron radiation sources, synchrotron beamlines and the radiation environment in synchrotron facilities are discussed. The review status on dosimetry studies for various synchrotron radiation beamlines is also discussed. The present status of dosimetry studies at synchrotron beamlines of Indus-2 and the gray areas are highlighted.

Chapter 2: Basic concepts in Monte Carlo simulation and its application in dosimetry using FLUKA Monte Carlo code are discussed. Fundamentals of thermoluminescence dosimetry and material characterization techniques along with the experimental set-ups used in this study are also described.

Chapter 3: Studies for source term determination of gas bremsstrahlung radiation and the effect of residual gas composition on gas bremsstrahlung dose from electron storage rings are discussed. Improved empirical relations and their understanding have been described.

Chapter 4: Experimental and simulation studies performed at synchrotron beamlines of Indus-2 for quantification of dose due to synchrotron radiation are discussed. Design of a primary standard (Free air ionization chamber) for synchrotron dosimetry is also discussed. X-ray diffraction (XRD) and X-ray absorption near edge spectroscopy (XANES) studies on CaSO₄:Dy

material to understand the underline mechanism due to high dose exposure are presented. An alternate to TL dosimetry technique for high dose estimation is also discussed.

Chapter 5: Radiation shielding studies on bending magnet and undulator based synchrotron beamlines of Indus-2 are presented.

Chapter 6: Optical elements of a synchrotron beamline and their design criteria are described. The design aspects of a synchrotron beamline on Indus-2, dedicated for radiation physics and safety research are presented.

Chapter 7: The summary and conclusions of the work along with the scope for future work are presented in this chapter.

Chapter 2

Materials and Methods

2.1 Introduction

Monte Carlo simulation and the experimental techniques used for the reported work in the thesis are described in this chapter. Since FLUKA Monte Carlo code was used extensively in the present research work, radiation transport theory used in FLUKA code is discussed. Thermoluminescence (TL) dosimeters used in the experiments and their TL mechanism are also discussed in detail. Experimental investigations like X-Ray Diffraction (XRD) and X-ray Absorption Near Edge Spectroscopy (XANES) techniques using synchrotron radiation at Indus-2 synchrotron facility are covered briefly in this chapter.

2.2 Monte Carlo simulation techniques

Over the years Monte Carlo simulation techniques have found many applications in wide variety of scientific studies including radiation dosimetry and shielding. Though Monte Carlo simulation technique started initially to study neutron diffusion problems, later on it has been extended to a variety of complex problems in most of the branches of science and mathematics. Large numbers of computer codes based on Monte Carlo techniques have been developed to address complex challenges in quantification of radiation dose and evaluation of shielding in high energy accelerators. With advanced modern computers, Monte Carlo codes have given insight to the complex problems, a priori. Monte Carlo method is a numerical technique based on random

numbers to obtain the sample values for the problem variables. Basic principle of operation includes repeated random sampling of probability distribution functions of the problem variables, till it converges to the correct solution. The result of Monte Carlo calculation is a possible outcome of the process with a finite uncertainty value, which can often be reduced by increasing random events of the process. Interactions of radiation with constituents of matter being statistical in nature have paved its way into Monte Carlo simulations and packages like EGSnrc [99], PENELOPE [100], MCNPX [101], FLUKA [102,103] and GEANT4 [104,105], etc. have been developed and applied for radiation transport calculations. High energy particle accelerators facilities around the world have used these Monte Carlo packages to quantify radiation environment as well as for radiation shield design. Monte Carlo codes like EGS and PENELOPE have limited applications for studying transport of electron, positron and photons only whereas codes like MCNPX, GEANT4 and FLUKA are more versatile and can handle large number of particles including proton, neutron, muon, neutrino and heavy ion etc. A comparison table showing overview and capabilities of these three codes is given in table 2.1.

Table 2.1: Comparison of MCNPX, GEANT4 and FLUKA MC code [50, 101-105]

Properties	MCNPX	GEANT4	FLUKA
Abbreviation	Monte Carlo N- Particle eXtended	GEometry ANd Tracking	FLUktuierende KAskade
Lab. affiliation	Los Alamos National Laboratory	CERN, IN2P3, INFN, KEK, SLAC, TRIUMF, ESA	CERN INFN
Language	Fortran 90/C	C++	Fortran 77
Release format	Source & binary	Source & binary	Source & binary
Input format	Free	C++ main Fixed geometry	Fixed or free

Input cards	~120	-	~85
Parallel Execution	Yes	Yes	Yes
Electron energy range (GeV)	$10^{-6} - 10^0$ GeV	$10^{-6} - 10^5$ GeV	$10^{-5} - 10^6$ GeV
<u>Scoring Cards</u>			
Flux: Volume	Yes	Yes	Yes
Surface	Yes	Limited	Yes
Point/Ring	Yes	No	No
Current	Yes	Limited	Yes
Charge	Yes	Yes	Yes
Particle density	Yes	Yes	No
Reaction rates	Yes	No	Star (inelastic)
Energy deposition	Yes	Yes	Yes
<u>Variance reduction</u>			
Region biasing	Yes	Yes	Yes
Weight cutoff	Yes	Yes	Yes
Weight window mesh	Yes	Yes	Yes
Energy biasing	Yes	No	Yes
Applications	Nuclear criticality safety, Fission and fusion reactor, decontamination, radiation shielding, detector design, radiation dosimetry, medical physics, accelerator target design, radiography etc.	space and cosmic ray, nuclear physics, accelerator radiation, radiation computation, medical physics etc.	Radiation shielding, target and detector design, accelerator radiation, activation studies, calorimetry, radiation dosimetry, medical physics, Accelerator Driven Systems, cosmic rays, neutrino physics, radiotherapy etc.

2.2.1 Radiation transport in Monte Carlo

In a typical Monte Carlo radiation transport code, each incident particle travels in discrete steps and undergoes various interactions along its way. Occurrence and outcome of the interaction at each step are decided through a random sampling (using a pseudo-random number generator) from the appropriate probability distributions governing the physical process. Therefore random number generator is the heart of any Monte Carlo code and the accuracy of the result depends on the randomness in the generated data as well as the probability distribution functions available for the problem being modeled. The energy and direction of the resultant particles of the event is calculated through random sampling of the appropriate differential cross sections. The secondary particles (along with their physical parameters) generated at any event are stored in memory bank of the code and are transported in the medium in the same manner [106]. All the particles are transported in the system until they reach user defined energy limit (transport cut-off).

Mathematically, Monte Carlo simulation for particle transport is equivalent to the evaluation of a definite integral equation called Boltzmann transport equation. The Boltzmann transport equation accounts for changes in the phase space number density. Each particle is represented by a point in phase space, where each phase space dimension corresponds to particle's degrees of freedom in space consisting of position (x, y, z) and momentum (p_x, p_y, p_z) or in energy and direction (E, θ, ϕ) . Sometimes time is also considered as a coordinate or as an independent variable. The change in phase space number density can be attributed to either creation/loss of particle or motion of the particles in phase space. The Boltzmann equation is a balance equation in phase space representing change in phase space density (Ψ) in an infinitesimal phase space volume as the difference between all production terms and the destruction terms. The production terms include source particles, in-scattering, particle production whereas the destruction terms

include absorption, out-scattering, decay etc. Mathematical representation of Boltzmann equation is given below [107].

$$\frac{1}{v} \frac{\partial \Psi(x)}{\partial t} + \vec{\Omega} \cdot \vec{\nabla} \Psi(x) + \Sigma_t \Psi(x) - S(x) = \int \int_{\Omega E} \Psi(x) \Sigma_s(x' \rightarrow x) dx' \quad \text{----- (2.1)}$$

Here x represents the phase space coordinates $(\vec{r}, \vec{\Omega}, E, t)$ and dx represents the phase space volume.

$\Psi(x)dx$ or $\Psi(\vec{r}, \vec{\Omega}, E, t) d\vec{r} d\vec{\Omega} dE dt$: Particle phase space density defined as density of particles in volume $d\vec{r}$ about \vec{r} , travelling in direction $d\vec{\Omega}$ about $\vec{\Omega}$, with energy dE about E and at time dt about t .

$\frac{1}{v} \frac{\partial \Psi(x)}{\partial t}$: Time-dependent density change, where v stands for particle velocity

$\vec{\Omega} \cdot \vec{\nabla} \Psi(x)$: Density change due to translational movement of the particles into or out of the volume of space of interest without change of energy and direction

$\Sigma_t \Psi(x)$: Absorption, where Σ_t is the total macroscopic cross section (or inverse of the mean free path)

$S(x)$: Source particles

$\int \int_{\Omega E} \Psi(x) \Sigma_s(x' \rightarrow x) dx'$: Change in density due to collision (or scattering) at x , where Σ_s is the macroscopic scattering cross section. This also refers to the production term in the volume of interest as it contributes to those particles which are in-scattered.

Instead of explicitly solving this complex integro-differential equation, Monte Carlo approach uses random sampling technique to find the average behavior of the particles inside the medium.

In Monte Carlo method, each particle is tracked from its birth to death through the defined

geometry and the outcome of its interactions (or events) is generated from probability distribution functions through random sampling. For simplification, most of Monte Carlo transport codes assume homogeneous medium, no interaction among particles (only interactions with constituents of medium) [107]. A simple algorithm showing Monte Carlo approach is shown in figure 2.1.

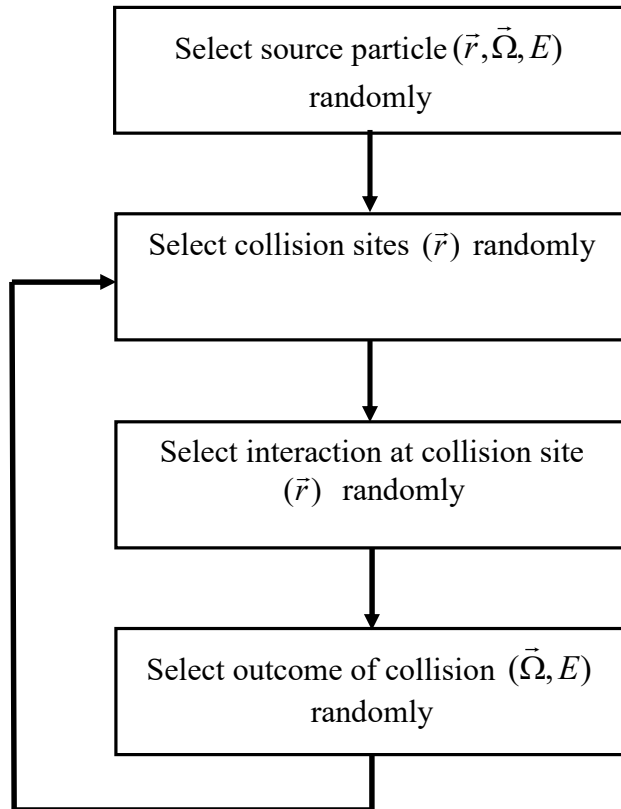


Figure 2.1: Simple algorithm on Monte Carlo approach

Thus Monte Carlo code is basically a software package, which includes the transport algorithms, random number generator, cross section data (for generating probability distribution function), wide variety of geometrical shapes or bodies for constructing the physical environment of the problem, scoring cards (estimators) and the program for analyzing the outcome of simulation.

The radiation environment in high energy accelerators is highly complex due to the high energy radiation (in the form of e^\pm , μ^\pm , protons, neutrons, photons etc), mixed field, high angular distribution and pulsed nature of radiation. Thus many times the experimental investigations to quantify the radiation levels in these facilities become very much challenging due to the limitations in conventional detectors. Therefore Monte Carlo packages are used frequently by the accelerator community for solving radiation safety problems. FLUKA Monte Carlo code has been used extensively in the research work, reported in this thesis. FLUKA code is chosen for the simulation studies as the code is extensively used for accelerator based radiation studies like shielding, dosimetry induced radioactivity etc. It also has the capability to transport sixty different particles in a wide energy range through complex geometries. The transport of synchrotron radiation including its polarisation effects and account for bound electron effects are the added advantages of FLUKA code. Special scoring options like dose equivalent using in-built fluence to dose conversion factors, radioactivity generation for complex irradiation profiles are also readily available in FLUKA for radiation safety studies.

2.2.2 FLUKA Monte Carlo code

FLUKA (FLUktuirende KAskade), a general purpose Monte Carlo code was developed and is being maintained through a joint project between INFN (Istituto Nazionale di Fisica Nucleare, Italy) and CERN (European Council for Nuclear Research, Switzerland) [102]. FLUKA is capable of transporting about 60 different elementary particles with energy range from thermal energy (neutrons), 100 eV (photons), 1 keV (all other particles) to \sim TeV energy through different media [102,108,109]. FLUKA also has provisions for transport of charged particle under electric and magnetic fields and can handle both polarized (e.g. synchrotron radiation) and optical photons (e.g. scintillation). The code has numerous applications in the following fields:

calorimetry, radiation detector design, shielding evaluation, radiation dosimetry and activation studies, neutrino physics, medical physics, cosmic ray studies, etc. Application of FLUKA in radiation shielding, residual activity, beam dump design and response of detectors for radiation safety at 7 TeV proton beam accelerator at Large Hadron Collider (LHC), the highest energy particle accelerator has accentuated its capabilities [110]. FLUKA code has been developed using FORTRAN 77 language. The complete package is handled through an advanced graphical user interface called as Flair used for preparation of input, geometry, scoring and visualization of results. FLUKA uses combinatorial geometry (CG) package, through which very complex geometries can be built using standard geometrical bodies and regions. The transport of electrons, positrons and photons in FLUKA is governed through Electro-Magnetic FLUKA (EMF), which handles all basic interactions like scattering, absorptions, bremsstrahlung emission, etc. Transport of low energy neutrons ($E < 19.6$ MeV) is performed through a multigroup algorithm, in which the cross-section library for neutron with energy range from thermal to 19.6 MeV is divided into 72 energy groups of approximately equal logarithmic width [102,108,109].

In FLUKA, users are provided with wide range of scoring cards (estimators) such as USRBDX, USRBIN, USRTRACK, USRYIELD to evaluate various physical quantities like fluence (spatial and energy spectrum), dose, radioactivity etc. The Boundary Crossing estimator (USRBDX) is used to estimate the double differential fluence or the current of particles as a function of energy, angle at a physical boundary between two space regions. The track length estimator (USRTRACK) calculates the fluence as a function of energy based on their path lengths within the region volume. Mesh binning estimator (USRBIN) provides spatial distribution of physical quantities like fluence, dose, activity etc. Estimator (USRFIELD) is used to find angular

distribution of particles. FLUKA can directly score dose equivalent by associating the estimators with dose equivalent conversion factors through AUXSCORE command. User can also set the cut off parameters through commands, PART-THRes (for hadrons and muons), EMFCUT (for electrons, positrons and photons) and LOWBIAS (for low-energy neutrons). Therefore FLUKA is an advanced versatile Monte Carlo package for solving radiation safety problems.

2.3 Thermoluminescence dosimetry

Thermoluminescence (also known as thermally stimulated luminescence) has been well known for a long period of time [111,112]. Thermoluminescence (TL) is a two step process, initially excitation through ionizing radiation followed by de-excitation in the form of light photons by heating. TL due to exposure from x-rays and radioactive substances was reported by Borgman [113]. The observed linear proportionality of TL intensity in specific materials with respect to the absorbed dose from ionizing radiation, suggested for potential application in radiation dosimetry. The application of TL in radiation dosimetry started in 1940s with conclusive works of Daniels et al. [114] and Cameron et al. [115] on LiF TL dosimeters. Properties like small physical size, availability in wide varieties, reusability, easy handling, wide dose linearity and relative energy independence have encouraged radiation professionals to opt for TL dosimetry application. In TL dosimetry, TL intensity as a function of temperature (called the glow curve) is generated and the area under the curve is calibrated using standard radioactive sources like Co-60 or Cs-137.

2.3.1 Principle of thermoluminescence (TL)

Theoretical model for understanding TL mechanism in materials was first proposed by Randall and Wilkins in 1945 [116] and later on improved by Garlick and Gibson in 1948 [117]. The TL mechanism is explained through electronic band model of solids [95,118-121]. As per the band

model, energy levels in valence band are completely filled with electrons and the conduction band is fully empty for insulators and semiconductors. The valence band and conduction band are separated by an energy gap called as forbidden band gap (E_g). In perfect crystal, no electrons are allowed to move inside the forbidden gap. However, if structural defects or impurities are present in the crystal lattice, there are finite localized states in the forbidden gap, where the occupancy of electrons is allowed. These metastable states act as trap centres for electrons (or holes) and on heating, TL is emitted out due to recombination of these charge carriers with other charge carrier of opposite sign at the recombination/luminescent centre. The simplified mechanism of TL phenomenon, explained with the help of energy band model, (Adopted from Ref [121]) is shown in figure 2.2.

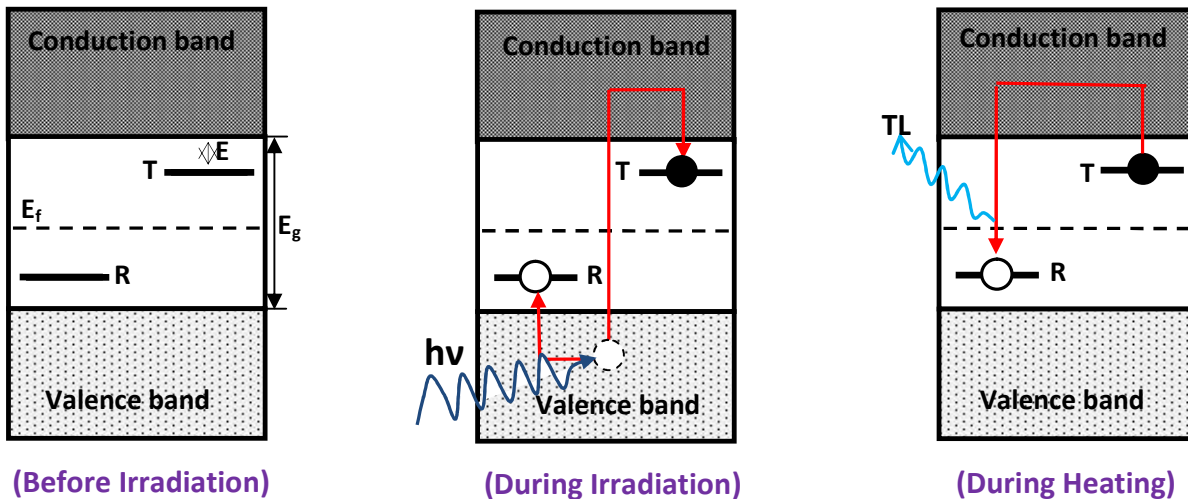


Figure 2.2: Mechanism of thermoluminescence. T and R represent electron and hole trap centres, respectively

Before irradiation, potential electron trap centre (T) and hole trap centre (R) are empty. During irradiation, on absorbing energy from radiation ($h\nu > E_g$), electrons move from valence band to conduction band. The freely moving electrons and holes either recombine with each other or get

trapped at respective trap centres. The direct recombination of free electrons and holes through emission of light occurs within 10^{-8} s. However, the charge carriers trapped in localized states, remain there for long time. These trapped electrons and holes can be released from the respective trap centres through thermal excitation. After releasing from the trap centres, these charge carriers move freely inside the crystal and recombine either through direct transition from conduction band to valence band or indirectly by recombining with previously trapped charge carrier of opposite sign, emitting luminescence. The temperature at which TL emission is observed, gives information of the trap depth and the TL intensity under the glow curve indicate the amount of carriers trapped at these sites.

2.3.2 Theory of thermoluminescence

The simple two level model showing thermoluminescence through indirect transition is shown in figure 2.2 above, where T and R represent electron trap centre and hole trap centre (also may act as recombination centre). The probability of an electron escaping from the trap centre T per unit time is given by Arrhenius equation as follows.

$$p = s \exp\left[-\frac{E}{k_B T}\right] \quad \text{----- (2.2)}$$

Where, s = Attempt to escape or frequency factor (s^{-1})

E = Trap depth or activation energy

k_B = Boltzmann constant (8.617×10^{-5} eV/K)

T = Absolute temperature

If the trap depth $E \gg k_B T_{ambient}$, substantial amount of electrons will remain trapped for a long period of time after the radiation exposure. During readout, temperature of the TL material is increased and thereby the probability of de-trapping and the recombination rate of electrons are

increased. Electrons on recombination with trapped hole centres, leaves the centre in excited state, following which light photon is emitted during de-excitation to the ground state. As per Randall-Wilkins model, TL intensity $I(t)$ is proportional to the rate of change of trapped electron density (n) at trap centres [116].

$$I(t) \propto -\frac{dn}{dt} \quad \text{----- (2.3)}$$

Where,
$$\frac{dn}{dt} = -np = -ns \exp\left[-\frac{E}{k_B T}\right] \quad \text{----- (2.4)}$$

From equation (2.4), it can be seen that TL intensity, $I(t)$ increases with temperature due to de-trapping and subsequent recombination of carriers and reaches a maximum as temperature is increased. Thereafter the intensity falls and thus the intensity profile (glow curve) shows a peak called as glow peak. Usually TL intensity is measured with a linear heating rate, $\beta = dT/dt$. Therefore the temperature at any instant is given as.

$$T(t) = T_{ambient} + \beta t \quad \text{----- (2.5)}$$

The famous Randall–Wilkins first-order expression of TL intensity at any temperature T' can be given as follows [116,121].

$$I(T) = -\frac{1}{\beta} \frac{dn}{dt} = -n_0 \frac{s}{\beta} \exp\left[-\frac{E}{k_B T}\right] \exp\left[-\frac{s}{\beta} \int_{T_{ambient}}^T \exp\left[-\frac{E}{k_B T'}\right] dT'\right] \quad \text{----- (2.6)}$$

Where,
$$n = -n_0 \exp\left[-\frac{s}{\beta} \int_{T_{ambient}}^T \exp\left[-\frac{E}{k_B T'}\right] dT'\right]$$

Here n_0 is the number density of trapped electrons at $t = 0$. From equation (2.6), TL intensity increases with temperature and reaches a maximum value at temperature T_m and falls afterwards.

Therefore at the peak temperature T_m , the condition for maxima ($dI/dt = 0$) gives [121]

$$\frac{\beta E}{k_B T_m^2} = s \exp\left[-\frac{E}{k_B T_m}\right] \quad \text{----- (2.7)}$$

From equation (2.7), it can be seen that peak temperature T_m is independent of n_0 and also increases with increase in trap depth (E) as more energy is required to release the charge carriers from deeper traps. Also, for a given trap depth (E), peak temperature (T_m) increases with increase in heating rate (β).

However, Randall-Wilkins model on thermoluminescence was based on assumption of negligible chances of re-trapping of electrons as compared to the chances for recombination during heating. In 1948, Garlick and Gibson [117] proposed a new model considering re-trapping of electrons during heating and because of the re-trapping of electrons, the light emission is delayed and the glow curve becomes symmetric compared to Randall-Wilkins model. Glow curve pattern for $\text{CaSO}_4:\text{Dy}$ and $\text{LiF}:\text{Mg,Ti}$ TL discs are shown in figure 2.3.

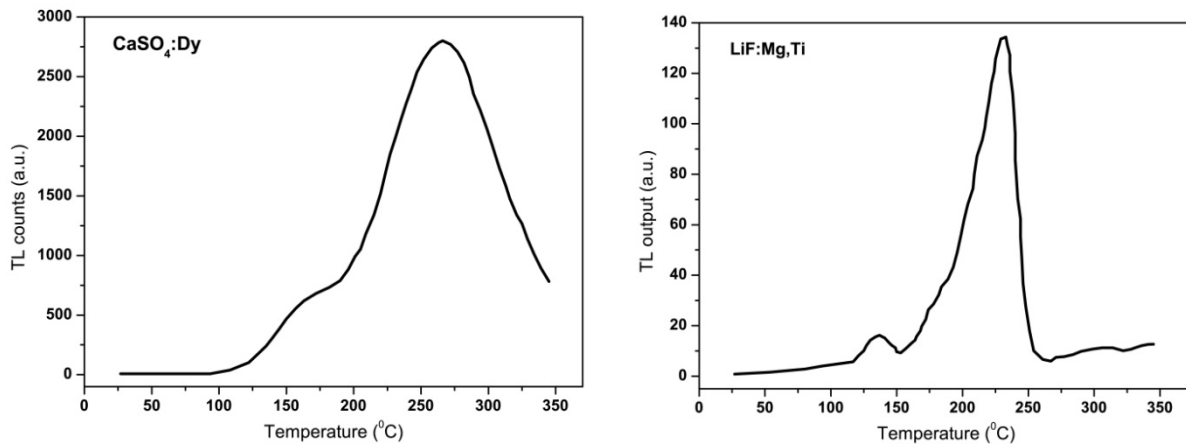


Figure 2.3: Glow curve patterns for $\text{CaSO}_4:\text{Dy}$ and $\text{LiF}:\text{Mg,Ti}$ TL discs

2.3.3 Thermoluminescence materials for dosimetry

Though a large number of materials show thermoluminescence property, only a few of them satisfy criteria for dosimetry applications. For dosimetry applications, TL materials should have good accuracy, high sensitivity, low fading, dose linearity and minimum energy dependency.

Commonly used TL phosphors in dosimetry include lithium fluoride (LiF), lithium borate ($\text{Li}_2\text{B}_4\text{O}_7$), magnesium borate (MgB_4O_7), calcium fluoride (CaF_2), calcium sulphate (CaSO_4), beryllium oxide (BeO), aluminium oxide (Al_2O_3), etc. with suitable dopants. The comprehensive discussions regarding preparation and properties of these TL materials are available in literature [94, 95, 122, 123]. Some of the important characteristics of the popular TL materials are given in table 2.2 [95]. In personnel dosimetry, the dose is assigned to radiation worker based on the TL output from the dosimeter which depends on the energy absorbed in the material. Thus in order to have better match between the energy absorbed in the material and the human body, it is preferred that the material shall be tissue equivalent i.e. the effective atomic number [124] of the material should be close to the effective atomic number of human tissue. Depending on the radiation qualities, like energy range and dose range, TL materials should be suitably selected for dosimetry applications.

Table 2.2: Comparison of important characteristics of the TL materials [95]

Phosphor	Glow peak temperature ($^{\circ}\text{C}$)	Effective atomic number (Z_{eff})	Sensitivity	Linear dose range (Gy)	Thermal fading
LiF:Mg,Ti	210	8.14	1.0	$5 \times 10^{-5} - 1$	~5-10% per year
LiF:Mg,Cu,P	232	8.14	25	$10^{-6} - 10$	-
$\text{Li}_2\text{B}_4\text{O}_7$:Mn	210	7.4	0.4	$10^{-4} - 3$	5% in 60 days
$\text{Li}_2\text{B}_4\text{O}_7$:Cu	205	7.4	8	$10^{-4} - 1000$	25% in 60 days
MgB_4O_7 :Dy/Tm:X	210	8.4	7	$10^{-5} - 1$	10% in 60 days
CaF_2 :Dy	200 240	16.3	16	$10^{-5} - 10$	25% in 4 weeks

CaSO ₄ :Dy	220	15.3	30	10 ⁻⁶ - 30	7-30% in 6 months
BeO	180-220	7.13	3	10 ⁻⁴ - 5 x 10 ⁻¹	7% in 2 months
Al ₂ O ₃	250	10.2	5	10 ⁻⁴ - 1	5% in 1 month

In India, monitoring of radiation workers in various radiation facilities is being carried out with CaSO₄:Dy PTFE (Teflon) based thermoluminescence dosimeter (TLD) badges [78,84,85]. This badge is used for monitoring dose due to β particles, x-rays, and γ -rays. Dysprosium (Dy) acts as the dopant and is added to CaSO₄ matrix at a level of approximately 0.05 mol% to prepare CaSO₄:Dy TL phosphor powder [89]. This phosphor has high TL sensitivity, simple glow curve structure, low fading (about 5% in 6 months) and easy to prepare. Being developed indigenously, it is cost effective for large scale personnel monitoring. To prepare CaSO₄:Dy Teflon embedded disc, phosphor powder is physically mixed with Teflon at liquid N₂ temperature in a weight ratio of 1:3 followed by cold pressing and annealing at ~400 °C uniformly. Annealing makes the disc rugged and easy to handle. The CaSO₄:Dy disc (in Teflon matrix) is having dose linearity up to 30 Gy and beyond that, it shows nonlinear trend i.e. supralinearity followed by saturation [94, 95].

2.3.4 Thermoluminescence in CaSO₄:Dy

The first proposed model by Nambi et al. [125] for understanding TL mechanism in CaSO₄:Dy was based on the TL emission spectra and electrons spin resonance (ESR) studies on different rare earth doped CaSO₄ material. According to this model, Dy³⁺ present in CaSO₄:Dy phosphor act as an electron trap centres and anion radicals like SO₄⁻, SO₃⁻, SO₂⁻ and O₃⁻ etc act as hole trapping sites. On gamma irradiation, Dy³⁺ state reduces to the Dy²⁺ state through electron

trapping and holes get trapped at hole trap centres. During readout through thermal activation, the holes get released from the anion radical sites and recombine either with trapped electrons at Dy^{2+} sites or at some unidentified host centres. As a result excited Dy^{3+} states are created through direct recombination or indirect transfer of energy (by resonance transfer or tunneling) to Dy^{2+} ions. These excited Dy^{3+} states emit characteristic light photons on returning to ground state and thermoluminescence results. Pictorial depiction of proposed redox model for understanding TL mechanism in $CaSO_4:Dy$ is shown in figure 2.4.

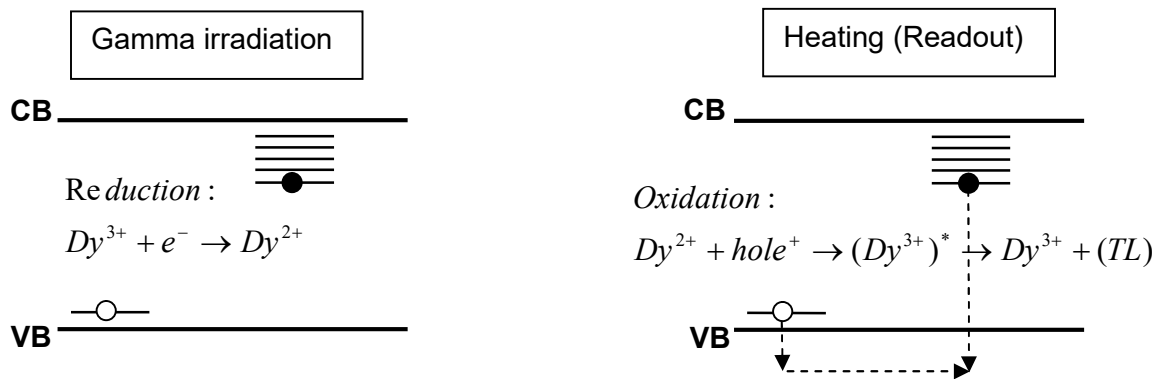


Figure 2.4: Nambi's redox model for thermoluminescence in $CaSO_4:Dy$

The reduction of Dy^{3+} to Dy^{2+} during gamma irradiation was observed in optical absorption studies [126]. Studies on TL emission spectra have confirmed the emission lines due to characteristic transitions of Dy^{3+} ion, through ${}^4F_{9/2} \rightarrow {}^6H_{15/2}$ (~475 nm), ${}^4F_{9/2} \rightarrow {}^6H_{13/2}$ (~570 nm), ${}^4F_{9/2} \rightarrow {}^6H_{11/2}$ (~660 nm), ${}^4F_{9/2} \rightarrow {}^6H_{9/2}$ (~750 nm) transitions [127,128]. The ESR study on Dy doped $CaSO_4$ demonstrated the formation of SO_4^- , SO_3^- , SO_2^- and O_3^- radicals and Dy^{2+} states during gamma irradiation and also reduction of a small percentage (< 1 %) of total Dy^{3+} to Dy^{2+} was observed through optical absorption studies [127].

Later on Morgan and Stoebe proposed another model to explain TL mechanism in $CaSO_4:Dy$ based on optical absorption studies [129]. From the study, it was observed that gamma

irradiation produces SO_4^- , SO_3^- , SO_2^- , O_3^- and O^- radicals in $CaSO_4:Dy$, only when Dy^{2+} is present in sample since gamma irradiated undoped $CaSO_4$ sample shows SO_4^- absorption line only. Study also revealed absence of the absorption peaks in annealed $CaSO_4:Dy$ samples, establishing the fact of oxidation of Dy^{2+} to Dy^{3+} by thermal treatment. Therefore the authors suggested a new model in which the energy transfer is occurring between an unidentified recombination centre to a nearby Dy^{3+} state and the final luminescence results from the relaxation of excited Dy^{3+} state to ground state. The suggested model for TL mechanism in $CaSO_4:Dy$ is depicted in figure 2.5.

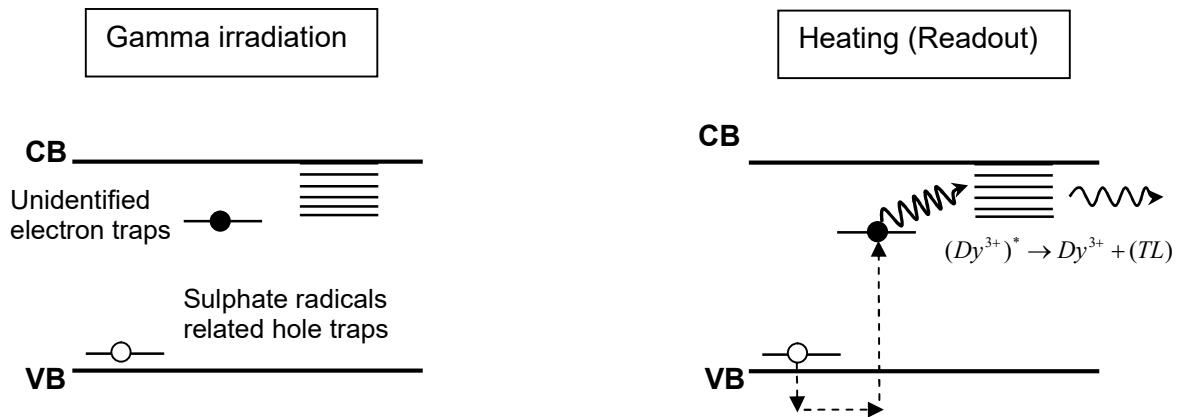


Figure 2.5: Stoebe's model for thermoluminescence in $CaSO_4:Dy$

2.4 X-ray diffraction (XRD)

X-ray diffraction (XRD) is a non-destructive technique in material science used for structural characterization of crystalline materials in terms of structure, phase identification, particle size, micro-strain etc. Atoms in a crystal are arranged in a periodic manner and will scatter the incident x-ray radiation in specific directions. The interference of these scattered waves form sharp maxima called as Bragg peaks. The pattern thus obtained is called as diffraction pattern and represents the periodicity of atoms within the crystal. The pictorial representation of XRD is

shown below.

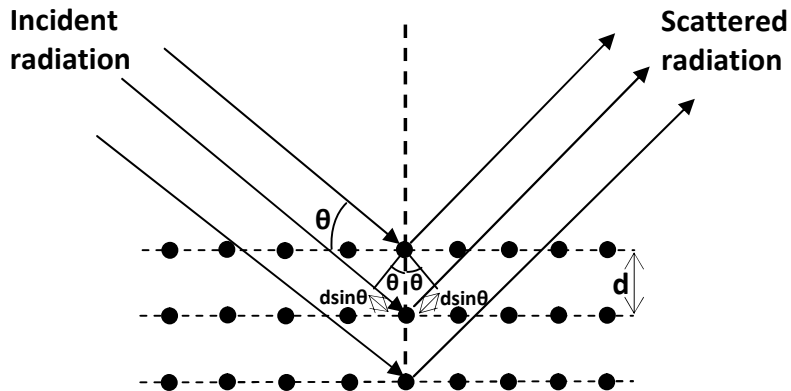


Figure 2.6: Schematic showing diffraction of X-ray radiation from a crystal

The angular position of Bragg peak ($2\theta_{hkl}$) is related to the inter-planar distance (d_{hkl}) by Bragg's law of diffraction and is given below.

$$2d_{hkl} \sin\theta_{hkl} = n\lambda \quad \text{----- (2.8)}$$

Where, d_{hkl} = spacing between lattice planes ($h k l$) ; h , k and l represent miller indices

$2\theta_{hkl}$ = angle of diffraction

λ = wavelength of x-ray

n = integer called the order of diffraction

In an experiment by using a monochromatic x-ray beam, information on d_{hkl} can be obtained through scanning the crystal at different incidence angles and measuring θ_{hkl} . Positions of Bragg peaks give information about the space group (i.e. structure of lattice) in crystal whereas the relative intensities of different peaks give information about of the basis (i.e. group of atoms or molecule at lattice point). Width of diffraction peaks provides information on the particle size and the micro-strain in crystal. In this work, structural information of CaSO₄:Dy powder samples has been studied at Angle Dispersive X-ray Diffraction (ADXRD) beamline at Indus-2 synchrotron radiation source.

2.4.1 Angle Dispersive X-ray Diffraction (ADXRD) beamline in Indus-2

ADXRD beamline is set up at bending magnet port (BL-12) and used for high resolution x-ray diffraction experiments on single crystal and polycrystalline samples. The beamline optics consists of slit systems, plane bendable pre-mirror, double crystal monochromator (DCM) and a post-mirror system (similar to pre-mirror). The pre-mirror system focuses (or collimates) synchrotron beam in the meridional direction. The DCM is based on Si (111) crystal pair used to monochromatise the synchrotron beam and focus the synchrotron beam in sagittal direction to the experimental station. Focused beam from post-mirror system reaches the experimental system through a precision slit system. Experimental station of beamline has dual experimental stations for XRD measurements: the first one is a six circle diffractometer (Huber model 5020) with NaI(Tl) scintillation detector and the second one is an image plate (Mar 345) area detector. The experimental stations are shown in figure 2.7. An ionization chamber is installed before the experimental station to measure the flux of incident beam [130]. We have used image plate area detector for XRD measurement of $\text{CaSO}_4:\text{Dy}$ powder samples. The XRD pattern obtained through the image plate is in the form of circular rings (Deby-Scherrer rings). These rings in image plate are converted into conventional intensity versus 2θ pattern using Fit2D software [131]. The wavelength (λ) of incident beam and the sample to detector distance (D) required to generate $I(2\theta)$ pattern are accurately calibrated using XRD pattern of LaB_6 NIST standard.

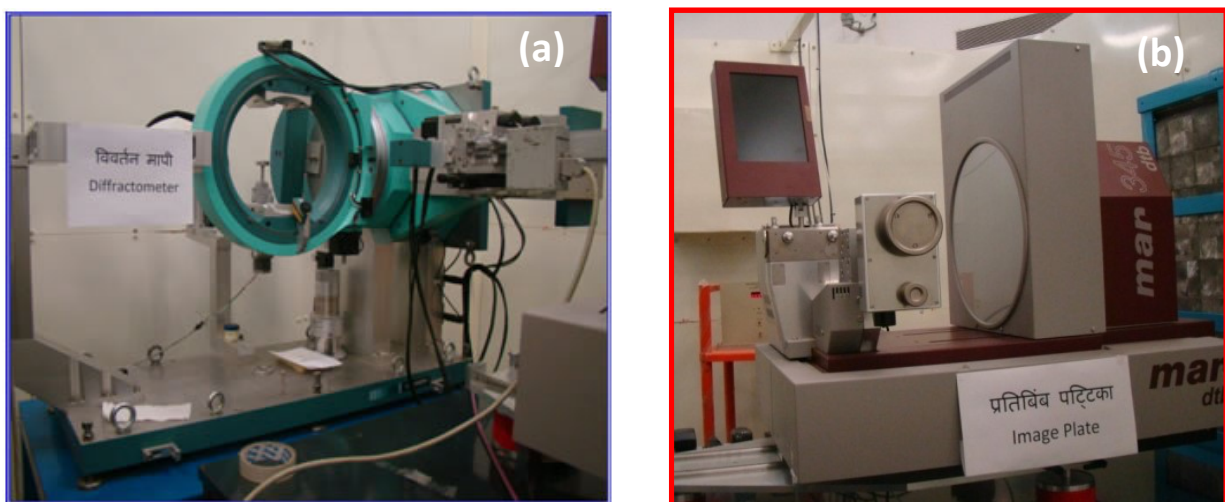


Figure 2.7: *Experimental station having (a) diffractometer with NaI(Tl) detector and (b) image plate (Mar 345 area detector)*

2.5 X-Ray Absorption Near Edge Structure (XANES) Spectroscopy

The X-ray Absorption Spectroscopy (XAS) represents absorption coefficient as function of photon energy as shown in figure 2.8. It consists of absorption edge characterized by sharp increase in absorption coefficient and some features (up to ~ 40 eV from the edge). This part is called X-Ray Absorption Near Edge Structure (XANES). Absorption coefficient beyond 50 eV to approximately 1000 eV (from the absorption edge) shows oscillating behavior and the oscillations are termed as Extended X-ray Absorption Fine Structure (EXAFS). The EXAFS part of the spectrum gives structural information like the co-ordination number, co-ordination length etc. of nearest neighbor of the absorbing atom. The XANES part gives information on the average oxidation state of the absorbing atom, geometry in which the absorbing ion is placed and density of states information on the unoccupied electronic states.

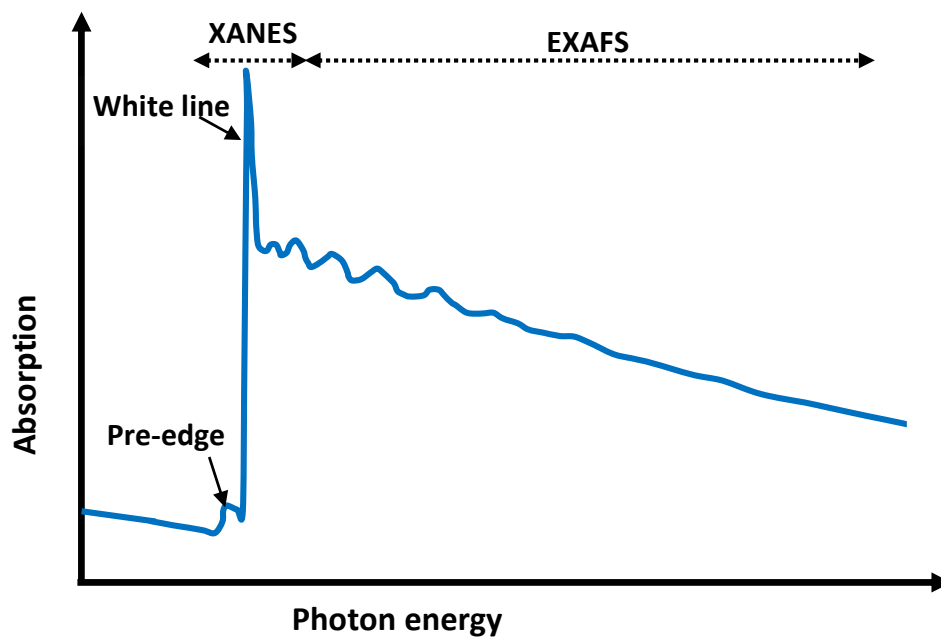


Figure 2.8: Typical X-ray absorption spectrum

In XANES part of the spectrum, sharp rise in absorbance is observed due to the transition of core level electrons to continuum or unoccupied bound states by the absorption of an incident photon and is called as white line. In some cases, small peak like structure (called as pre edge) is observed just before the start of the white line and is primarily due to weak quadrupolar transitions of electrons to empty bound states inside the sample. Though the transition probability is controlled by dipolar selection rules, the pre-edge features are relatively weak in intensity because of forbidden (very small probable) transitions.

XAS measurements can be performed in three modes, viz. transmission, fluorescence and total electron yield. The experimental set up is shown in figure 2.9. In the transmission mode, absorption curve is generated using two identical ion chambers, measuring incident and transmitted flux (in terms of ion current). For thick and low doping samples, fluorescence mode is preferred and similarly for soft X-ray beam energies, total electron yield from the sample are recorded to generate absorption spectrum.

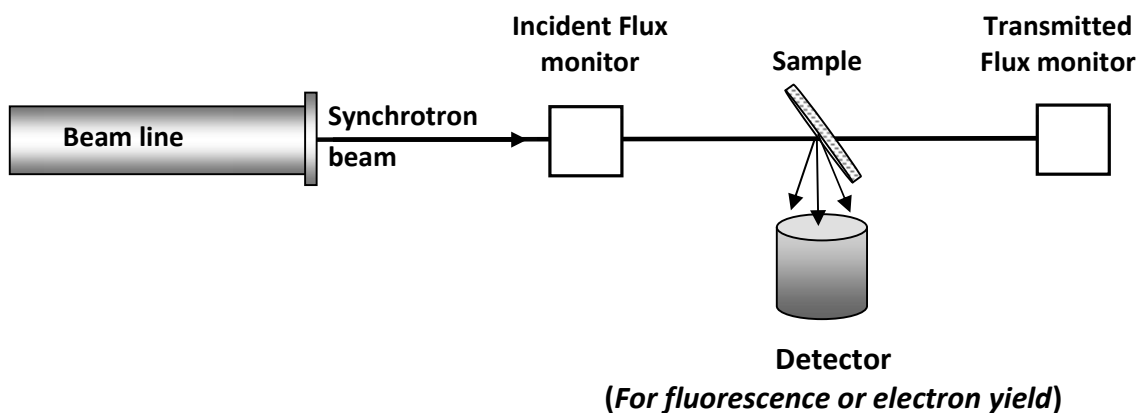


Figure 2.9: Experimental set up for XAS measurement at synchrotron beamline

For this reported work, XANES technique is used for studying behavior of $\text{CaSO}_4:\text{Dy}$ samples at ADXRD beamline (BL-12), Indus-2. Since the samples are thick disc ($800\ \mu\text{m}$) and the doping concentration is small, the fluorescence mode is chosen for XANES measurement. Vortex silicon drift detector (SDD) is used to measure the fluorescence from the sample. Since SDD is an energy dispersive detector, during the measurement suitable channel in the detector is selected with maximum fluorescence yield. The total counts observed in the selected channels with respect to the current in ion chamber are recorded to generate XANES spectrum.

Chapter 3

Gas bremsstrahlung radiation dosimetry studies

3.1 Introduction

In synchrotron radiation sources, relativistic electrons are circulated inside storage ring to produce synchrotron radiation. The storage rings are maintained at ultra high vacuum (nTorr) to reduce electron beam loss due to scattering with gas molecules in the vacuum chamber. Inelastic scattering of electrons with residual gas molecules will produce bremsstrahlung radiation and is called as gas bremsstrahlung. The gas bremsstrahlung photons channel to beamline along with the synchrotron radiation (see figure 1.4) and pose radiation hazard to beamline users. Because of the higher energies compared to synchrotron photons, the gas bremsstrahlung requires special attention for their mitigation. Also these photons on further interaction with the beamline components produce scattered photons and photo-neutrons, which complicate the radiation environment in synchrotron beamline. Hence gas bremsstrahlung is treated as major radiation hazard in synchrotron beamlines.

The gas bremsstrahlung radiation is similar to a thin target bremsstrahlung and is emitted out in a very narrow cone (\sim mrad). Because of strong angular distribution, broad energy range and accompanying high intense synchrotron radiation, gas bremsstrahlung poses challenges in detection and measurement. Monte Carlo techniques are extensively used to simulate gas bremsstrahlung radiation and evaluation of shielding requirements for synchrotron beamlines

worldwide. The empirical relation (equation 1.21) for absorbed dose rate was deduced by Tromba et al. is for electron energy ranging from 500 MeV to 10 GeV passing through air target at atmospheric pressure using the Monte Carlo code, EGS4 [31]. In this study, the angular distribution of gas bremsstrahlung photons showed larger broadening due to multiple scattering of electrons with air molecules [32,51]. With the suppression of multiple Moller scattering effects at atmospheric pressure, the empirical relation was later modified using FLUKA Monte Carlo code for electron energy range from 100 MeV to 1 GeV [32]. Because of highly forward peaked nature, the authors have used scoring areas 0.59, 0.16 and 0.0059 cm² for electron energies 100, 250 and 500-1000 MeV, respectively for calculating fluence of bremsstrahlung photons. A similar study for the estimation of gas bremsstrahlung dose at Advanced Photon Source has used scoring radius of 0.02 cm for 7 GeV positron beam passing through 15 m straight section using FLUKA code [51]. The decrease in scoring radius increases absorbed dose and simultaneously the computation time also increases to reduce statistical error. The scoring radius should be large enough to save computation time and simultaneously small enough to avoid underestimation of fluence and absorbed dose [32,51]. Therefore optimization of the scoring radius is desirable for gas bremsstrahlung dose estimation. The above studies have pointed out the importance of the optimization of scoring radius for estimation of gas bremsstrahlung dose.

The reported empirical relations for the estimation gas bremsstrahlung dose were based on the simulation studies with air at atmospheric pressure in the straight section. In real scenario, the composition of gas inside the vacuum chamber at ultra high vacuum (UHV) condition is significantly different from that of air because of the different evacuation efficiencies for different gas molecules while pumping. Composition of air at atmospheric pressure is dominated

by nitrogen (78%) followed by oxygen (21%) whereas the composition of residual gas inside storage ring at UHV condition is dominated by hydrogen. Some of the recent studies had attempted to simulate gas bremsstrahlung radiation for actual residual gas composition in synchrotron storage rings of National Synchrotron Radiation Research Center (NSRRC), Taiwan and Iranian Light Source Facility (ILSF), Iran using FLUKA Monte Carlo code [33,34]. These studies were more focused to generate gas bremsstrahlung radiation properties specific to the facilities. However no systematic study was reported on gas bremsstrahlung dose with respect to actual vacuum conditions of the storage ring.

From literature survey, it has been found that there is a lack of empirical relation for gas bremsstrahlung dose estimation for medium energy electron storage rings ($E_0 > 1$ GeV). Also the effect of residual gas composition on gas bremsstrahlung radiation has not been properly addressed. Therefore in the present work,

- i) Benchmarking of the simulation methodology for gas bremsstrahlung radiation is performed with reference to reported data for 7 GeV positron storage ring at Advanced Photon Source.
- ii) Spectral and angular behavior of gas bremsstrahlung radiation for electron storage rings ($1 \text{ GeV} < E_0 < 5 \text{ GeV}$) is studied using FLUKA code and an empirical relation for gas bremsstrahlung dose is then deduced for medium energy electron storage rings.
- iii) FLUKA simulation studies are performed to investigate the effects on energy distribution, angular distribution and absorbed dose rate of gas bremsstrahlung due to different residual gas molecules and their mixtures. From the study, a modified empirical relation is deduced for estimation of gas bremsstrahlung dose for actual residual gas mixture.

These studies are then applied to Indus-2 storage ring for evaluating gas bremsstrahlung dose.

3.2 Benchmarking studies on simulation of gas bremsstrahlung radiation using FLUKA

To validate the simulation methodology, a benchmark study is performed for gas bremsstrahlung radiation due to 7 GeV positron using FLUKA Monte Carlo code and the results are compared to the published data for 7 GeV positron storage ring at Advanced Photon Source (APS) by Ipe et al. (1994) [51].

The simulation geometry is made based on the design parameters of Advanced Photon Source (APS) [beam energy = 7 GeV, length of the straight section = 15 m and distance of the experimental station of the beamline (scoring medium: tissue phantom) from the start of the straight section = 32.6 m]. Pencil beam of positron ($E_0 = 7$ GeV) is allowed to pass through air target of length 15 m (radius = 5 cm) to generate gas bremsstrahlung radiation. 30 cm thick ICRU tissue phantom is used to score depth dose profile. The ICRU tissue [132] comprises of four elements: Hydrogen (10.12%), Carbon (11.1%), Nitrogen (2.6%) and Oxygen (76.18%). The simulation geometry is shown in figure 3.1.

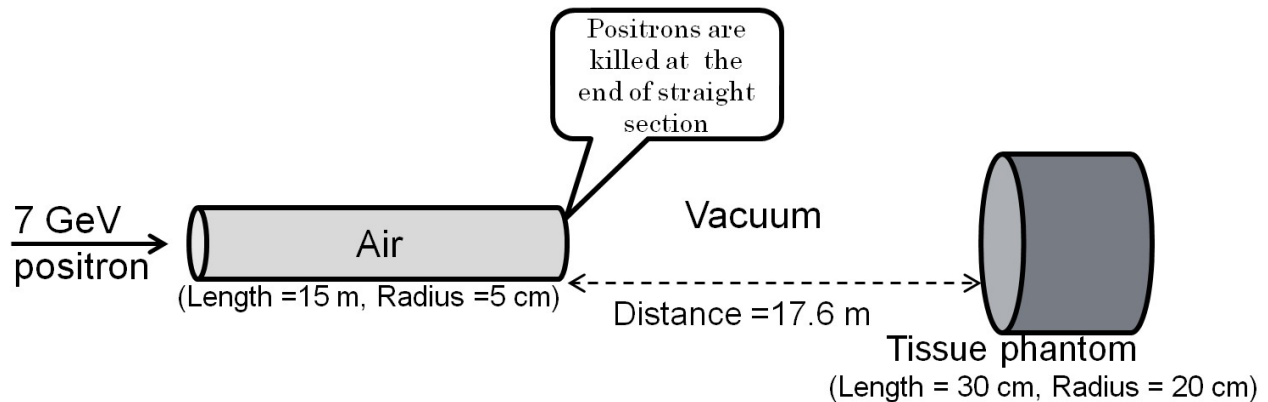


Figure 3.1: Geometry used in FLUKA simulation for benchmark study

In actual scenario, the positron beam particles are bent by the dipole magnet of the storage ring and thus will not travel down the synchrotron beamline. Therefore in the simulation, positrons are killed intentionally at the end of the straight section using a high transport cut-off equal to the

incident energy in order to avoid its contribution to gas bremsstrahlung dose. Transport cut-offs for photon and electron/positron are set as 1 and 10 keV, respectively in air and tissue phantom. Pressure of air in the straight section is set at 1 atmosphere (760 torr) to produce sufficient interactions and reduce statistical error. The corresponding results are then normalized to vacuum pressure (~ 1 nTorr) in the straight section. The interaction probability through multiple scattering events is very low at \sim nTorr pressure as the number of gas molecules is significantly lower as compared to that for 1 atmospheric pressure. Therefore multiple scattering effects at atmospheric pressure are intentionally suppressed for all the simulation studies by setting threshold for Moller scattering of electrons at 10 MeV, minimizing the angular divergence due to the production of δ -rays [32].

Gas bremsstrahlung is highly forward peaked in nature and hence the scoring radius plays a crucial role in dose estimation. Scoring radius is the radius of the scoring area of the detector (tissue phantom) used for estimation of the dose. The scoring radii ($r = 0.4$ cm and 0.02 cm) are used in order to benchmark the depth dose profile reported by Ipe et al. [51]. The gas bremsstrahlung spectrum, effect of scoring radius on gas bremsstrahlung dose rate, effect of suppression of multiple scattering on depth dose profile and radial dose profile are compared to the published data and shown in figure 3.2 to figure-3.5.

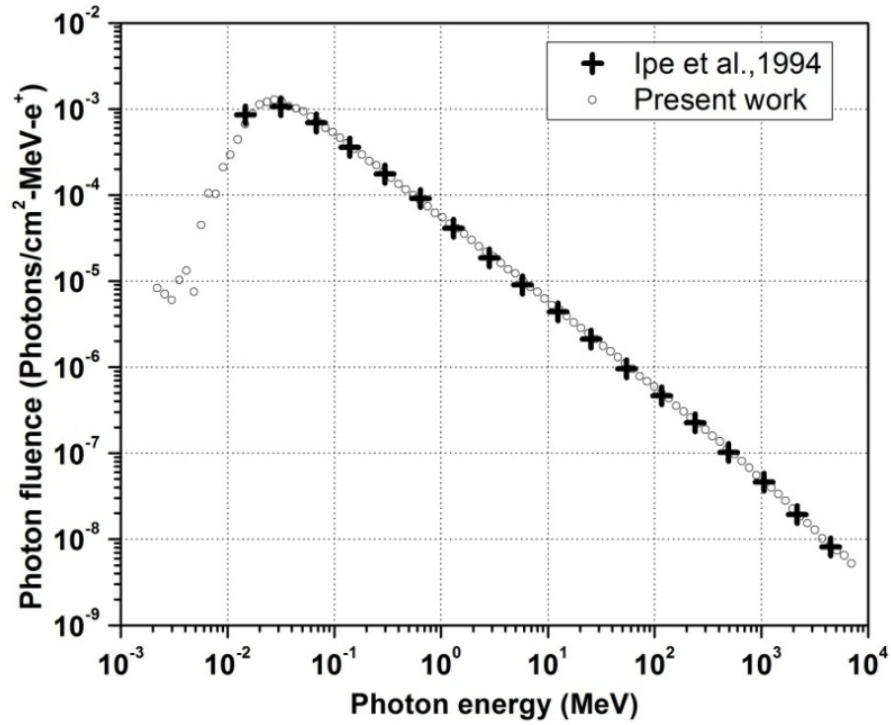


Figure 3.2: Gas bremsstrahlung spectrum from 7 GeV positron beam for $L = 15$ m

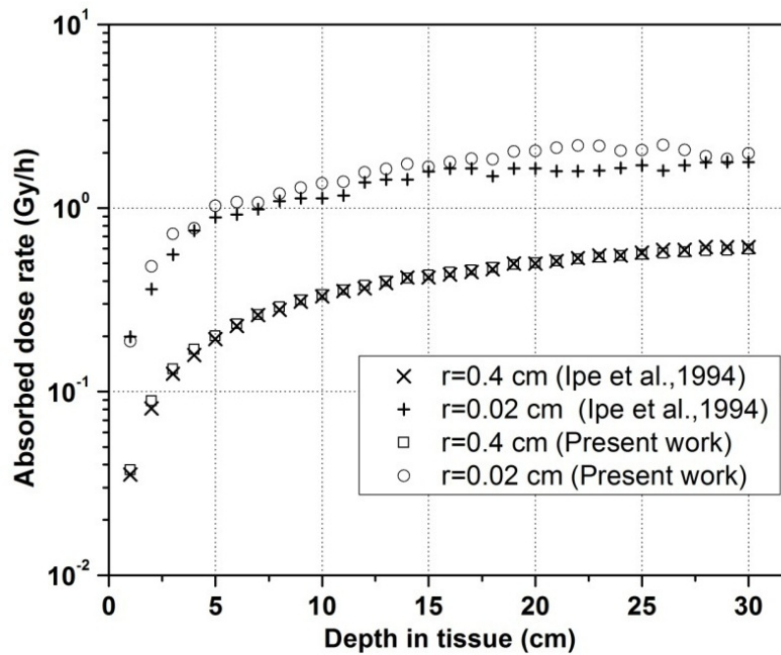


Figure 3.3: Depth dose profile inside tissue phantom for scoring radius 0.02 and 0.4 cm

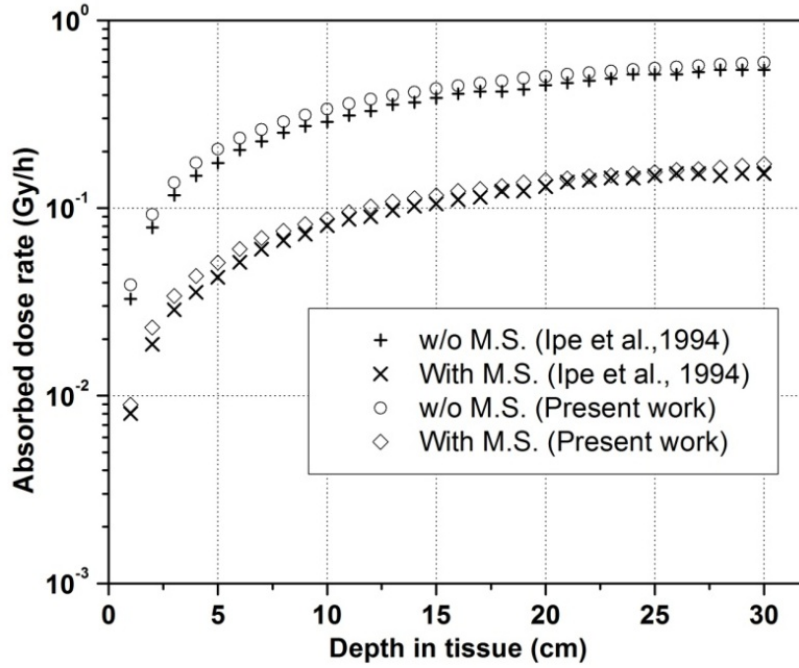


Figure 3.4: Effect of suppression of multiple scattering (M.S.) on depth dose profile

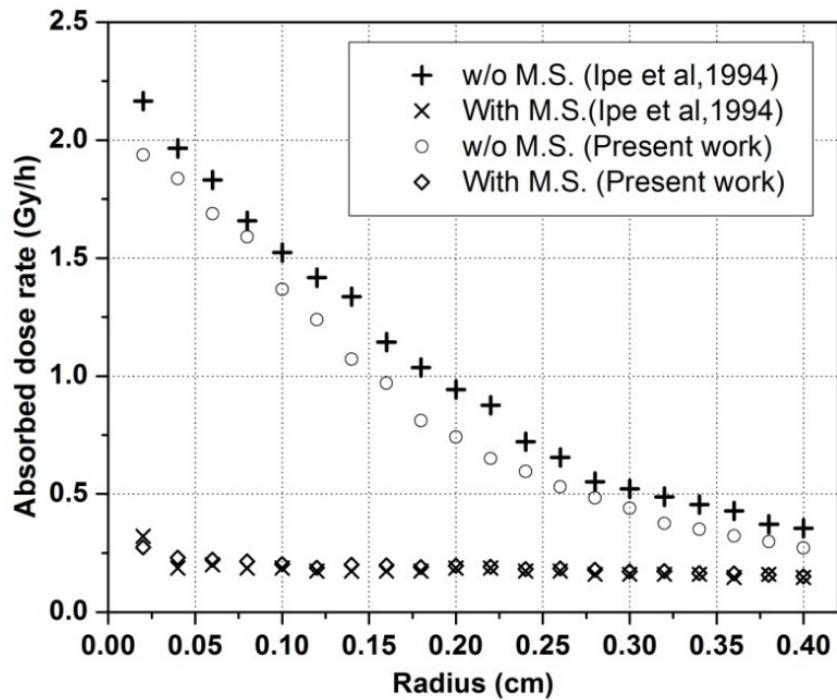


Figure 3.5: Effect of multiple scattering on radial dose distribution in tissue phantom

The gas bremsstrahlung spectrum is found to be extending up to the incident beam energy and dose build up in tissue phantom due to high energy photons are clearly visible in figure 3.3 and figure 3.4. Increase in dose due to the suppression of multiple scattering events in air target (refer figure 3.4 and figure 3.5) is also an important observation from the simulation study. In the benchmarking study, the results obtained are found to be in very good agreement with the published data. The small variation in the data points for without multiple scattering cases may be attributed to the Roger's dose conversion factors used by Ipe et al. whereas in the present work only absorbed energy in the medium is scored for the estimation of the dose. Based on the study, the optimized parameters for simulation on gas bremsstrahlung radiation are listed in table 3.1.

Table 3.1: Optimised parameters for studying gas bremsstrahlung radiation

Parameters	Values
Target gas	Air
Pressure of gas	1 atm (= 760 Torr)
Tissue phantom	Dimension: Length = 30 cm & Radius = 15 cm
	Composition: Hydrogen (10.12%); Carbon (11.1%); Nitrogen (2.6%); Oxygen (76.18%)
Transport cutoff [#]	
Electron and Positron	10 keV (Air target & ICRU Tissue)
Photon	1 keV (Air target & ICRU Tissue)
Threshold for Moller scattering	10 MeV

[#]Note: Transport cut off for beam particles at the end of air target (killing region) is set as the incident beam energy.

3.3 Simulation of gas bremsstrahlung dose for medium energy electron storage rings

The angular distribution and depth dose profile for gas bremsstrahlung radiation due to 1 to 5 GeV electron beam passing through straight section lengths in the range 1 to 10 m are studied using FLUKA. Simulation parameters are given in table 3.1. The bremsstrahlung spectrum, angular distribution and absorbed energy density are scored using USRBDX, USRYIELD and USRBIN scoring cards, respectively. The scoring area for dose calculation in tissue phantom is decided based on the angular divergence of gas bremsstrahlung radiation. The statistical uncertainties in simulated data achieved are within $\pm 7.4\%$.

Angular distribution of the gas bremsstrahlung radiation in tissue phantom for 1 m straight section due to 1 to 5 GeV electron beam is shown in figure 3.6.

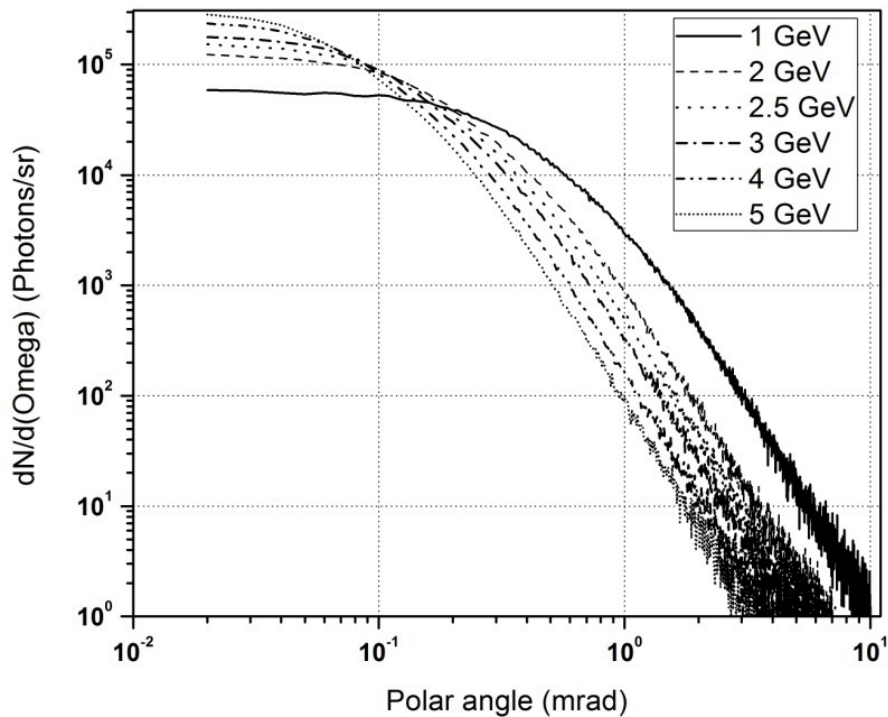


Figure 3.6: Angular distribution of the gas bremsstrahlung radiation

Figure 3.6 reflects the sharp angular behavior of gas bremsstrahlung radiation confined within a cone of 1 mrad angle and beyond the emission cone, there is very small number of photons

leading to high statistical uncertainties. The angular distribution shows a nearly flat region up to 0.1 mrad emission angle for beam energies up to 3 GeV. Therefore using 0.1 mrad as an optimized scoring angle, the scoring radius for dose estimation in tissue phantom is calculated using the expression

$$r(mm) = 0.1(mrad) \times d(m) \quad \text{----- (3.1)}$$

Here d is the distance of tissue phantom from end of the straight section.

The gas bremsstrahlung dose rate due to electron beam ($E_0 = 1$ to 3 GeV) for different straight section lengths ($L = 1$ to 10 m) and target to detector distances ($d = 1$ to 50 m) are generated.

Absorbed dose rate as a function of the parameter $L/d(L+d)$ is shown in figure 3.7.

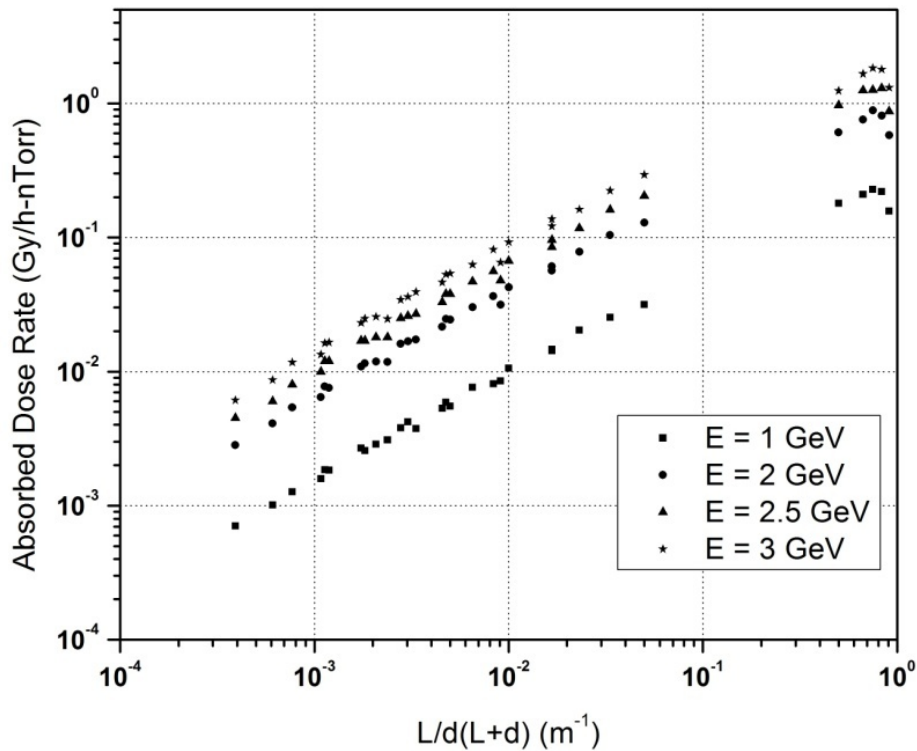


Figure 3.7: Absorbed dose rate as a function of $L/d(L+d)$ for 1 to 3 GeV electron beam [normalized to 300 mA (1.875×10^{18} e⁻/s)]

The dependence on the geometry is reported to have a good correlation with the observed bremsstrahlung dose data in terms $L/d(L+d)$ (Refer equation 1.23). The fit of the data points (figure 3.7) gives an empirical formula for absorbed dose rate, which is applicable for electron ($E_0 = 1$ to 3 GeV), length of straight section ($L = 1$ to 10 m) and target to detector distance ($d = 1$ to 50 m), is given in equation 3.2.

$$\dot{D}(\text{Gy}/h) = 9.1 \times 10^{-26} \left(\frac{E_0}{mc^2} \right)^{1.92} \left[\frac{L}{d(L+d)} \right]^{0.78} I \left(\frac{P}{P_0} \right) \quad \text{----- (3.2)}$$

Here E_0 = Energy of electron (MeV), mc^2 = Rest mass energy of electron = 0.511 MeV, L = Length of the straight section (m), d = Distance from the end of straight section (m), I = Beam current (e^-/s), P = Pressure inside the straight section (Torr), $P_0 = 1.33 \times 10^{-7}$ Pa (10^{-9} Torr). The corresponding co-efficient, exponent for energy and length terms in the expression (refer equation-1.23) reported in literature [32] are 2.5×10^{-27} , 2.67 and 1.0 respectively.

3.3.1 Comparison with experimental data

For validation of the simulation methodology and proposed empirical relation, the obtained absorbed dose data are compared with the available experimental data for ADONE storage ring [32, 23] and are shown in table 3.2. For comparison, the dose data for the experiment conditions (as per the literature) are also simulated using FLUKA code and are listed in table 3.2.

Table 3.2: Comparison of simulated gas bremsstrahlung dose with experiments

Experimental condition at ADONE storage ring	Absorbed dose rate (x 10 ⁻⁵ Gy/h-mA)			
	Experimental result	Present rtudy (FLUKA Simulation)	Proposed empirical relation (Eq. 3.2)	Ferrari et al. (1993) (Eq. 1.23)
E = 1500 MeV, L= 6 m, d =15 m, P = 1 nTorr (with 0.5 mm Cu as synchrotron stopper)	20.0 (with 0.5 mm Cu as synchrotron stopper)	24.6 (with 0.5 mm Cu & r = 1.5 mm)	11.8 (without any intervening medium)	54.0 (without any intervening medium)
E = 550 MeV, L= 6 m, d = 9 m, P = 1 nTorr (with 12 mm SS as synchrotron stopper)	2.30 (with 12 mm SS as synchrotron stopper)	3.47 (with 12 mm SS & r = 0.9 mm)	3.32 (without any intervening medium)	8.65 (without any intervening medium)

The simulated data are found to have a good match with the reported experimental data whereas, the data obtained using the expression (equation 1.23) suggested by Ferrari et al. are showing quite higher values. The difference in absorbed dose rate from the proposed empirical relation with respect to the experimental data may be attributed to the effect of intervening medium used during the experiment. In high energy regime, photon while interacting with the intervening medium is expected to give higher dose due to cascade effect.

3.3.2 Application of the study for Indus-2

This study is extended to evaluate the gas bremsstrahlung radiation from 2.5 GeV storage ring (Indus-2). Applying this methodology, energy spectrum and photon fluence as a function of

straight section length ($L = 1$ to 10 m) are evaluated and are shown in figure 3.8 and 3.9 respectively.

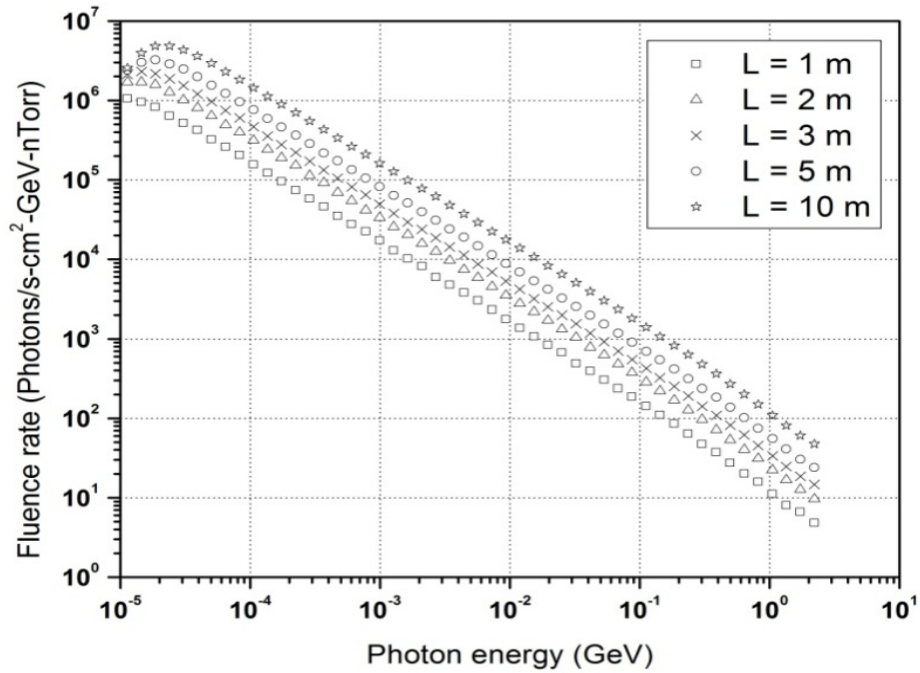


Figure 3.8: Gas bremsstrahlung spectrum as a function of straight section length

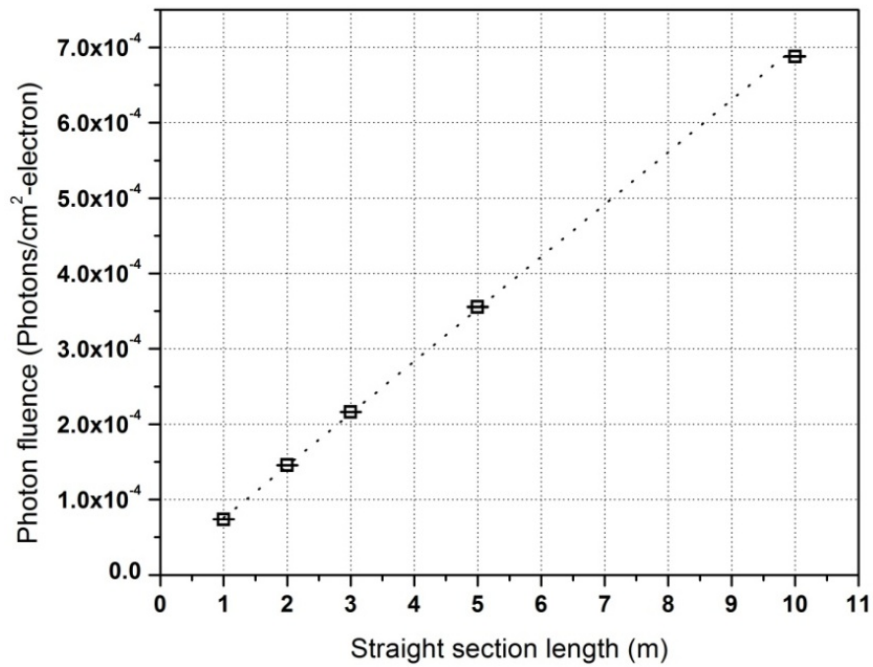


Figure 3.9: Gas bremsstrahlung photon fluence as a function of straight section length

The energy of bremsstrahlung photons is found up to 2.5 GeV and a linear rise in photon fluence with increase in straight section length is observed. Because of strong photoelectric absorption by air molecules like oxygen, fall in fluence for photon energies less than 20 keV is observed in the energy spectra. The behaviour is in agreement with reported result [33]. The variation of fluence with photon energy shows approximately k^{-1} dependency, where k is the photon energy and can be attributed to thin target bremsstrahlung spectrum [46]. Since the air target thicknesses (1 – 10 m) are much smaller than the radiation length (~ 300 m) in air [133] the resulting bremsstrahlung emission is similar to that from a thin target. The variation of absorbed dose as a function of distance of tissue phantom for straight section length varying between 1 to 10 m is shown in figure 3.10. Comparison of absorbed dose as a function of $[L/d(L+d)]$ obtained from the present study and that obtained from the empirical relation suggested by Ferrari et al. [32] is shown in figure 3.11.

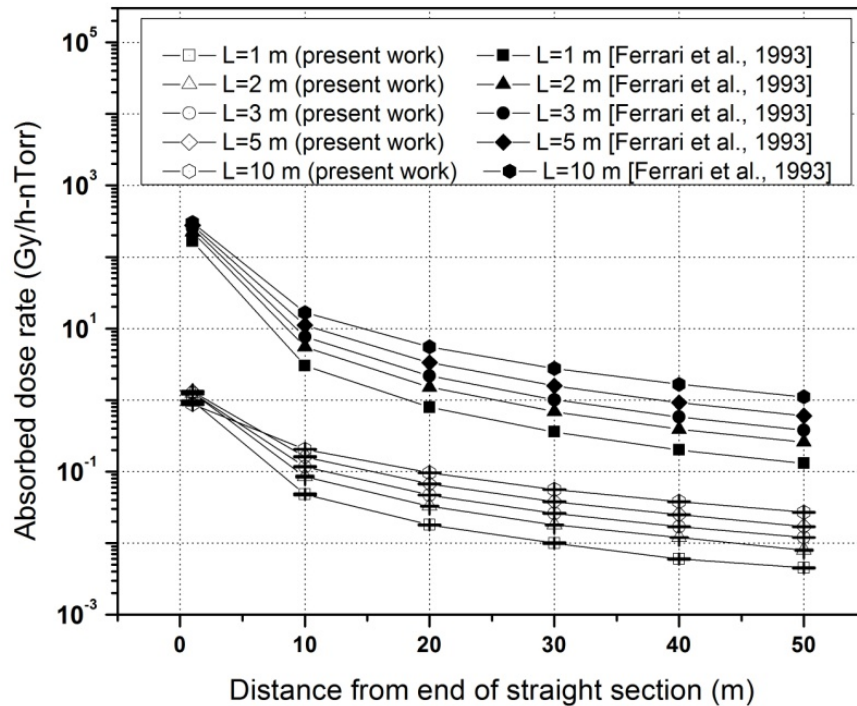


Figure 3.10: Absorbed dose rate as a function of distance from straight section ($E_0 = 2.5$ GeV, $I = 300$ mA)

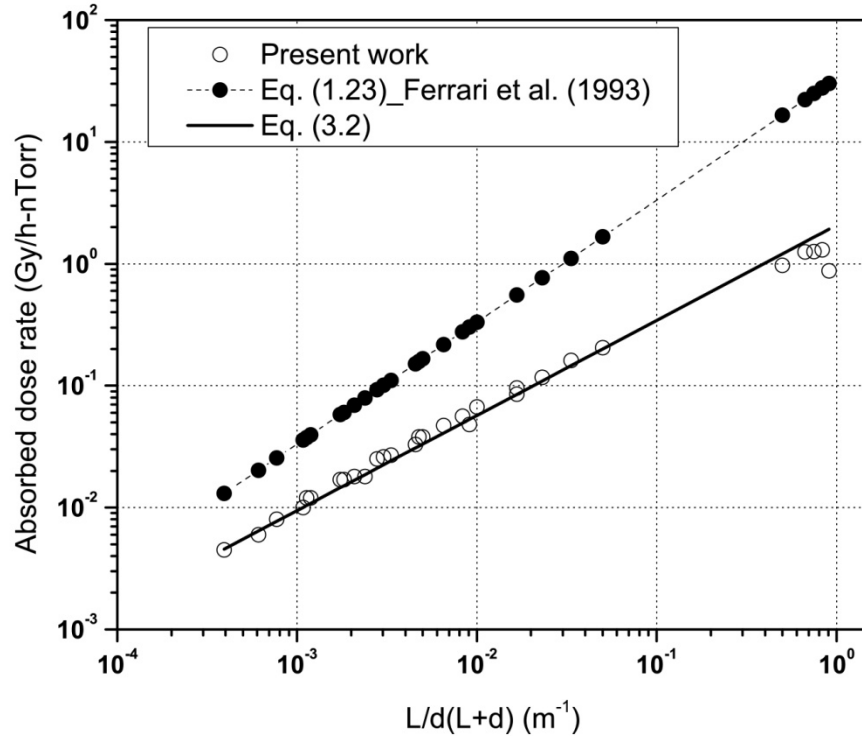


Figure 3.11: Comparison of simulated data and the proposed empirical relation to that of Ferrari et.al. (1993)

From the figures, it is observed that the absorbed dose rate calculated using the empirical relation (equation 1.23) suggested by Ferrari et al. is showing higher values than the estimated dose rate in the present work. The difference in the values can be attributed to the following reasons

- i) The energy dependency of $E^{1.92}$ in the proposed empirical relation is significantly different from $E^{2.67}$ reported by Ferrari et al.
- ii) The energy validity of the Ferrari's empirical relation is only up to 1 GeV.
- iii) Optimized scoring area (based on constant emission angle of 0.1 mrad) is used in the present study.

The simulated absorbed dose data at larger values of $L/d(L+d)$ are found to underestimate the data obtained using empirical relation (equation 1.23) which can be attributed to the smaller scoring radius (as d is small) leading to higher uncertainties.

From this study, it is concluded that determining scoring radius using emission angle (0.1 mrad) for electron storage rings up to 3 GeV is a reasonable and practical approach for determining the gas bremsstrahlung dose.

3.4 Effect of residual gas molecules on gas bremsstrahlung radiation

This study is attempted to investigate the dependency of residual gas composition on gas bremsstrahlung energy spectrum, angular distribution and dose. Simulation studies in respect of these parameters are performed with residual gas molecules like H₂, CH₄, CO, N₂, CO, O₂ and CO₂ (actually present in storage rings at ultra high vacuum) independently for medium energy electron storage rings with different straight section lengths using FLUKA Monte Carlo code. In addition, the studies are performed with residual gas mixture present inside vacuum chamber of NSRRC (Taiwan) and Indus-2 (India) storage rings to establish an empirical relation for calculation of gas bremsstrahlung dose rate.

3.4.1 Residual gas composition in electron storage rings

In Indus-2 storage ring, 15 numbers of residual gas analysers (LEDA-MASS, UK) are installed for monitoring of residual gas composition and leak detection [134]. The composition of residual gas in Indus-2 storage is measured using RGA installed on downstream of undulator vacuum chamber (straight section). The gas composition obtained for Indus-2 along with data from NSRRC and ILSF storage rings [33, 34] and that of air are listed in table 3.3. The corresponding volume fraction is graphically shown in figure 3.12.

Table 3.3: Composition of residual gas in electron storage rings (in comparison with air)

Residual gas	Volume fraction (%)			
	<i>Indus-2 (India)</i>	<i>NSRRC (Taiwan)</i>	<i>ILSF (Iran)</i>	<i>Air</i>
H ₂	78.51	93.00	80.00	-
CO	13.77	4.40	12.00	-
CO ₂	2.75	1.20	5.00	0.039
CH ₄	2.51	0.90	2.00	-
H ₂ O	2.23	0.50	0.50	-
N ₂	0.20	-	-	78.09
O ₂	0.03	-	-	20.95
Ar	-	-	0.50	0.93

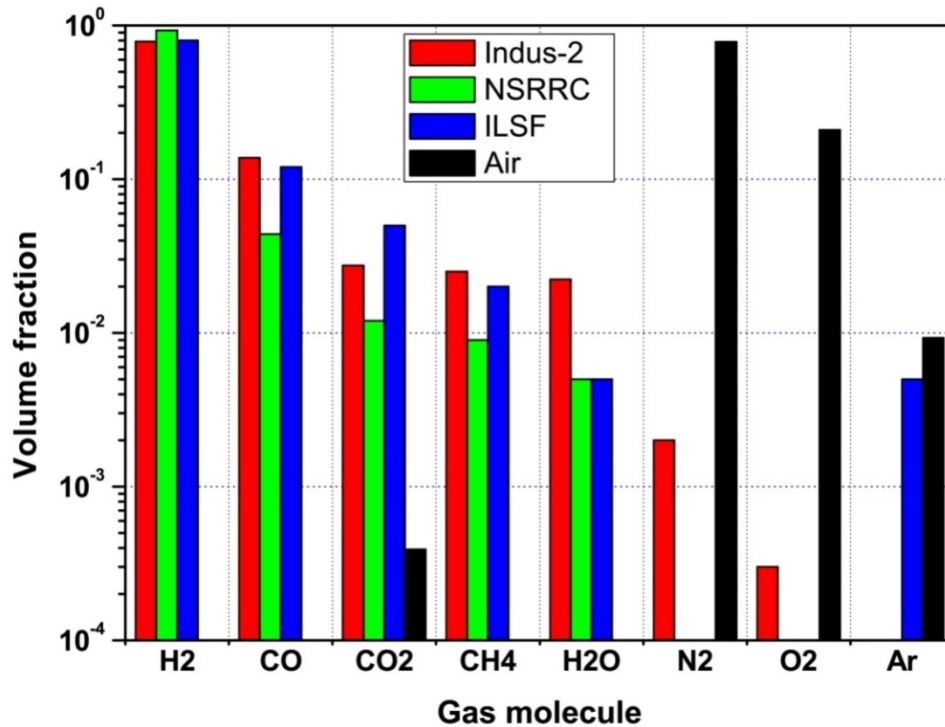


Figure 3.12: Composition of residual gases in Indus-2, NSRRC and ILSF storage rings in comparison with air

The measured RGA data of Indus-2 storage ring indicate maximum volume fraction of H₂ (78.51 %) followed by CO (13.77 %), CH₄, CO₂, water vapor (~2.5 %) and N₂ and O₂ in traces. This is in contrast with composition of air, which is used worldwide for the calculation of bremsstrahlung dose rate from electron storage rings. Though the residual gas composition in

ILSF and NSRRC storage rings is different from that of Indus-2 storage ring, primarily the composition is dominated by hydrogen followed by gases containing carbon similar to Indus-2. It is also to be highlighted that the residual gas composition does not remain constant throughout the storage ring at ultra high vacuum (UHV) condition but changes from one position to another depending on vacuum load, pumping speed and degassing rate of chamber material.

Effective atomic number of gaseous composition is calculated using the following relation [19,135].

$$Z_{eff} = \frac{\sum_i a_i \frac{Z_i^2}{A_i}}{\sum_i a_i \frac{Z_i}{A_i}} \quad \text{----- (3.3)}$$

Here Z_i , A_i and a_i represent atomic number, atomic mass and mass fraction of i^{th} constituent element respectively. Effective atomic number (Z_{eff}) and molecular mass (A) of the gaseous compositions are listed in table 3.4.

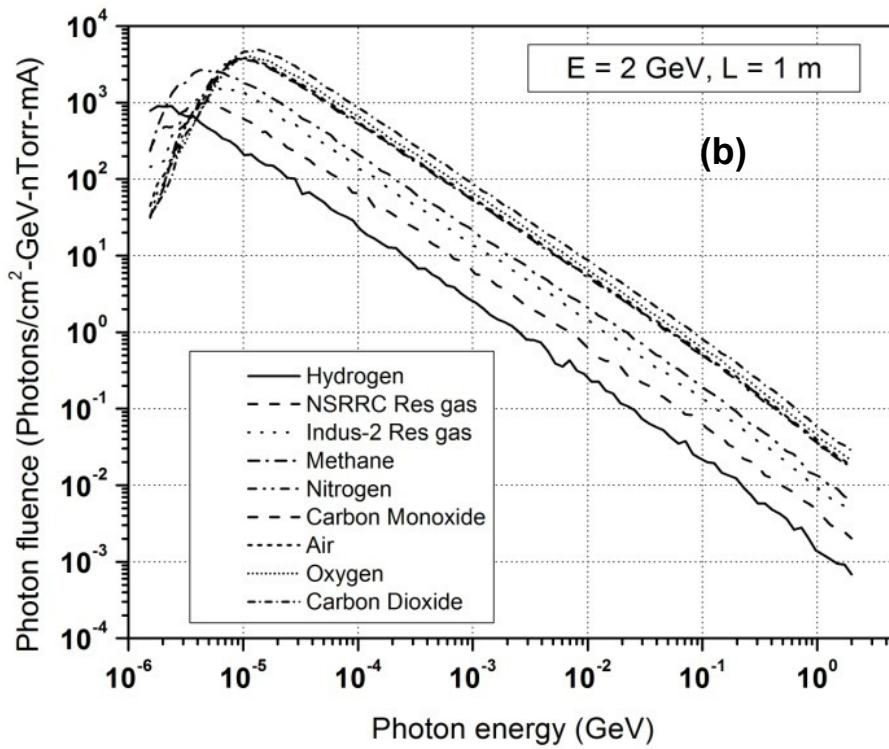
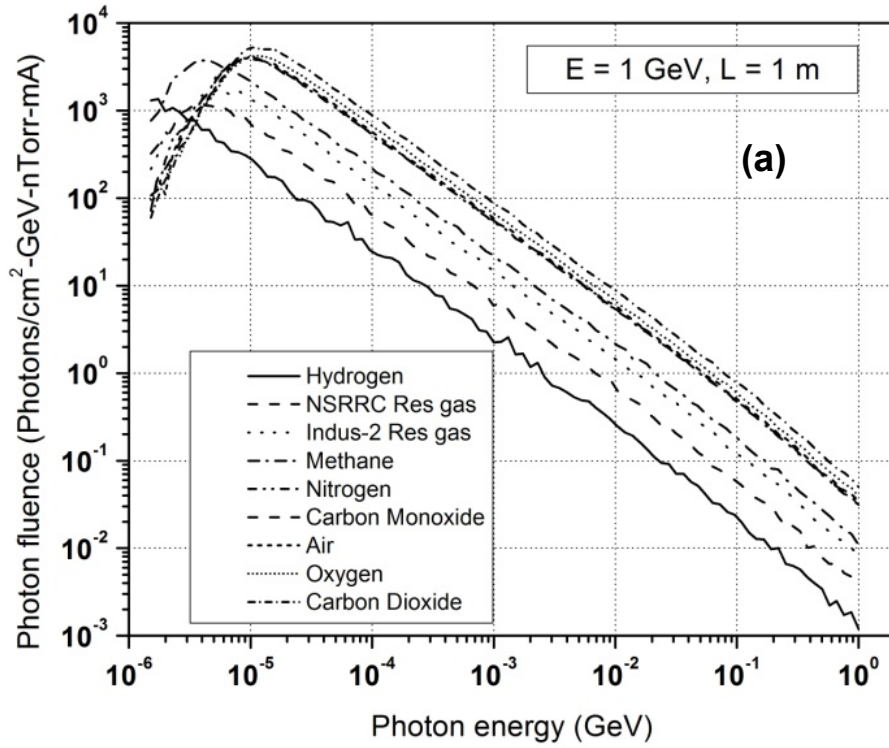
Table 3.4: Effective atomic number of residual gas and gas mixtures

Residual gas/ gaseous mixtures	Effective atomic number (Z_{eff})	Density (g/cc)	Molecular mass (A) (g/mol)	$Z_{eff}^* A$
H ₂	1	8.99E-05	2.02	2.02
CH ₄	4	6.67E-04	16.04	64.16
N ₂	7	1.25E-03	28.02	196.14
CO	7.14	1.17E-03	28	199.92
O ₂	8	1.43E-03	32	256.00
CO ₂	7.45	1.25E-03	44.01	327.87
Air	7.36	1.21E-03	28.97	213.22
NSRRC Res gas	2.2	1.73E-04	3.87	8.51
Indus-2 Res gas	3.86	3.36E-04	7.52	29.03

Effective atomic numbers of residual gaseous composition in different storage rigs are different from each other as well as to that of air. Therefore in the simulation study, variation in gas bremsstrahlung radiation characteristics with respect to the primary beam energy, length of straight section, distance from the straight section and the composition of gas inside straight section are investigated.

Electron in the energy range 1 to 3 GeV is allowed to pass through straight sections of different lengths containing different gases (or gas mixtures) for the production of gas bremsstrahlung. The gas bremsstrahlung dose is scored in a tissue phantom placed at different distances (1 – 50 m) from the straight section. The scoring area for dose calculation in tissue phantom is decided based on the angular divergence of gas bremsstrahlung radiation. The statistical uncertainties in simulated data are achieved within $\pm 6.7\%$.

Gas bremsstrahlung spectra due to 1, 2 and 3 GeV electrons passing through 1 m straight section containing different gas molecules and gaseous mixtures are shown in figure 3.13 (a-c). Energy of bremsstrahlung photons ranges up to the incident electron energy. The spectral behavior suggests variation of fluence with photon energy (k) approximately as k^{-1} , representing thin target bremsstrahlung. A peak in low energy region appears in spectra due to strong photo-electric absorption of low energy photons.



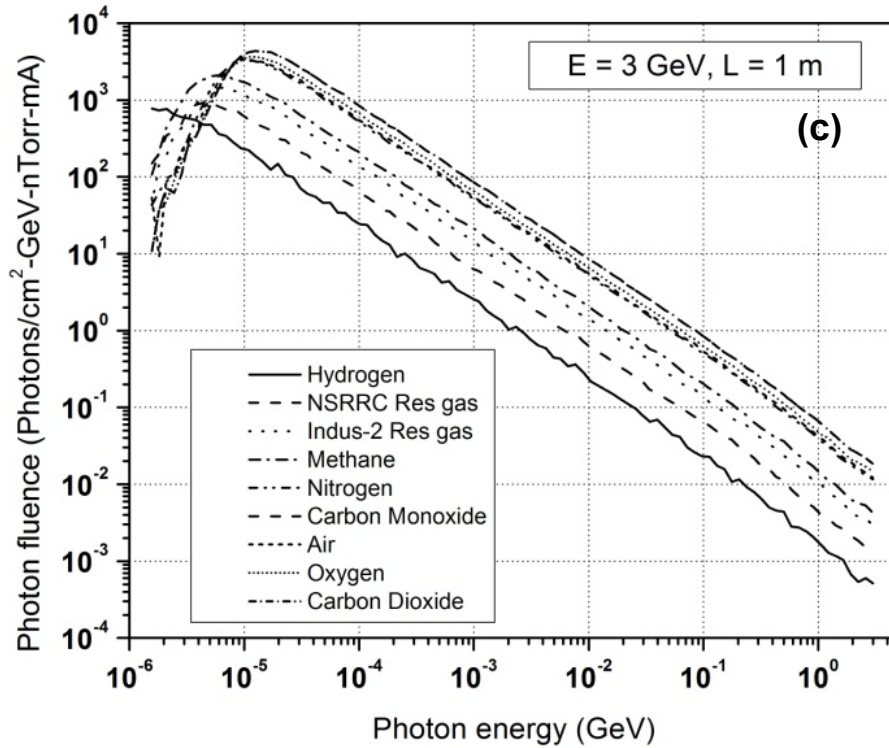
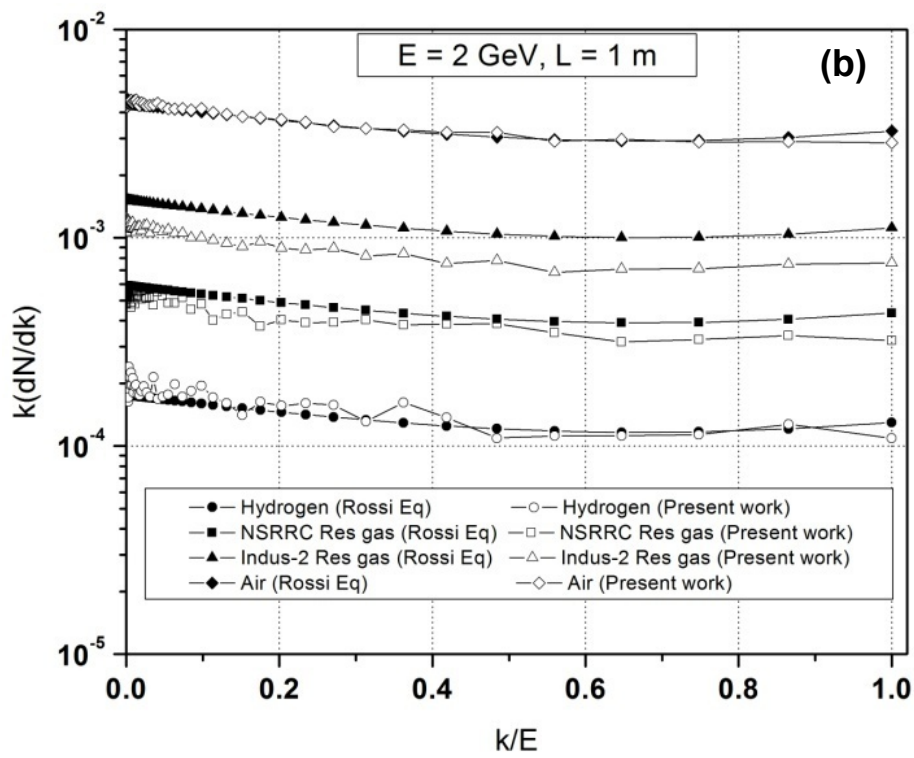
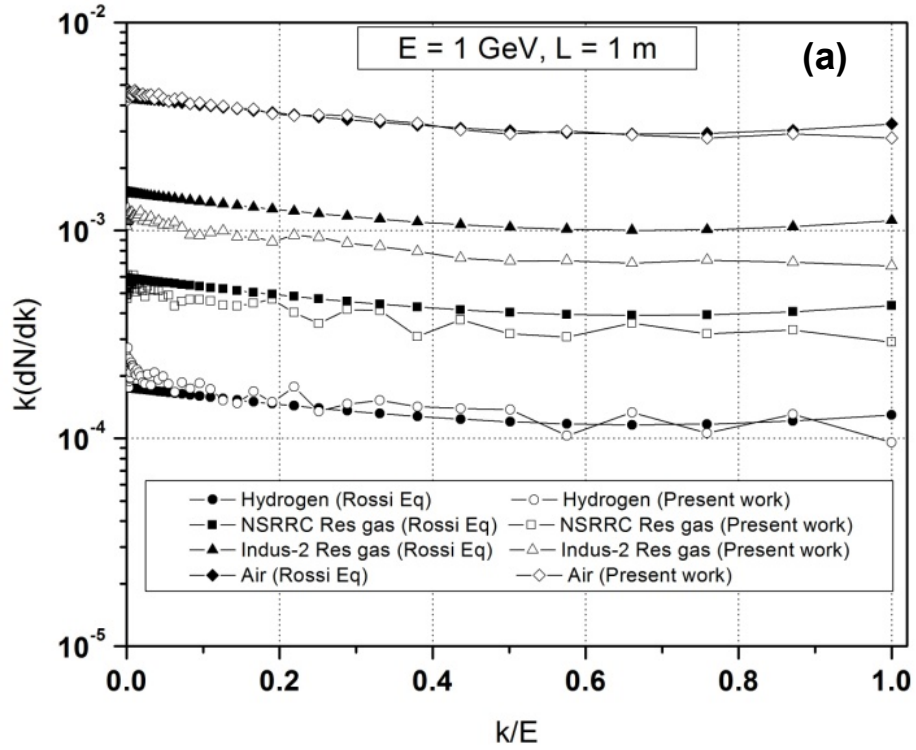


Figure 3.13: Gas bremsstrahlung spectrum for (a) 1 GeV, (b) 2 GeV and (c) 3 GeV electrons from 1 m straight section for different gas compositions

The simulated gas bremsstrahlung spectrum for hydrogen (being most abundant element inside storage ring at UHV condition), residual gas composition of NSRRC, Indus-2 storage rings and air are compared with the analytical expression (equation 1.9) suggested by Rossi [25]. The bremsstrahlung spectrum, $k(dN/dk)$ as a function of k/E are plotted in figure 3.14 (a-c), dN/dk is the number of photons within dk about k when one electron with energy E passes through an path length of 1 g-cm^{-2} . The results are in good agreement with the predicted spectrum by Rossi's expression over the entire energy range.



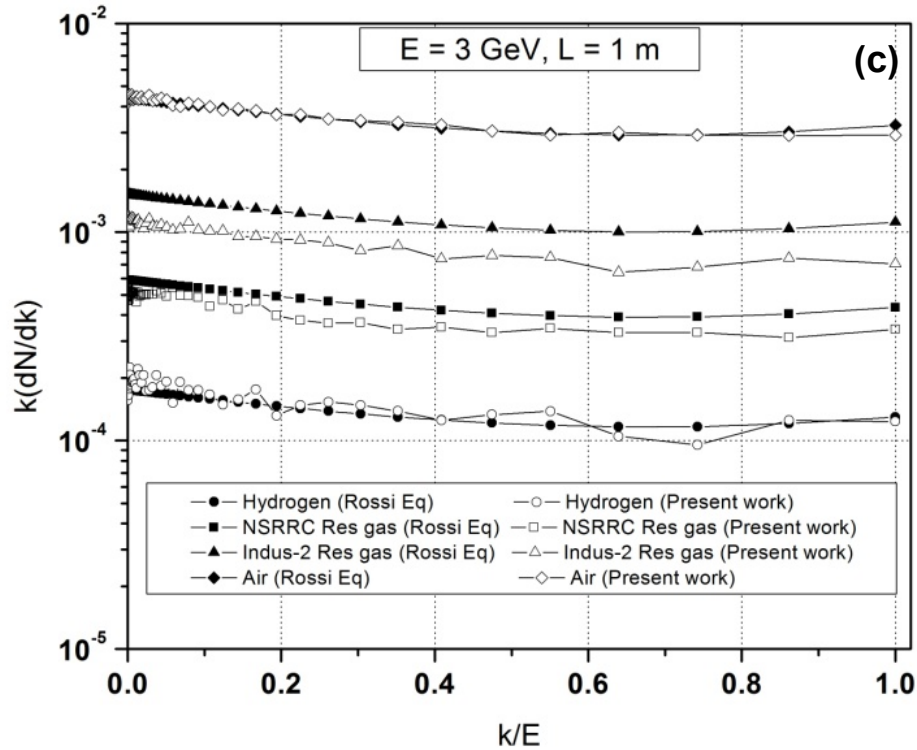


Figure 3.14: Gas bremsstrahlung spectrum $k(dN/dk)$ as a function of k/E for (a) 1 GeV, (b) 2 GeV and (c) 3 GeV electron

Effect of gas bremsstrahlung photon fluence on target length is studied by simulating the bremsstrahlung energy spectra for 3 GeV electron beam by varying straight section lengths from 1 to 10 m. Gaseous mixture used in the simulation is kept same as that of residual gaseous composition of Indus-2 storage ring. The gas bremsstrahlung spectra and total photon fluence for different lengths of target are shown in figure 3.15 (a-b). The observed peak of the spectrum shifts to higher energy as the length of target increases, suggesting the increase in absorption of low energy photons as the length of straight section is increased. The total photon fluence is found to increase linearly with the length of the straight section. The variation of gas bremsstrahlung photon fluence with respect to residual gas molecule composition is studied for 1 – 3 GeV electrons passing through 1 m straight section and is shown in figure 3.16. The study

showed a nonlinear rise in fluence as a function of ($Z_{\text{eff}} \cdot \text{Molecular mass}$) of the gaseous composition.

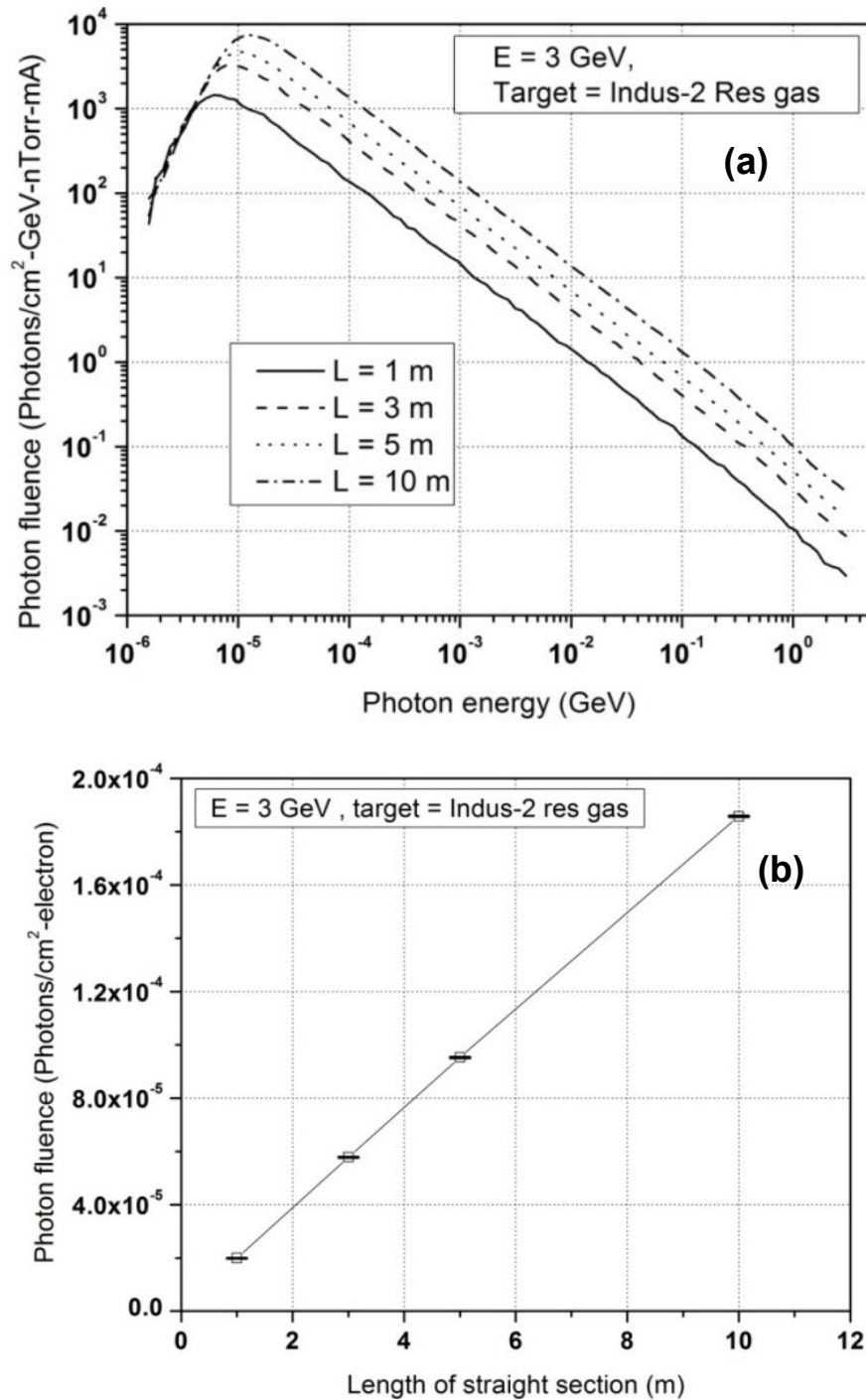


Figure 3.15: (a) Gas bremsstrahlung spectrum and (b) photon fluence from 3 GeV electron beam as a function of straight section length.

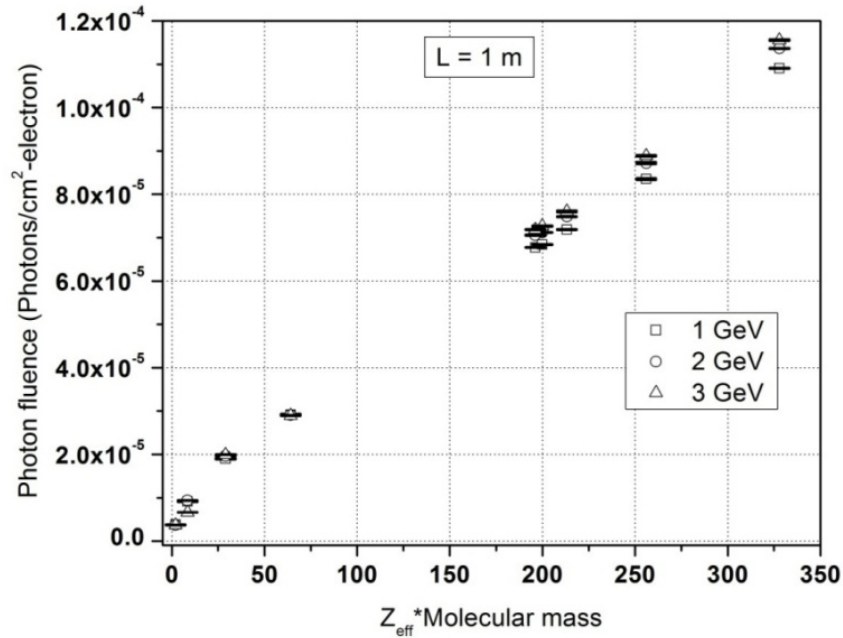
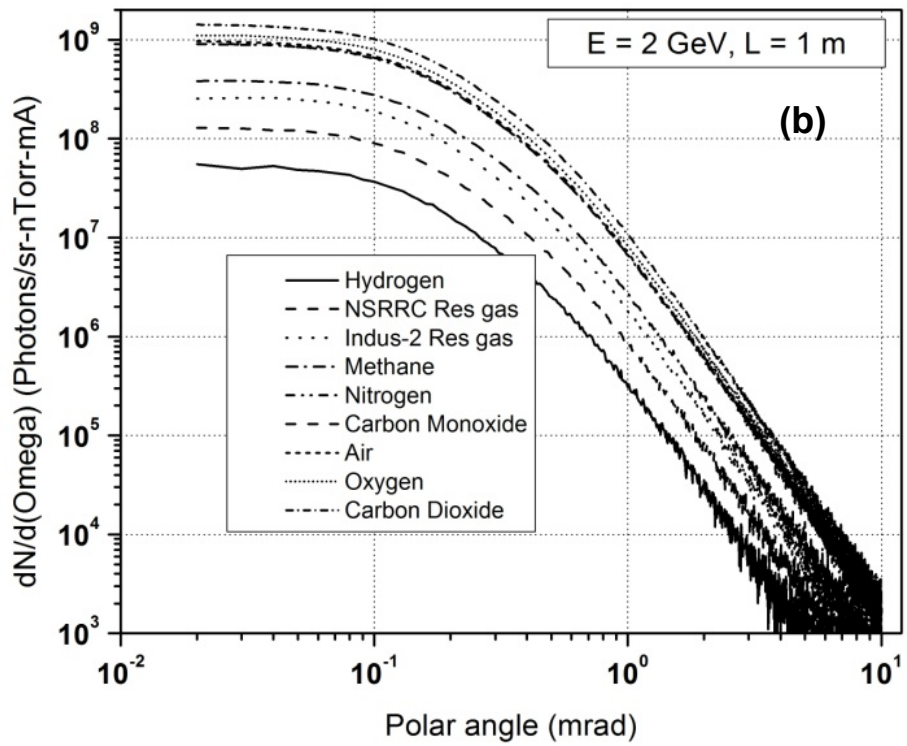
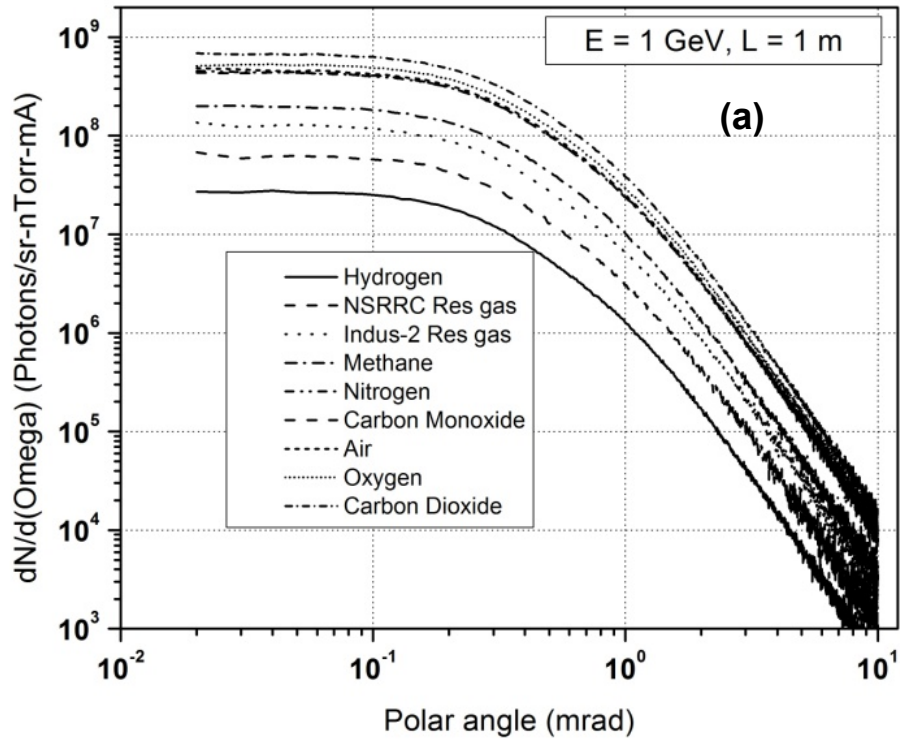


Figure 3.16: Gas bremsstrahlung photon fluence due to 1, 2 and 3 GeV electron beam from 1 m straight section as a function of $Z_{eff} * A$.

The angular distribution of gas bremsstrahlung photons generated by 1, 2 and 3 GeV electrons for different gaseous composition are also studied and shown in figure 3.17 (a-c).



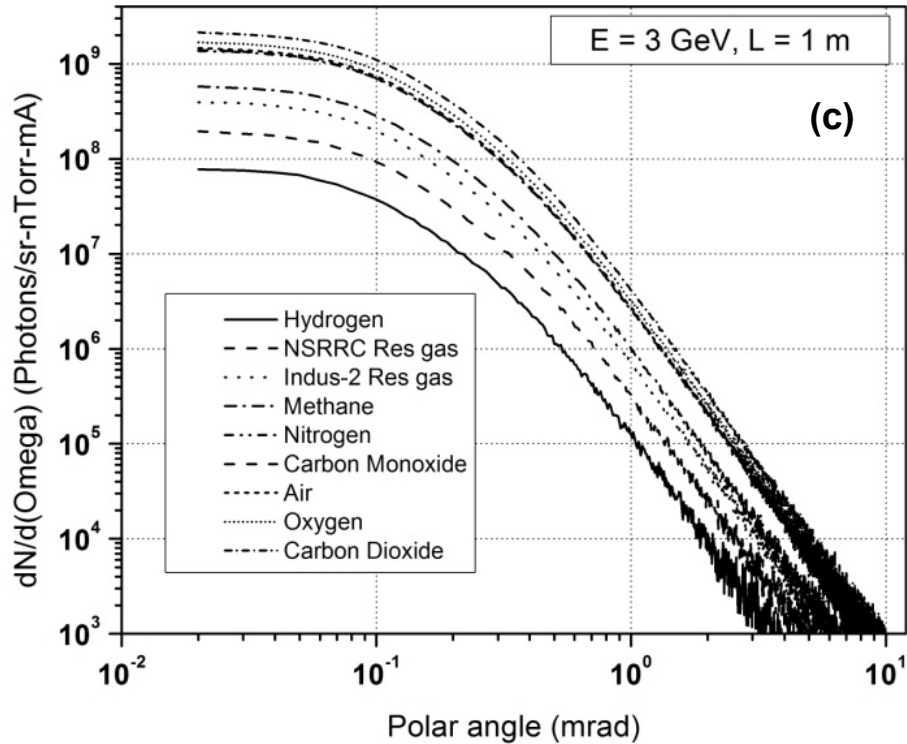
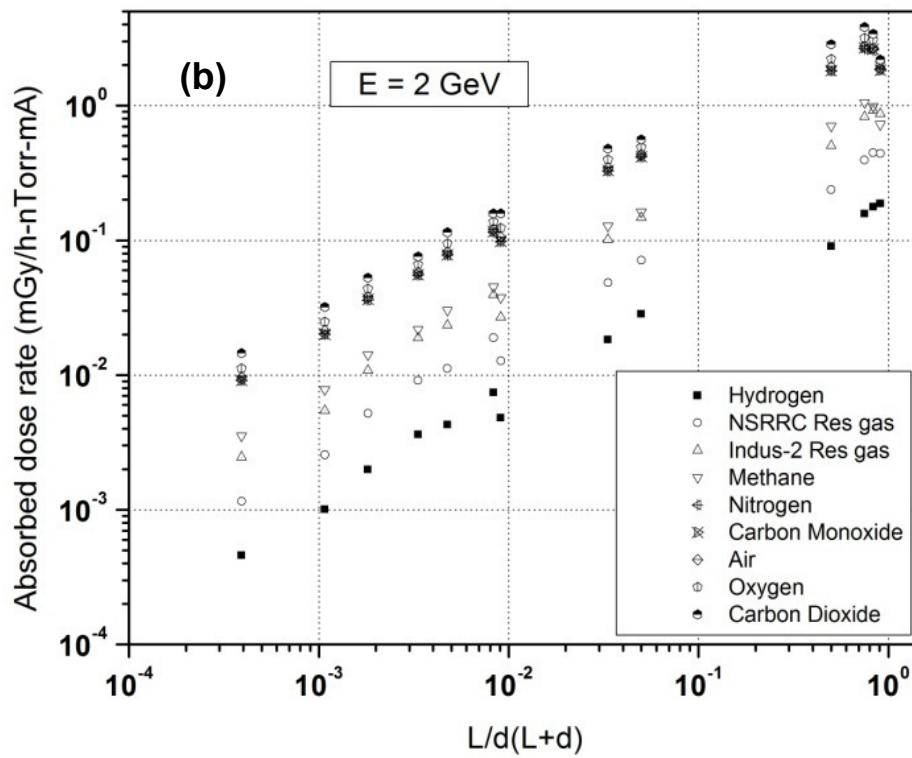
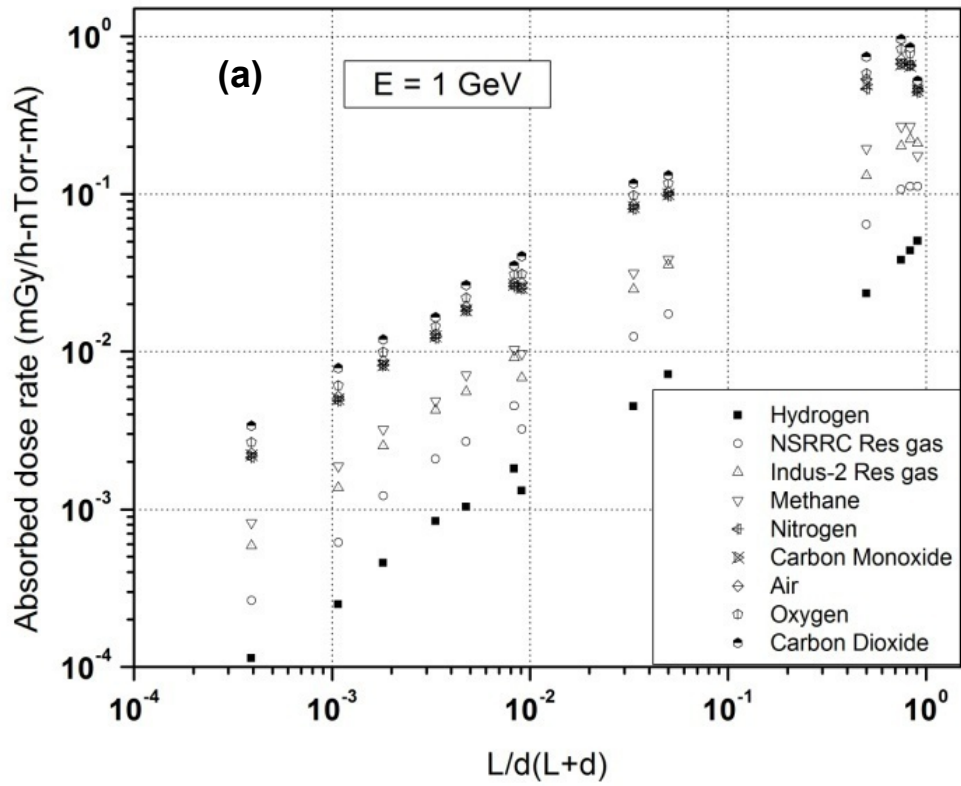


Figure 3.17: Angular distribution of gas bremsstrahlung photons from different gaseous compositions in 1 m straight section for (a) 1 GeV, (b) 2 GeV and (c) 3 GeV electrons.

The angular distribution shows a nearly flat region up to 0.1 mrad emission angle for beam energy up to 3 GeV for all gaseous compositions similar to that of air mentioned in previous sections. Since 0.1 mrad is found to be an optimized emission cone, scoring radius in tissue phantom for gas bremsstrahlung dose estimation is calculated using equation 3.1. The gas bremsstrahlung dose is scored for primary beam energies ($E = 1, 2$ and 3 GeV), straight section lengths ($L = 1, 5$ and 10 m) and target to detector distances ($d = 1, 10, 30$ and 50 m). The variation of absorbed dose rate for different gaseous mixtures with $L/d(L+d)$ are plotted in figure 3.18 (a-c).



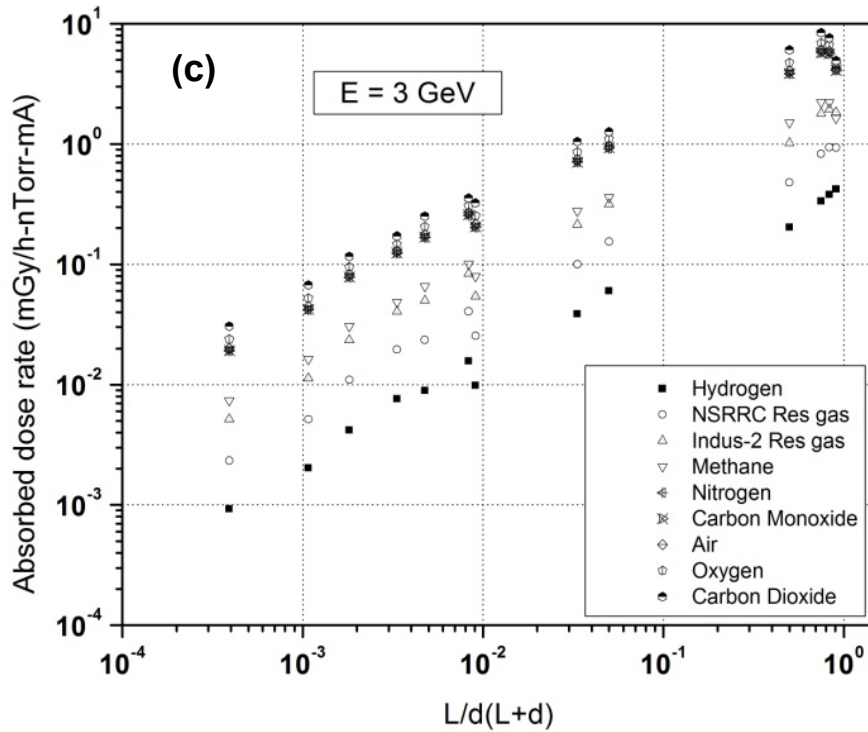


Figure 3.18: Absorbed dose rate as a function of $L/d(L+d)$ for different gas composition due to (a) 1 GeV, (b) 2 GeV and (c) 3 GeV electrons.

From the study (figure 3.18), a residual gas correction factor $(Z_{eff} \times A)^{0.66}$ is obtained for the earlier deduced empirical relation (equation 3.2) for air medium and the modified expression is given below.

$$\dot{D}(Gy/h) = 9.1 \times 10^{-26} \left(\frac{E}{mc^2} \right)^{1.92} \left[\frac{L}{d(L+d)} \right]^{0.78} I \left(\frac{P}{P_0} \right) \left(\frac{Z_{eff}^i \times A^i}{Z_{eff}^{air} \times A^{air}} \right)^{0.66} \quad \text{----- (3.4)}$$

Where notations E , mc^2 , L , d , I , P and P_0 carry same meaning as in equation (3.2). Z_{eff} and A represent effective atomic number and molecular mass (g/mol), respectively of the residual gas.

Therefore the actual gas bremsstrahlung dose rate can be obtained by using empirical relation (equation 3.4). The values for Z_{eff} and A can be estimated by considering the residual gases in vacuum environment of storage ring.

3.4.2 Comparison with experimental data

The gas bremsstrahlung spectra from ADONE [23] and NSRRC [33] storage rings have been reported by Rindi et al. (1982) and Sheu et al.(2004) respectively for actual residual gas composition. FLUKA simulation study is performed to generate gas bremsstrahlung spectra in these storage rings using the reported residual gas composition. A comparison of simulated spectra with the reported data is shown in figure 3.19.

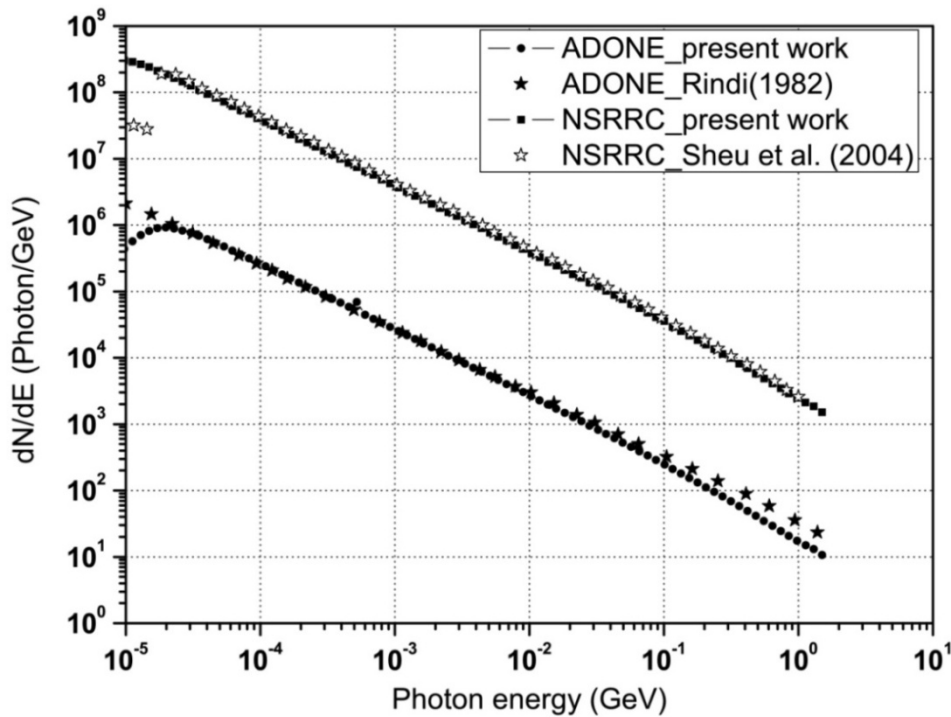


Figure 3.19: Gas bremsstrahlung spectra in ADONE and NSRRC storage ring for actual gas composition

The simulated spectra are found to have very good match with the reported data for NSRRC storage rings except at lower energy photons ($E < 20$ keV), where a sharp dip is observed in the reported data by Sheu et al. (2004). The authors Sheu et al. (2004) have attributed this sharp dip in the spectrum to the absorption of low energy photons by the water cooled aluminium flange placed at the end of the straight section whereas in the present simulation study no such end flange is used. The measured gas bremsstrahlung dose rate at ADONE storage ring ($E = 1.5$

GeV, $L = 6$ m and $d = 15$ m) is reported as 20×10^{-2} mGy/h-mA-nTorr [23]. The measurement was performed using LiF dosimeter (TLD-100) with 0.5 mm copper sheet so as to shield the synchrotron radiation. The typical volume fractions of the composition of the residual gas mixture at ADONE storage ring was reported to be H₂ (14.1), N₂ (1.5), CH₄ (4.8), H₂O (13.4), CO (49.5), Ar (5.4) and CO₂ (11.3). For comparison, the experimental condition is simulated as per the present methodology. The simulated absorbed dose rate is found to be $(19.9 \pm 0.05) \times 10^{-2}$ mGy/h-mA-nTorr with 0.5 mm copper in front of tissue phantom and shows very good match with the reported experimental data. Using the composition of the residual gas mixture, effective atomic number (Z_{eff}) and molecular Mass (A) for ADONE storage ring are calculated to be 8.3 and 24.88 g/mol respectively. The calculated dose rate using equation (3.4) for residual gas in ADONE storage ring ($E = 1.5$ GeV, $L = 6$ m, $d = 15$ m, $Z_{eff} = 8.3$, $A = 24.88$ g/mol) is found to be 11.5×10^{-2} mGy/h-mA-nTorr and is also fairly matches to the experimental data. Comparison among the simulation methodology and the empirical relations for air and actual residual gas with the reported experimental data is given in table 3.5.

Table 3.5: Comparison of calculated and experimental gas bremsstrahlung dose

Experimental condition at ADONE storage ring	Absorbed dose rate ($\times 10^{-5}$ Gy/h-mA)				
	Experimental result	Air as target gas		ADONE residual gas as target gas	
		<i>FLUKA simulation</i>	<i>Eq. (3.2)</i>	<i>FLUKA simulation</i>	<i>Eq. (3.4)</i>
$E = 1.5$ GeV, $L = 6$ m, $d = 15$ m, $P = 1$ nTorr (with 0.5 mm Cu as synchrotron stopper)	20.0	24.6 ± 0.6 (with 0.5 mm Cu & $r = 1.5$ mm)	11.8	19.9 ± 0.05 (with 0.5 mm Cu & $r = 1.5$ mm)	11.5

From the table, the smaller difference among the calculated dose rate from air and the actual residual composition in ADONE storage ring can be attributed the combined effect of Z_{eff} and molecular mass of the gases. The Z_{eff} and molecular mass of the residual gas composition are 8.3 and 24.88 g/mol respectively whereas for air composition the values are 7.36 and 28.97 g/mol. Whereas using the suggested empirical relation for the case of Indus-2 (2.5 GeV), the gas bremsstrahlung dose rate is 3.7 times higher for air target than the actual residual gas composition. Thus it is very important to note that the Z_{eff} and molecular mass is a deciding factor for the gas bremsstrahlung dose. Some of the earlier studies for 2.5 GeV storage ring at Photon Factory [30], 3 GeV storage ring at SSRL [46] and 1.5 GeV ADONE [136] storage ring have indicated higher simulated data (with air target) as compared to experimental data and can be attributed to higher effective atomic number and molecular mass of air as compared to the real gaseous mixture during the experiment. Also these studies have pointed out the variation in results on the difference in vacuum pressure in the storage ring and other experimental conditions. Therefore the composition of residual gas inside the storage ring is an equally important factor in the estimation of the gas bremsstrahlung dose and the empirical relation (equation 3.4) will give a more realistic estimation of gas bremsstrahlung dose in electron storage rings.

3.5 Summary and conclusion

The characteristics of gas bremsstrahlung radiation in high energy electron storage rings ranging from 1 to 5 GeV passing through air medium are studied using FLUKA Monte Carlo code. The bremsstrahlung energy spectra are found to range up to the incident electron energy with the spectral behaviour as that of a thin target bremsstrahlung. From the angular distribution, an optimized emission angle of 0.1 mrad for electron energy up to 3 GeV is observed, which can be

applied to find out the scoring radii at different distances for estimation of gas bremsstrahlung dose. The variation of absorbed dose is studied with respect to the length of straight section length ($L= 1 - 10$ m) and distance from the straight section ($d = 10 - 50$ m). From the study, an empirical relation for dose estimation is deduced. The absorbed dose value obtained from the present study is validated with the reported experimental data at 1.5 GeV and is found to be in very good agreement. From the study, it is found that determining scoring radius using emission angle (0.1 mrad) is a reasonable and practical approach, in comparison to optimizing scoring radius for estimation of absorbed dose for electron storage rings up to 3 GeV.

The study is extended to observe the effect on gas bremsstrahlung radiation due to residual gas composition inside storage rings maintained at ultra high vacuum. The simulated gas bremsstrahlung spectra for various gas and gaseous mixtures are compared with spectrum predicted by Rossi's analytical formula and found to be in very good agreement. Variation of absorbed dose rate with $L/d(L+d)$ for different gaseous compositions is studied. From the study, a factor $(Z_{eff} \times A)^{0.66}$ is obtained as a residual gas correction term in the empirical relation to calculate the gas bremsstrahlung dose rate. The modified empirical relation is expected to have better predictive power for different vacuum environments. From the study, it is concluded that gas bremsstrahlung dose rate from the actual residual gaseous mixture in electron storage rings is lower than that estimated by assuming air. The simulation methodology is also applied to 2.5 GeV electron storage ring for calculating the gas bremsstrahlung dose. This study is useful for shielding evaluation of insertion device beamlines for medium energy synchrotron radiation sources.

Chapter 4

Synchrotron radiation dosimetry studies

4.1 Introduction

Synchrotron radiation is the second major radiation hazard after gas bremsstrahlung in any synchrotron beamline. Because of ultra high intensity and low energy, synchrotron radiation is a potential radiation hazard in the beamline. Synchrotron radiation being low energy photons up to few keV can give acute skin dose on exposure. Both primary (direct) and scattered synchrotron radiation from the beamline components are significant and need special attention to ensure safety of users.

Indus-2 synchrotron facility (Appendix-A) is designed to accommodate 26 synchrotron beamlines. Out of 26 beamlines, 21 beamlines are planned on bending magnets and 5 on insertion devices. The energy span of synchrotron radiation at Indus-2 lies from infra red to hard x-ray with critical wavelength of 1.98 \AA^0 ($\sim 6.3 \text{ keV}$) for bending magnet sources. Some beamlines use soft x-ray part of the synchrotron beam and thus the complete beamline including experimental station is maintained at ultra high vacuum. However, most of the beamlines utilize hard x-ray part of synchrotron radiation and the experiments in these beamlines are performed in air. Thus the radiation safety issues in hard x-ray beamlines are stringent due to the high intensity synchrotron radiation. The radiation, when incident on experimental sample and beamline components, gets scattered at wide angles. Hence the beamlines using hard x-ray act as potential

source of radiation and are hazardous for persons working near the beamlines. In order to ensure safety of synchrotron users and workers, adequate shielding and safety system are designed and implemented. The beamline components are housed in properly designed shielded hutch. The layout of a typical hard x-ray beamline in Indus-2 is shown in figure 4.1.

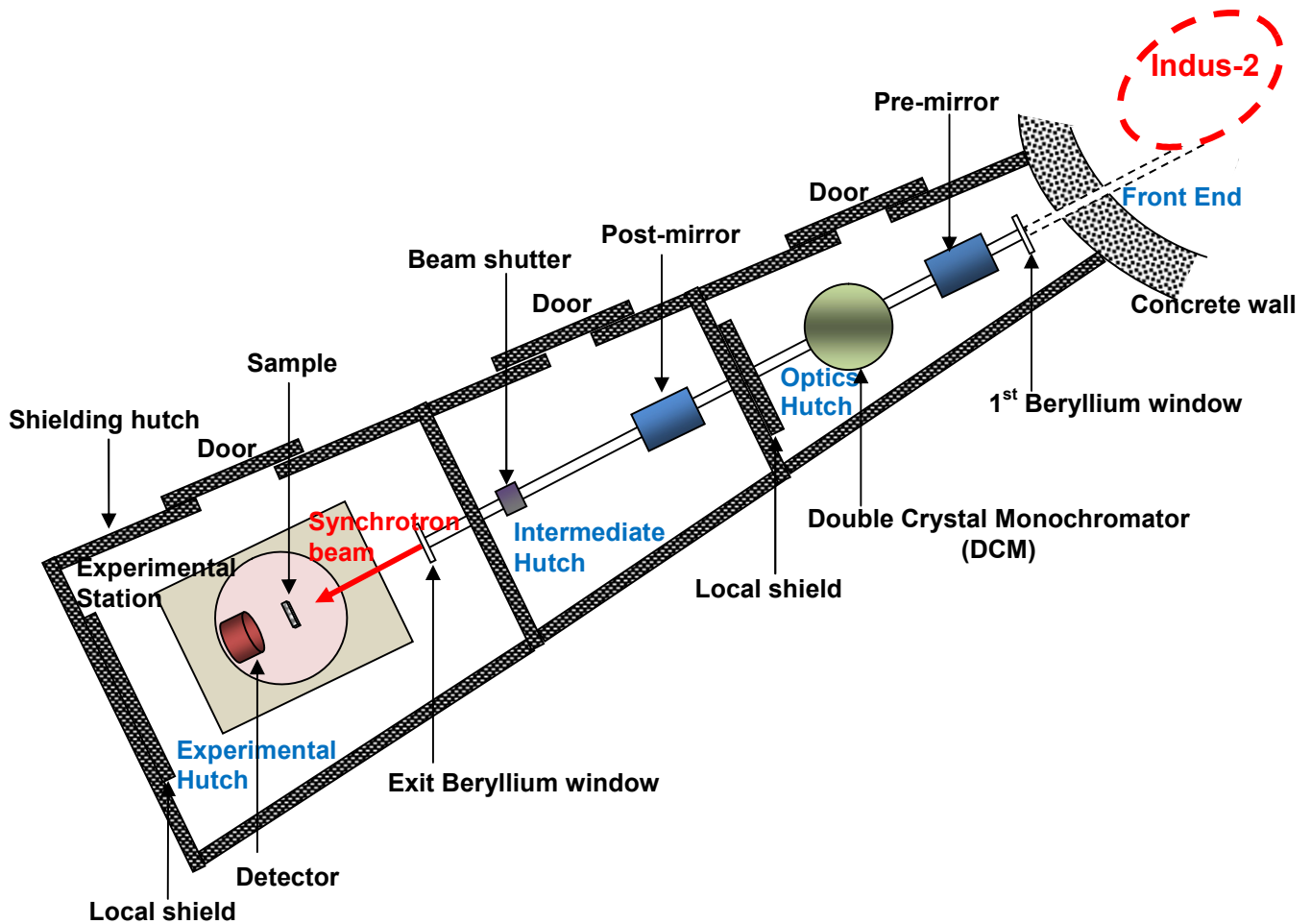


Figure 4.1: Schematic layout of a synchrotron beamline at Indus-2 showing various hutch compartments and optical elements housed in these compartments (not to scale)

In Indus-2, the hard x-ray beam energies from bending magnet sources range from 4 keV to 100 keV but the useful flux is limited up to 30 keV for monochromatic beam applications. The low energy cut off is due to the beryllium window (200 μm thick) placed at the end of the front end.

Depending upon the type of the experiment, different beamlines use different range of photon energies. Synchrotron beamlines utilizing single energy, small energy band (~100-500 eV) and full spectrum are respectively called as monochromatic, pink and white beamlines.

In the energy regime (4-100 keV), photoelectric effect is the dominant interaction mechanism. Since the photoelectric effect has a strong dependency on the energy of photon and the atomic number of material, the energy response of dosimetry devices for synchrotron radiation needs special attention. Quantification of high dose due to intense synchrotron beam also poses challenge to conventional TL dosimetry. Therefore evaluation of radiation dose levels, energy dependency of dosimetry devices and detection techniques for synchrotron beamlines are addressed in the present study. The objective of the work described in this chapter is

- i) To evaluate accidental radiation exposures likely to be received by a beamline user due to direct and scattered synchrotron beam and the shielding requirement.
- ii) To evaluate the energy response of the personnel dosimetry device (CaSO₄:Dy based TLD badge) to synchrotron radiation.
- iii) To study the effect of high dose on CaSO₄:Dy TL dosimeters using X-ray Diffraction (XRD) and X-ray Absorption Near Edge Structure (XANES) spectroscopic techniques.
- iv) To design of a primary standard (free air ionization chamber) for dosimetry in synchrotron beamlines.

4.2 Evaluation of synchrotron radiation dose in Indus-2

Indus-2 synchrotron radiation spectrum in the energy range 4 to 100 keV is used as the incident beam in FLUKA simulation for the evaluation of the absorbed dose and shielding thickness. The obtained FLUKA simulation results are compared with experimental data. For studying scattered radiation dose, experiment is performed at beamline BL-11, Indus-2 and the experimental

conditions are simulated using FLUKA code. The simulation studies are also extended to evaluate thickness of lead for radiation shielding of the beamlines.

4.2.1 Synchrotron radiation spectrum in Indus-2

The synchrotron radiation spectrum for 2.5 GeV electron bending through 5.5 m bending radius is generated using a Fortran program developed by Alberto Fasso [137]. The program gives output in differential flux (dN/dE) per electron where N and E represent number and energy of photons, respectively. The generated synchrotron energy spectrum in the energy range 4 to 100 keV (normalized to design electron beam current of 300 mA) is shown in figure 4.2.

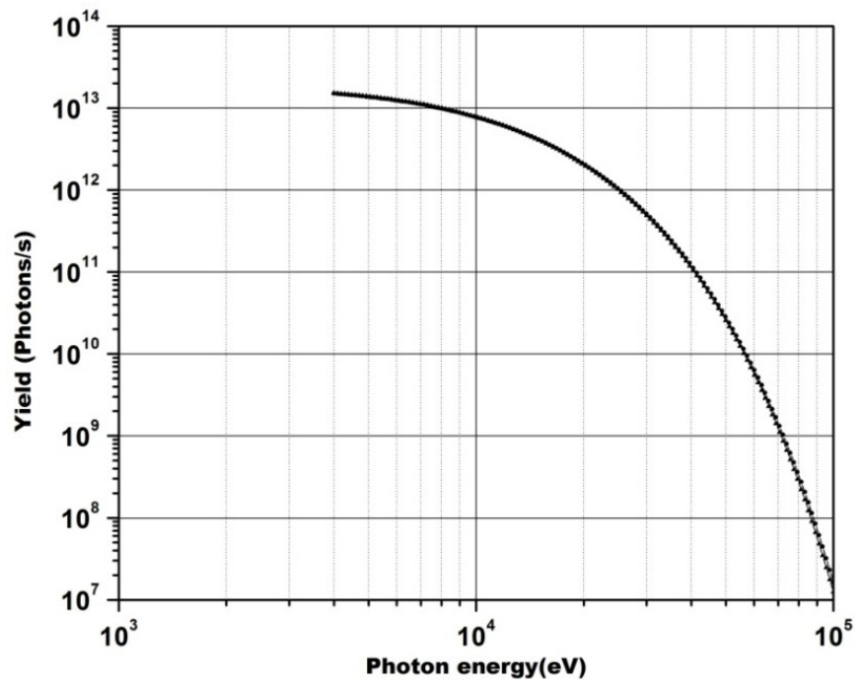


Figure 4.2: Synchrotron radiation spectrum in Indus-2 (300 mA at 2.5 GeV)

4.2.2 Absorbed dose rate due to direct synchrotron radiation

The absorbed dose rate in water phantom due to direct synchrotron radiation is simulated using FLUKA Monte Carlo code. The synchrotron spectrum (figure 4.2) is allowed to incident on water phantom (10 mm x 10 mm x 300 mm). The geometry used in the simulation study is shown in figure 4.3.

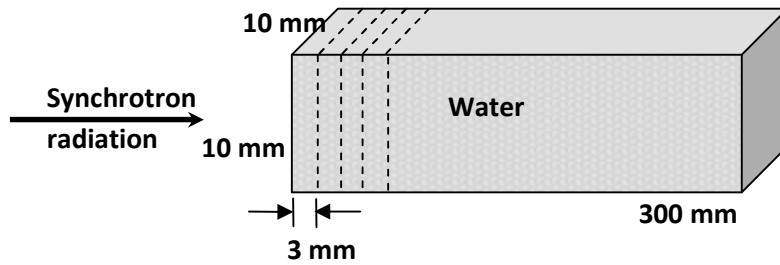


Figure 4.3: Geometry used in the simulation study

USRBIN scoring is used in the simulation for determination of absorbed energy. Electron and photon transport threshold are set at 1 keV using EMFCUT. The results from the USRBIN estimator are given in terms of GeV/cm^3 -primary electron for absorbed energy. USRBIN output is converted to absorbed dose rate in Gy/h using the total number of electrons in Indus-2 storage ring. Simulation is performed for 10^7 histories and the statistical errors found are within 1% for all data points. The depth dose profile inside the water phantom is shown in figure-4.4.

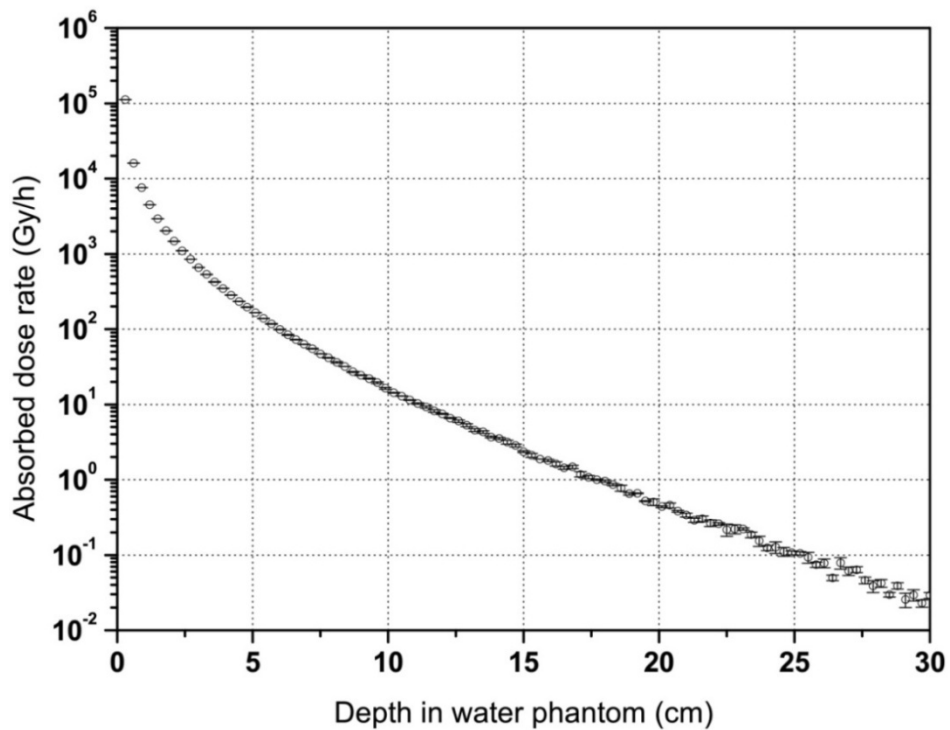


Figure 4.4: Depth dose profile in water phantom due to direct synchrotron radiation

Synchrotron radiation gets attenuated significantly within the depth of water because of its low energy and the maximum absorbed dose rate of 1.12×10^5 Gy/h is observed at the surface of water phantom. From the study, it is found that during accidental exposure to direct synchrotron radiation, absorbed dose to the skin will be of the order of 10^5 Gy/h.

4.2.2.1 Measurement of direct dose at synchrotron beamlines

During commissioning trail of Indus-2, direct synchrotron dose is measured at Lithography beamline (BL-7) using thin mylar (1 mg/cm^2) window ion chamber. This ion chamber (400 cc, air) was designed and developed by Electronics Division, Bhabha Atomic Research Centre (BARC) for low energy photon measurements [138]. The specification of the ion chamber is given in table 4.1.

Table 4.1: Specifications of detector used for direct synchrotron dose measurement

Specification	Details
Detector type	Ion chamber
Fill gas	Air
Sensitive volume	400 cc
Window	Mylar (1.0 mg/cm^2)
Applied Voltage	1 kV
Measuring range	$1 - 10^3$ R/h (Low range) $10^2 - 10^5$ R/h (High range)
Sensitivity	40 pA/R/h for Co-60 gamma energies 36 pA/R/h for Cu K_{α} X-ray energy (8.04 keV)

During the experiment, the ion chamber is placed just after the beryllium window, at the end of the front end (see figure 4.1). The measured ion current from ion chamber is converted to absorbed dose rate (relative dose rate with respect to Co-60). The synchrotron dose rate is found

to be 3.83×10^3 Gy/h-mA for stored current of 36 to 32 mA at 2.0 GeV beam energy in Indus-2. Synchrotron dose is also measured at Energy Dispersive X-ray Diffraction beamline (BL-11) using circular LiF:Mg,Ti (TLD-700) TL dosimeter during trial operation of Indus-2. The TLD-700 discs are read in HARSHAW TLD reader (Model 3500) at a heating rate of $5 \text{ }^\circ\text{C/s}$ in the temperature range of $50\text{--}280 \text{ }^\circ\text{C}$. Because of high synchrotron dose, the dose is evaluated using the calibration factor obtained for Co-60 dose range of $100\text{--}500$ Gy. Direct synchrotron dose rate is found to be 268 Gy/h-mA at BL-11 for 2.0 GeV beam energy. Synchrotron dose measurement at Angle Dispersive X-ray Diffraction beamline (BL-12) using a free air ion chamber detector gave dose rate of 104.08 Gy/h-mA for 1.72 GeV beam energy [43]. The intensity of synchrotron radiation is directly proportional to I (stored electron beam current) and E^4 (electron beam energy) of the storage ring. Thus on extrapolation of these measured data to design parameters of Indus-2 ($I = 300$ mA, $E = 2.5$ GeV beam energy), the dose rates due to direct synchrotron radiation is found to be 1.96×10^5 and 1.39×10^5 Gy/h at BL-11 and BL-12 respectively. Comparison of the simulated and experimental results is given in table 4.2. From the table, it is observed that the simulated data is in very good agreement with the measured data.

Table 4.2: Comparison of the simulated and experimental results

Technique	Simulation/Experimental condition	Detector used	Absorbed dose rate (Gy/h-300 mA)
<i>Simulation</i>			
FLUKA	4-100 keV spectrum	30 cm water phantom	1.12×10^5
<i>Experiment</i>			
At BL-11	White synchrotron beam	TLD-700	1.96×10^5
At BL-12		Free air ion chamber	1.39×10^5

4.2.3 Absorbed dose rate due to scattered synchrotron radiation

4.2.3.1 Experiment

Scattered synchrotron radiation dose rate from different targets are measured at BL-11, Indus-2 using thin mylar window ion chamber detector (FLUKE Model 451B, Australia make). This detector is having a movable beta window (440 mg/cm^2) in front of thin mylar window (1.7 mg/cm^2) for segregation of low energy photons. The specification of the FLUKE-451B ion chamber is given in table 4.3.

Table 4.3: Specifications of FLUKE-451B ion chamber

Specification	Details
Detector type	Ion chamber
Radiation detected	α particles $> 7.5 \text{ MeV}$, β particles $> 100 \text{ keV}$ & γ photons $> 7 \text{ keV}$
Fill gas	Air
Sensitive volume	349 cc
Window	Mylar (6.6 mg/cm^2) with 440 mg/cm^2 beta slide for beta particle detection
Measuring dose range	0 – 500 mSv/h (with $\pm 10\%$ accuracy)

Three disc targets (Aluminium, Copper and Tantalum), each of 25.4 mm diameter and 5 mm thickness are used as scatterer and placed in white synchrotron beam path at BL-11. Scattered dose rate at three different angles i.e. 90° , 120° and 150° (with respect to the beam direction) are measured simultaneously using the thin window ion chamber detectors, placed at a distance of 0.64 m from the target. During the experiment, full synchrotron spectrum from Indus-2 is allowed to hit the target. The detectors are kept in integrated mode for 5 minutes and the corresponding doses are recorded. During measurement, the beta window is kept open to allow the synchrotron radiation to reach the detector volume. Three sets of measurements are

performed for each target. Photograph along with the schematic diagram of the experimental setup is shown in figure 4.5.

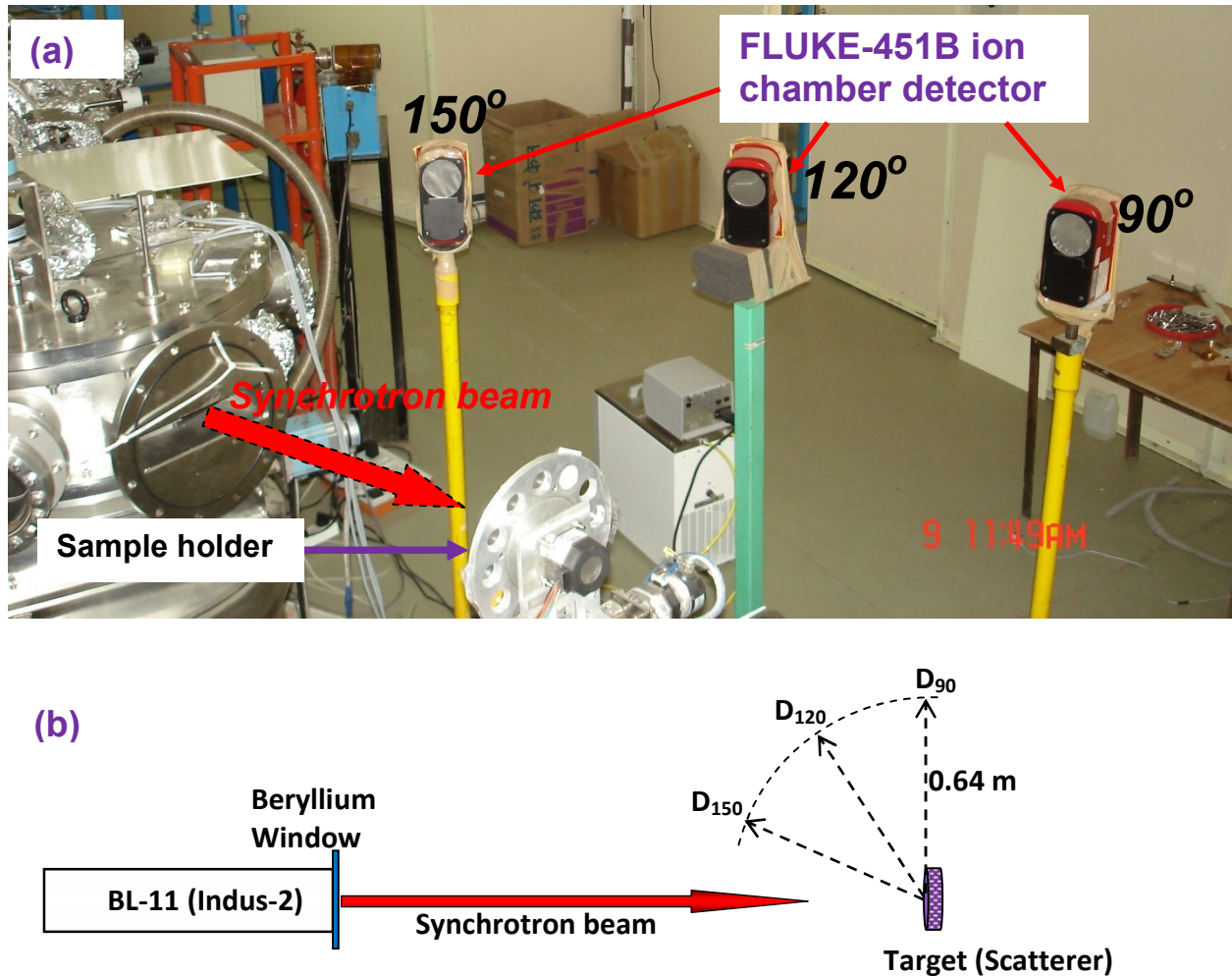


Figure 4.5: Photograph (a) and the schematic diagram (b) of the experimental set-up

Since the synchrotron beam is always accompanied by gas bremsstrahlung radiation from storage ring, the scattered dose due to gas bremsstrahlung radiation is measured with beta slide window closed condition. In this condition, the synchrotron radiation is absorbed by the window. The integrated dose due to scattered bremsstrahlung radiation in all the detectors is found to be zero for 5 minutes duration. This confirms that the contribution of scattered bremsstrahlung radiation is insignificant.

4.2.3.2 Simulation

The above experiment is simulated using FLUKA Monte Carlo code. The white synchrotron beam in the energy range 4 to 100 keV is allowed to incident on Al, Cu and Ta targets, each of 5 mm thickness and 25.4 mm diameter. The energy absorption in three spherical detectors (medium-water) kept at 0.64 m from the target at 90° , 120° and 150° is scored. The radius of detector is kept 42 mm so as to match the volume of ion chamber detector used in the experiment. The transport cutoffs for electron, positron and photon are set at 1 keV. The simulation is carried out for 5×10^8 histories.

The angular distribution of scattered synchrotron dose rates, normalized to electron beam current (both experimental and simulated data) are shown in figure 4.6.

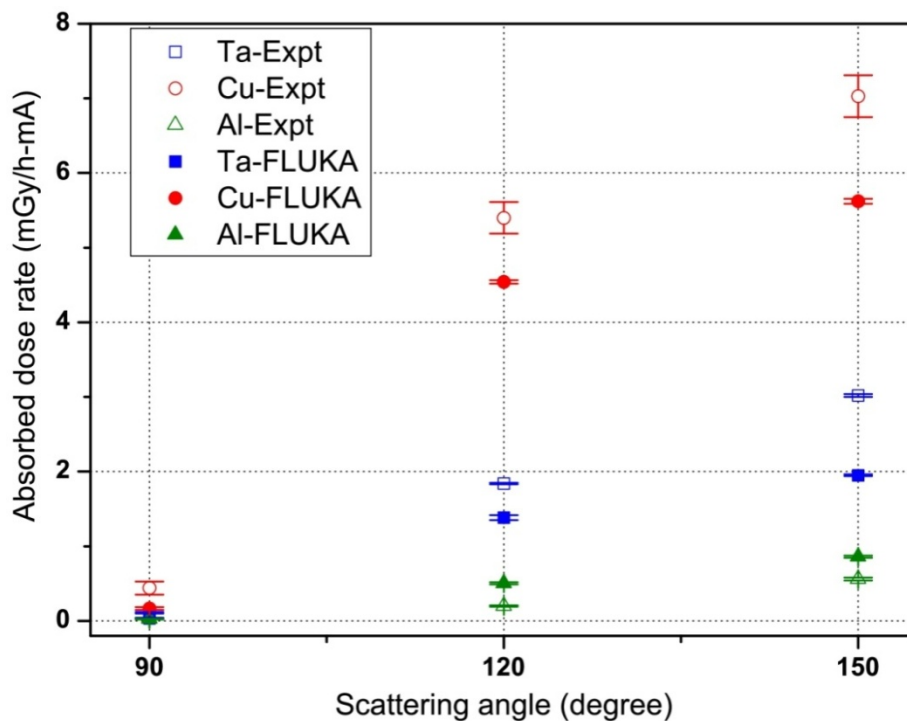


Figure 4.6: Angular distribution of scattered synchrotron radiation from Aluminium, Copper and Tantalum targets

The dose rate shows an increasing trend as the scattering angle is increased. Scattered dose rate from Cu target is found to be the highest at all the angles, although the atomic number of Cu is lower than Ta. The observed higher scattered dose rate from Cu than Ta can be attributed to the photoelectric absorption of incident synchrotron photons and following fluorescence emission. The K-absorption edge of Al, Cu and Ta are 1.56, 8.98, 67.42 keV respectively. Due to the abundance of photons near Cu K-edge, maximum resonance absorption and subsequent de-excitation through characteristic fluorescent emission give rise to higher dose rate. Al target is showing minimum scattered dose rate, which can be attributed to lower photoelectric absorption and also low fluorescence efficiency (because the energy of the incident photons is much higher than its K-edge). From the study, it is observed that the scattered synchrotron dose has a strong dependency on the incident energy spectrum and the atomic number of scatterer. The scattered dose rate from different target materials does not vary in proportion to the atomic number but strongly depends on the incident energy and subsequent resonance absorption followed by fluorescence emission from the target material. The maximum scattered dose rate for design stored beam current of 300 mA, extrapolated from the experimental data works out to be 2.1 Gy/h at 0.64 m at 150°. Using this data, the thickness of lead for lateral shielding wall (side wall) for white synchrotron beamline hutches of Indus-2 is calculated and 1 mm lead is found to be the optimized shield thickness for achieving regulatory limit of 1 µSv/h for full occupancy [139].

4.2.4 Evaluation of shielding thickness

FLUKA simulation is carried out to evaluate lead thickness of the front wall of the shielding hutch. The synchrotron spectrum (figure 4.2) is allowed to incident on lead target (10 mm x 10 mm) with thickness varying from 1 to 4 mm. The absorbed dose rate is scored in the water phantom (300 mm x 300 mm x 300 mm) placed after the lead target. The lateral dimension of

water phantom is set 300 mm for scoring both primary and secondary radiation emanating from the lead target. The variation in dose rate with lead thickness is shown in figure 4.7.

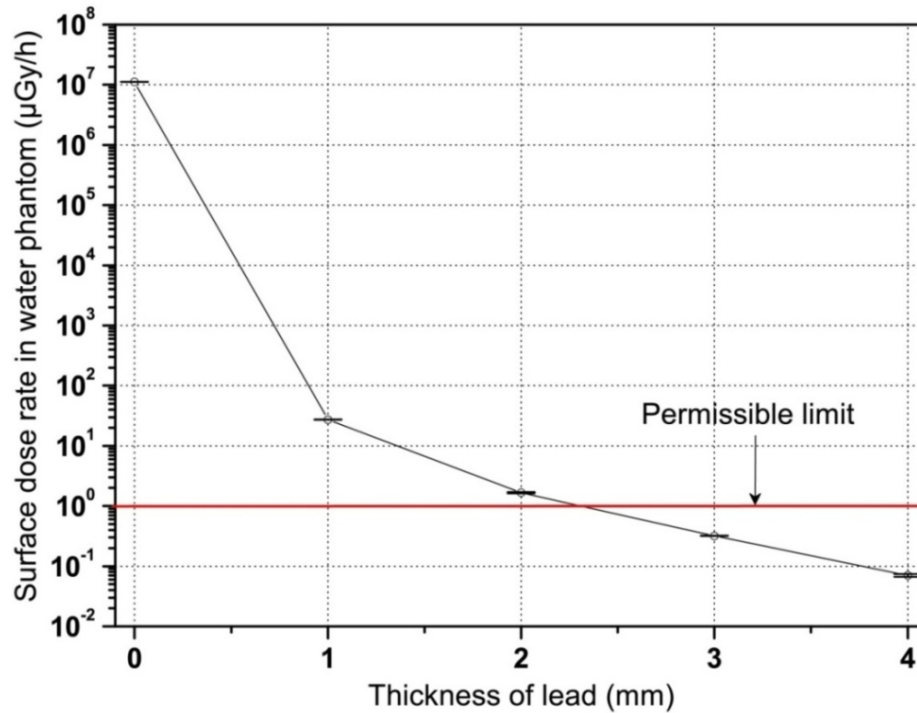


Figure 4.7: Surface dose rate in water phantom with respect to lead thickness

Significant reduction in surface dose rate in water phantom is observed with increase in lead thickness. The synchrotron spectrum (figure 4.2) of Indus-2 has a broad range covering from 4 to 100 keV, in which flux of high energy photons ($E > 50$ keV) are 3-6 orders lesser than the low energy photons (~ 10 keV). Therefore drastic fall of the dose rate, by 6 orders of magnitude is observed with 1 mm of lead because of strong attenuation of low energy photons. However with addition of further lead thicknesses, the absorbed dose rate shows a near exponential fall due to the attenuation of the high energy part of the synchrotron spectrum. As per the regulatory norms in India, the permissible effective dose limit for normally accessible area (full occupancy) is 1 $\mu\text{Sv/h}$ [139]. Thus lead shield thickness of 3 mm is found adequate to reduce absorbed dose to

permissible limit and thickness of the front wall (lead) for the synchrotron beamline hutch is set as 3 mm.

4.3 Response of personnel dosimetry device to synchrotron radiation

Personnel dose monitoring is one of the important part of radiation safety programme of any radiation facility. The personnel dose monitoring in all radiation facilities across India is carried out using $\text{CaSO}_4:\text{Dy}$ based thermoluminescence dosimeter (TLD) badge. This badge is also used for personnel monitoring of radiation workers in synchrotron beamlines of Indus-2. The badge was originally designed for monitoring beta and gamma dose in mixed radiation environment at nuclear reactors and radiation processing facilities across the country [78]. The over-energy response of $\text{CaSO}_4:\text{Dy}$ at low energy (< 100 keV) is compensated using metal filters. The schematic of the TLD badge is shown in figure 4.8. The badge has three TL discs (D1, D2 and D3) each of 0.8 mm thickness, mounted on an aluminium card. The card is placed inside the plastic cassette having different filters on both front and backside of the cassette. The disc D1 is kept under metal filters, 0.6 mm aluminium followed by 1.0 mm copper. The disc D2 is kept under 1.6 mm thick PMMA (Perspex) filter and the disc D3 is left open from both sides [85,92].

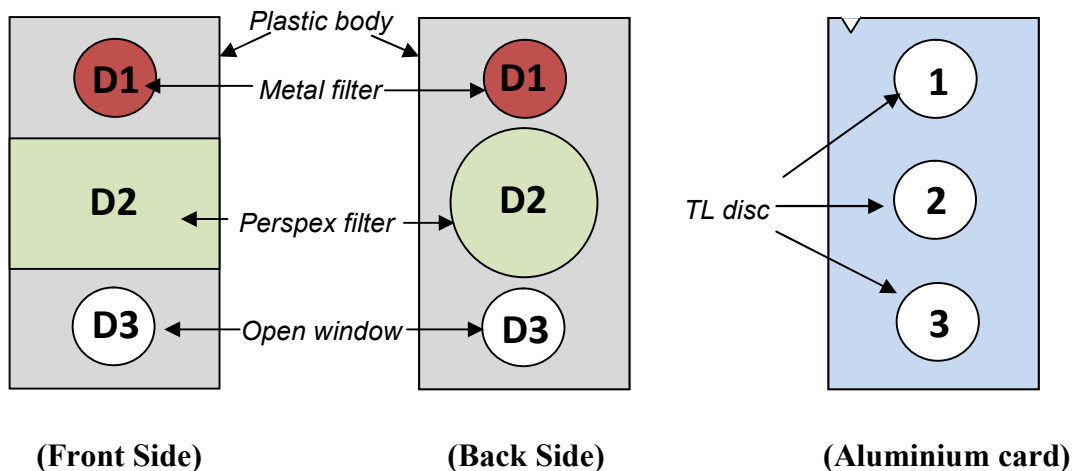


Figure 4.8: Schematic of the TLD badge

The energy dependence of the badge for photon energy from 30 keV to 1.25 MeV has been reported. The metal filter (combination of copper and aluminium) modifies the over-response to 65% at about 60 keV and 25% under-response at 30 keV, compared to a flat response at energies above 200 keV (see figure 1.9) has been achieved [77]. The energy response is extended down to 17 keV using several proposed algorithms [82-85].

The majority of synchrotron beamlines in Indus-2 is hard x-ray beamlines and use monochromatic photon energies in the range 5 to 30 keV. Some of the beamlines also utilize full white synchrotron beam for specific applications. Though independent studies have been reported on energy response of bare $\text{CaSO}_4:\text{Dy}$ and $\text{LiF}:\text{Mg,Ti}$ to synchrotron radiation in energy range 7 to 35 keV at various synchrotron beamlines [86-88] but the response of the TLD badge to has not been studied. Therefore in the present work, energy response of the badge to synchrotron radiation is studied with $\text{CaSO}_4:\text{Dy}$ and $\text{LiF}:\text{Mg,Ti}$ using Monte Carlo simulation and experiment at Indus-2 synchrotron beamline.

4.3.1 Simulation for energy response of the TLD badge

Simulation study is performed for monoenergetic photons in the energy range of 5 to 100 keV using FLUKA Monte Carlo code. In addition to the study on response for monoenergetic photons, response to white synchrotron radiation spectrum in energy range 4 to 100 keV is also simulated.

The geometry of TLD badge is prepared using FLAIR in FLUKA code, taking into account of the actual dimension and materials used in the badge (figure 4.9).

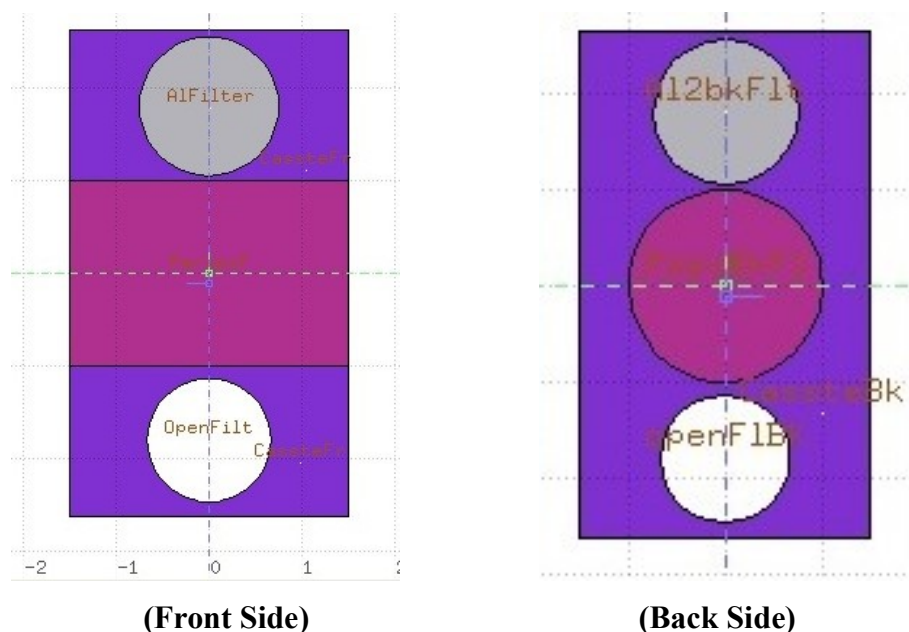


Figure 4.9: Simulation geometry of the TLD badge generated using FLAIR

A broad beam of photons (monoenergetic/full spectrum) is allowed to incident normally on the badge and the absorbed doses in TL discs are obtained by scoring absorbed energy density through USRBIN estimator. Transport cut-offs for electron/positron and photon in all media are set at 1 and 0.1 keV respectively using EMFCUT card. For estimation of relative response of TL discs with respect to human body, absorbed dose in ICRU tissue is calculated using mass energy absorption coefficient of ICRU tissue (4 components) for monoenergetic photons from National Institute of Standards and Technology (NIST) database [140]. In case of white synchrotron spectrum, the energy absorption is simulated for both TLD badge and ICRU tissue independently. The ICRU tissue size is kept the same as that of TL disc. The composition of different materials used in simulation study is listed in table 4.4 [89,132]. The relative response is calculated by taking the ratio of absorbed dose in TL disc and ICRU tissue. The statistical uncertainties in the simulation results are achieved within $\pm 7\%$.

Table 4.4: Composition of materials used in simulation study

Compound	Density (g/cc)	Fraction of the constituents
CaSO ₄ :Dy [#]	2.96	O: 0.4698; S: 0.23539 Ca: 0.29421; Dy: 0.00059
LiF:Mg,Ti [#]	2.635	Li: 0.26753; F: 0.73226 Mg: 0.000187; Ti: 0.0000184
ICRU Tissue [#]	1.0	H: 0.101172; C: 0.111 N: 0.026; O: 0.761828
Plastic [#]	1.127	H: 0.101327; C: 0.775501 N: 0.035057; O: 0.052316 F: 0.017422; C: 0.018378
Perspex ^{\$}	1.19	H: 8.0; C: 5.0; O: 2.0

Note: # represents mass fraction and \$ represents atomic fraction

4.3.2 Experimental verification

Experimental study is carried out at x-ray imaging beamline (BL-4), Indus-2 to verify the simulation results. This beamline uses a double-crystal monochromator (DCM) with a pair of Si (111) crystals to select desired energy from white synchrotron spectrum with an energy resolution ($\Delta E/E$) better than 10^{-3} [141]. The energy of synchrotron photons from the DCM is calibrated using absorption edges of metal foils. Monochromatic photons of energies 10, 15 and 20 keV are used for the study. Circular TL discs are placed inside the TLD badge [separately for CaSO₄:Dy (TLD-900) and LiF:Mg,Ti (TLD-700)] under different filters. Then the badges are exposed to 10, 15 and 20 keV monochromatic photons at the beamline. The synchrotron beam of size 100 mm (H) x 1 mm (V) is allowed to incident normally on the badge placed on the sample holder. Because of small vertical size as compared to the badge size, TLD badge is scanned in vertical direction to have uniform exposure. The photograph of the experimental set up is shown in figure 4.10.

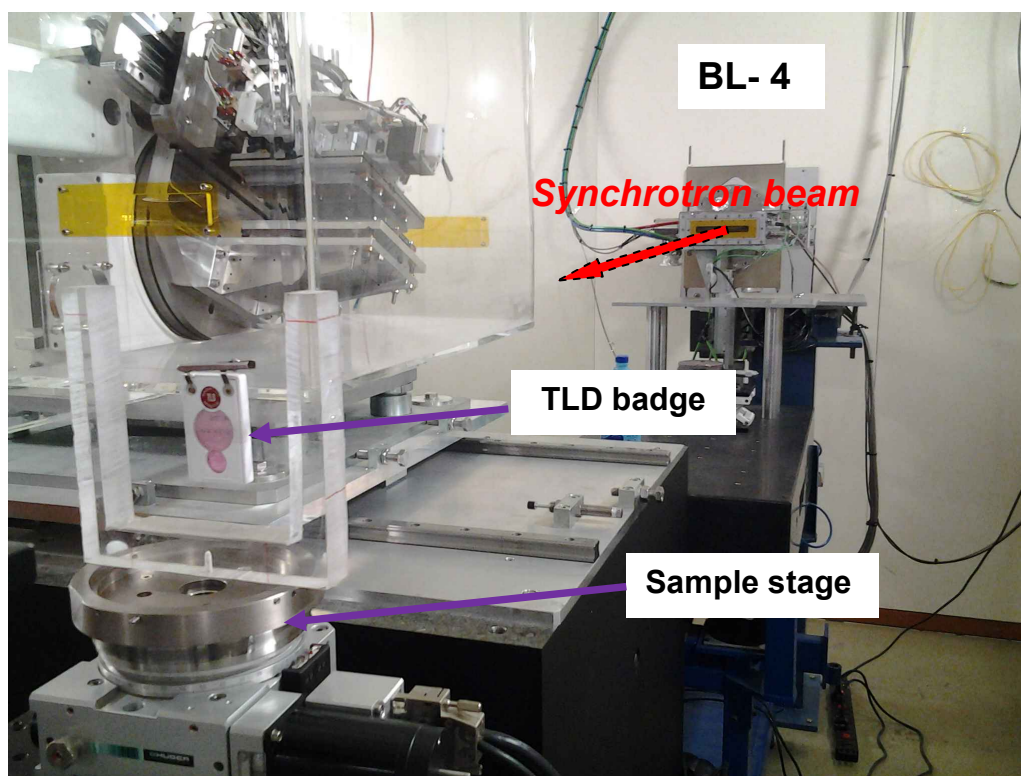


Figure 4.10: Experimental set up at BL-4 (Indus-2)

The TL discs are read in a HARSHAW TLD reader (Model no. 3500) at a heating rate of 5 °C/s in the temperature range of 50–280 °C. Because of low energy photon exposure, exposed surface of TL disc is placed facing the photomultiplier tube (PMT) of TLD reader during TL readout. Absorbed dose from the TL discs are evaluated using calibration factor obtained for Co-60 source. Considering the fact that self attenuation [141] and TL efficiency of TL phosphors are crucial parameters while estimating dose due to low energy photons, the relative TL efficiency factors for PTFE embedded CaSO₄:Dy and LiF:Mg,Ti discs are used to calculate the dose [143].

4.3.3 Theoretical calculation for energy response

The relative response $\left(\frac{\mu_{en}}{\rho}\right)_{Tissue}^{TL}$ of bare TL materials is also theoretically calculated as the ratio between the mass energy absorption coefficients of the material to that of the ICRU tissue using mass energy absorption coefficients of CaSO₄, LiF and ICRU tissue from National Institute of

Standards and Technology (NIST) database. However the mass energy absorption coefficient doesn't include the attenuation of low energy photons by the TL material, which is a crucial factor in low energy regime. Hence the self-attenuation correction factor (f_{att}) of TL material for the low energy photons is calculated using the following expression [144].

$$f_{att} = \frac{1 - [\exp(-(\mu/\rho)\rho d)]}{(\mu/\rho)\rho d} \quad \text{----- (4.1)}$$

Here (μ/ρ) , ρ and d represent attenuation coefficient, density and thickness of the TL material respectively. Calculated relative response of mass energy absorption coefficients with and without self attenuation correction is shown in figure 4.11. It is important to mention that the under response behavior of CaSO_4 is higher than that of LiF for photon energies ≤ 8 keV due to stronger absorption by CaSO_4 .

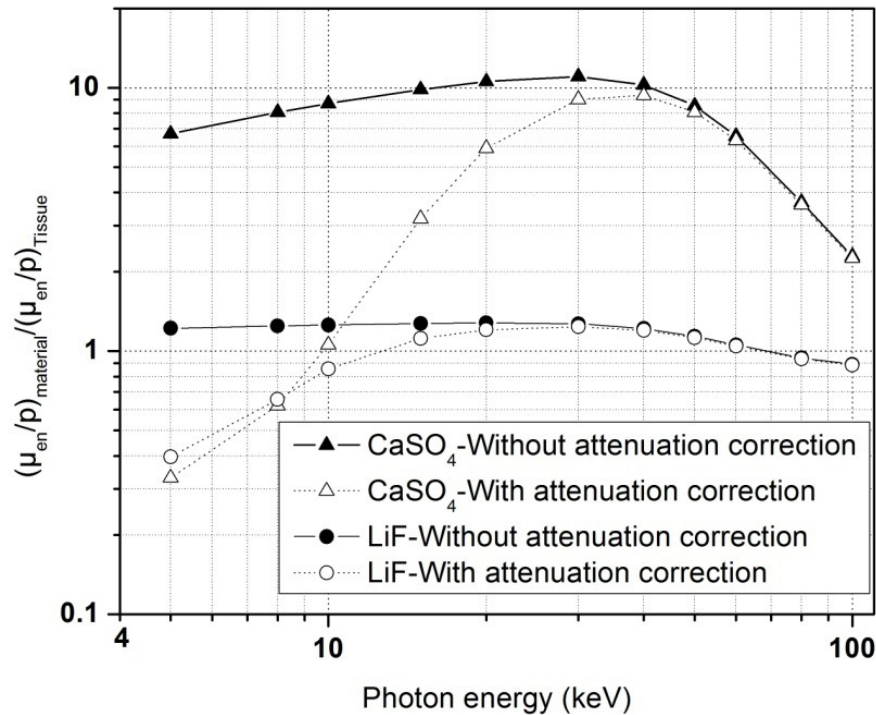


Figure 4.11: Relative response of CaSO_4 and LiF with and without self attenuation correction for synchrotron produced low energy photons

4.3.4 Discussion of the results

The average energy for synchrotron spectrum is calculated using the following expression [145].

$$E_{avg} = \frac{\sum_{i=1}^n Y(E_i) E_i \Delta E_i}{\sum_{i=1}^n Y(E_i) \Delta E_i} \quad \text{----- (4.2)}$$

Here $Y(E_i)$ represents photon yield at energy E_i . The average energy for synchrotron spectrum from Indus-2 (figure 4.2) is found to be 8.5 keV. Hence the simulation results for white synchrotron spectrum are presented at its average energy (8.5 keV). The relative response of $\text{CaSO}_4:\text{Dy}$ and $\text{LiF}:\text{Mg,Ti}$ discs (under metal, perspex filter and open window) with respect to ICRU tissue at different photon energies along with average energy of the spectrum are shown in figure 4.12.

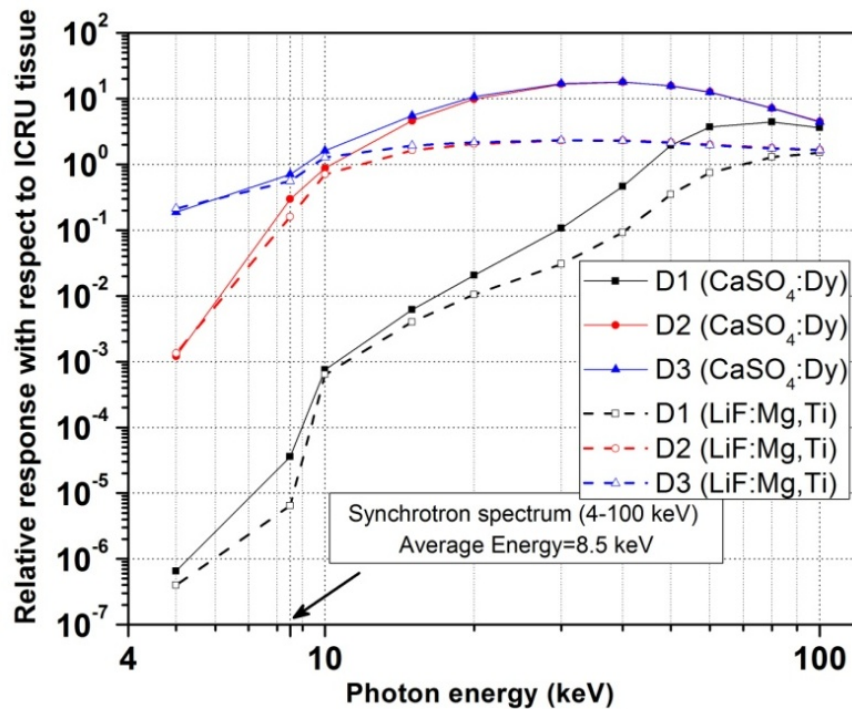


Figure 4.12: Relative energy response of $\text{CaSO}_4:\text{Dy}$ and $\text{LiF}:\text{Mg,Ti}$ TL discs under metal (D1), Perspex (D2) and open window (D3)

It is observed that TL materials in open window (D3) and perspex filter (D2) showed almost similar response in energy range 15 to 100 keV and below 15 keV, the disc D2 showed lower response because of the attenuation in perspex filter. Below 40 keV, metal filter (D1) showed under response because of stronger attenuation. Discs under filters including open window showed under response for photons below 10 keV as well as white synchrotron spectrum (Average energy - 8.5 keV). The trend in graph reflects higher response for monochromatic beam as compared white synchrotron spectrum. This is due to the contribution from lower and higher energy photons in the spectrum other than 8.5 keV. The relative response of disc D3 is found to show similar trend to that of $\left(\frac{\mu_{en}}{\rho}\right)_{Tissue}^{TL}$ of CaSO_4 and LiF TL materials with self attenuation correction (see figure 4.11), reflecting under response behavior of TL discs in energy region less than 10 keV due to self attenuation.

The calculated disc ratios i.e. D2/D1, D3/D1 and D3/D2 for $\text{CaSO}_4:\text{Dy}$ and $\text{LiF}:\text{Mg,Ti}$ for photon energy range from 5 to 100 keV and synchrotron spectrum (4 -100 keV) are shown in figure 4.13. Disc ratio is calculated by taking ratio of absorbed dose in two discs.

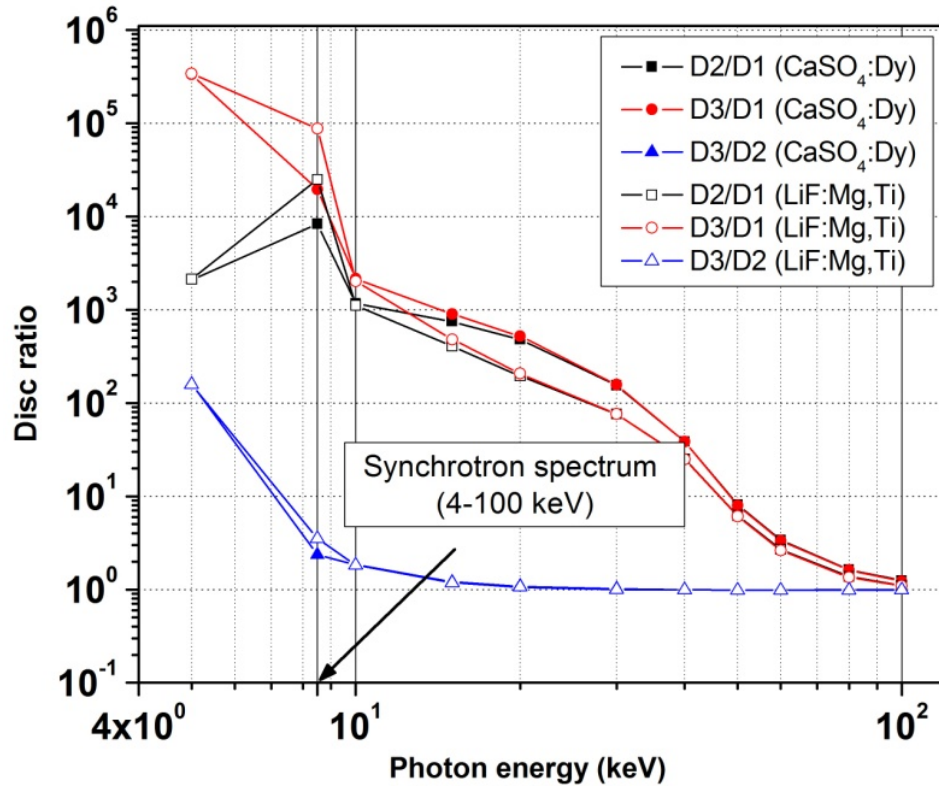


Figure 4.13: Disc ratio D3/D1, D2/D1 and D3/D2 for $\text{CaSO}_4:\text{Dy}$ and $\text{LiF}:\text{Mg,Ti}$ discs

The disc ratios D2/D1 and D3/D1 at all energies showed high values compared to D3/D2 which indicate strong attenuation by metallic filter. D3/D2 showed close match for both the TL materials.

The experimental disc ratios (D2/D1, D3/D1 and D3/D2) obtained for photon energies 10, 15 and 20 keV for $\text{CaSO}_4:\text{Dy}$ and $\text{LiF}:\text{Mg,Ti}$ along with simulation results are shown in figure 4.14.

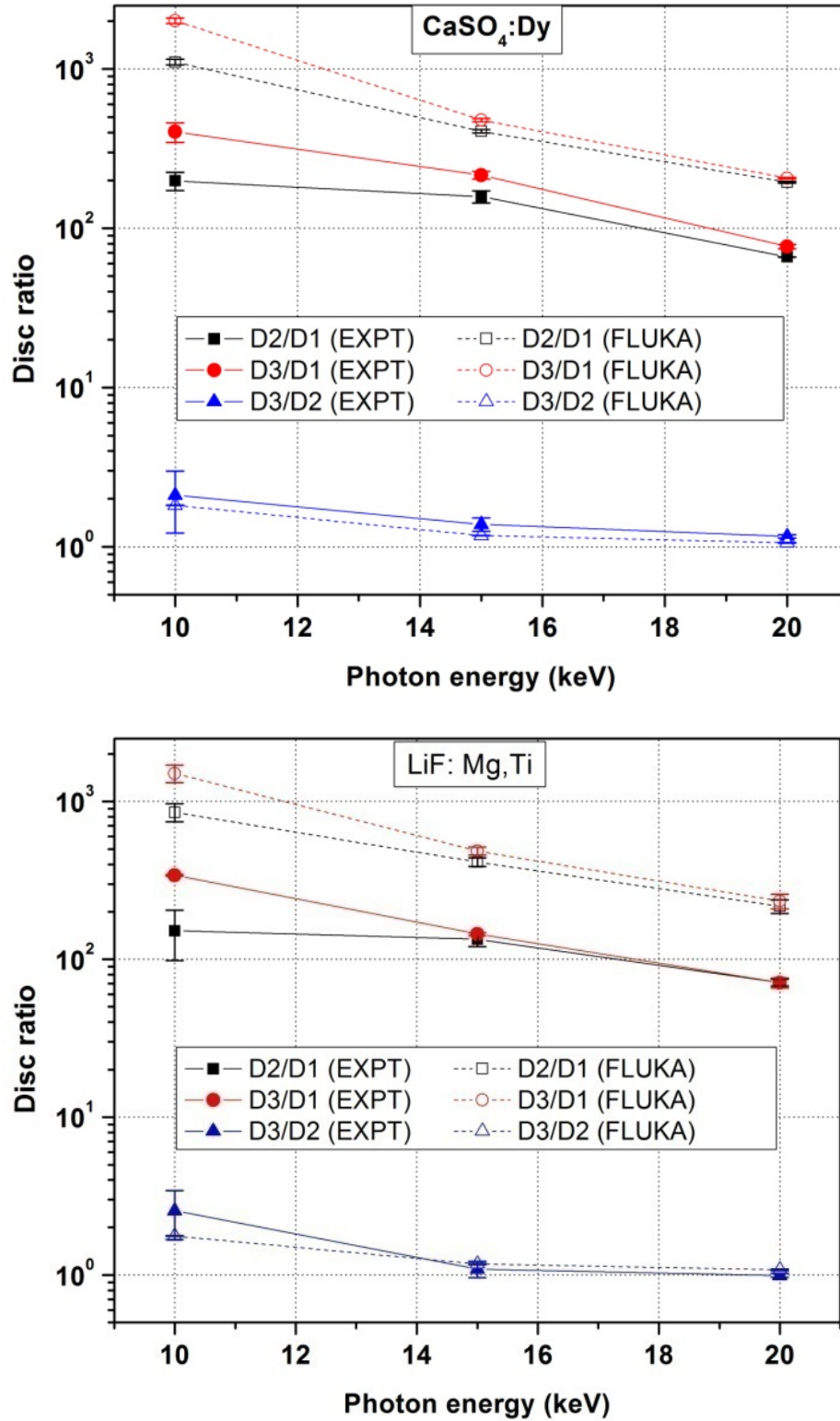


Figure 4.14: Disc ratio $D3/D1$, $D2/D1$ and $D3/D2$ for $CaSO_4:Dy$ and $LiF:Mg,Ti$ discs

The D2/D1, D3/D1 and D3/D2 are found to decrease as the energy of photon increases. The results also indicated a good match between the experimental and simulation data for disc ratio D3/D2 and the ratio approaches 1 as the photon energy increases from 10 to 20 keV. However the simulation results for disc ratios D3/D1 and D2/D1 are found to be higher than the experimental results at 10, 15 and 20 keV. This may be due to significantly low dose on disc D1 on account of heavy attenuation due to metal filter and associated simulation/measurement errors.

In order to calculate the magnitude of attenuation, attenuation factor for filters are calculated using linear attenuation coefficient data from National Institute of Standards and Technology (NIST) database and are shown in table 4.5.

Table 4.5: Calculated flux attenuation factors for the filters of the badge

Photon energy (keV)	1.6 mm Perspex	0.6 mm Al + 1 mm Cu
10	5.31E-01	1.39E-86
15	8.12E-01	4.22E-30
20	8.98E-01	4.07E-14

It can be seen clearly from table 4.5 that metal filter (D1) is a very strong absorber for the photon energies used in the study and thus the response of disc D1 under metal filter is not due to transmitted primary incident photons but because of the scattered radiation from surroundings. Hence the observed difference between simulation and experimental results for disc ratios D2/D1 and D3/D1 can be attributed to the scattering contribution within the TLD badge which has strong dependency on the geometry and the material properties like roughness, impurity and elemental composition.

From the study, it is concluded that LiF:Mg,Ti TL material shows better flat response than CaSO₄:Dy and therefore seems to be a better TL material for dosimetry in synchrotron beamlines in comparison to CaSO₄:Dy. The thickness of TL material also has a strong energy dependency for low energy photons below 10 keV. It is also inferred that the response of CaSO₄:Dy TL disc under perspex filter or open window can be used to evaluate dose from synchrotron radiation with appropriate calibration factors.

4.4 Estimation of high dose in CaSO₄:Dy TL materials using X-ray Absorption Near Edge Structure (XANES) spectroscopy

The CaSO₄:Dy TL disc is having dose linearity up to 30 Gy and beyond that, it shows nonlinear trend i.e. supralinearity followed by saturation [94,95]. Thus the dose estimation in the linear region is relatively easy using Co-60 or Cs-137 calibration factor whereas beyond 30 Gy, dose estimation using the glow curve is prone to errors because of nonlinear growth, shift of high-temperature shoulders and saturation effects [96]. In past, attempts to estimate the correct dose in the supralinear region have been made but no correlation between glow peak temperature and supralinearity could be established [97]. Thus at high dose, the conventional TL dosimetry using CaSO₄:Dy can lead to over or underestimation of actual dose received. An attempt is made to study the changes in lattice structure and electronic structure of CaSO₄:Dy after exposure to high dose using X-ray diffraction (XRD) and X-ray Absorption Near Edge Structure (XANES) spectroscopic techniques at BL-12, Indus-2.

CaSO₄:Dy TL material in powder and disc form are initially annealed at 400 °C for 1 hour and then exposed to 180 Gy to 1000 Gy in gamma irradiation chamber at RRCAT. The TL discs are placed in the sample holder of the irradiation chamber (BRIT, Gamma Chamber-900), consisting of a set of stationary Cobalt-60 source pencils in a cylindrical cage and delivering a dose rate of

0.85 kGy/h. X-ray diffraction (XRD) and X-ray Absorption Near Edge Structure (XANES) measurements are carried out at used Angle Dispersive X-ray Diffraction beamline (BL-12), Indus-2. The XANES measurement of $\text{CaSO}_4:\text{Dy}$ samples along with the standard reference for Dysprosium (Dy_2O_3) is performed at L_3 edge (7.79 keV) of Dysprosium in energy range of 60 eV below and above the absorption edge using synchrotron radiation. These measurements are performed in fluorescence mode using the energy dispersive Silicon drift detector.

The normalized L_3 edge XANES spectra of $\text{CaSO}_4:\text{Dy}$ samples (exposed to gamma dose ranges 0 – 1000 Gy) and the standard Dy_2O_3 sample are shown in figure 4.15. Three important regions in the spectra are marked as *p*(pre-edge), *s*(shoulder) and *w*(white line).

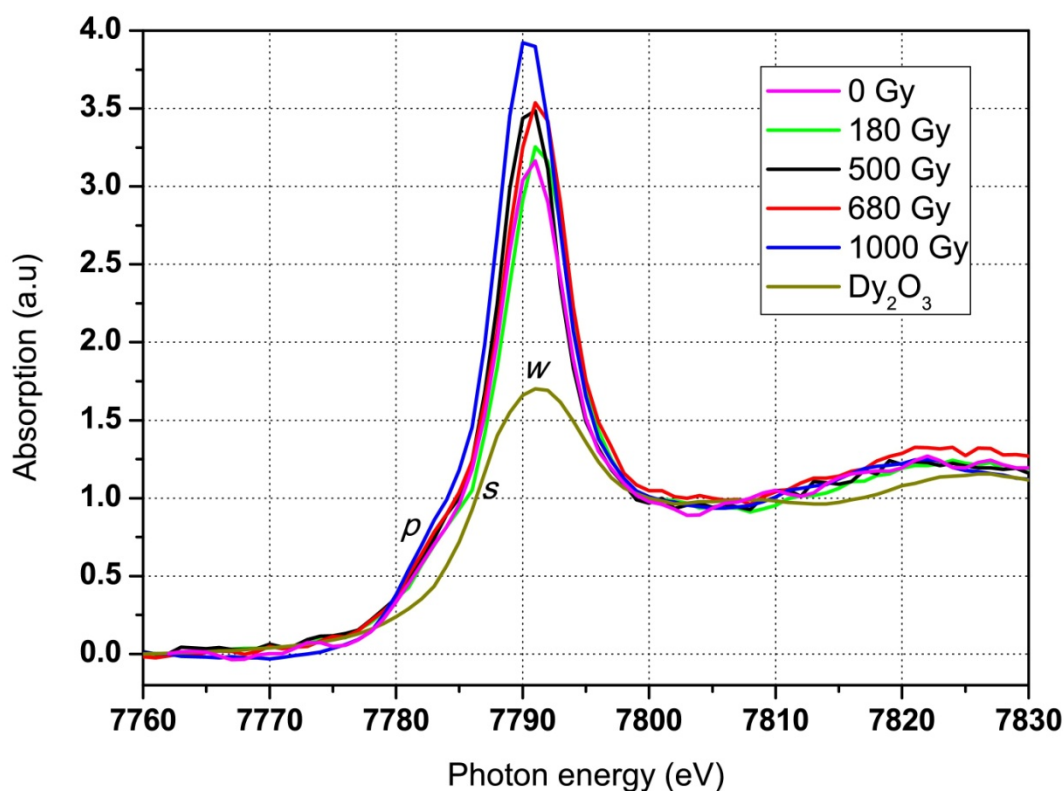


Figure 4.15: XANES spectra of reference standard (Dy_2O_3) and $\text{CaSO}_4:\text{Dy}$ samples

The white line in the spectra represents the transition from $2p_{3/2}$ state of Dy atoms to the continuum state. The pre-edge feature in the spectra can be attributed to +2 oxidation state of Dy

atom as observed in the case of transition metal oxides due to 1s-3d quadrupole (QP) transition [146]. The QP transition is normally forbidden but is allowed because of hybridization between transition metal (3d-state) and oxygen (2p-state). From literature, the observed peak positions of the white line and pre-edge are also found to be in agreement with that of $K_x\text{Dy}@C_{82}$, where the variation in oxidation states from Dy^{3+} to Dy^{2+} has been attributed to the intercalation of K metal into $\text{Dy}@C_{82}$ crystal [147]. It is important to highlight that this pre-edge is missing in reference standard (Dy_2O_3), suggesting the absence of Dy^{2+} in the sample. On subtracting the $\text{CaSO}_4:\text{Dy}$ spectra from Dy_2O_3 spectrum, the pre-edge features in $\text{CaSO}_4:\text{Dy}$ samples can be prominently seen and are shown in figure 4.16.

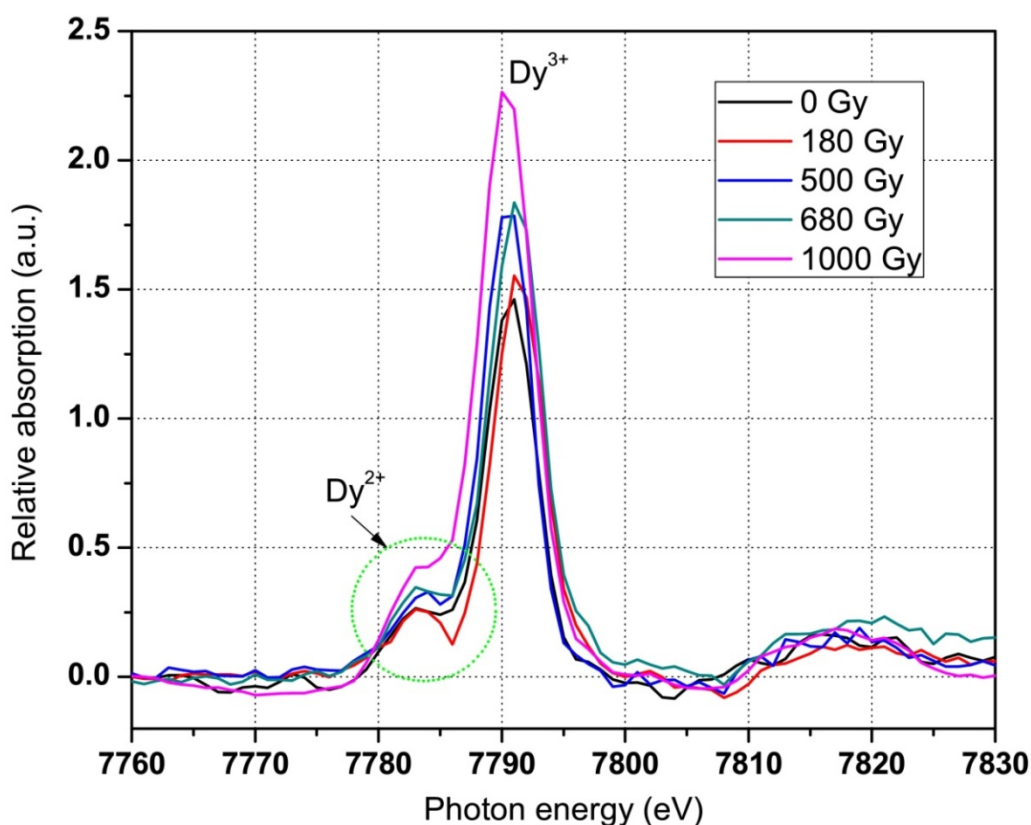


Figure 4.16: Relative XANES spectra of $\text{CaSO}_4:\text{Dy}$ with respect to standard Dy_2O_3

Thus the observed pre-edge peaks give direct experimental evidence of reduction of Dy^{3+} to Dy^{2+} on gamma exposure and is in agreement with the redox model of TL mechanism in $\text{CaSO}_4:\text{Dy}$ suggested by Nambi et al. [125] (The detail description of the redox model is given in section 2.3.4). From figure 4.16, increase in the pre-edge intensity with gamma dose is also observed as the concentration of Dy^{2+} is expected to increase with gamma dose.

The white line at 7791 eV in the spectra is also showing a increasing trend with gamma dose, which can be attributed to the transitions of electrons from $2p_{3/2}$ state of Dy atoms to additional localized states (formed by gamma irradiation) in the continuum. The net area under the XANES spectra, after subtracting the area of zero dose sample is plotted as a function of gamma dose in figure 4.17.

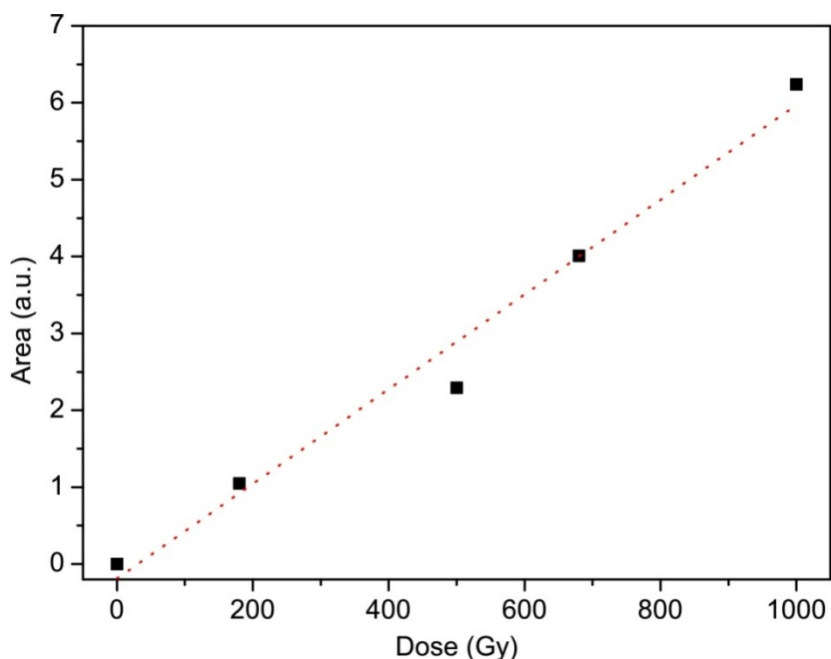


Figure 4.17: Relative areas under XANES spectra as function of absorbed dose

The linear rise in area under XANES spectra with absorbed dose can be correlated with the following functional relationship.

$$\text{Absorbed dose (Gy)} = k (\text{Area}) \quad \text{----- (4.3)}$$

Where k is a constant and its value is found to be 166. The true dose and the estimated dose in $\text{CaSO}_4:\text{Dy}$ samples obtained from equation 4.3 are given in the table 4.6.

Table 4.6: Comparison between the actual and the estimated dose

Sample No.	Actual dose received (Gy)	Calculated dose (Gy)
#1	0	0
#2	180	174.9 ± 0.09
#3	500	382.6 ± 0.19
#4	680	668.3 ± 0.33
#5	1000	1040 ± 0.52

The suggested relation gives a reasonable fit in the dose range up to 1000 Gy. Hence the XANES is proposed as a technique to estimate high dose from TL materials where conventional TL technique is not suitable.

The obtained XRD patterns of $\text{CaSO}_4:\text{Dy}$ samples (unirradiated, 500 Gy and 1000 Gy) are shown in figure 4.18. The patterns do not show any change in crystal structure due to high gamma dose up to 1000 Gy. The orthorhombic phase of CaSO_4 with lattice parameters $a = 6.993$, $b = 7.001$, $c = 6.241 \text{ \AA}$ and space group Bmmb (63) for $\text{CaSO}_4:\text{Dy}$ is confirmed from the JCPDS Card no. 37-1496. However, the observed differences in relative intensities of various Bragg peaks may be due to the preferred orientation of some peaks, indicating structural recrystallization on gamma irradiation which can affect the electronic structure and thus support the observed variations in XANES study.

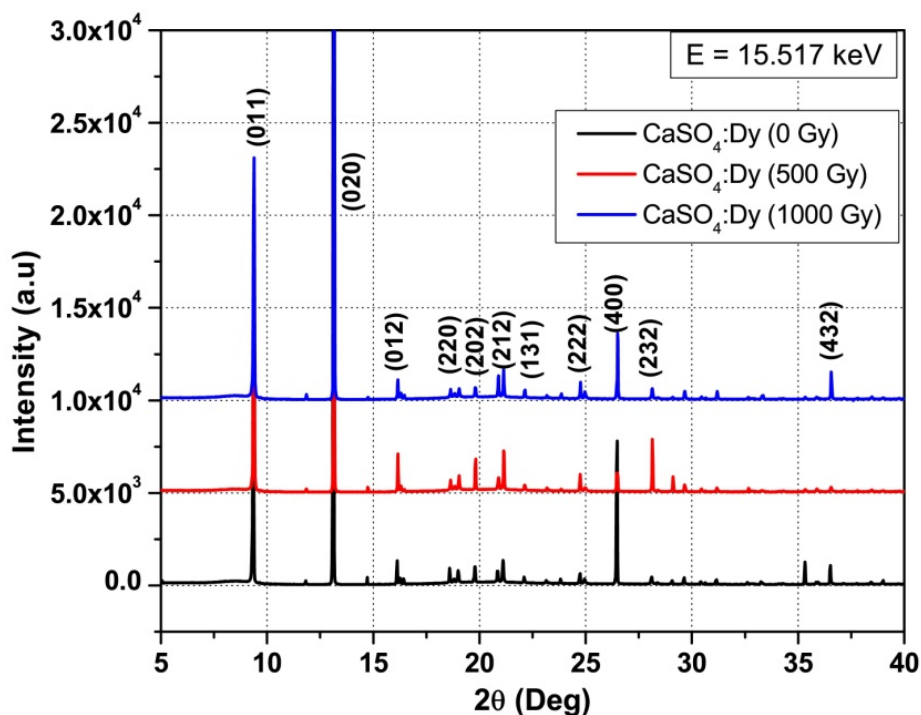


Figure 4.18: XRD pattern of $\text{CaSO}_4:\text{Dy}$ samples

From the study, it is concluded that pre-edge gives conclusive evidence of Dy^{3+} transition to Dy^{2+} on gamma ray irradiation and also gives an experimental proof of redox model proposed by Nambi et al. [125]. White line in XANES spectrum increases with dose and the area under the XANES spectrum is found to vary linearly with absorbed dose. Hence XANES can be used as a technique for high dose estimation from TL materials where conventional TL dosimetry is not suitable.

4.5 Design of primary standard for dosimetry at synchrotron beamlines in Indus-2

Most of the hard X-ray beamlines in Indus-2 use synchrotron radiation in energy range 5 to 35 keV in monochromatic mode and a few utilize complete spectrum in white mode. In past, for developing area radiation monitors for synchrotron beamlines, air kerma measurement at synchrotron beamline of Indus-2 was attempted using small portable free air ion chamber (Indus-2 parameters: E_0 : 1.722 GeV, I := 20.81 mA) [43]. The spacing between the electrodes of the

free air ion chamber (FAIC) was kept 10 mm, aiming for measurement of low energy synchrotron radiation up to 10 keV. Therefore need for a FAIC for synchrotron radiation up to 50 keV in Indus-2 is felt and the present work discusses the design aspects of the FAIC.

Synchrotron spectrum in energy range of 1 to 100 keV from bending magnet of Indus-2 for design parameters: 2.5 GeV beam energy and 300 mA beam current is generated using XOP software [148]. The absorbed dose rate in air is calculated using mass energy absorption coefficients from National Institute of Standards and Technology (NIST) database from the spectrum. The photon flux and the absorbed dose rate in air are shown in figure 4.19. It can be seen from figure 3.18 that in energy range 1 to 50 keV, the reduction in flux is nearly 3 orders of magnitude whereas the dose rate drastically reduces by 6 orders of magnitude.

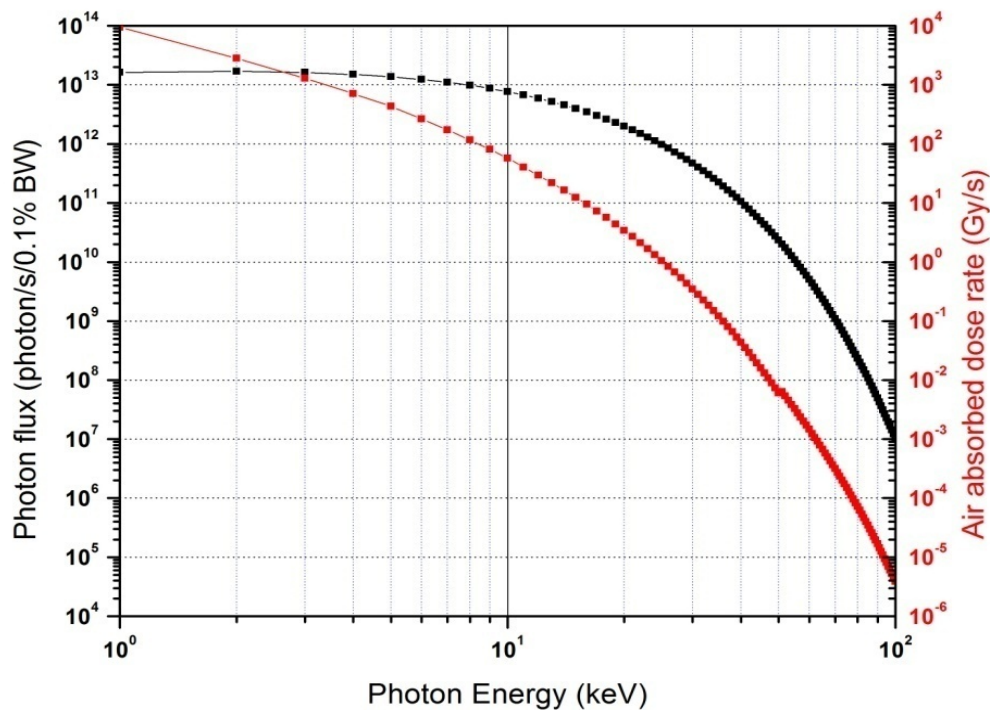


Figure 4.19: Photon flux and the air dose rate as a function of energy of synchrotron radiation from Indus-2 bending magnet

In monochromatic mode, the synchrotron flux at source point reduces by 4 to 5 orders on reaching the experimental station due to transmission losses through the optical elements like mirror, double crystal monochromator and slits of the synchrotron beamlines. The measured monochromatic photon flux in energy range 5 to 35 keV at imaging beamline of Indus-2 (stored current of 120 mA at 2.5 GeV) was found within 10^7 - 10^9 photons/mm²/s [141]. Therefore the expected dose rate for the monochromatic beam at experimental station will be of the order of few mGy/s. Based on these parameters for energy range and expected dose rate, a free air ionization chamber is designed for dosimetry application at Indus-2 beamlines.

4.5.1 Working principle of FAIC

To set this instrument as a primary standard for air kerma measurement, principal condition of establishing charged particle equilibrium is desired. Charged particle equilibrium (CPE) condition basically represents the conservation of charged particles in the region of interest. Under CPE, the energy loss due to a charged particle leaving the region of interest is compensated by the entering of an identical charged particle (produced outside) to the region of interest and the relationship between absorbed dose (D_{air}), collision kerma ($K_{c,air}$) and exposure (X) for air can be expressed as follows (Appendix-B).

$$D_{air} = K_{c,air} = X \left(\frac{W}{e} \right)_{air} \quad \text{----- (4.4)}$$

Where $\left(\frac{W}{e} \right)_{air}$ = mean energy per charge in air = 33.97 J/C

The design and operation principle of a parallel plate type FAIC are discussed below. A schematic layout (adopted from Ref [40]) of a parallel-plate free-air chamber enclosed in a lead shielded box to prohibit scattered radiation is shown in figure 4.20.

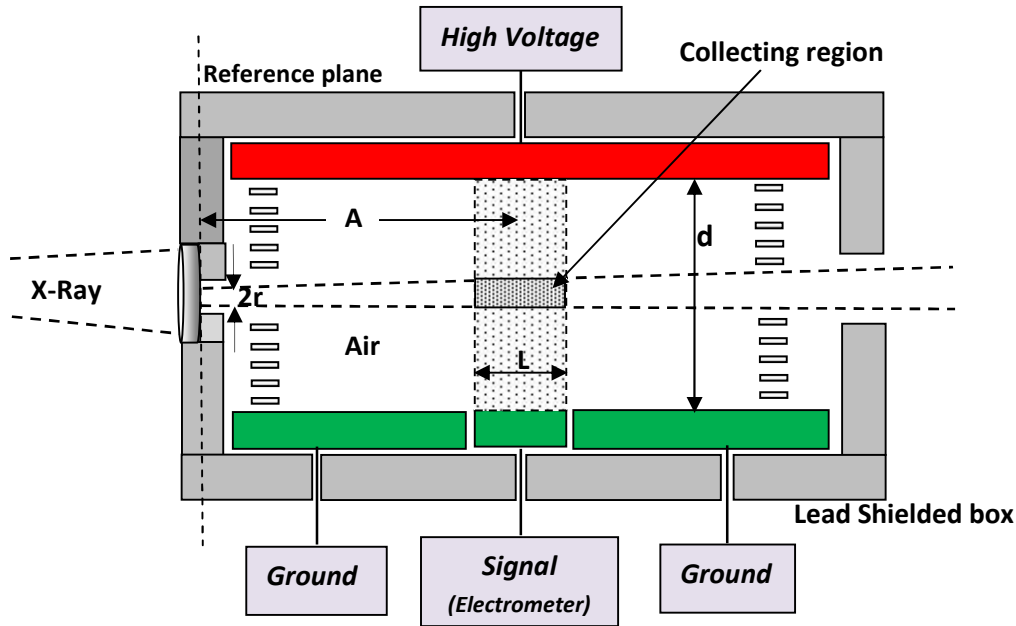


Figure 4.20: Schematic layout of parallel plate type FAIC

The major elements in a FAIC with their role and design criteria [40] are listed in table 4.7.

Table 4.7: Major elements of FAIC

Elements	Action	Design criteria
Entrance diaphragm	Define the charge collection region (or measuring volume) in air	Photon beam should completely cover the entrance diaphragm
High Voltage & Collector electrodes	An electric field is set between the electrodes by applying a polarizing potential to the HV electrodes and the signal (current) is measured from the collector electrode.	i) The electrode separation (d) should be sufficiently large enough so that all the secondary electrons deposit their complete energy inside the air of the chamber and cannot reach either electrode. ii) Since electrons have equal chance of moving in

		sideward direction, the width of collector must be same as the electrode separation (d) to attain CPE.
i) Guard electrodes &/or ii) Guard rings	i) Two co-planar guard electrodes with gap 'x' on each side of collector which helps in producing field uniformity and defining the electric field lines between HV electrode and collector. ii) Sometimes a set of wires (or annular plates) are placed parallel to the electrodes with electrically biased in uniform steps to establish parallel equipotential electric field planes between the electrodes.	High level of parallism should be maintained between guard plate - signal electrode and the rings.
Attenuation length (A)	Attenuation length is the distance between the reference plane of the diaphragm and the centre of the collecting region and helps in maintaining CPE	Attenuation length should be more than the maximum range of secondary electrons to attain CPE. Normally the distance between the collecting region and the rear exit hole is also set equal to the attenuation length.
Shielding box	Shields the unwanted scattered radiation from surroundings during measurement	Transmission through shielding wall should be negligible

The air kerma rate is calculated using following expression [40].

$$K_{air} = \left(\frac{I}{m_{air}} \right) \left(\frac{W}{e} \right)_{air} \left(\frac{1}{1-g} \right) \prod_i k_i \quad \text{----- (4.5)}$$

Where, I = measured current from the collector, m_{air} = mass of air (in measuring volume), g = bremsstrahlung correction factor and k_i = correction factors.

Since the density of air is a function of temperature and pressure of air during measurement, the mass of air can be calculated using the following expression [40].

$$m_{air} (g) = 0.001293 * V * \left(\frac{273.2}{T} \right) * \left(\frac{P}{760} \right) \quad \text{----- (4.6)}$$

Here T (K) and P (mm of Hg) represent temperature and pressure of air respectively. V (cm^3) represents volume of the collection region, usually calculated by multiplying area of entrance diaphragm and the effective length of collecting region. Effective length of charge collection region is calculated as $L + \left(\frac{x}{2} \right) + \left(\frac{x}{2} \right) = (L + x)$, where L is length of collector and x is the gap between collector and guard electrode. Thus the volume of the collection region can be written as $V_{air} = \pi r^2 (L+x)$. Precise measurement of aperture of diaphragm, length of electrodes, gap between the collector-guard electrodes, parallelism and co-planarity of the electrodes play crucial role in level of accuracy in determining air kerma. Therefore various correction factors (k_i) are incorporated in the calculation to correct the limitations in the design criteria of FAIC and the experimental/environmental conditions during the measurement. The correction factors [40] are listed below.

- i) *Air attenuation factor* (k_{at}): Correction due to air attenuation of photons reaching the collection region

- ii) *Humidity correction factor (k_h)*: Correction due to change in air density with humidity resulting in error in mass of air calculation. For relative humidity of 20 % to 80 %, this factor can be taken as a constant value (0.998 with 0.1 % uncertainty) [149].
- iii) *Recombination correction factor (k_r)*: Correction for loss of signal due to recombination of charges
- iv) *Polarization correction factor (k_p)*: Correction for dissymmetry of ion collection
- v) *Electric field distortion correction factor (k_{Field})*: Correction due to distortion of electric field resulting in error in volume calculation.
- vi) *Scattered and fluorescence photons correction factor (k_s & k_f)*: Correction due to scattered photons and fluorescence in air e.g. Argon can produce fluorescence photons of 3.2 keV.
- vii) *Transmission correction factor (k_{tr})*: Correction due to transmission of primary and scattered photons through diaphragm and shielding wall.

Out of these factors, the air attenuation factor is most dominant one in low energy range. In past Monte Carlo simulation codes like FLUKA, PENELOPE and EGS Monte Carlo code have been used for evaluation of these correction factors [150-155]. The correction factors can be evaluated for the achieved dimensions of elements of FAIC after the fabrication.

4.5.2 Design parameters of FAIC for Indus-2 synchrotron beamlines

The expected dose rate at the experimental station of Indus-2 synchrotron beamlines varies from Gy/s to mGy/s for white to monochromatic beam respectively. Also the maximum energy range for photon is considered to be 50 keV for the design calculation of FAIC for Indus-2. Considering 50 keV as the primary photon energy, the maximum CSDA range of secondary electrons (50 keV) in air at ambient temperatures and pressures is 40.7 mm, calculated from National Institute of Standards and Technology (NIST) database. Thus the collector length (L)

and the gap between guard and collector (x) are set as 40 and 0.5 mm respectively to have effective length of the collecting region as 40.5 mm. To maintain CPE, the electrode separation (d) and width (w) are set as 60 mm which is nearly 50 % higher than the maximum range of secondary electrons. Similarly attenuation length (A) is set as 65 mm, necessary for maintaining CPE and also shows $\sim 85\%$ transmission for 50 keV photons (as calculated from National Institute of Standards and Technology - NIST database [156]). Burn et al. has suggested for ~ 70 mm electrode separation (d), sufficient enough to maintain measurement uncertainty within 0.1% for x-ray spectra up to 50 keV [40]. Typical value for attenuation length (A) in FAICs ranges from 40 to 100 mm for low-energy (10-50 kV) X-ray standards. The design parameters of the free air ionization chamber for application in Indus-2 synchrotron beamlines are listed in were evaluated based on energy and radiation field intensity of the synchrotron beam. Both energy and expected field intensity are very crucial parameters for deciding the electrode gap. The major design parameters are given in table 4.8. To obtain accurate data from the FAIC, the error in the dimension of the electrodes, aperture, electrode separation, gap between guard and collector plates is expected to be within 1%. The planeness and parallelism is also targeted to be within 100 μm . Correction factors for temperature and pressure during the measurement will also be very crucial in deciding the level of accuracy in the measured data.

Table 4.8: Parameters of FAIC for Indus-2 synchrotron beamlines

Parameter	Value (mm)
Aperture diameter ($2r$)	8
Attenuation length (A)	65
Collector length (L)	40
Gap between guard and collector (x)	0.5
Electrode separation (d)	60
Electrode width (w)	60
Lead shielding thickness	3

In order to calculate the applied potential, the charge collection efficiency f as a function exposure rate is calculated using Mie's formula [157-159].

$$f = \frac{1}{1 + \frac{\xi^2}{6}} \quad \text{----- (4.7)}$$

$$\text{Where } \xi = m \left(\frac{d^2 \sqrt{q}}{V} \right)$$

Here m is a constant ($=36.7$), d = Plate separation (cm), q = ionization rate ($\text{esu.cm}^{-3} \cdot \text{s}^{-1}$) and V = applied potential (Volt). The charge collection efficiency of the chamber ($d=60$ mm) for exposure rate from 1 mR/s to 100 R/s as a function of applied potential is shown in figure 4.21.

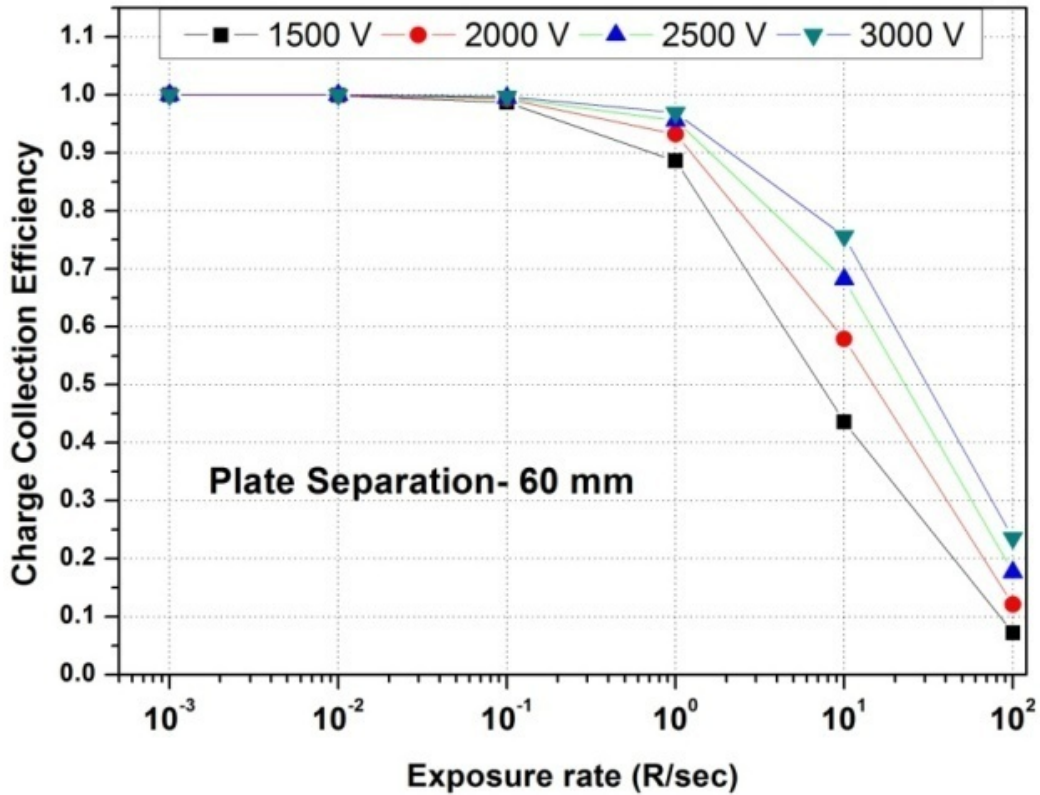


Figure 4.21: Charge collection efficiency exposure rate range 1 mR/s to 100 R/s at different applied potential

Therefore the design parameters of free air ionization chamber are evaluated for exposure rate range 1 mR/s to 100 R/s for dosimetry application in Indus-2 synchrotron beam lines. The charge collection efficiency for electrode separation of 60 mm is found to be > 95 % for exposure level of 1 R/sec with applied potential of 2500 V.

4.6 Summary and conclusion

Intense and broad spectrum of synchrotron radiation, especially in hard x-ray range is a potential source of radiation hazard in synchrotron beamlines. Therefore quantification of primary and scattered synchrotron radiation in beamlines is essential for ensuring radiation safety. Indus-2, 2.5 GeV electron storage ring provides intense synchrotron beam with energy ranging from infra-red to hard x-ray with critical wavelength 1.986 \AA ($\sim 6.3 \text{ keV}$). Most of the synchrotron

beamlines utilize monochromatic beam ranging between 4 to 30 keV and a few beamlines use full spectrum for material characterization. The beamlines are housed in shielded hutches to mitigate the radiation hazards due to direct and scattered synchrotron radiation.

Quantification of high dose due to direct and scattered synchrotron beam is performed with FLUKA Monte Carlo code. Experimental studies are performed for confirming the simulated data and the data from experiment and simulation study are found to be in good agreement. Calculations show that, accidental exposure to direct synchrotron radiation will give localized absorbed dose rate as high as 10^5 Gy/h to the skin of exposed person. The shielding estimation indicates that in the case of bending magnet beamlines, 3 mm lead is sufficient to reduce the absorbed dose to permissible limit. For the case of scattered synchrotron beam, angular distribution of radiation dose from Aluminium, Copper and Tantalum is also evaluated. The maximum scattered dose rate at 1 m in 150° from the copper target is found to be ~ 2.1 Gy/h for design stored current (300 mA). However the scattered dose rate from different target materials showed strong dependency on the incident energy of synchrotron radiation due to dominance of photoelectric effect resulting in resonance absorption and subsequent fluorescence emission from the target material.

Energy response of the personnel dosimetry device (TLD badge) at Indus-2 to monochromatic and white synchrotron beam is evaluated for $\text{CaSO}_4:\text{Dy}$ and $\text{LiF}:\text{Mg,Ti}$ TL materials. TL material in open window (D3) and perspex filter (D2) showed almost similar response in energy range 15 to 100 keV and below 15 keV, the disc D2 showed lower response because of the attenuation in perspex filter. But the disc D1 under metal filter showed under response for energy below 40 keV due to stronger attenuation. All the discs showed under response in monochromatic synchrotron below 10 keV and white synchrotron spectrum (Average energy -

8.5 keV). Effect of attenuation in bare TL materials, also affects energy response and because of stronger absorption CaSO_4 showed higher under response than that of LiF TL material for photon energies ≤ 8 keV. The disc ratios D_2/D_1 , D_3/D_1 and D_3/D_2 are found to decrease as the energy of photon increases. Disc ratio D_3/D_2 tends to 1 as the energy of photon increases from 10 to 20 keV and showed good match between simulation and experiment. However the simulation results for disc ratios D_3/D_1 and D_2/D_1 are found to be higher than the experimental results at 10, 15 and 20 keV due to heavy attenuation in metal filter leading to simulation/measurement errors and contribution from the scattered radiation from the surroundings.

XANES measurement on $\text{CaSO}_4:\text{Dy}$ samples exposed to high dose up to 1000 Gy gives a direct evidence of Dy^{3+} transition to Dy^{2+} on gamma ray irradiation and confirms redox model proposed by Nambi et al. Also the white line in XANES spectrum found to increase linearly with increasing dose and hence provides an alternate technique for estimation of high dose from TL materials where TL technique is not suitable.

A primary standard (free air ionization chamber) is designed for air kerma measurement in Indus-2 synchrotron beamlines. Based on the energy and intensity of synchrotron beam at Indus-2, the design parameters are optimized. The charge collection efficiency of the free air ionization chamber with electrode separation of 60 mm is found to be $> 95\%$ for exposure level of 1 R/sec with applied potential of 2500 V.

Chapter 5

Radiation shielding studies on synchrotron beamlines

in Indus-2

5.1 Introduction

Synchrotron radiation is transported to the experimental station through specially designed beamlines. The beamline is connected to the storage ring through a set of hardware called the front end. The front end in Indus-2 is nearly 14 m long section, consisting of systems for beam defining, beam position monitoring, storage ring vacuum protection and radiation as well as heat load protection. The front end has various safety and beam defining components like fast closing shutter, water cooled shutter, safety shutter, collimator, fixed mask etc [160]. The safety shutter is made up of a thick densimet block and acts as a radiation stopper. For hard x-ray beamlines, the front end is connected to the beamline through water cooled beryllium window (200 μm thick) placed at the end of the front end. All the beamline components are enclosed inside shielded hutch due to high radiation hazard. In many cases, the beamline hutch is divided into three sections; optics hutch, intermediate hutch and experimental hutch (see figure 1.2). The optics and intermediate hutches mostly cover major beamline components like mirror, monochromators and slits whereas the experimental hutch encloses experimental station with sample holder and detector systems. During sample changing, the synchrotron beam is stopped

by safety shutter (30 cm thick densimet) placed at the beamline frontend. The safety shutter prohibits both synchrotron and gas bremsstrahlung radiation reaching the beamline hutch during sample changing and maintenance of the beamline. In some beamlines, additionally synchrotron beam stop (called as beam shutter) is placed in the optics/intermediate hutch to obstruct the beam from reaching experimental station during sample changing. Major components of front-end (adopted from Ref.[160]) like collimator, fixed mask, fast closing shutter, water cooled shutter, photon beam position monitor, safety shutter etc. are shown in figure 5.1.

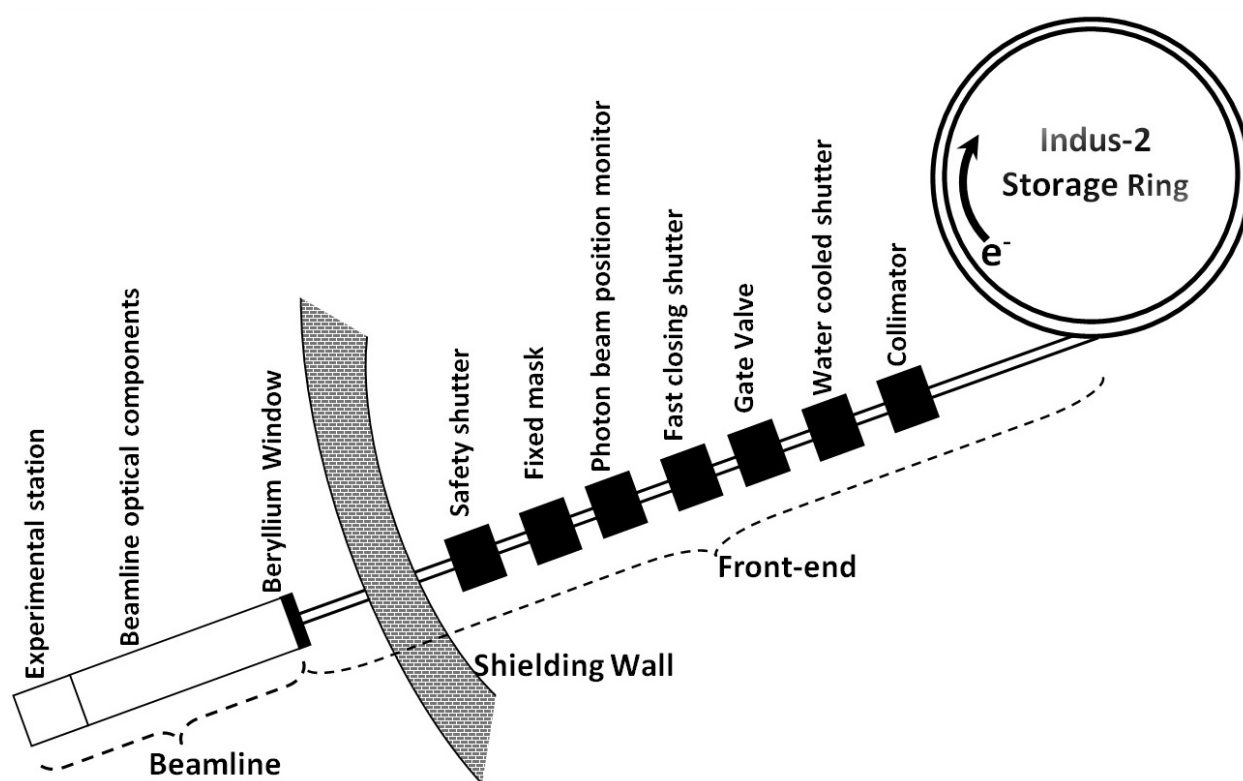


Figure 5.1: Schematic layout of the front end for the synchrotron beamline in Indus-2 (not to scale)

Radiation scenario in synchrotron beamlines is complex due to high flux, broad spectrum of synchrotron photons ranging from infrared to hard x-ray and the high energy gas bremsstrahlung photons. On interacting with optical elements (like slits, mirrors, monochromators and beam

stops etc.), both synchrotron and gas bremsstrahlung radiation produce scattered radiation all around the beamline. In addition photo-neutrons are also produced due to interaction of high energy gas bremsstrahlung radiation with beamline components. Because of their low energies, both direct and scattered synchrotron radiation can be shielded using few mm thick lead sheets. However the gas bremsstrahlung radiation due to its high energy is more penetrating and hence thick lead or tungsten blocks (called as gas bremsstrahlung stop) are used to shield the radiation. The intensity of radiation in beamlines varies as the design specification of each beamline is different from each other. The design specification of the beamline depends on the synchrotron source (bending magnet or insertion device), usable energy range (white, pink or monochromatic) and the beamline components. The primary hazard of gas bremsstrahlung radiation depends on source type (bending magnet or insertion device). Large number of independent studies using Monte Carlo codes like EGS4, FLUKA, etc. have been performed in past to evaluate the shielding requirements for bending magnet and insertion device beamlines in various synchrotron facilities [48-69]. In addition to the studies on generic safety issues arising due to gas bremsstrahlung, photoneutron and synchrotron radiation, specific studies were conducted to address the implication on radiation safety due to possible channeling of electrons into the front end. Though the miss-steering of the electron beam entering the beamline has less probability but the radiation risks due to the event cannot be ignored [60,72]. Accelerator physicists in NSLS-II have reported the possibility of channeling of electrons into the front end due to change in lattice magnetic field settings. In this condition, the electron beam will be intercepted by the front end components like fixed mask or safety shutter and can create radiation hazard in the beamline. Therefore radiological consequences on experimental hall of NSLS-II beamline due to the missteering of electron beam into the beamline were evaluated

using FLUKA Monte Carlo code [72]. Also in XFEL beamline at Japan, as a safety measure a sweep magnet is installed in the downstream of bending magnet at XFEL to avoid radiological consequence due to streaming of 8 GeV electrons into XFEL beamline because of accidental power loss in the bending magnet [60]. Hence the radiation scenario in a synchrotron beamline has strong dependence on its optical components. Worldwide independent approach to evaluate shielding requirements for shielding hutch of individual synchrotron beamlines have been taken up with the help of analytical code (STAC8) and Monte Carlo codes (EGS-4, FLUKA, etc.).

In this chapter, radiation shielding studies performed on a bending magnet beamline (Scanning Extended X-ray Absorption Fine Structure - SEXAFS) and an undulator beamline (Atomic, Molecular and Optical Spectroscopy- AMOS) as representative examples of beamlines in Indus-2 are discussed. Radiation shielding requirements for solid bremsstrahlung, gas bremsstrahlung radiation, photo-neutrons and synchrotron radiation components are evaluated using FLUKA code. Dose due to channeling of electrons in to the beamline and also the scattering of gas bremsstrahlung and synchrotron radiation from the beamline components are studied to evaluate the shielding requirements.

5.2 Radiation shielding studies for SEXAFS beamline (bending magnet beamline)

Scanning EXAFS (SEXAFS) beam line on Indus-2 is used for studying local structural properties around a specific element of the material. SEXAFS beamline uses a silicon mirror kept at grazing incidence for focusing the synchrotron beam to the double crystal monochromator (DCM). DCM acts as the energy selector and the monochromatic synchrotron beam from the DCM is focused to the sample location at the experimental station. The schematic layout of the beamline is shown in figure 5.2.

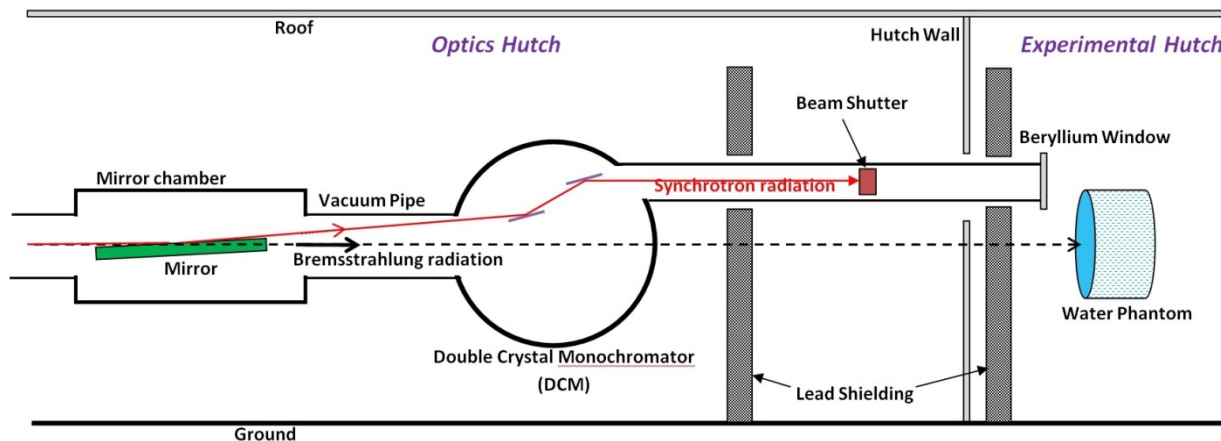


Figure 5.2: Schematic layout of SEXAFS beamline (not to scale).

In addition to the safety shutter in the front end, this beamline has a beam shutter made up of 50 mm copper, which is placed just before the experimental hutch. The beam shutter is used to stop the synchrotron beam from reaching the experimental station during sample changing. At this condition, the safety shutter located at the front end of the beamline remains in open condition and potential radiation hazard due to the channeling of the stored electrons to the beamline exists in case of accidental beam loss in the storage ring. The channeled electrons will hit the beamline component (silicon mirror) and will produce solid bremsstrahlung photons and photo-neutrons. Thus there exists a potential for radiation exposure from gas bremsstrahlung, solid bremsstrahlung and photo-neutrons to the users during sample changing at the experimental station. Therefore the radiological implications in the experimental hutch due to the introduction of the beam shutter are studied. Radiation source term due to solid bremsstrahlung, gas bremsstrahlung and photo-neutron radiation at experimental hutch of SEXAFS beamline are studied. The gas bremsstrahlung dose in the beamline is calculated using analytical method. Subsequently the shielding evaluation of the beamline is also performed using FLUKA code. The detailed simulation of dose rate from each component is described in the following section.

5.2.1 Dose equivalent rate due to channeled electrons

Simulation is performed for dose estimation due to catastrophic loss of stored electrons at the silicon mirror. In catastrophic loss, one bunch of electrons out of 291 bunches (for 300 mA stored current) is assumed to be channeled into the beamline. Also two such events occurring per day are assumed for dose calculation. For estimating the shielding requirements, simulations are carried out to determine dose rate in the experimental hutch for unshielded and with 10 and 20 cm lead shielding.

In simulation study, 2.5 GeV electron with beam size 0.02 cm (H) and 0.02 cm (V) is allowed to incident on silicon mirror at grazing angle of 0.2 degree. A stainless steel cylindrical flange of 4.3 cm thickness is placed at a distance of 6 m from mirror in order to include the intervening structural materials like flanges, DCM chamber wall etc. The dose equivalent at sample location is scored using 30 cm water phantom placed at 15.64 m from the mirror. The geometry used for simulation is shown in figure 5.3.

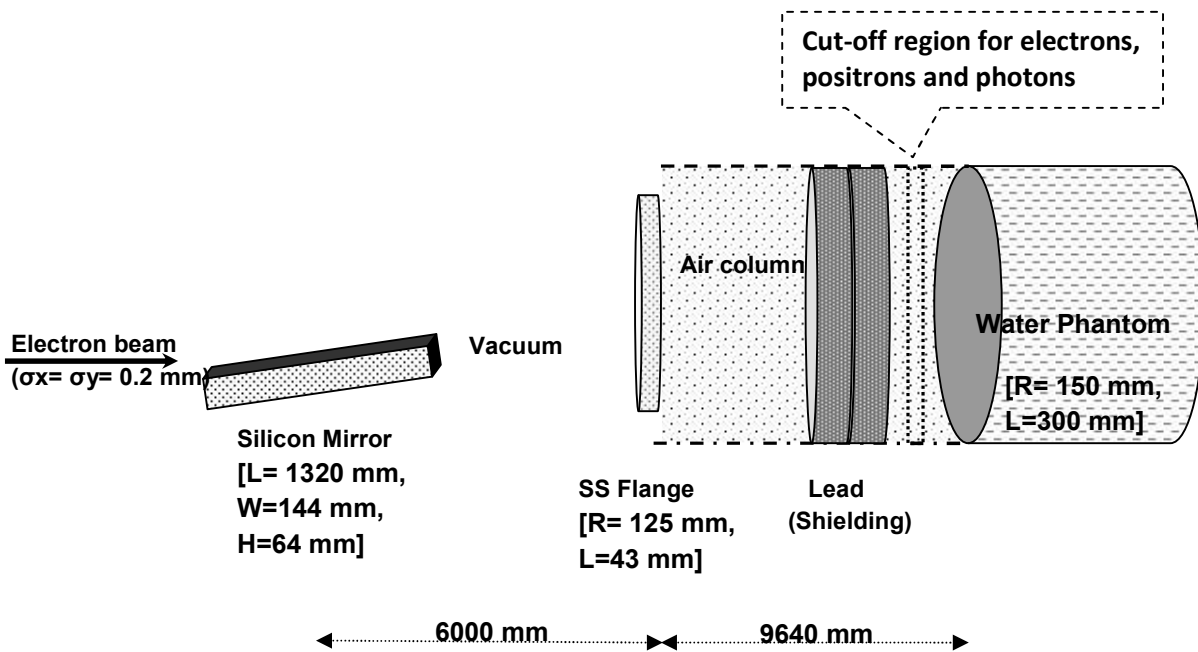


Figure 5.3: Geometry used for bremsstrahlung photon and photo-neutron dose estimation

The electron (2.5 GeV) on hitting the beamline components will produce bremsstrahlung photons, secondary electrons, positrons (through EM cascade) and photo-neutrons, which will deposit their energy in the water phantom. The transport threshold for electrons, positrons and photons is set at 10 MeV. For photo-neutron dose evaluation, the electrons, positrons and photons generated from target are killed in a thin region (10 mm air column) just before the water phantom by setting high transport cut-off (2.5 GeV). The energy density absorbed in the water phantom is scored using the USRBIN scoring card with bin size 3 mm along beam direction. The dose per bunch for 300 mA stored current in Indus-2 is calculated using normalization factor of 5.59×10^9 electrons/bunch.

5.2.2 Gas bremsstrahlung dose evaluation

Gas bremsstrahlung dose at the experimental station ($r = 34$ m) of the beamline due to 2.5 GeV electrons ($I = 1.875 \times 10^{18}$ e⁻/s) passing through bending magnet section ($L = 0.1$ m; $P = 10^{-8}$ torr) is calculated using equation 1.21. [The equation 1.21 can be applied to gas bremsstrahlung dose in bending magnet case, as the path length of the electrons in case of bending magnet beamline is very small compared to that in insertion device beamline and the effect of multiple scattering on gas bremsstrahlung dose in bending magnet can be ignored.]

The photon attenuation coefficients (high energy limit) of 0.42 cm^{-1} and 0.054 cm^{-1} for lead and silicon, respectively are used in order to account for the attenuation effect of the mirror and the lead shielding on gas bremsstrahlung dose at the experimental station. Silicon thickness of 66 cm (i.e. half of the total length of the mirror) is used for calculation of attenuated gas bremsstrahlung dose rate.

5.2.3 Discussion of the results

The unshielded bremsstrahlung dose rate in water phantom due to channeled electrons striking silicon mirror is calculated. The bremsstrahlung fluence generated from the silicon mirror is shown in figure 5.4. The corresponding maximum unshielded dose in water phantom is found to be 78 μSv per bunch. Similar calculations are performed with 10 and 20 cm lead shielding in front of the water phantom to evaluate the shielding requirement and the estimated dose rates are given in table 1.

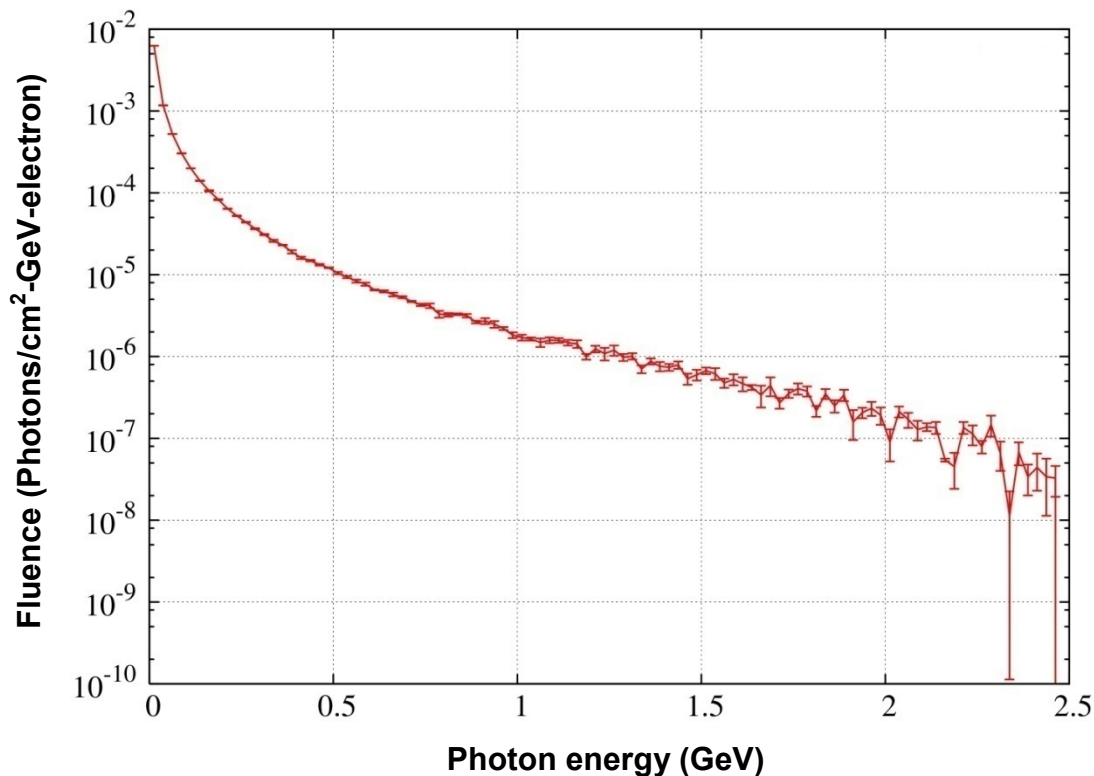


Figure 5.4: Solid bremsstrahlung spectrum generated from mirror due to 2.5 GeV electrons

The simulated photo-neutron spectra for unshielded and with shielding (10 and 20 cm lead) are shown in figure 5.5. From the figure, it is clear that 10 cm lead shield increases the neutron fluence through photo-neutron reaction of bremsstrahlung photons with lead. However on further increase in lead thickness (20 cm), attenuation of the high energy neutrons through inelastic

scattering is observed. Photo-neutron spectrum inside water phantom shows dominance in energy region $< 10\text{keV}$. Therefore the energy absorbed in water phantom due to neutrons is converted to dose equivalent using radiation weighting factor of 5. The photo-neutron dose rates obtained with and without shielding are given in table 5.1.

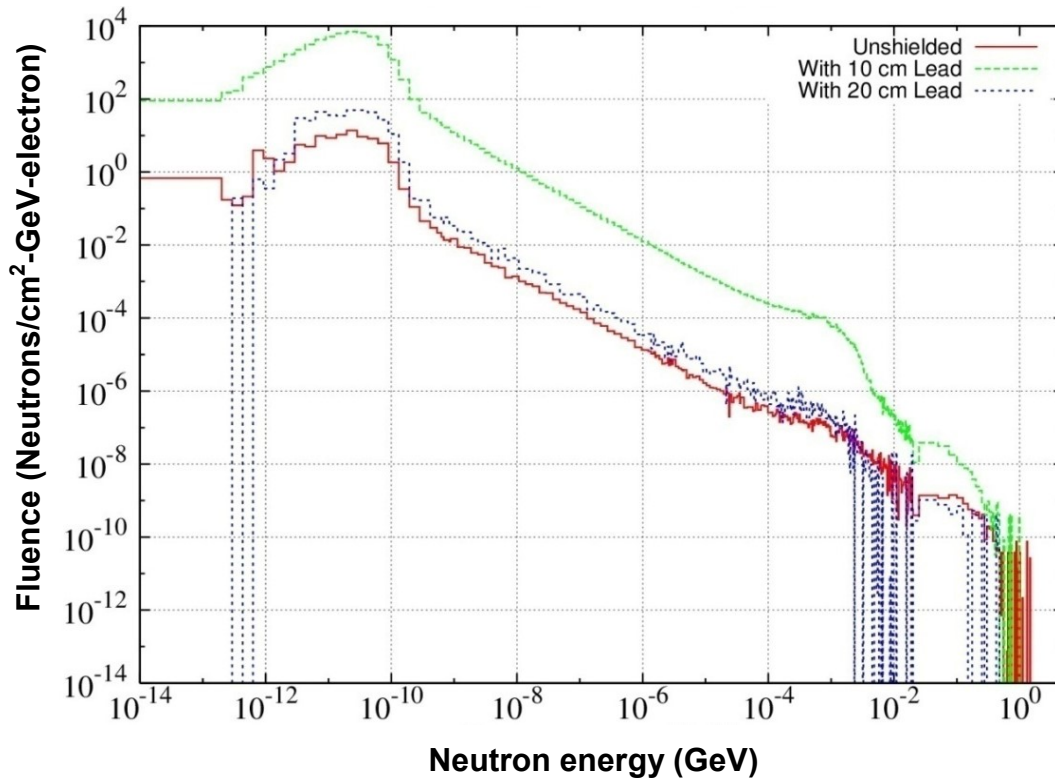


Figure 5.5: Photo-neutron spectrum inside water phantom

Table 5.1: Estimated dose rate at the experimental hutch

Radiation type	Dose equivalent rate ($\mu\text{Sv/day}$)		
	Unshielded	With 10 cm Lead	With 20 cm Lead
Gas bremsstrahlung	52976.00	22.48	0.34
Solid bremsstrahlung	155.80	10.54	0.22
Photo-neutrons	0.04	2.18	0.01
Total	53131.84	35.20	0.57

The net unshielded dose rate at the experimental station is found to be 53 mSv/day and is dominated by the gas bremsstrahlung. The contribution of photo-neutron is insignificant. The bremsstrahlung dose rate reduces significantly by the introduction of 10 cm lead however, increase in photo-neutron dose is observed. This is because of the generation of high energy neutrons from the lead shielding by the bremsstrahlung photons as shown in figure 5.5. The dose reduced to 0.57 μ Sv/day by the introduction of 20 cm lead shielding, which can be attributed to the shielding of high energy neutrons through inelastic scattering with lead. Therefore the total dose rate at the experimental station with 20 cm lead shielding is found to be within the acceptable limit.

5.3 Radiation shielding studies for AMOS beamline (Insertion device beamline)

Atomic, molecular and optical science (AMOS) beamline is an insertion device beamline in Indus-2. A planar permanent magnet undulator (U1) is used as the source of ultraviolet to soft x-ray photons for the beamline [161]. U1 has been installed at 10.4 m long straight section (LS-2) of Indus-2. A mirror is kept at a distance of 18.5 m from the centre of U1 undulator inside the optics hutch for focusing of the synchrotron beam. The mirror acts as the first scattering element for gas bremsstrahlung radiation and source of photo-neutrons in the beamline. In addition, intense synchrotron radiation in hard x-ray range from the undulator is also evaluated independently to ensure adequacy of the shielding. Radiation dose due to gas bremsstrahlung radiation, photo-neutron and synchrotron radiation are simulated and the shielding parameters are optimized to achieve regulatory dose limit for continuous occupancy outside the optics hutch.

5.3.1 Gas bremsstrahlung dose rate in beamline hutch

The direct gas bremsstrahlung and scattered gas bremsstrahlung dose rates in the beamline are simulated. For evaluating the gas bremsstrahlung stop (BR stop), simulation is performed to study the energy spectrum, angular distribution and dose profile of the gas bremsstrahlung radiation for the following components.

- i) Direct gas bremsstrahlung
- ii) Scattered gas bremsstrahlung dose from mirror assembly (inside hutch)
- iii) Scattered bremsstrahlung dose outside the hutch

5.3.1.1 Direct gas bremsstrahlung dose

The schematic diagram of the geometry used for evaluation of unshielded gas bremsstrahlung dose is shown in figure 5.6. A pencil beam of electrons of energy 2.5 GeV is allowed to pass through 10.4 m air target at NTP to generate gas bremsstrahlung radiation. The simulation parameters used in this study are kept same as the optimized parameters (refer table 3.1). Dose equivalent rate is scored through USRBIN scoring card using fluence to dose equivalent conversion coefficients through AUXSCORE card. The fluence spectrum is obtained using USRTRACK scoring card and output data are scaled to actual pressure of 1 nTorr. The statistical uncertainties in the results are found to be within $\pm 3.0\%$. However in the fluence spectrum, statistical uncertainties for the lower energy end (< 10 keV) are higher because of the strong attenuation of low energy photons. The direct (unshielded) gas bremsstrahlung radiation from the straight section is simulated at a reference point (located at a distance of 1 m from the mirror in the forward direction). For scoring the dose rate, the tissue phantom is placed at a distance of 19.5 m from the centre of straight section.

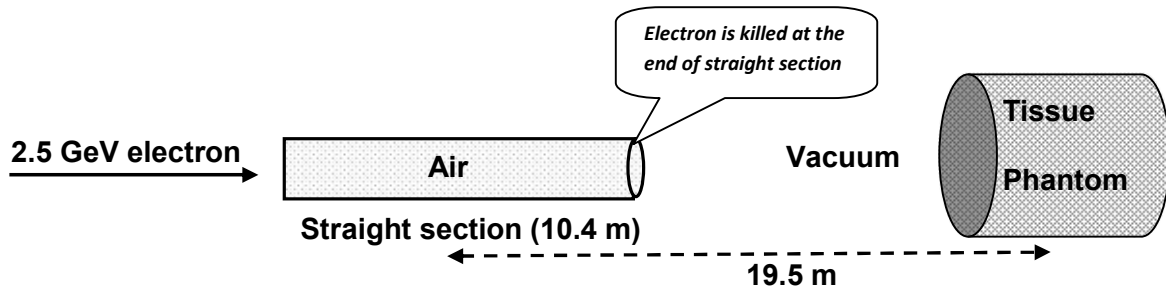
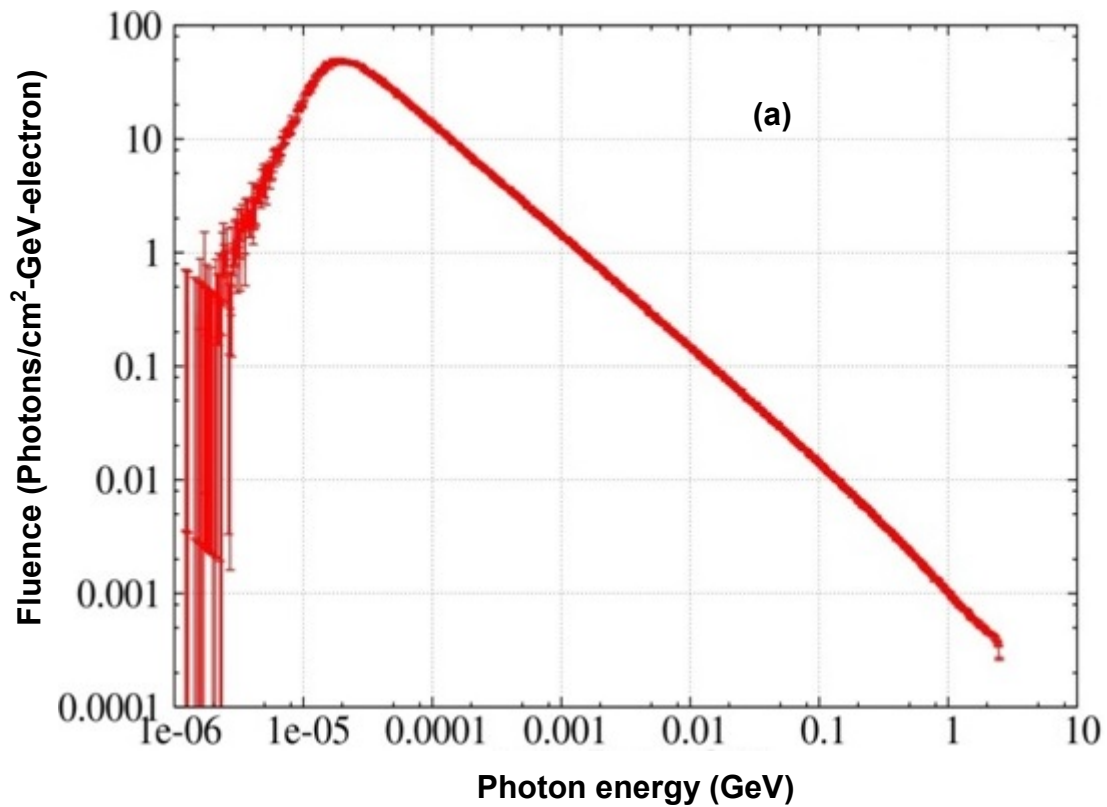


Figure 5.6: Geometry used for estimation of unshielded gas bremsstrahlung dose

Gas bremsstrahlung energy spectrum and corresponding depth dose inside tissue phantom are shown in figure 5.7 (a) and (b), respectively.



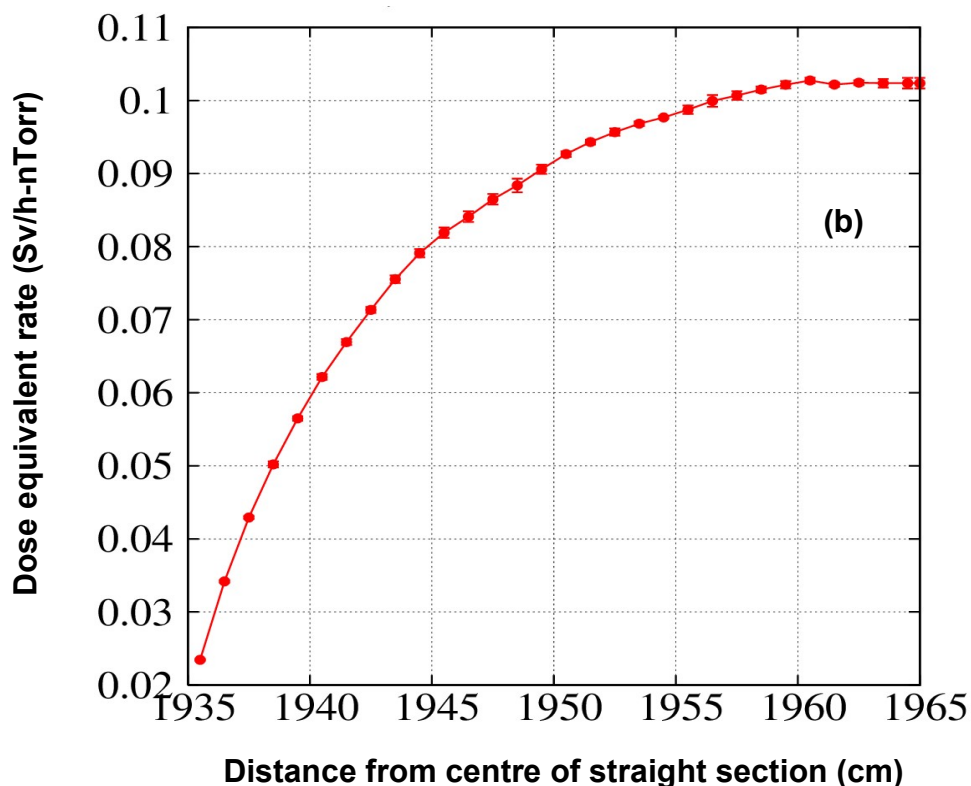


Figure 5.7: (a) Gas bremsstrahlung spectrum and (b) the depth dose inside tissue phantom

The energy spectrum is found to extend up to 2.5 GeV and the dose equivalent rate within the phantom is found to increase with respect to the depth. The increase in depth dose profile is the direct indication of the presence of high energy photons in the gas bremsstrahlung spectrum. The estimated gas bremsstrahlung dose rate is found to be 102.7 mSv/h-nTorr at a distance of 19.5 m from the straight section for 200 mA stored current in Indus-2. [Indus-2 has design parameter for stored current of 300 mA, however it has been commissioned at 200 mA]

5.3.1.2 Scattered gas bremsstrahlung dose from the mirror assembly (inside the hutch)

Scattered gas bremsstrahlung radiation inside the optics hutch is simulated using the silicon mirror, inclined at 10^0 with respect to synchrotron beam axis. This mirror is placed at a distance of 18.5 m from the centre of the straight section. Two tissue phantoms are placed at a distance of

1 m from the silicon mirror in forward (0°) and lateral (90°) direction. A schematic diagram of the geometry used for the simulation is shown in figure 5.8.

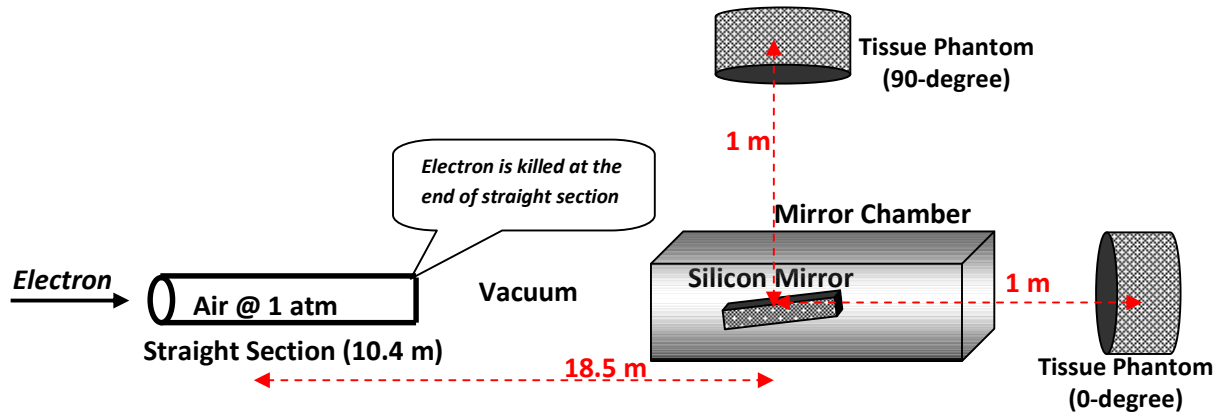


Figure 5.8: Geometry used for bremsstrahlung dose evaluation in 0° and 90° from the mirror

The gas bremsstrahlung energy spectrum and corresponding estimated dose equivalent rate in the tissue phantoms (0° and 90°) are shown in figure 5.9 and figure 5.10, respectively.

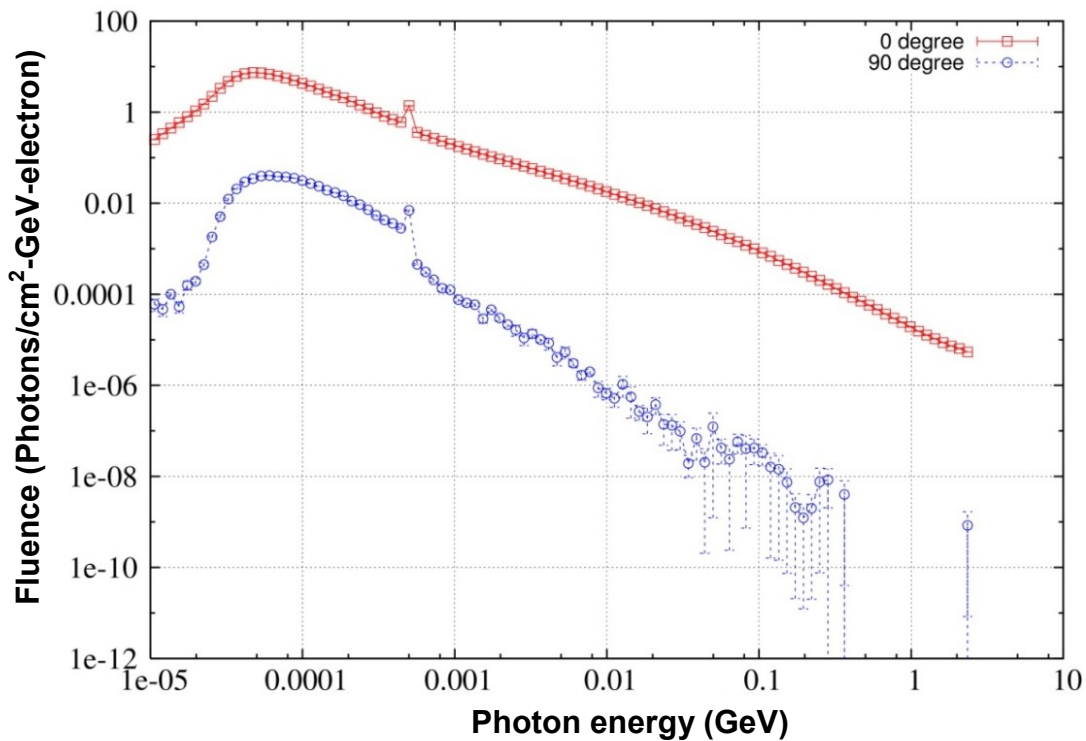


Figure 5.9: Scattered gas bremsstrahlung spectra from mirror in 0 and 90 -degree direction

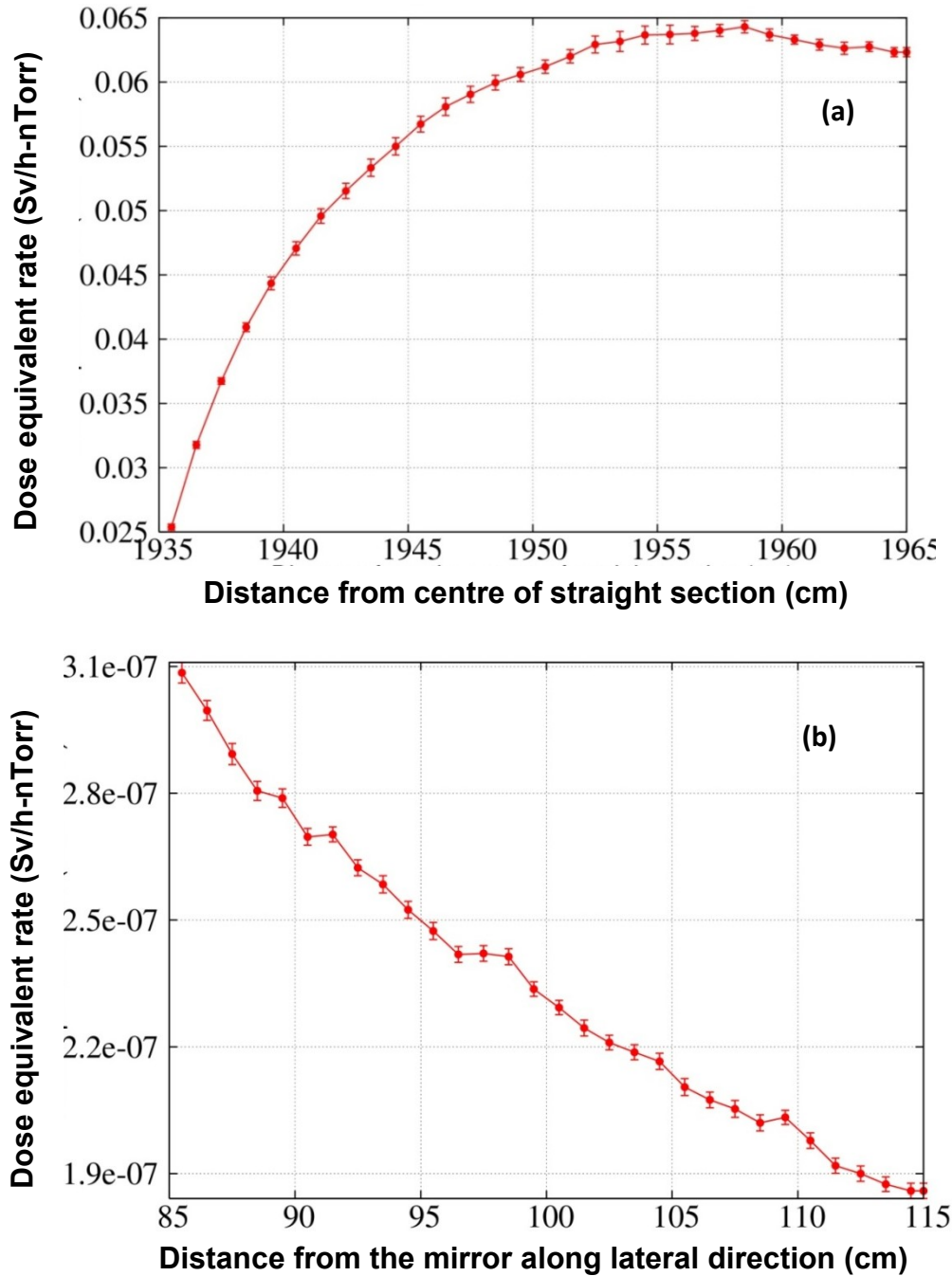


Figure 5.10: Depth dose profile inside tissue phantom in (a) 0° and (b) 90°

The discontinuity observed in the primary and scattered gas bremsstrahlung spectra is due to the 511 keV peak produced by positron annihilation with the medium (mirror). At higher energy, discontinuity is due to relatively lower flux and high statistical error. The dose build up in tissue

phantom is observed only in the forward direction (0^0) due to high energy photons whereas a decreasing trend in lateral direction (90^0) is observed indicating relatively low energy photons, in consistent with the energy spectrum (figure-5.9). The maximum dose equivalent rates at 1 m along forward (0^0) and lateral (90^0) direction are found to be 64.3 mSv/h-nTorr and 0.31 μ Sv/h-nTorr respectively.

5.3.1.3 Scattered gas bremsstrahlung dose (outside the hutch)

In order to study the local shielding requirement for direct gas bremsstrahlung radiation, a gas bremsstrahlung stop is optimised using FLUKA simulation. The geometry of the complete beamline used for the simulation is shown in figure 5.11. The direct gas bremsstrahlung spectrum is allowed to fall on the mirror and dose equivalent rates outside the hutch wall are estimated. Four tissue phantoms (D1, D2, D3 and D4) are placed at selected locations to evaluate scattered dose around optics hutch.

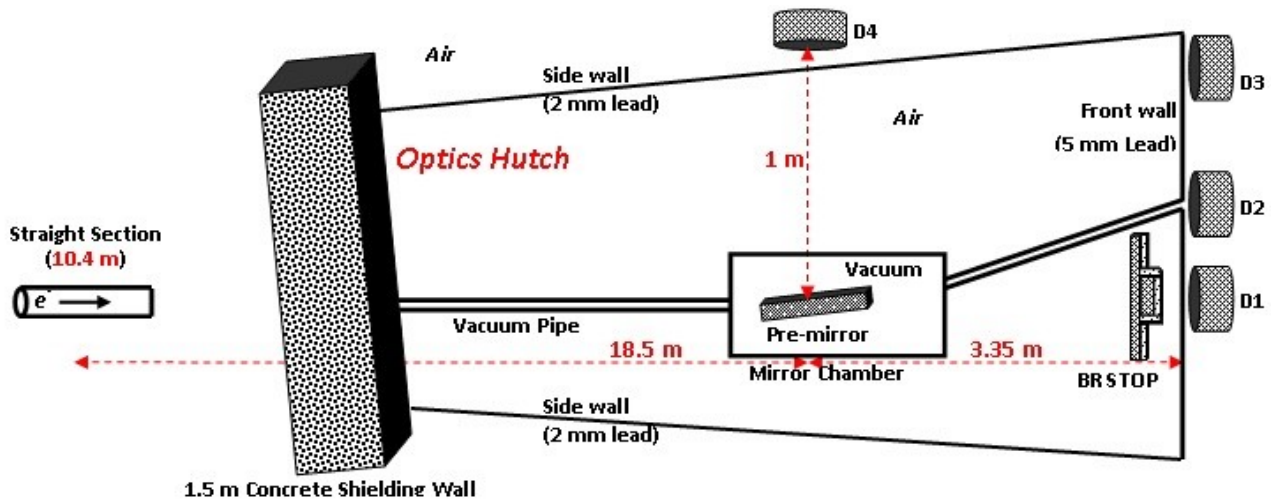


Figure 5.11: Geometry used for bremsstrahlung dose evaluation outside hutch

The simulation is performed with varying lead thicknesses for 10, 15 and 20 cm to optimize of bremsstrahlung (BR) stop. The forward (0^0) gas bremsstrahlung dose rates for 10 to 15 cm of lead are found to be 254 and 15.4 μ Sv/h-nTorr respectively. An optimized thickness of 20 cm is

deduced as the BR stop thickness along the central axis as it brings down the dose rate outside the shielding wall to $1 \mu\text{Sv/h}$. The lateral dimension of BR stop is then optimized by taking the advantage of the angular distribution of scattered gas bremsstrahlung radiation from the mirror chamber. In the lateral direction, a thickness of 10 cm is found to be adequate to maintain radiation levels outside the hutch within the acceptable limit. The dimensions of the optimized BR Stop are shown in figure 5.12.

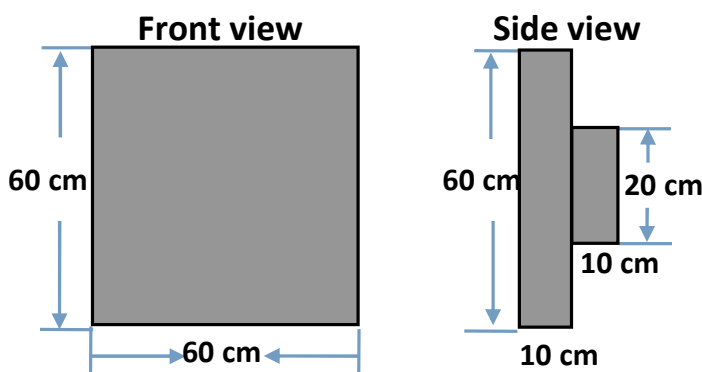


Figure 5.12: Optimized gas bremsstrahlung stop

5.3.2 Photo-neutron dose rate in beamline hutch

Since the photo nuclear cross-section is smaller as compared to cross-section for electromagnetic interactions, LAMBIAS card is used in simulation to reduce photon interaction length for nuclear inelastic interactions by a factor of 50. From the study, it has been observed that though 20 cm thick lead (BR stop) is sufficient enough to reduce gas bremsstrahlung dose within the regulatory limit ($1 \mu\text{Sv/h}$) but it enhances the photo-neutron dose rate. With the addition of 15 cm polyethylene (density – 0.93 g/cc) to the BR stop as neutron shielding, the dose rate outside the hutch is found to reduce to permissible level.

The spatial distribution of dose equivalent rate due to photons and photo-neutrons around the beamline are shown in figure 5.13. The dose equivalent rates due to photons and photo-neutrons with and without optimized shielding from four detectors for 200 mA stored current are shown in

table 5.2. The tissue phantom at beam pipe hole (D2) is found to show higher dose equivalent rate ($1.27 \mu\text{Sv/h}$) than the permissible limit. Therefore this annular space between the beam pipe and the hutch wall near the beam hole needs to be plugged with lead wool to reduce the dose rate to acceptable levels.

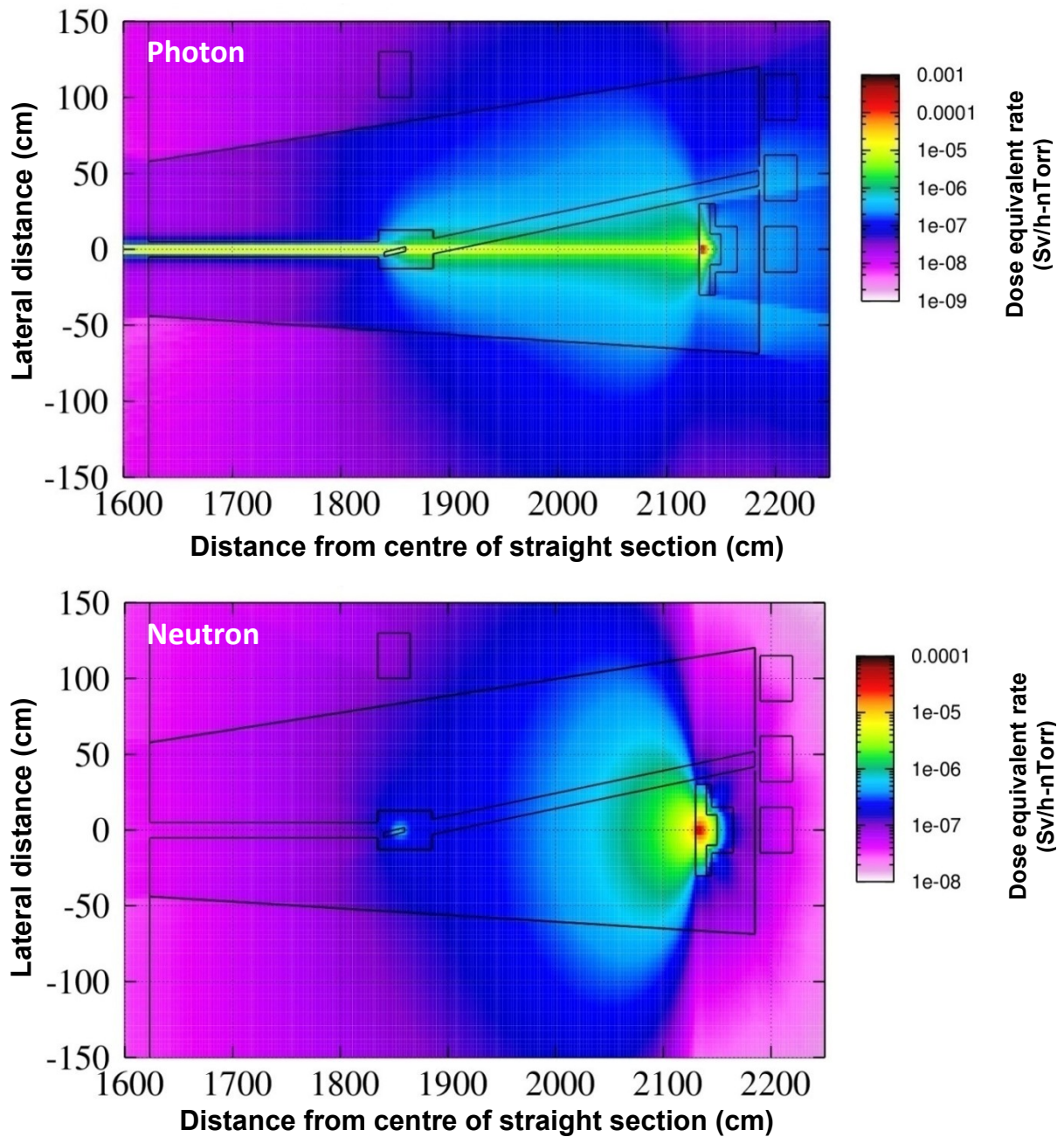


Figure 5.13: Spatial distribution of photon and neutron dose equivalent rate around the beamline

Table 5.2: Gas bremsstrahlung (BR) and photo-neutron dose rate in the beamline

Detector	Dose Equivalent rate for 200 mA stored current in Indus-2 ($\mu\text{Sv/h-nTorr}$)							
	Unshielded	With Mirror assembly	With BR stop and hutch walls			With BR stop, Neutron shielding and hutch walls		
	<i>Gas BR</i>	<i>Gas BR</i>	<i>Gas BR</i>	<i>Photo-neutron</i>	<i>Total</i>	<i>Gas BR</i>	<i>Photo-neutron</i>	<i>Total</i>
Forward (0^0): D1	102730	64300	0.58	6.63	7.21	0.22	0.07	0.29
Beam pipe hole: D2	-	-	1.12	1.49	2.61	0.94	0.33	1.27
Corner of hutch: D3	-	-	0.24	0.15	0.39	0.24	0.26	0.50
Lateral (90^0): D4	-	0.31	0.06	0.11	0.17	0.06	0.12	0.18

5.3.3 Synchrotron radiation dose rate in beamline hutch

The beamline has planned to utilize synchrotron photons (6 - 250 eV) from the undulator (U1). To produce sufficient intensity of low energy photon at 6 eV, the undulator needs to be operated with high deflection parameter (K). In this condition, additionally unwanted high energy synchrotron photons in the energy range 1 to 100 keV will also be produced. These high energy x-ray photons will channel in to the beamline and pose radiation hazard. Therefore in order to study the adequacy of the radiation shielding of the beamline, synchrotron radiation in energy range 1 to 100 keV from U1 undulator (with $K \sim 12$) for 200 mA stored current is generated using SPECTRA code [162] and is shown in figure 5.14. The complete spectrum is programmed through a subroutine (source.f) in FLUKA to simulate direct and scattered dose in the beamline. To evaluate the unshielded synchrotron dose, the spectrum is allowed to incident directly on 30 cm tissue phantom and the depth dose profile is scored. The depth dose profile obtained is presented in figure 5.15. The maximum dose equivalent rate of 7.24×10^4 Sv/h for 200 mA

stored current in Indus-2 is observed at the surface of the tissue phantom.

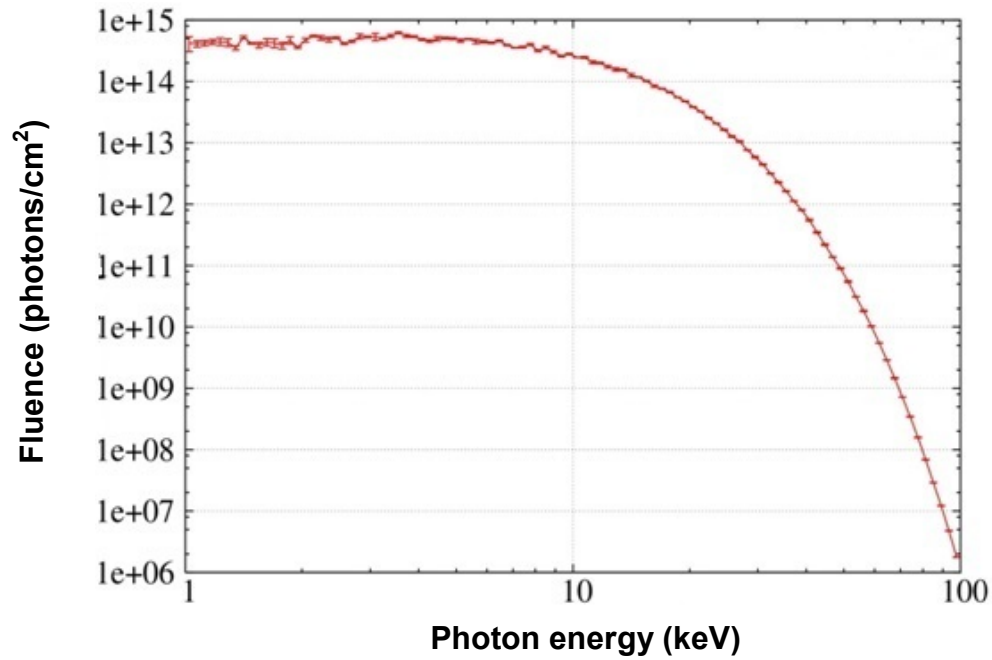


Figure 5.14: Synchrotron spectrum from undulator (U1) for 200 mA at 2.5 GeV

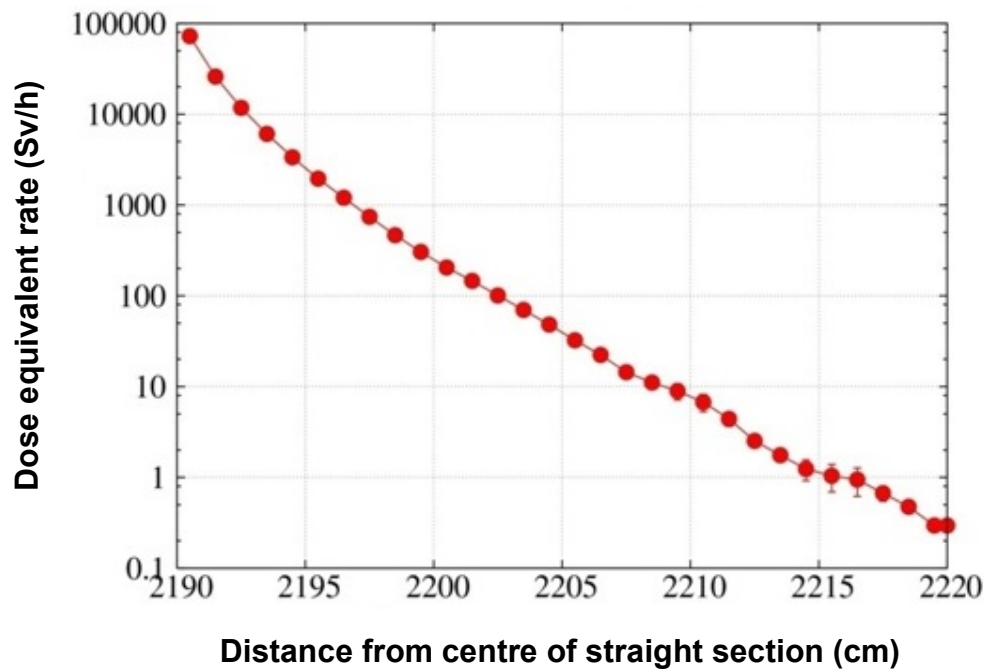


Figure 5.15: Depth dose profile inside tissue phantom due to direct synchrotron beam

To study the scattered dose in the beamline, the synchrotron photon spectrum (figure 5.14) is transported through the beamline components housed inside the optics hutch (front wall - 5 mm lead and sidewall - 2 mm lead). The dose equivalent rates are scored in the tissue phantoms D1, D2, D3 and D4 placed around the hutch. The spatial distribution of dose equivalent rate due to synchrotron radiation around the beamline is shown in figure 5.16. The scattered synchrotron dose rate in all the detectors for 200 mA stored current in Indus-2 are found to be less than the background radiation level ($0.1 \mu\text{Sv/h}$).

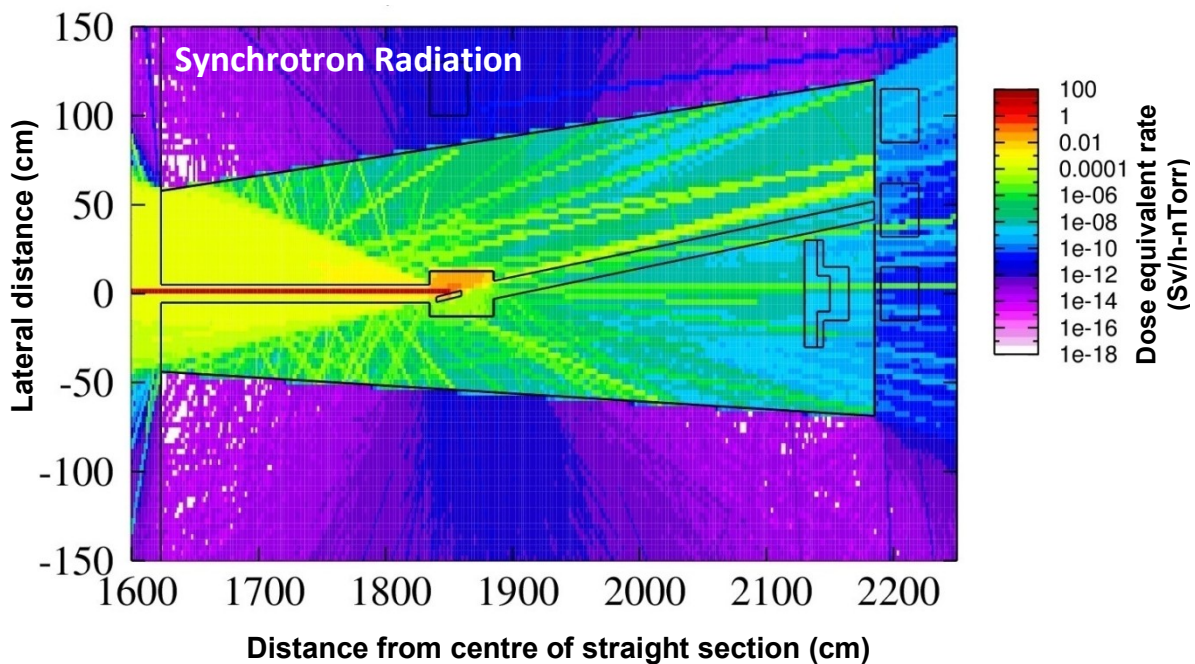


Figure 5.16: Spatial distribution of synchrotron dose equivalent rate around the beamline

5.4 Summary and conclusion

Radiation environment in a synchrotron beamline is complex because of the mixed field from high energy gas bremsstrahlung photons, photo-neutrons and intense synchrotron radiation. Radiation environment in SEXAFS (bending magnet) beamline and AMOS (Insertion device) beamline of Indus-2 synchrotron facility are studied for designing shielding. Primary and the scattered radiation from the beamline components are studied using FLUKA code. The energy

spectrum, angular distribution and depth dose profile of the radiation in the beamlines are studied to optimize shielding requirements.

The radiological implication due to the introduction of the beam shutter in SEXAFS beamline (BL-9) is studied for gas bremsstrahlung, channeled electrons (in the event of beam loss) and photo-neutrons. From the study, it is observed that 10 cm lead shielding is sufficient enough to attenuate the bremsstrahlung photons but it increases the neutron dose at the experimental station and by increasing the lead thickness to 20 cm, the dose rate reduced to acceptable limits. Radiation environment in insertion device (undulator) based AMOS beamline is also studied to evaluate the shielding requirements. The direct gas bremsstrahlung in the insertion device beamline is found to extend up to the primary energy of the electron in the storage ring and also responsible for photo-neutron production in the beamline. As the intensity of gas bremsstrahlung radiation in insertion device beamline is high compared to that of a bending magnet beamline, the angular distribution of scattered bremsstrahlung from the first scattering element decides the lateral dimension of the gas bremsstrahlung shield.

Chapter 6

Design of synchrotron radiation beamline for radiation physics research

6.1 Introduction

Synchrotron radiation sources are being extensively used worldwide for material characterization in the field of material science, environmental science, biology, industrial applications, etc. Synchrotron radiation beamlines are designed and developed to provide researchers with good quality intense photon beam. A synchrotron beamline is an arrangement of several optical elements used to transport synchrotron beam from the source point to the sample point; tailoring the beam properties like beam size, photon flux, energy selection, energy resolution, etc as per the experimental requirement. The photograph of a typical beamline of Indus-2 is shown in figure 6.1.

A Synchrotron radiation facility has many synchrotron beamlines and each beamline is planned and designed for specific applications like x-ray diffraction, x-ray fluorescence, x-ray absorption spectroscopy, photoelectron spectroscopy, reflectivity, lithography, imaging, etc. Because of the vast spectrum of the synchrotron photons, the beamline can also be designed in different energy ranges like hard x-ray, soft x-ray, VUV, visible or IR. In addition diagnostic beamlines are also developed for characterization of the electron beam circulating in the storage ring. Every

synchrotron beamline in a synchrotron facility is unique in the sense of usable energy range, flux, beam size and divergence of the available photon beam. Various ray tracing software like Shadow (developed at CXrL, University of Wisconsin) [163], RAY (developed at BESSY, Berlin, Germany) [164], Spectra (developed at RIKEN SPring-8 Center, Japan) [162] have been developed for modeling the propagation of synchrotron beam through the optical elements of the beamline.

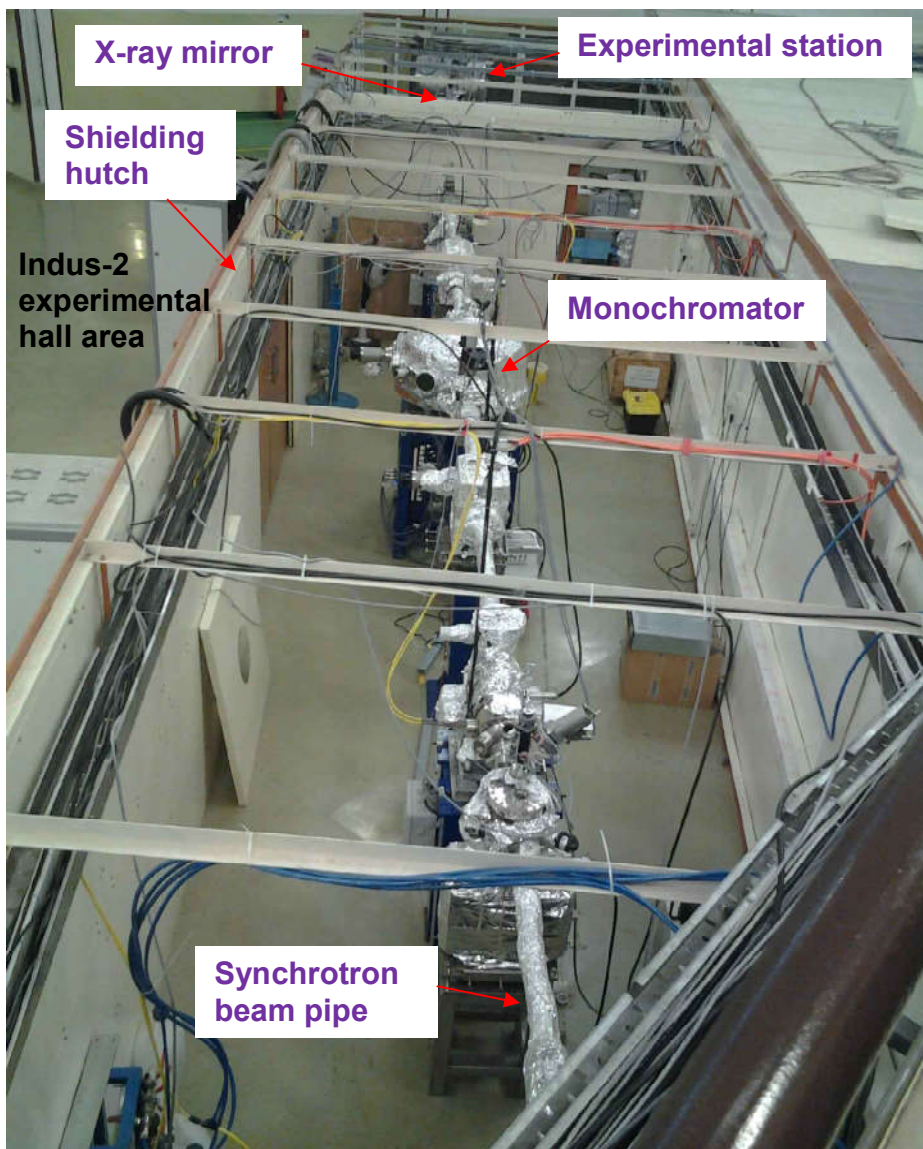


Figure 6.1: Beamline components of a typical beamline of Indus-2

A beamline is proposed to be set up at one of the beam ports (bending magnet) of Indus-2 for carrying out radiation physics and safety research. The proposed beamline is expected to provide an experimental facility for a variety of experiments on dosimetry, ozone generation related studies, Linear Energy Transfer (LET) studies of low energy radiation, radiobiology, studies on optical fiber sensors, radiation damage, etc. The beamline is planned for dual mode operation i.e. full synchrotron spectrum (4 - 50 keV) without focusing and white beam (4 - 30 keV) with focusing to the experimental station. The beamline will consist of beryllium windows, slits, beam viewer, wire scanner, x-ray mirror, sample stage and detector stage.

Literature study is performed for understanding the design aspects of the synchrotron beamlines and utilisation of RAY program in design optimisation. Based on the literature study, the design parameters of the optical components of the proposed beamline are optimized using RAY program for achieving desired beam qualities like energy range, beam size and intensity. The design criteria of various optical elements, methodology for ray tracing calculations using RAY program and the design aspects of proposed beamline are briefly discussed in the following sections.

6.2 Optics for hard x-ray synchrotron beamline

Optical components in hard x-ray synchrotron beamlines are critically designed to achieve desired intensity, size, energy resolution and energy range of the photons at the experimental station, keeping the brilliance of emitted beam conserved as far as possible. Designing optics for synchrotron radiation is more challenging as compared to that for visible light due to low wavelength of x-rays, high heat load and broad energy range. Since most of the components in beamline are maintained at ultra high vacuum, vacuum compatibility of the components is also important. The standard components in a synchrotron beamline are windows/filters, slits, photon

shutters, mirrors, monochromator, etc. The parameters playing crucial role in beamline design are described below.

- i) **Aberration:** With increased size of the optics, geometrical aberrations become inevitable. So the optics design should be such that these are minimized. Usually 1:1 and 1:3 focusing are found to be the optimum solutions for minimizing aberrations.
- ii) Requirement of grazing incidence of synchrotron beam on mirrors increases the size of the mirrors (≥ 1 m) and makes optical aberrations significant.
- iii) Because of the low wave length of photons, surface roughness in mirrors should be very small (RMS roughness \sim few \AA).
- iv) Water cooling design is critical. The flow should not exceed streamline flow conditions to ensure limited vibration of optics. The design should be such that the streamline flow should provide adequate cooling.

Therefore the design of the optical elements should be to minimize scattered photons and also to achieve the above goals. The design criteria [5-7] of some important optical components are discussed briefly in the following paragraphs.

- a) **Windows and Filters:** In hard x-ray beamlines, low Z materials like beryllium, diamond or some polymeric free standing foils ~ 100 μm thickness are used as windows for dual purpose of vacuum isolation between beamline and storage ring as well as to transmit hard x-rays. These windows are water cooled to tackle high heat load due absorption of low energy radiation. The lower limit to energy range of the beamline actually comes from the windows.
- b) **Slit System:** Movable metallic plates made up of high atomic number elements like tungsten are mostly used to define the synchrotron beam size. Mostly 4 blade systems are used to define horizontal and vertical beam size as per the requirement. This also helps in shielding

of unwanted scattered radiation and thereby reducing heat load on crucial components like mirrors and monochromators. The position of the slit system in the beamline is critical and should be designed to take care of the scattered photons from reaching the experimental station.

- c) **Mirror:** Mirrors play crucial role in beamline optics as steering and focusing elements for synchrotron beam. Absorption is the dominant mechanism when the x-rays incident normally or at a wider angle on materials. However, if the angle of incidence is made very small ($\theta < \theta_c$), total external reflection occurs and the reflectivity is close to 100%. Therefore the x-ray mirror is set at very small angle of the order of few mrad (called as grazing incidence) to steer the incident beam and the maximum angle at which total external reflection occurs is called the critical angle (θ_c) [7]. The critical angle, as a function of the wavelength of incident photon and the atomic number of the material, is expressed as follows [165].

$$\theta_c \propto \lambda \sqrt{Z} \quad \text{----- (6.1)}$$

So the angle of incidence is decided by the lowest λ to be used in the beamline. It is desired to make θ as large as possible because for larger θ , mirror size is smaller. Hence θ_c should be the largest possible which can be achieved by coating high Z material. Normally noble metals like Au, Pt, Rh, etc. are used as coating for hard x-ray mirrors.

The efficiency for focusing by mirrors also depends on the imperfections like surface roughness and slope errors present on coated surface. Usually these mirrors are very long (~ 1 m) in order to accept at least $\pm \sigma$ (σ is the standard deviation of gaussian beam) of incident synchrotron beam. Depending on the beamline requirement, the mirrors are manufactured in various geometrical shapes, e.g. planar, spherical, cylindrical, elliptic, parabolic and toroidal

with minimum slope errors and RMS surface roughness. Radii of curvature for meridional and sagittal focusing through a toroidal mirror are shown in figure 6.2 and can be mathematically expressed as follows.

$$R_m = \frac{2}{\sin\theta} \left[\frac{pq}{p+q} \right] \quad \text{----- (6.2)}$$

$$R_s = 2\sin\theta \left[\frac{pq}{p+q} \right] \quad \text{----- (6.3)}$$

Where, R_m , R_s are the meridional and sagittal radii of curvatures, respectively. p , q and θ are the object distance, image distance and the angle of incidence, respectively.

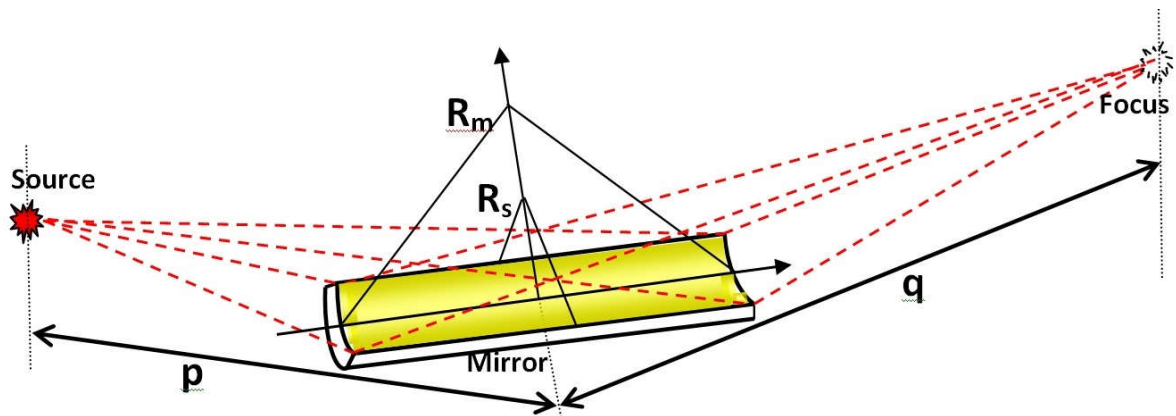


Figure 6.2: Meridional and sagittal focusing using a toroidal mirror

The x-ray mirrors are also provided with water cooling to avoid deformations in surface due to high heat load of synchrotron radiation spreading over a large surface area. Usually x-ray mirrors are ~ 1 m length with meridional and sagittal radius of curvature of the order of kilometers and centimeters, respectively.

- d) Monochromator:** Monochromator is used as an energy selector for the broad spectrum of incident synchrotron beam. For hard x-ray beamlines, monochromators use two perfect crystals (typically silicon, germanium, diamond) to monochromatize the beam. The

condition for x-ray diffraction is governed by Bragg's law (equation 2.8). Hence simultaneously radiation of wavelengths $\lambda, \lambda/2, \lambda/3, \dots, \lambda/n$ are diffracted from the crystal as far as the reflections are not forbidden by the crystal structure. In a double crystal monochromator, two parallel crystals are used to produce collimated monochromatic beam parallel to incident white x-ray beam.

- e) **X-ray detectors:** Variety of x-ray detectors are commercially available depending on requirement of experiment. These detectors can be broadly classified into three categories, viz. point detectors, position sensitive detectors and energy dispersive detectors. Detectors like ionization chamber, pin diode, NaI(Tl) scintillation detector, etc. are used as integrating detector for photon flux counting. Similarly detectors like charge coupled device (CCD), scintillator based pixel detectors, pin diode arrays detector, image plate, etc. are used for measuring spatial distribution of photons. Most commonly used detectors are energy dispersive detectors like Silicon drift detectors (SDD), high purity germanium detector (HPGe), which provide spectral distribution of photons. The suitability of any detector depends on its energy range, dynamic range, energy resolution and noise etc. required for the specific experiment.

6.3 Ray tracing calculations

Dedicated software programs have been developed at various synchrotron facilities for designing beamline optics. Programs like SHADOW, RAY, SPECTRA are being extensively used by synchrotron community to optimize the design parameters of optical elements prior to setting up of the facility at synchrotron radiation sources. RAY program has been used in the present study to design a synchrotron beamline at Indus-2.

RAY is a very versatile ray tracing program developed at BESSY [164,166]. The recent version

of RAY program consists of graphical user interface (GUI) for user inputs and made the user interaction much simpler through online visualization of ray tracing results through integrated image viewing tool [167]. The process of ray tracing through RAY program includes

- i) Generation of synchrotron radiation from bending magnets and insertion devices as per the input parameters of the synchrotron source like electron beam energy, current, beam size and divergence etc.
- ii) Randomly traces the rays through the optical elements and calculate the spatial and energy distribution of the rays at the image point.
- iii) Surface roughness, slope errors, thermal deformation and also the mechanical misalignment in the optical elements can be incorporated to achieve results approaching reality.
- iv) Image patterns, intensity profile, energy distribution and angular divergence of the rays at any position from the source point (or at the optical element) are recorder and plotted on the graphical user interface.

Ray tracing calculation in RAY program is done through Monte Carlo procedure, by randomly distributing the rays within the source and movement of rays is calculated through probability distribution function of angle and position. Similarly polarization property of source, reflection and diffraction phenomena at optical elements are also simulated by applying random variables on functional characteristics depending upon the type of optical element. The results give decent idea of the flux, energy resolution, beam size and polarization of photon beam at the experimental station. Ray tracing is useful in optimum selection of shape, radii of curvatures, RMS roughness and figure errors of the optical elements. A stringent requirement on error parameters will make the optics very expensive but may not be required for the proposed experiments on the beamline.

6.4 Optics design calculation for radiation physics beamline

The design parameters of optical components for the proposed beamline at Indus-2 are evaluated using RAY programme. This beamline is planned for dual mode operation i.e. full synchrotron spectrum (4-50 keV) without focusing and white focused beam (4-30 keV) at the experimental station. The requirement of focused beam is to deliver high dose rate on small size samples. The aim of the design study is as follows.

Dual mode: 1) Unfocused mode

Energy range: 4-50 keV

Beam size: Unfocussed (slits are used to limit the beam size)

2) Focused mode

Energy range: 4-30 keV

Maximum beam size: ~ 100 mm (H) x 0.5 mm (V)

Aberration free

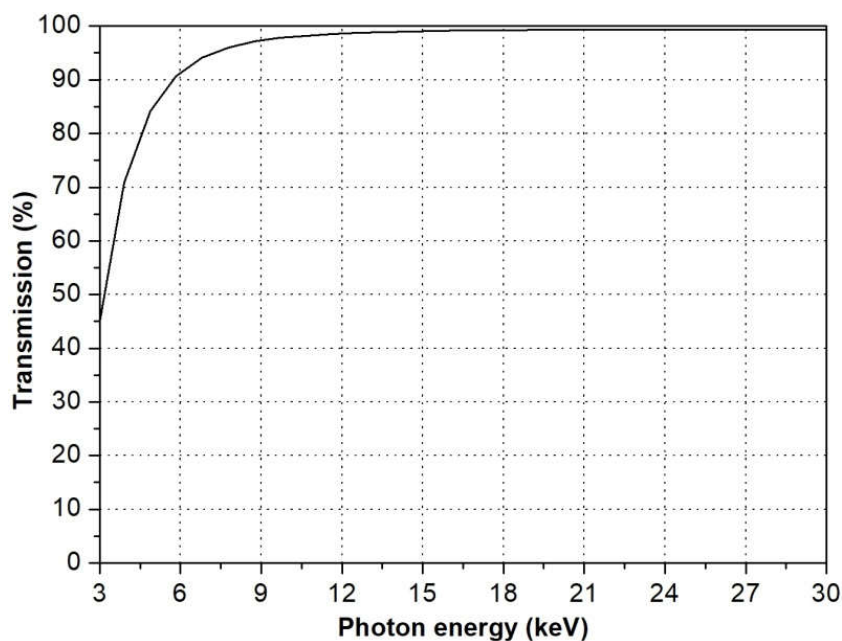
No energy resolution requirement

Therefore a cylindrical mirror (with a curvature in meridional direction) at a distance of 16.5 m from the tangent point is chosen for vertical focusing of the beam to the experimental station. Optimization study of surface roughness and slope errors in mirror are performed to achieve desired beam qualities. Ray tracing is performed with two slit systems before and after mirror for horizontal and vertical collimation of synchrotron beam. The electron beam parameters of Indus-2 synchrotron source used in RAY program for optics design study are given in table 6.1.

Table 6.1: Electron beam parameters used in ray tracing calculations

Parameters	Value
Electron beam energy (E_0)	2.5 GeV
Bending radius (ρ)	5.5 m
Electron beam size (x, y) at centre of bending magnet	(0.234 mm, 0.237 mm)
Electron beam vertical divergence (γ)	0.062 mrad

The synchrotron beam from Indus-2 storage ring is transported to the beamline through the front end of nearly ~ 15 m length. During transport through front end, synchrotron beam is first collimated by fixed mask having 3 mrad (horizontal) and 2 mrad (vertical) divergences. Front end is connected to the beamline through a water cooled beryllium window (200 μm thick) for vacuum isolation. Therefore low energy part of the synchrotron beam (< 4 keV) gets cut off from the continuum and rest of the hard x-ray part is transported to the beamline. The transmission curve for 200 μm beryllium foil (density- 1.834 g/cc) for x-rays up to 30 keV is shown in figure-6.3 [168].

**Figure 6.3: X-ray transmission curve for 200 μm thick beryllium window**

The beam acceptance for the beamline is 3 mrad (H) and the total power accepted in the beamline is ~ 90 watts. The integral flux of photons calculated for the white spectrum for Indus-2 parameters is of the order of 10^{17} photons/s/0.1% BW. The optical layout of the beamline is shown in figure 6.4.

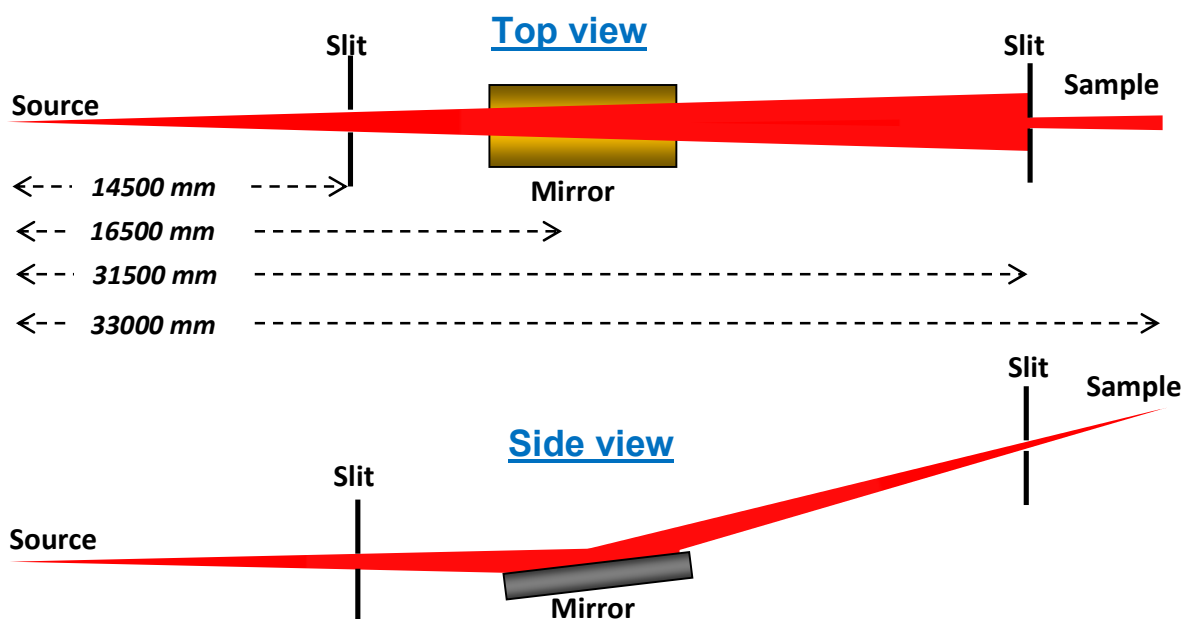


Figure 6.4: Optical layout of the beamline showing photon beam tracing in focused mode

For obtaining the full synchrotron spectrum (4 - 50 keV), the beamline will have a provision for retracting the mirror and the diverging beam with full spectrum will reach the experimental station. The beam size can be varied using 4 jaw slit systems depending on the user requirement. In addition, to increase the intensity of x-ray, a cylindrical mirror will be used as a vertical focusing element. However the focused beam will have limited energy range of 4-30 keV only. The complete layout of the proposed synchrotron beamline with the critical elements like beryllium windows, gate valves, slit systems, mirror assembly, beam viewer systems, experimental station, etc. is shown in figure 6.5. There will be one more beryllium window after the 2nd slit system placed near to the experimental station. The complete beamline will be

maintained at high vacuum condition till this 2nd beryllium window. A small section of chamber with kapton window and filled with helium gas will be attached to the 2nd beryllium window for protection against oxidation of beryllium foil while in contact with air at atmospheric pressure. The synchrotron beam passes through air after the kapton window and reaches sample position. Sample will be exposed to synchrotron beam at experimental stage in air at atmospheric pressure.

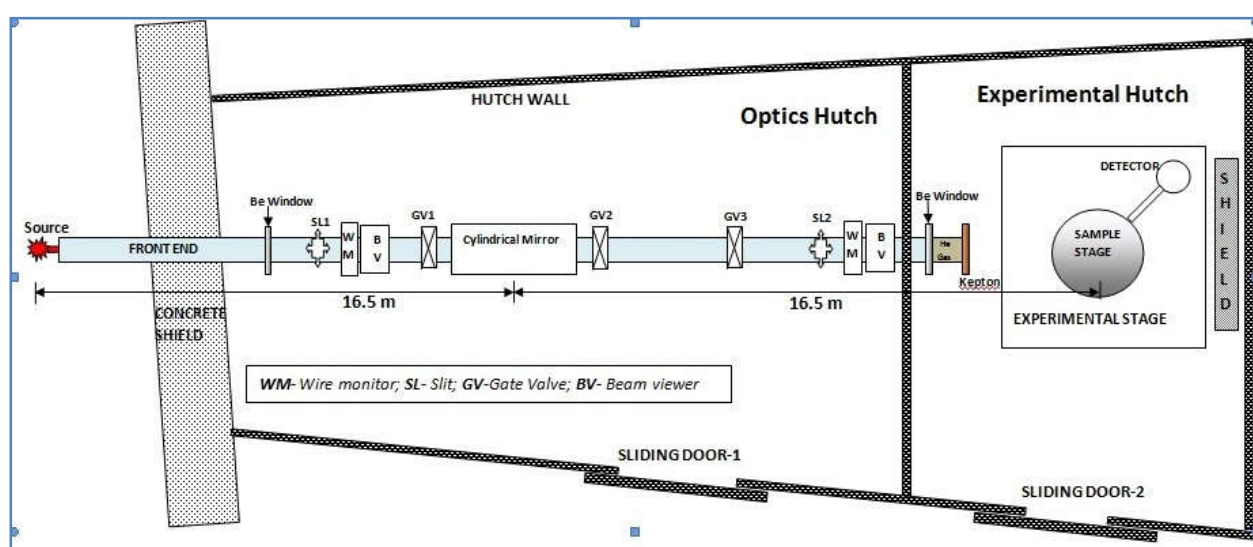


Figure 6.5: Proposed layout of the synchrotron beamline

The ray tracing calculations are performed using RAY program to simulate the imaging properties of synchrotron beam at the optical components and at the focus position (sample location) at the experimental station. The program is utilized to optimize the crucial parameters of the cylindrical mirror like radius of curvatures, surface roughness and slope errors etc.

The grazing incidence of 3 mrad (0.17 degree) with respect to mirror surface is used. Reflectivity as function photon energy for rhodium, gold and platinum coated mirror surfaces is shown in figure 6.6 [169]. From the figure, it is clear that rhodium provides better reflectivity for energy range up to 20 keV. Whereas gold and platinum provide better reflectivity for higher energy up

to 30 keV as compared to rhodium, but show decrease in reflectivity for photon energies 11 to 14 keV because of the absorption at L-edges of platinum and gold, respectively. Thus gold is chosen as the material for reflective surface of the cylindrical mirror.

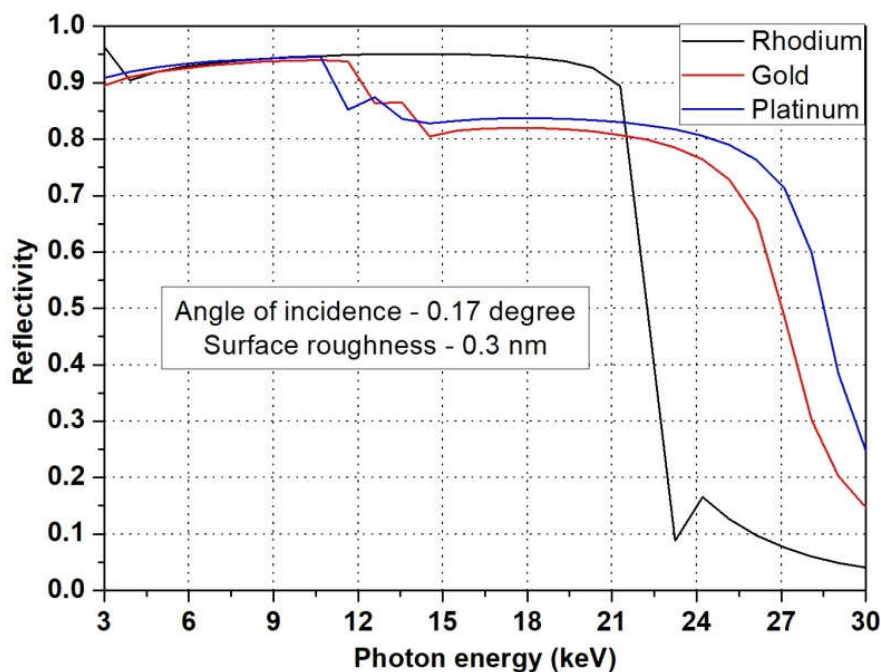


Figure 6.6: Reflectivity of rhodium, gold and platinum coated mirror

Ray tracing calculations are performed to simulate the imaging property of the focused beam at sample position using the beamline photon acceptance and optical design parameters as given in table 6.2.

Table 6.2: Beamline acceptance and optical design parameters

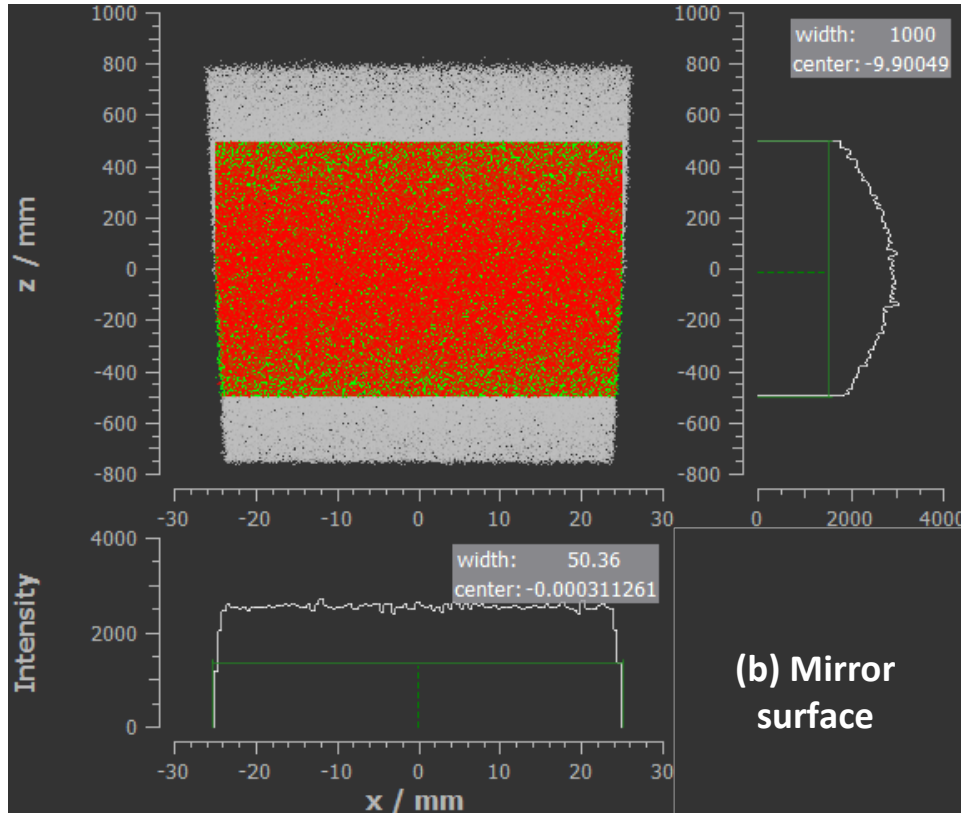
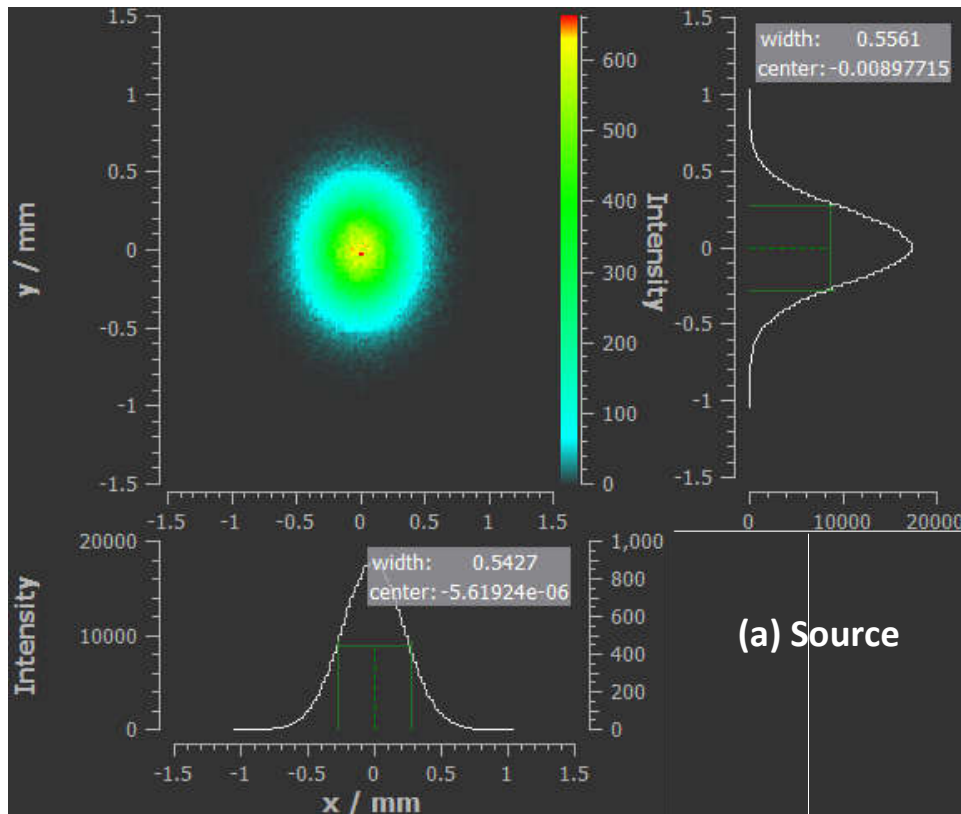
Parameters	Value
Horizontal divergence of source	3 mrad
Energy range of source	4 - 30 keV
Distance of 1 st Optical element from source (Slit-1)	14.5 m
Distance of 2 nd Optical element from source (Mirror)	16.5 m
Distance of 3 rd Optical element from source (Slit-2)	31.5 m
Distance of image position from source	33.0 m

Optimization studies for the meridional radius of curvature, slope error, surface roughness with the size and intensity of image beam are performed to evaluate the design parameters of the cylindrical mirror. The calculated design parameters from the study are listed in table 6.3.

Table 6.3: Design parameters of the cylindrical mirror

Parameters	Value
Shape	Tangential cylinder
Mirror size (L x W x H)	1000 x 50 x 20 mm
Tangential radius of curvature	5.6 km \pm 2%
Substrate material	Silicon
Coating material & thickness	Gold (\sim 50 nm)
Roughness	< 0.3 nm
Slope error (tangential)	< 1'' (\sim 5 μ rad)
Slope error (sagittal)	< 5'' (\sim 25 μ rad)

The footprints of the synchrotron beam at different optical elements are shown in figure 6.7 (a - d). Figure 6.7 (a) shows the footprint of the synchrotron beam at origin point with beam size 0.5 mm (H) x 0.5 mm (V) at 1 σ . Figure 6.7 (b) shows the footprint of synchrotron beam on the mirror surface with acceptance for optical area of 1000 mm x 50 mm. Figure 6.7 (c) shows the vertically focused beam at slit-2 with opening area 94 mm (H) x 0.5 mm (V) placed before sample position. Because of the vertical focusing by the cylindrical mirror, the vertical size of beam at slit-2 position is reduced to \sim 1 mm. Figure 6.7 (d) shows the footprint of final image spot at sample position (after vertical focusing by the mirror and collimation by slit-2).



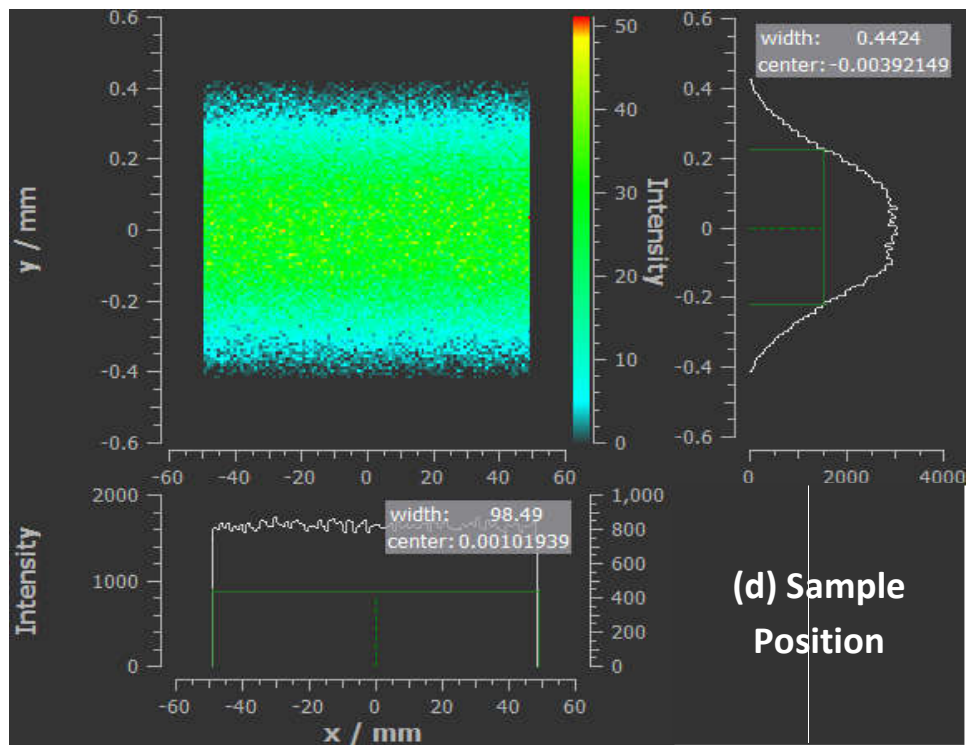
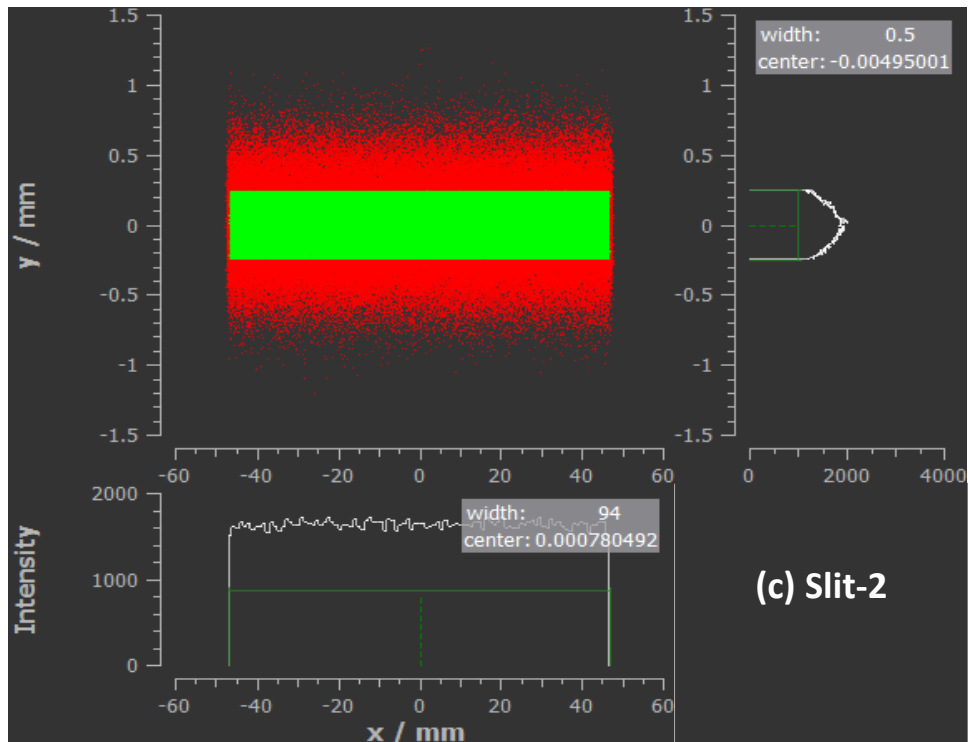


Figure 6.7: Footprint of synchrotron beam at (a) source, (b) mirror surface, (c) slit-2 after mirror and (d) sample position

The variations in image properties at sample position are calculated by varying vertical opening of slit-2 width from 0.5 to 1 mm and listed in table 6.4. The variation in energy spectra of synchrotron beam at source, mirror and sample position at experimental station are shown in figure 6.8.

Table 6.4: Source and image beam properties

Beam	Horizontal & Vertical beam sizes (mm)	Intensity (%)
Source	0.549 (H) x 0.557 (V)	100.0
Image-1 [#]	98.49 (H) x 0.672 (V)	47.3
Image-2 ^{\$}	98.49 (H) x 0.442 (V)	33.1

Note: Post mirror slit vertical width: 1 mm (#), 0.5 mm (\$)

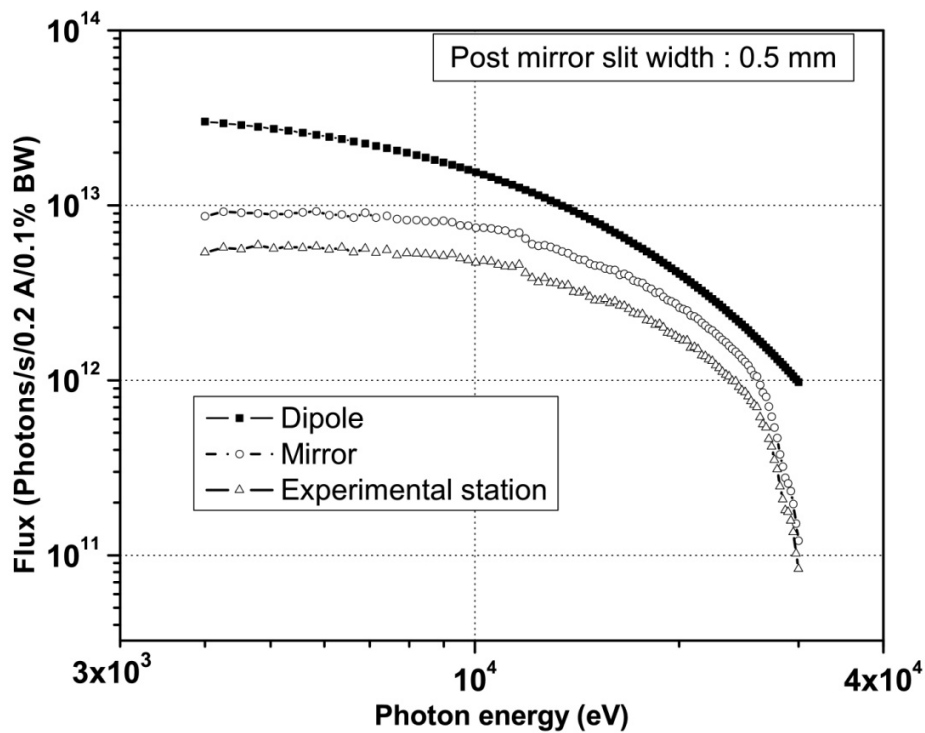


Figure 6.8: Spectral distribution at source point, mirror and image spot at experimental station

From figure 6.8, it is observed that the flux of synchrotron beam from mirror and at sample position reduces at faster rate after 25 keV and can be attributed to poor reflectivity from gold surface for photon energies higher than 25 keV.

6.5 Summary and conclusion

The design parameters of optical components for a white synchrotron beam line for applications in radiation physics research is evaluated using ray tracing programme “RAY”. The optimized parameters for meridional radius, surface roughness, meridional and sagittal slope errors are 5600 m, 0.3 nm, 1 arsec and 5 arcsec, respectively. Synchrotron beam spot of size 98.49 mm (H) x 0.672 mm (V) with ~ 47% intensity (with post mirror slit vertical width of 1 mm) is achieved at the experimental station.

The design of the beamline is done such that the experiments can be performed in full white spectrum with bigger beam size and also with focused beam at the experimental station. The integrated flux expected at the focal spot is $\sim 10^{17}$ photons/s/0.1% BW. Provision for 4-blade slit system has been incorporated in the design in order to reduce the photon flux at the experimental station for specific dosimetry experiments where low flux is required.

Chapter 7

Summary and conclusions

Synchrotron radiation sources are high energy electron accelerators (storage rings) capable of delivering intense photons with wide energy spectrum ranging from infra-red to hard x-rays. In these sources, relativistic electrons under the influence of transverse magnetic field emit electromagnetic radiation called as the synchrotron radiation. The synchrotron radiation is transported to the experimental station through beamline. Every synchrotron beamline is unique in terms of energy range, photon flux, beam size and its divergence and is designed to fulfill the requirements of different experimental investigations. The radiation environment in a synchrotron beamline is primarily dominated by gas bremsstrahlung radiation, whose energy extends up to the primary energy of the electron in the storage ring. Primary bremsstrahlung x-rays on interaction with beam line components produce photo-neutrons via photonuclear reactions, secondary electrons, positrons and photons through electromagnetic cascade. Intense synchrotron radiation especially in hard x-ray range is also a potential radiation hazard, which gets absorbed completely within few millimeters of the human body giving rise to very high skin dose locally. Both gas bremsstrahlung and synchrotron radiation are emitted in a very narrow cone and hence highly angular dependent. Thus the radiation scenario in a synchrotron beamline is complex and challenging. Extensive literature studies have revealed the grey areas especially in gas bremsstrahlung dose estimation, dosimetry of low energy photons and high dose

measurement at synchrotron beamlines which motivated to investigate these unexplored areas. The reported empirical relation in literature for estimation gas bremsstrahlung dose rate is deduced from simulations carried out with air target and validated up to 1 GeV beam energy. Therefore the gas bremsstrahlung dose for actual residual gas composition inside storage ring at ultra high vacuum, which is significantly different from air composition and with higher beam energy are studied. Similarly lack of energy response of dosimetry devices in synchrotron energy range (< 30 keV) are equally important for proper assessment of dose to the synchrotron beamline users. Also the nonlinear and saturation problem in conventional thermoluminescence dosimeters are major issues to be addressed for high dose dosimetry. The design of primary standard dosimeter for absolute dosimetry and calibration of detectors in synchrotron radiation is also essential. The necessity of a dedicated beamline for radiation physics research with synchrotron radiation is strongly felt to generate useful data on radiation protection. The research work reported in the thesis is primarily focused on these important aspects of radiation dosimetry in synchrotron beamlines.

In the present work, simulation studies on gas bremsstrahlung spectra and its angular distribution and depth dose profile from air target have resulted in optimization of the scoring radius. Based on the study, a constant emission cone (0.1 mrad) to evaluate the scoring radius has been deduced for dose estimation at medium energy electron storage rings up to 3 GeV. From the study, an empirical formula for gas bremsstrahlung dose rate is established which has better fitting of the dose data with experimental data. This study is further extended to investigate the effect of residual gas composition present inside vacuum chamber (at ultra high vacuum) on gas bremsstrahlung properties. From the study, a vacuum correction factor has also been suggested to the proposed empirical relation for gas bremsstrahlung dose estimation. These studies have

been applied for the shielding evaluation of synchrotron beam lines of Indus-2 (2.5 GeV). As far as synchrotron radiation dosimetry is concerned, dose due to direct and scattered synchrotron radiation are evaluated using FLUKA code and validated through experimental studies performed at the beam lines of Indus-2. The maximum absorbed dose rates in direct and scattered synchrotron beam are found to be of the order of 10^5 Gy/h and 2 Gy/h, respectively for the Indus-2 design parameters (300 mA, 2.5 GeV) and found to be very useful for shielding evaluation of synchrotron beamlines. The simulation methodologies used to generate useful data on gas bremsstrahlung radiation and synchrotron radiation are applied in radiation shielding studies for bending magnet and insertion device beamlines of Indus-2. Fluence distribution, energy spectra and dose equivalent rate due to gas bremsstrahlung, photo-neutron and synchrotron radiation around the beamline components and the shielding hutch are studied. Based on the study, gas bremsstrahlung stop and photo-neutron shielding are optimized to achieve acceptable dose limits stipulated by regulatory agency.

Study on the energy response of $\text{CaSO}_4:\text{Dy}$ and $\text{LiF}:\text{Mg,Ti}$ thermoluminescence detectors for synchrotron radiation has provided useful data on effect of dosimeter material thickness and metal filters (used in personnel dosimetry device). From the study, $\text{LiF}:\text{Mg,Ti}$ is found to show better energy response than $\text{CaSO}_4:\text{Dy}$ for the range of energies covered by synchrotron radiation. Also $\text{CaSO}_4:\text{Dy}$ is found to show high under response than $\text{LiF}:\text{Mg,Ti}$ for photon energies ≤ 8 keV because of self-attenuation.

Study on effect of high gamma dose (tens of Gy and above) on $\text{CaSO}_4:\text{Dy}$ TL dosimeter using X-ray Absorption Near Edge Structure (XANES) spectroscopy has provided a direct experimental evidence of Dy^{3+} transition to Dy^{2+} on gamma ray irradiation as proposed by redox model of TL emission from $\text{CaSO}_4:\text{Dy}$. The observed linear increase in the area under XANES

spectrum with dose has enabled us to propose this technique for gamma dosimetry in the dose range where conventional thermoluminescence technique is not suitable. In addition, for set up of a unique facility (synchrotron beamline) for radiation physics research, optical design parameters of the beamline at Indus-2 synchrotron facility are optimized and crucial parameters such as meridional radius, surface roughness, meridional and sagittal slope errors of the cylindrical mirror are evaluated through RAY tracing calculations and are reported in the thesis.

The results obtained from the present work provide useful information on radiation dosimetry aspects of synchrotron beamlines worldwide. Empirical formula for gas bremsstrahlung dose in synchrotron beamlines and application of x-ray absorption spectroscopy techniques for dosimetry in high dose region are very important contributions presently made. The studies on design aspects of primary standard for dosimetry and the optical design of synchrotron beamlines will also provide valuable information for future studies in this field.

Future Scope

The present study on gas bremsstrahlung radiation indicates the importance of optimization of emission angle for dose estimation. However a generalized expression for gas bremsstrahlung dose based on angular dependency needs to be investigated to extend the energy range of the expression beyond 3 GeV. Both experimental and simulation studies will be necessary tool for the comprehensive study on gas bremsstrahlung radiation. In addition the study on scattered gas bremsstrahlung radiation to evaluate angular distribution of scattered dose and its dependency on scattering material is needed.

In order to avoid self-attenuation, dosimetry using thin film dosimeters like radiochromic films [170] seems to be potential dosimeters for dosimetry in synchrotron radiation beamlines. Extensive studies on the energy response, dose response of these film dosimeters will provide

useful information for potential application in synchrotron radiation dosimetry. Also the effect of polarization property of synchrotron radiation on dosimetry is quite challenging and interesting. As the conventional thermoluminescence dosimetry technique using macroscopic TL materials is not suitable for high dose estimation; TL material in nano scale has promising scope for high dose estimation. Thus the suitability and standardization of dosimetry techniques for synchrotron radiation beamlines are the unexplored areas and need detail investigation. The spectrometry of synchrotron radiation using passive dosimeters through unfolding techniques is interesting and widens the scope for future work.

References

1. Synchrotron radiation sources, N. Marks, Radiation Physics and Chemistry **45** (3), pp. 315-331 (1995).
2. Synchrotron radiation sources, K. Wille, Reports on Progress in Physics **54**, pp. 1005-1068 (1991).
3. Synchrotron Radiation Sources – Present Capabilities and Future Directions, H. Winick, Journal of Synchrotron Radiation **5**, pp.168–175 (1998).
4. Website: <http://www.lightsources.org/what-light-source>
5. Soft X-ray and extreme Ultraviolet radiation principles and applications, D. Attwood, Cambridge University Press (1999).
6. Synchrotron Radiation Basics, Methods and Applications, S. Mobilio, F. Boscherini and C. Meneghini, Springer (2015).
7. An Introduction to Synchrotron Radiation Techniques and Applications, P. Willmott, Willey (2011).
8. Elements of Modern X-ray Physics, J. Als-Nielsen and D. McMorrow, Willey (2011).
9. Comparison of design and practices for radiation safety among five synchrotron radiation facilities, J. C. Liu, S. H. Rokni, Y. Asano, W. R. Casey, R. J. Donahue and P.K. Job, Radiation Measurements **41**, S206–S220 (2007).
10. Website: http://www.rreat.gov.in/technology/accel/isrf_index.html.
11. Commissioning of the Indus-2 storage ring, V.C. Sahni, Asian Particle Accelerator Conf. Proc., Raja Ramanna Centre for Advanced Technology, Indore (2007).
12. Indus synchrotron source:A national facility, S. K. Deb, AIP Conf. Proc. **1447**, pp.56-59 (2012).

13. Indus-2 Synchrotron Radiation Source: current status and utilization, S. K. Deb, G. Singh and P. D. Gupta, *Journal of Physics: Conf. Series* **425**, 072009 (2013).
14. *Particle Accelerator Physics II*, H. Wiedemann, Berlin: Springer Verlag (1996).
15. *Introduction to Intrabeam Scattering*, A. Sorensen, CERN Accelerator School, CERN 87-10 (1987).
16. Operational radiation protection in synchrotron light and free electron laser facilities, J. C. Liu, S. H. Rokni and V. Vylet, *Radiation Protection Dosimetry* **137** (1–2), pp. 18–34 (2009).
17. *High energy astrophysics*, M. S. Longair, Cambridge University Press (1981).
18. *Radiation Detection and Measurement*, G.F. Knoll, 2nd ed., John Wiley & Sons (1988).
19. Radiological Safety aspects of the operation of electron linear accelerators, W.P. Swanson, IAEA Tech. Rep. 188 (1979).
20. Basic aspects of high energy particle interactions and radiation Dosimetry, ICRU Report 28, International Commission on Radiation Quantities and Units (1978).
21. *Radiation Physics for personnel and environmental protection*, J. D. Cossairt, Fermilab report TM-1834, Revision 14 (2016).
22. Bremsstrahlung source term estimation for high energy electron accelerators, M. K. Nayak, T. K. Sahu, H. G. Nair, R. V. Nandedkar, T. Bandyopadhyay, R. M Tripathi, P. R. Hannurkar and D. N. Sharma, *Radiation Physics and Chemistry* **113**, pp. 1-5 (2015).
23. Gas bremsstrahlung from electron storage rings, A. Rindi, *Health Physics* **42**, pp.187-193 (1982).
24. Radiation protection at synchrotron radiation facilities, J. C. Liu and V. Vylet, *Radiation Protection Dosimetry* **96** (4), pp. 345–357 (2001).
25. *High Energy Particles*, B. Rossi, Prentice-Hall Inc., Englewood, NJ (1952).

26. Particle Accelerator Physics, H. Wiedemann, Springer (2007).
27. Electron Induced Cascade Showers, W. R. Nelson, T. M. Jenkins, R. C. McCall and J.K. Cobb, *Physical Review* **149** (1), pp.201-208 (1966).
28. Luminosity measurement at Adone by single and double bremsstrahlung, H. C. Dehne, M. A. Preger, S. Tazzari and G. Vignola, *Nuclear Instruments and Methods* **116** (2), pp. 345-359 (1974).
29. Measurement of absorbed dose in water irradiated by 2.5-GeV bremsstrahlung, S. Ban, H. Hirayama and S. Miura, *Health Physics* **53** (1), pp. 67-72 (1987).
30. Gas bremsstrahlung in 2.5 GeV electron storage ring, S. Ban, H. Hirayama and S. Miura, *Health Physics* **57** (3), pp. 407-412 (1989).
31. Gas bremsstrahlung from electron storage rings: a Monte Carlo evaluation and some useful formulae, G. Tromba and A. Rindi, *Nuclear Instruments and Methods in Physics Research A* **292**, pp.700-705 (1990).
32. Estimation of fluence rate and absorbed dose rate due to gas bremsstrahlung from electron storage rings, A. Ferrari, M. Pelliccioni and P.R. Sala, *Nuclear Instruments and Methods in Physics Research B* **83**, pp.518-524 (1993).
33. Gas bremsstrahlung and induced photoneutrons in the NSRRC's electron storage ring: A comparison of measurements and simulations, R. J. Sheu, J. P. Wang, R. D. Sheu and S. H. Jiang, *Nuclear Instruments and Methods in Physics Research B* **217**, pp.555-563 (2004).
34. Monte Carlo and analytical calculations for characterization of gas bremsstrahlung in ILSF insertion devices, E. Salimi, J. Rahighi, D. Sardari, S. R. Mahdavi and M. L. Rachti, *Journal of Instrumentation* **9** (2014).
35. Dose response of various radiation detectors to synchrotron radiation, T. Kron, L. Duggan,

- T. Smith, A. Rosenfeld, M. Butson, G. Kaplan, S. Howlett and K. Hyodo, *Physics in Medicine and Biology* **43**, pp.3235–3259 (1998).
36. Characterisation of the low-energy X ray response of Polish TLDs to synchrotron radiation and the determination of some TLD quantities, N. E. Ipe, A. Fassò, K. R. Kase, R. Kaur, P. Bilski and P. Olko, *Radiation Protection Dosimetry* **84** (1-4), pp.169–173 (1999).
37. Low-energy x-ray dosimetry studies (6 to 16 keV) at SSRL beamline 1-5, N. E. Ipe, S. Chatterji, A. Fassò, K. R. Kase, R. Seefred, P. Olko, P. Bilski, and C. Soares, *AIP Conf. Proc.* **417**, pp.197-203 (1997).
38. Responses of LiF TLDs to 10-40 keV monoenergetic photons from synchrotron radiation, N. Nariyama, S. Tanaka, M. Yoshizawa, H. Hirayama, S. Ban, H. Nakashima, Y. Namito and Y. Nakane, *Radiation Protection Dosimetry* **49** (4), pp.451–457 (1993).
39. Responses and glow curves of $\text{Li}_2\text{B}_4\text{O}_7:\text{Cu}$, BeO and $\text{CaSO}_4:\text{Tm}$ TLDs to 10-40 keV monoenergetic photons from synchrotron radiation, N. Nariyama, S. Tanaka, Y. Nakane, Y. Asano, H. Hirayama, S. Ban, H. Nakashima and Y. Namito, *Radiation Protection Dosimetry* **74** (3), pp.155–161 (1997).
40. Free-air ionization chambers, D. T. Burns and L. Buermann, *Metrologia*, **46**, pp.S9–S23 (2009).
41. Absolute air-kerma measurement in a synchrotron light beam by ionization free-air chamber, M. Bovi, R.F. Laitano, M. Pimpinella, M. P. Toni, K. Casarin, E. Quai, G. Tromba, A. Vascotto and D. Dreossi, Workshop on “Absorbed dose and air kerma primary standards”, Paris, 9-11 May (2007).
42. Development of a portable free-air ionization chamber as an absolute intensity monitor for high-energy synchrotron radiation up to 150 keV, N. Nariyama, N. Kishi and S. Ohnishi,

- Nuclear Instruments and Methods in Physics Research A **524**, pp.324–331 (2004).
43. Development of ion chambers for the measurement of low energy synchrotron radiation, A. K. Mahant, S. K. Singh and V. S. Panyam, Nuclear Instruments and Methods in Physics Research A **601**, pp.354–357 (2009).
 44. Air kerma rate measurements using a cylindrical free-air ionization chamber on the 05B1-1 beamline at the Canadian Light Source, D. Anderson, A. Siegbahn, G. Fallone and B. Warkentin, Medical Physics **43** (8) Part 2, 4939 (2016).
 45. Estimating the absolute flux distribution for a synchrotron X-ray beam using ionization-chamber measurements with various filters, A. W. Stevenson and F. Di Lillo, Journal of Synchrotron Radiation **24**, pp.939–953 (2017).
 46. Gas bremsstrahlung and associated photon-neutron shielding calculations for electron storage rings, J. C. Liu, W. R. Nelson and K. R. Kase, Health Physics **68** (2), pp.205-213 (1995).
 47. Characteristics of shielding design calculation for the SPring-8 synchrotron radiation beamlines, Y. Asano and N. Sasamoto, Radiation Protection Dosimetry **82** (3), pp. 167–174 (1999).
 48. A study on radiation shielding and safety analysis for a synchrotron radiation beamline, Y. Asano, JAERI-Research 2001-006 (2001).
 49. Dose calculations using MARS for bremsstrahlung beam stops and collimators in APS beamline stations, J. C. Dooling, ANL/APS/TB-54 (2010).
 50. Radiation safety for electron accelerators: Synchrotron radiation facility, Y. Asano, Radiation Protection and Environment **35** (3&4), pp.135-144 (2012).
 51. Gas bremsstrahlung considerations in the shielding design of the Advanced Photon Source

- synchrotron radiation beam lines, N. E. Ipe and A. Fasso, Nuclear Instruments and Methods in Physics Research A **351**, pp.534-544 (1994).
52. PHOTON; A user's manual, D. Chapman, Brookhaven National Laboratory Informal Report 40822 (1988).
 53. Experimental verification of PHOTON: A program for use in x-ray shielding calculations, E. Bräuer and W. Thomlinson, Nuclear Instruments and Methods in Physics Research A **266**, pp.195-198 (1988).
 54. Development of shielding design code for synchrotron radiation beam line, Y. Asano and N. Sasamoto, Radiation Physics and Chemistry **44** (1–2), pp.133-137 (1994).
 55. Comparison of synchrotron radiation calculations between analytical codes (STAC8, PHOTON) and Monte Carlo codes (FLUKA, EGS4), J. C. Liu, A. Fasso, A. Prinz, S. Rokni and Y. Asano, Radiation Protection Dosimetry **116** (1–4), pp. 658–661 (2005).
 56. Secondary bremsstrahlung dose rates from glancing incidence target, P.K. Job and D.R. Haeffner, Review of Scientific Instruments **67**, 3376 (1996).
 57. Radiation shielding of insertion device beamlines using a mirror as the first optical element, W. Yun, B. Lai, K. J. Randall, S. Davey, D. R. Haeffner, P. K. Job, and D. Shu, Advance Photon Source Report ANL/APS/TB-21 (1995).
 58. ALS synchrotron radiation shielding, R.J. Donahue, LBL-37801-UC-413 (1995).
 59. Shielding design calculation for SPring-8 beamlines using STAC8, Y. Asano, Journal of Synchrotron Radiation **5**, p.615-617 (1998).
 60. Characteristics of radiation safety for synchrotron radiation and X-ray free electron laser facilities, Y. Asano, Radiation Protection Dosimetry **146** (1–3), pp. 115–118 (2011).
 61. Radiological design study of First Optics Enclosure against secondary gas bremsstrahlung

- for the Canadian Light Source, J. Asai and H. Hirayama, *Nuclear Instruments and Methods in Physics Research A* **517**, pp. 9–18 (2004).
62. Shielding design study against gas bremsstrahlung for the CLS first optics enclosures, J. Asai and H. Hirayama, *Radiation Measurements* **41**, pp. S186–S193 (2007).
63. Radiation shielding considerations against gas bremsstrahlung for the BioXAS beamlines at the Canadian Light Source, J. Asai and I. Coulthard, *Nuclear Instruments and Methods in Physics Research A* **622**, pp. 492–501 (2010).
64. Radiation shielding study against gas bremsstrahlung for the BMIT POE3 at the Canadian light source, J. Asai, T. W. Wysokinski, D. Chapman and C. Mullin, *Radiation Physics and Chemistry* **80**, pp.716–722 (2011).
65. Synchrotron radiation shielding design for the Brockhouse sector at the Canadian light source, B. Bassey, B. Moreno, A. Gomez, A. S. Ahmed, D. Ullrich and D. Chapman, *Radiation Physics and Chemistry* **98**, pp.109–112 (2014).
66. Shielding calculations for the National Synchrotron Light Source-II experimental beamlines, P. K. Job and W. R. Casey, *Nuclear Instruments and Methods in Physics Research A* **698**, pp.196–201 (2013).
67. Radiation safety analysis for the experimental hutches at the Linac coherent light source at SLAC, X.S. Mao, S.H. Rokni and H. Vincke, *Nuclear Instruments and Methods in Physics Research A* **562**, pp.963–966 (2006).
68. NSLS-II beamline scattered gas bremsstrahlung radiation shielding calculation, R. Popescu, Z. Xia, P. Job and Wah-Keat Lee, *AIP Conf. Proc.* **1741**, 030019 (2016).
69. Generic radiation safety design for SSRL synchrotron beamlines, J. C. Liu, A. Fasso, H. Khater, A. Prinz and S. Rokni, *Radiation Measurements* **41**, pp.S156–S162 (2007).

70. Gas bremsstrahlung shielding calculation for first optic enclosure of ILSF XPD beamline, H. B. Jalali, E. Salimi and J. Rahighi, *Applied Radiation and Isotopes* **129**, pp.62-66 (2017).
71. Radiation shielding design for Dream-Line beamline at SSRF, J. Xu, X. Xia, J. Lv, Y. Sheng and L. Liu, *Conf. Proc. C1205201 4011- 4013*, 3rd International Particle Accelerator Conference (IPAC 2012), New Orleans, Louisiana (2012).
72. Radiological implications of top-off operation at national synchrotron light source-II, P.K. Job and W. R. Casey, *Nuclear Instruments and Methods in Physics Research A* **648**, pp.15–21 (2011).
73. Response of monitoring instruments to high-energy photon radiation, Haridas G., K. K. Thakker, S. D. Pradhan, A. R. Nayak and A. M. Bhagwat, *Nuclear Instruments and Methods in Physics Research A* **449**, pp.624-628 (2000).
74. Dose build up correction for radiation monitors in high-energy bremsstrahlung photon radiation fields, Haridas G. Nair, M. K. Nayak, Vipin Dev, K. K. Thakkar, P. K. Sarkar and D. N. Sharma, *Radiation Protection Dosimetry* **118** (3), pp.233-237 (2006).
75. Determination of dose-build-up thickness for absorbed dose measurement in high energy electron-photon radiation at electron storage rings, Haridas G. Nair, Vipin Dev, M. K. Nayak, K. K. Thakkar, P. K. Sarkar and D. N. Sharma, *Radiation Protection Dosimetry* **121** (2), pp.92-98 (2006).
76. Radiation safety considerations of the operation of Indus-1 synchrotron radiation source, G. Haridas, M. K. Nayak, Vipin Dev, D. Verma and K. K. Thakkar, *Asian Particle Accelerator Conf. Proc.*, Raja Ramanna Centre for Advanced Technology (RRCAT), Indore, (2007).
77. Experimental determination of bremsstrahlung dose rate due to accidental beam loss in Indus-1 storage ring, Haridas G., D. Verma, P. K. Sahani, M. K. Nayak, K. K. Thakkar and

- Sarkar P. K, Indian Journal of Pure and Applied Physics **50**, pp.462-464 (2012).
78. A personnel dosimeter TLD badge based on CaSO₄:Dy teflon TLD discs, K. G. Vohra, R. C. Bhatt, B. Chandra, A. S. Pradhan, A. R. Lakshmanan and S. S. Shastry, Health Physics **38**, pp.193–197 (1980).
79. Calculated energy dependence of some RTL and RPL detectors, P. Bassi, G. Busuoli and O. Rimondi, Applied Radiation Isotopes **27**, pp.291-305 (1976).
80. Photon energy dependence of CaSO₄:Dy embedded teflon TLD discs, A. S. Pradhan, R. K. Kher, A. Dere and R. C. Bhatt, Applied Radiation Isotopes **29**, pp.243-245 (1978).
81. Metal filters for the compensation of photon energy dependence of the response of CaSO₄:Dy-Teflon TLD discs, A. S. Pradhan and R. C. Bhatt, Nuclear Instruments and Methods **166**, pp. 497-501 (1979).
82. Dose computation algorithm for individual thermoluminescence dosimetry, A. V. Dere, K. L. Popli, J. S. Nagpal, D. K. Kapoor and P. H. Patel, Bulletin of Radiation Protection **16**, 54–56 (1993).
83. Measurement of personal dose equivalents H_p(10) and H_p(0.07) by TLD badge—response in mixed fields of low energy X-rays and high energy gamma rays, A. S. Pradhan, R. R. Bihari, K. Srivastava and A. K. Bakshi, Proc. of the 24th IARP Conf. on Radiation Protection in Nuclear Fuel Cycle, KAPS, pp.223–229 (1999).
84. Development of an algorithm for TLD badge system for dosimetry in the field of X and gamma radiation in terms of H_p(10), A. K. Bakshi, K. Srivastava, G. Varadharajan, A. S. Pradhan and R. K. Kher, Radiation Protection Dosimetry **123** (2), pp.148–155 (2007).
85. Development of an algorithm for evaluating personal doses due to photon fields in terms of operational quantities for TLD badge system in India, S. M. Pradhan, C. Sneha, G.

- Chourasiya, M. M. Adtani, S. M. Tripathi and S. K. Singh, *Radiation Protection Dosimetry* **136** (3), pp.176–184 (2009).
86. Low energy X-ray dosimetry studies (7 to 17.5 keV) with synchrotron radiation, N. E. Ipe, H. H. Bellamy, J. R. Flood, K. R. Kase, K. J. Velbeck and R. A. Tawil, *Radiation Protection Dosimetry* **66**, pp.69-74 (1996).
87. Calculated energy dependence of CaSO₄:Dy TL phosphor and phosphor embedded Teflon for X and gamma rays, Jai-Kwon Chang, Young-Mi Nam, Jang-Lyul Kim, V. Chang and Bong-Hwan Kim, *Radiation Measurement* **33**, pp.675–678 (2001).
88. Energy response study of thermoluminescent dosimeters to synchrotron radiation in the energy range 10-35 keV, A. K. Bakshi, B. S. Dhabekar, S. Chatterjee, V. J. Joshi and R. K. Kher, *Indian Journal of Engineering and Material Sciences* **16**, pp.172-174 (2009).
89. Study on the response of thermoluminescent doseimeters to synchrotron radiation: experimental method and Monte Carlo calculations, A. K. Bakshi, S. Chatterjee, T. Palani Selvam and B. S. Dhabekar, *Radiation Protection Dosimetry* **140** (2), pp.137–146 (2010).
90. Response of CaSO₄:Dy based TL doseimeter system to high-energy photon beams: theoretical simulation, S. Chatterjee, A. K. Bakshi, and R. K. Kher, *Radiation Protection Dosimetry* **129** (4), pp. 456-462 (2008).
91. Estimation of bremsstrahlung photon energy in the environment of high-energy electron accelerator using CaSO₄:Dy based TL doseimeter, A. K. Bakshi, M. K. Nayak, G. Haridas, S. Chatterjee and R. K. Kher, *Radiation Protection Dosimetry* **128** (1), pp.43-48 (2007).
92. Response of CaSO₄:Dy phosphor based TLD badge system to high energy electron beams from medical linear accelerator and estimation of whole body dose and skin dose, S. Chatterjee, A. K. Bakshi, R. A. Kinshikar, G. Chourasiya and R. K. Kher, *Radiation*

- Measurement **44**, pp.257–262 (2009).
93. Studies on the response of the TLD badge for high-energy photons, M. Kumar, R. K. Kher, G. Sahni and K. Chhokra, *Radiation Protection Dosimetry* **128** (3), pp. 266-273 (2008).
 94. Calcium sulfate activated by Thulium or Dysprosium for thermoluminescence dosimetry, T. Yamashita, N. Nada, H. Onishi and S. Kitamura, *Health Physics* **21**, pp. 295-300 (1971).
 95. *Thermoluminescence of Solids*, S. W. S. Mckeever, Cambridge University Press (1985).
 96. Gamma radiation induced changes in the glow curve of CaSO₄: Dy TLD phosphor, J. K. Srivastava and S. J. Supe, *Radiation Effects* **45**, pp.13- 18 (1979).
 97. Glow peak temperature, supralinearity and LET dependence of TLDs—correlation studies, A. S. Pradhan and A. K. Bakshi, *Radiation Protection Dosimetry* **119** (1–4), pp. 276–279 (2006).
 98. Stability of CaSO₄:Dy thermoluminescent phosphor in high dose region, J. K. Srivastava and S. J. Supe, *Nuclear Instruments and Methods* **155**, pp.233-235 (1978).
 99. The EGSnrc code system: Monte Carlo simulation of electron and photon transport, I. Kawrakow E. Mainegra-Hing, D. W. O. Rogers, F. Tessier and B. R. B. Walters, National Research Council of Canada, Ottawa, NRCC Report PIRS-701 (2018).
 100. PENELOPE-2011 A Code System for Monte Carlo simulation of electron and photon transport, F. Salvat, J. M. Fernández-Varea and J. Sempau, OECD NEA/NSC/DOC(2011)5 (2011).
 101. Review of Monte Carlo Particle Transport Codes and Overview of Recent MCNPX Features, G. McKinney, J. Durkee, J. Hendricks, M. James, D. Pelowitz, and L. Waters, International Workshop on Fast Neutron Detectors and Applications, Cape Town, South Africa, 3 - 6 Apr 2006, pp.088, Proceedings of Science FNDA2006 (2006).

102. Fluka: a multi-particle transport code, A. Ferrari, P. R. Sala, A. Fassò and J. Ranft, CERN-2005–10, INFN TC_05/11 SLAC-R-773 (2005).
103. The FLUKA Code: Developments and challenges for high energy and medical applications, T.T. Böhlen, F. Cerutti, M.P.W. Chin, A. Fassò, A. Ferrari, P.G. Ortega, A. Mairani, P.R. Sala, G. Smirnov and V. Vlachoudis, Nuclear Data Sheets **120**, pp.211-214 (2014).
104. GEANT4-a simulation toolkit, S. Agostinelli et al., Nuclear Instruments and Methods in Physics Research A **506** (3), pp.250–303 (2003).
105. The GEANT4 collaboration, Recent developments in Geant4, M. Asai, A. Dotti, M. Verderi and D. H. Wright, Annals of Nuclear Energy **82**, pp.19–28 (2015).
106. A Monte Carlo primer for health physicists, J. E. Turner, H. A. Wright and R. N. Hamm, Health Physics **48** (6), pp.717-733 (1985).
107. Radiation transport calculations and simulations, A. Fasso, A. Ferrari and P. R. Sala, Radiation Protection Dosimetry **137** (1–2), pp.118–133 (2009).
108. The FLUKA code: description and benchmarking, G. Battistoni, F. Cerutti, A. Fasso, A. Ferrari, S. Muraro, J. Ranft, S. Roesler and P.R. Sala, Proc. of Hadronic Shower Simulation Workshop 2006, AIP Conf. Proc. **896**, pp. 31–49 (2007).
109. Applications of FLUKA Monte Carlo code for nuclear and accelerator physics, G. Battistoni et al., Nuclear Instruments and Methods in Physics Research B **269** (24), pp.2850–2856 (2011).
110. The application of the Monte Carlo code FLUKA in radiation protection studies for the Large Hadron Collider, G. Battistoni et al., Progress in Nuclear Science and Technology **2**, pp.358-364 (2011).
111. Thermoluminescence and Thermoluminescent Dosimetry, Y. S. Horowitz, CRC Press, Boca

- Raton, Florida (1984).
112. Thermoluminescence and its applications: An Introduction, R. K. Bull, International Journal of Radiation Applications and Instrumentation. Part D. Nuclear Tracks and Radiation Measurements **11** (1–2), pp.105-113 (1986).
113. Thermoluminescence Provoquee par les Rayons de M. Roentgen et les Rayons de M. Becquerel, I. L. Borgman, Comptes Rendus **124**, No. 895-896, (1897).
114. Thermoluminescence as a research tool, F. Daniels, C. A. Boyd and D. F. Saunders, Science **117**, 343 (1953).
115. Thermoluminescent dosimetry, J. R. Cameron, N. Suntharalingam, and G. N. Kenney, University of Wisconsin Press, Madison (1968).
116. Phosphorescence and electron traps I. The study of trap distributions, J. T. Randall and M. H. F. Wilkins, Proc. of the Royal Society A **184** (999), pp.365-389 (1945).
117. The electron trap mechanism of luminescence in sulphide and silicate phosphors, G. F. J. Garlick and A. F. Gibson, Proc. of the Physical Society **60**, pp.574-590 (1948).
118. The theoretical and microdosimetric basis of thermoluminescence and applications to dosimetry, Y. S. Horowitz, Physics in Medicine & Biology **26** (4), pp.65-824 (1981).
119. Handbook of thermoluminescence, C. Furetta, World Scientific, Singapore (2003).
120. Applied thermoluminescence dosimetry, M. Oberhofer and A. Scharmann, Lectures of a course held at the Joint Research Centre of the Commission of the European Communities, Ispra, Italy, Adam Hilger Ltd, Bristol (1981).
121. Theory of thermoluminescence, A. J. J. Bos, Radiation Measurements **41**, pp.S45–S56 (2007).
122. Preparation and properties of thermoluminescent materials, J. Azorin, C. Furetta and A.

- Scacco, *physica status solidi (a)* **138**, pp.9-46 (1993).
123. Preparation methods of thermoluminescent materials for dosimetric applications: An overview, J. Azorin, *Applied Radiation and Isotopes* **83** Part C, pp.187-191 (2014).
124. Calculated effective atomic number and kerma values for tissue-equivalent and dosimetry materials, C. A. Jayachandran, *Physics in Medicine & Biology* **16** (4), pp.617-623 (1971).
125. Thermoluminescence of CaSO₄ doped with rare earths, K. S. V. Nambi, V. N. Bapat and A. K. Ganguly, *J. Phys. C: Solid State Phys.* **7** (1974).
126. Valency conversions in rare-earth ions of gamma irradiated CaSO₄ phosphors, K. S. V. Nambi and V. N. Bapat, *J. Phys. C: Solid St. Phys.* **13**, pp.1555-1557 (1980).
127. Thermoluminescent spectra and optical absorption in CaSO₄:Dy, R. J. Matthews and T. G. Stoebe, *J. Phys. C: Solid State Phys.* **15**, pp.6271-6280 (1982).
128. *Optical Spectra of Transparent Rare Earth Compounds*, S. Hufner, New York: Academic Press (1978).
129. Optical absorption and luminescent processes in thermoluminescent CaSO₄:Dy, M. D. Morgan and T. G. Stoebe, *J. Phys.: Condens. Matter* **I**, pp.5773-5781 (1989).
130. Angle Dispersive X-ray Diffraction beamline on Indus-2 synchrotron radiation source: Commissioning and first results, A. K. Sinha, A. Sagdeo, P. Gupta, A. Upadhyay, A. Kumar, M. N. Singh, R. K. Gupta, S. R. Kane, A. Verma, and S. K. Deb, *Journal of Physics: Conf. Series* **425**, 072017 (2013).
131. Calibration and correction of spatial distortions in 2D detector systems, A. P. Hammersley, S. O. Svensson, and A. Thompson, *Nuclear Instruments and Methods in Physics Research A* **346**, pp.312-321 (1994).
132. Website: <http://physics.nist.gov/cgi-bin/Star/compos.pl?matno=262>.

133. Website: http://pdg.lbl.gov/2014/AtomicNuclearProperties/HTML/air_dry_1_atm.html.
134. Residual gas analysis system of synchrotron radiation source Indus-2, K.V.A.N.P.S. Kumar, N. J. Bhange, P. K. Gothwal, P. Fatnani, S. K. Shukla and R. Sridhar, Proc. of the Indian Particle Accelerator Conference (InPAC), VECC, Kolkata, 19-22 Nov (2013).
135. Radiation Oncology Physics: A handbook for teachers and students, E. B. Podgorsak, International Atomic Energy Agency (2005).
136. Gas bremsstrahlung: a comparison of measurements and simulations, A. Esposito, A. Ferrari, L. Liberatori and M. Pelliccioni, Nuclear Instruments and Methods in Physics Research B **88**, pp.345-349 (1994).
137. Website: http://www.fluka.org/web_archive/earchive/new-fluka-discuss/1183.html
138. Development of prototype ambient synchrotron radiation monitors for Indus-2 SRS beam lines, V. Dev et al., RRCAT report, RRCAT/2007-04 (2007).
139. Safety guidelines on accelerators, AERB Safety Guidelines No. AERB/SG/IS-5 (2005).
140. Website: <https://physics.nist.gov/PhysRefData/XrayMassCoef/tab4.html>
141. Design, development and first experiments on the X-ray Imaging Beamline at Indus-2 synchrotron source RRCAT, India, A. K. Agrawal, B. Singh, Y. S. Kashyap, M. Shukla, P. S. Sarkar and A. Sinha, Journal of Synchrotron Radiation **22**, pp.1531–1539 (2015).
142. Self-absorption effect in LiF thermoluminescent dosimeters, B. Mukherjee, N. Vana, Nuclear Instruments and Methods in Physics Research **226**, pp.572-573 (1984).
143. Determination of self attenuation coefficient and relative TL efficiency of CaSO₄:Dy, LiF:Mg,Cu,P and LiF:Mg,Ti TLDs – An alternate approach, A. K. Bakshi, S. Chatterjee, T. Palani Selvam, V. J. Joshi and M.P. Chougankar, Nuclear Instruments and Methods in Physics Research B **269**, pp.2107–2110 (2011).

144. Modelling of the thermoluminescence response of LiF:Mg,Cu,P (MCP-N) detectors after doses of low energy photons, P. Olko, P. Bilski, M. Budzanowski, M. P. R. Waligo'wski, A. Fasso and N. Ipe, *Radiation Protection Dosimetry* **84** (1–4), pp. 103–108 (1999).
145. Calculation of photoneutrons produced in the targets of electron linear accelerators for radiography and radiotherapy applications, W. L. Huang, Q.F. Li and Y. Z. Lin, *Nuclear Instruments and Methods in Physics Research B* **229** (3-4), pp.339-347 (2005).
146. Structural investigations on $\text{Co}_{3-x}\text{Mn}_x\text{TeO}_6$; ($0 < x < 2$); High temperature ferromagnetism and enhanced low temperature anti-ferromagnetism, H. Singh, A. K. Sinha, H. Ghosh, M. N. Singh, P. Rajput, C. L. Prajapat, M. R. Singh and G. Ravikumar, *Journal of Applied Physics* **116**, 074904 (2014).
147. Crystal structure and electronic transport of $\text{Dy}@C_{82}$, Y. Kubozono, Y. Takabayashi, K. Shibata, T. Kanbara, S. Fujiki, S. Kashino, A. Fujiwara and S. Emura, *Physical Review B* **67**, 115410 (2003).
148. XOP 2.1 - A New Version of the X-ray Optics Software Toolkit, M. S. del Rio and R. J. Dejus, *AIP Conf. Proc.* **705**, 784 (2004).
149. Conception and realization of a parallel-plate free-air ionization chamber for the absolute dosimetry of an ultrasoft X-ray beam, J. E. Groetz, N. Ounoughi, C. Mavon, A. Belafrites, and M. Fromm, *Review of Scientific Instruments* **85**, 083304 (2014).
150. Correction factors for the INER-improved free-air ionization chambers calculated with the Monte Carlo method, Uei-Tyng Lin and Chien-Hau Chu, *Applied Radiation and Isotopes* **64**, pp.608–614 (2006).
151. Correction factors for free-air ionization chambers for X-rays transmitted through a diaphragm edge and scattered from the surface of the diaphragm aperture, T. Kurosawa and

- N. Takata, Report CCRI(I)/05-27 (2005).
152. Re-determination of the k_{sc} , k_e , k_{fl} correction factors for low and medium energy X-ray air kerma measurement by the ENEA-INMRI free air chambers, R.F. Laitano, M. Pimpinella, M. P. Toni, M. Quini and M. Bovi, Report CCRI(I)/05-31 (2005).
153. Free-air chamber correction factors for electron loss, photon scatter, fluorescence and bremsstrahlung, D. T. Burns, Report CCRI(I)/01-36 (2001).
154. Calculation of photon scattering and transmission correction factors for a free air ionization chamber at Nuclear Science and Technology Research Institute in Iran, S. Kashian, M.R. Eskandari, G. Raisali and H. Khalafi, *Annals of Nuclear Energy* **42**, pp.158–160 (2012).
155. Design and preliminary test of a free-air ionization chamber for low-energy X-ray, Jin-Jie Wu, Yuan-Di Yang, Pei-Wei Wang, Jing Chen and Jia-Cheng Liu, *Chinese Physics C* **35** (6), pp. 576-579 (2011).
156. Website: <https://physics.nist.gov/PhysRefData/XrayMassCoef/ComTab/air.html>
157. Introduction to radiological physics and radiation dosimetry, F. H. Attix, Wiley-VCH, Germany, (1985).
158. Ionization chambers, J. W. Boag, *The dosimetry of ionizing radiation*, Vol. II, pp.169–235, Academic Press (1987).
159. EGS4 application to design of parallel-plate free-air ionization chamber for high-energy synchrotron radiation, N. Nariyama, N. Kishi, T. Itoh, S. Taniguchi and T. Moriya, *Proc. of the Tenth EGS4 Users' Meeting in Japan*, KEK Proc. 2002-18, pp.19-24 (2002).
160. Design and development of front-end components of Indus-2 bending magnet beamlines, V. K. Raghuvanshi, V. P. Dhamgaye, A. K. Singh and R. V. Nandedkar, *AIP Conf. Proc.* **879**, pp.631-634 (2007).

161. An undulator based high flux and high resolution beamline for Atomic, Molecular and Optical Science (AMOS) research at INDUS-2 synchrotron radiation source (SRS), A. K. Das, B. N. Rajasekhar and N. K. Sahoo, BARC Report – BARC/2014/E/008 (2014).
162. SPECTRA: a synchrotron radiation calculation code, T. Tanaka and H. Kitamura, *Journal of Synchrotron Radiation* **8**, pp.1221–1228 (2001).
163. SHADOW: A synchrotron radiation ray tracing program, B. Lai and F. Cerrina, *Nuclear Instruments and Methods in Physics Research A* **246**, pp.337-341 (1986).
164. RAY, the BESSY ray trace program, F. Schafers, BESSY Technical Report 202/96 (1996).
165. Optical design of an X-ray absorption spectroscopy beamline at Indus-2 synchrotron radiation source, N. C. Das, S. N. Jha and A. P. Roy, Bhabha Atomic Research Centre Report No. BARC/1999/E/035 (1999).
166. Modern developments in X-ray and neutron optics, A. Erko, M. Idir, T. Krist and A. G. Michette, Springer (2008).
167. RAY-UI: A powerful and extensible user interface for RAY, P. Baumgärtel, M. Witt, J. Baensch, M. Fabarius, A. Erko, F. Schäfers, and H. Schirmacher, *AIP Conf. Proc.* **1741**, 040016 (2016).
168. Website: http://henke.lbl.gov/optical_constants/filter2.html.
169. Website: http://henke.lbl.gov/optical_constants/mirror2.html
170. Passive and real-time radiation monitoring at FEL facilities using radiochromic films, bubble detectors and thermoluminescent dosimeters, B. Mukherjee, S. Ruzin, M. Leuschner, 8th International Workshop on Radiation Safety at Synchrotron Radiation Sources (RadSynch-2015), DESY, Germany, pp. 35-40 (2015).

APPENDIX A

Indus Synchrotron Radiation Source

Indus synchrotron radiation facility houses two synchrotron radiation sources, Indus-1 and Indus-2 operating round the clock mode at Raja Ramanna Centre for Advanced Technology (RRCAT), Indore. Indus-1 is a 450 MeV, 100 mA electron storage ring emitting radiation in infrared to soft x-ray region (critical wavelength - 61 \AA^0) and operating since 1999. Presently there are five beamlines operational and two beamlines is under commissioning phase at Indus-1. Indus-2 is a 2.5 GeV, 200 mA electron storage ring with critical wavelength of $\sim 2 \text{ \AA}^0$ (for bending magnet) operating in round the clock mode. Indus-2 can accommodate 21 bending magnet and 5 insertion device beamlines, out of which at present 13 bending magnet based beamlines (10 hard x-ray beamlines and 3 soft x-ray beamlines) are operational and being used by researchers from various universities, national institutes and laboratories across the country. For enhancing utilization through higher brilliance and broad energy range (ultraviolet to hard x-ray), Indus-2 has been designed to accommodate five insertion devices (3 undulators, 1 wiggler and 1 wavelength shifter), out of which 3 undulators have already been commissioned.

Indus synchrotron facility consists of 20 MeV Microtron (electron injector), a 450/550 MeV booster synchrotron, 450 MeV storage ring (Indus-1) and 2.5 GeV electron storage ring (Indus-2). 20 MeV electron beam from microtron is fed to booster synchrotron through transport line-1 (TL-1) where its energy is increased to 450 MeV / 550 MeV. 450 MeV electron beam from

Booster is injected (through the transport line TL-2) and stored in Indus-1 storage ring for synchrotron beam utilization. For Indus-2 injection, 550 MeV beam from the booster is transported through transport lines TL-2 and TL-3. Injection process continues till Indus-2 accumulates desired beam current and thereafter electron beam energy is increased to 2.5 GeV. The facility was originally designed for 300 mA stored current at 2.5 GeV beam energy [1-4] but operated up to 200 mA at 2.5 GeV. A schematic layout of Indus synchrotron facility (Adopted from Ref. [1]) is shown in figure A.1. The major parameters of Indus-1 and Indus-2 synchrotron source are listed in table A.1. Synchrotron spectrum in Indus-1 and Indus-2 are shown in figure A.2.

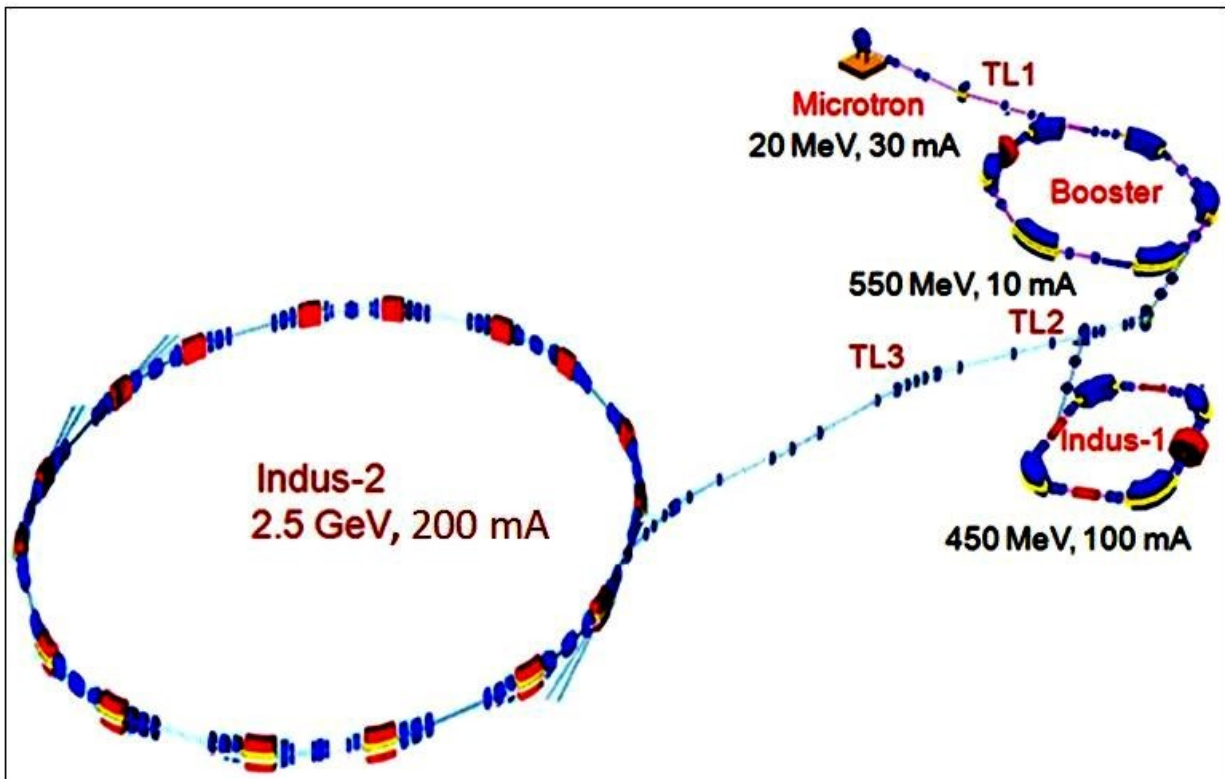
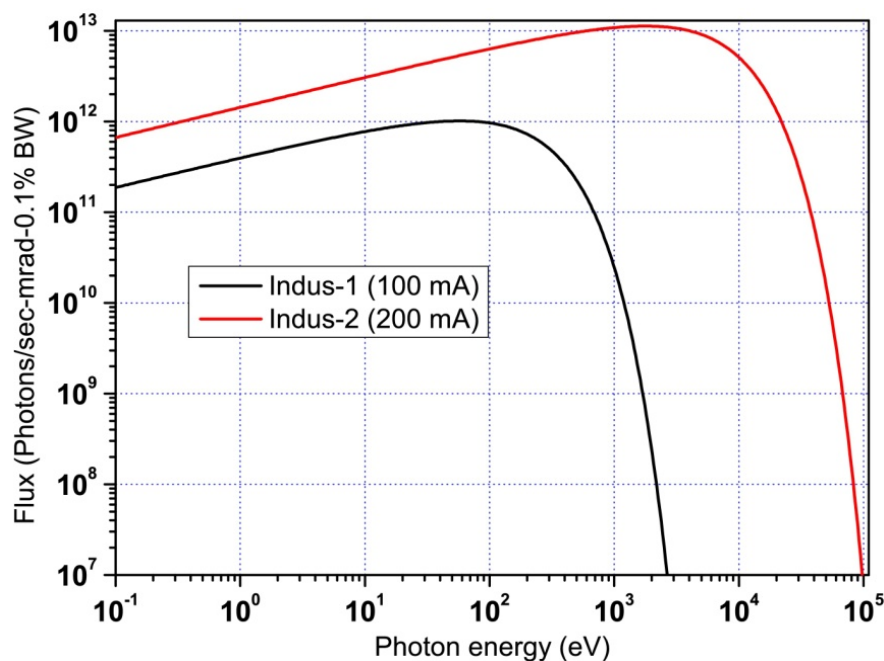


Figure A.1: Schematic layout of Indus synchrotron facility showing Microtron, Booster, Indus-1 and Indus-2 synchrotron sources

Table A.1: Major parameters of Indus-1 and Indus-2 synchrotron sources

Parameters	Indus-1	Indus-2
Beam energy (Injection)	450 MeV	550 MeV
Beam energy (Storage)	450 MeV	2500 MeV
Beam current	100 mA	200 mA
Circumference	18.97 m	172.47 m
No. of Dipole magnets (Magnetic field)	4 (1.5 Tesla)	16 (1.5 Tesla)
Critical Wavelength (Bending magnet)	61 Å	1.98 Å
Synchrotron beamlines	7	26

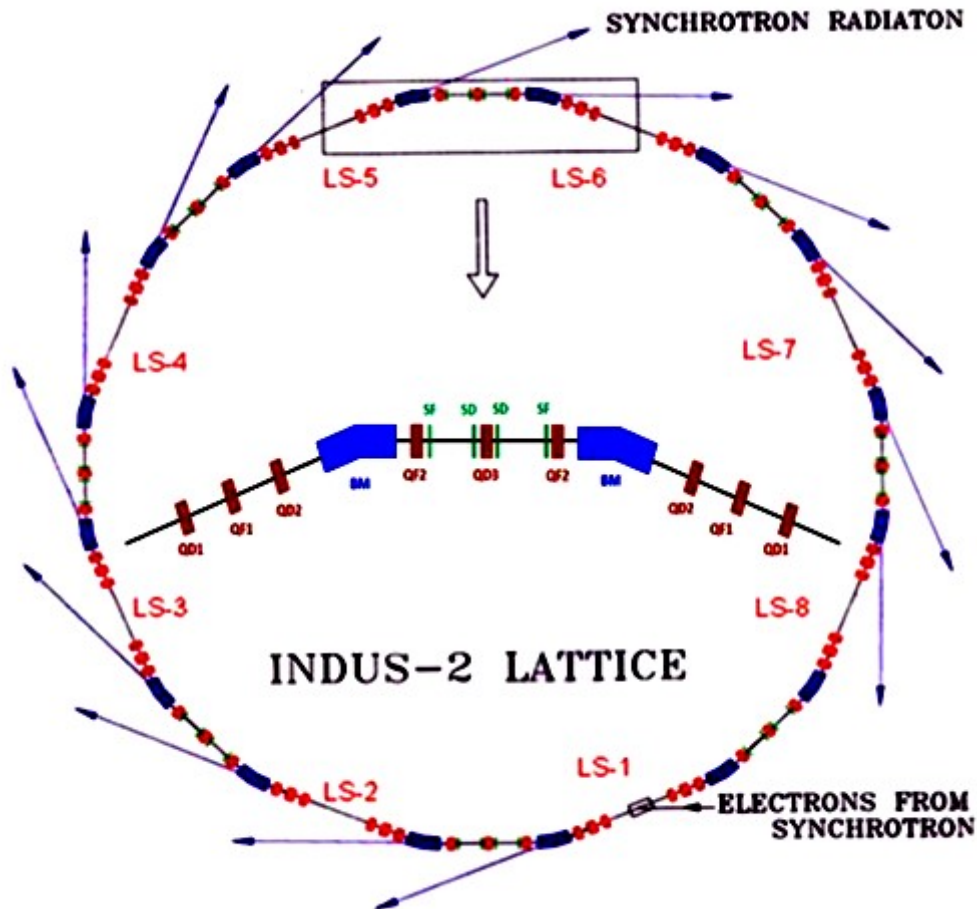
**Figure A.2: Synchrotron spectra from bending magnet in Indus-1 and Indus-2 storage ring**

A. Radiation and its safety measures in Indus-2

1. Indus-2 synchrotron radiation source

Indus-2 storage ring is third generation light source comprising of 16 bending magnets (BM), 72 quadrupole magnets (QF/QD) and 32 sextupole magnets (SF/SD). These magnets in the storage ring are arranged in a periodic fashion forming 8 unit cells called as lattice. Additional 48 horizontal and 40 vertical steering magnets are also distributed over the storage ring for the

correction in closed orbit distortion. The storage ring has eight long straight sections, where two sections are reserved for RF cavities, one section for injection septum and five sections for insertion devices [1-2]. Indus-2 storage ring along with the lattice structure [1-2] is shown in the figure A.3.



Note: LS: Long Straight section; BM: Bending Magnet; QD: Defocusing Quadrupole; QF: Focusing Quadrupole; SF: Focusing Sextupoles; SD: Defocusing Sextupoles

Figure A.3: Schematic diagram of Indus-2 DBA (Double Bend Achromat) lattice

The photographs of some sections of Indus-2 storage ring showing the RF cavities and the front end of a bending magnet beamline are shown in figure A.4.

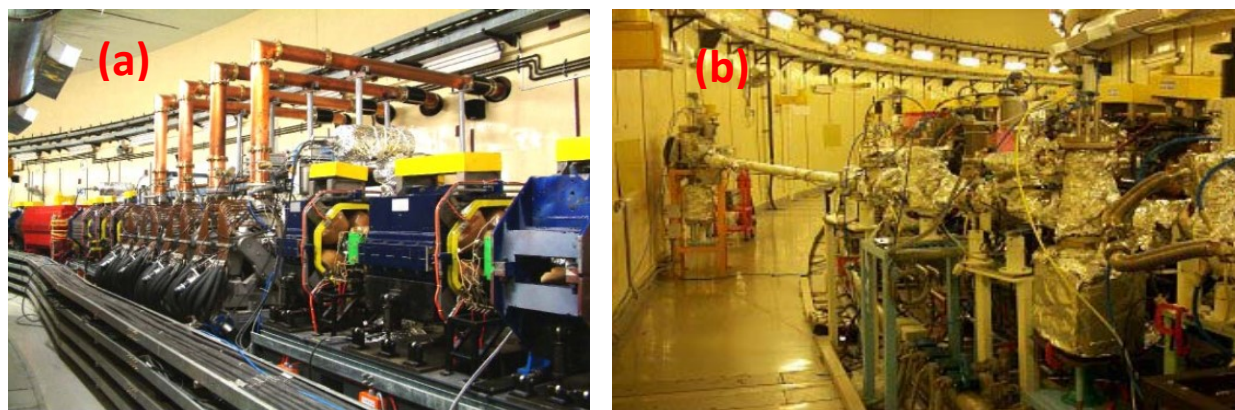


Figure A.4: Photograph of the Indus-2 storage ring (a) RF cavities section (b) Frontend of bending magnet beamline from the ring

Indus-2 is originally designed for beam current of 300 mA at 2.5 GeV beam energy with a lifetime of about 24 hrs. In Indus-2, synchrotron radiation generated from 1.5 Tesla bending magnets has critical wavelength of 1.98 Å. The first synchrotron light in Indus-2 was observed in December 2005 and regularly operating at 200 mA at 2.5 GeV [3-4]. Indus-2 is planned to accommodate 21 Bending Magnet (BM) and 5 Insertion Device (ID) beamlines, out of which 13 BM beamlines are operational and some BM beamlines as well as ID beamlines are in installation stage. The utilization of the planned beamlines in Indus-2 is listed in table A.2.

Table A.2: Indus-2 synchrotron beamlines and their utilisation

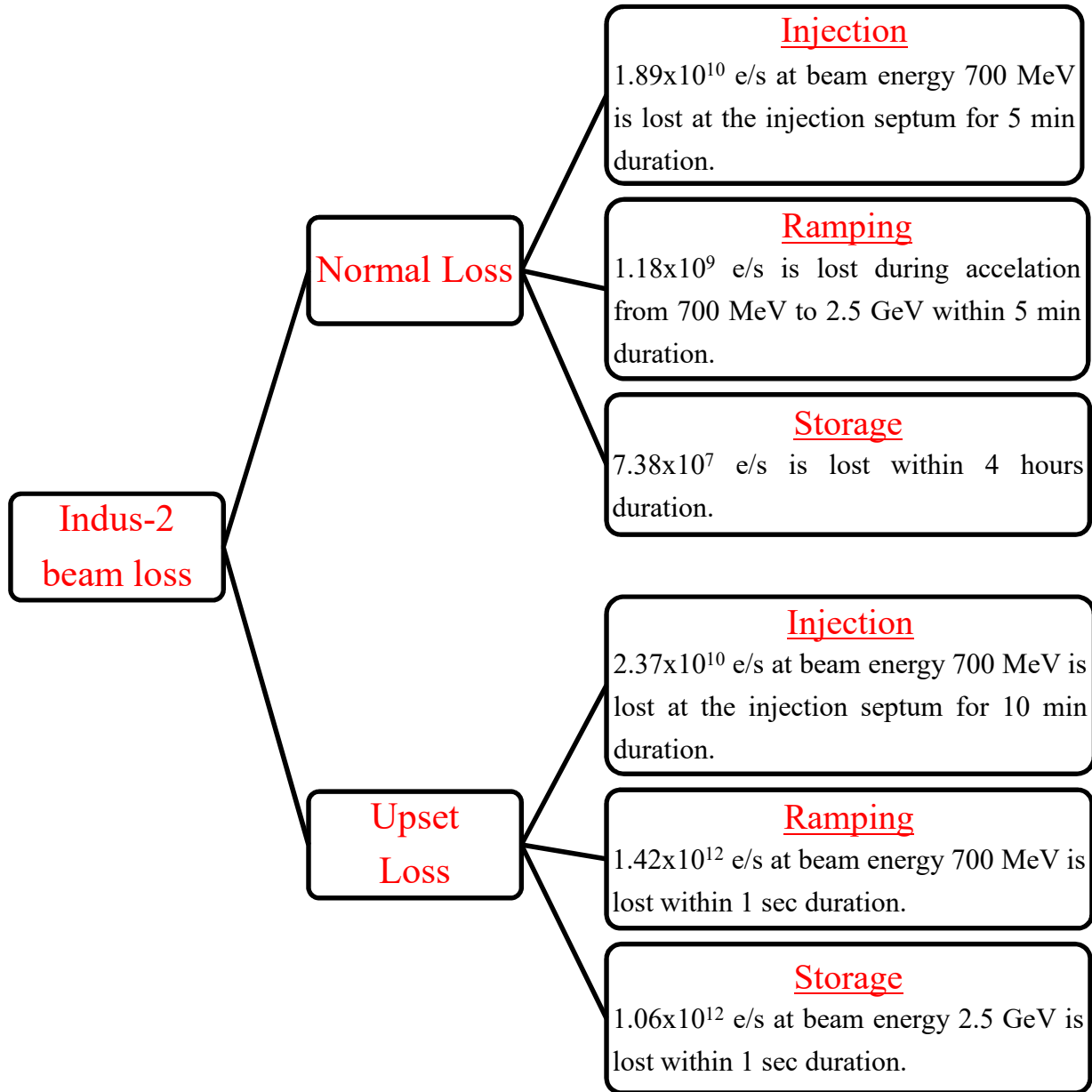
Beamline No.	Name of Beamline	Source	Typical experiments/ applications
BL-1	Soft X-ray Absorption Spectroscopy	Bending magnet	Absorption in thin films and bulk for information on chemical state and near neighbor environment
BL-3	Soft X-ray Reflectivity	Bending magnet	Surface and interface characterization of multilayer, thin film and X-ray optics
BL-4	X-ray Imaging	Bending magnet	X-ray phase contrast imaging and tomography of materials for engineering

			and biomedical application
BL-7	Soft & Deep X-ray Lithography	Bending magnet	Development of high aspect ratio structure for MEMS, X-ray optics, micro-devices etc.
BL-8	DEXAFS (Dispersive Extended X-Ray Absorption Fine Structure)	Bending magnet	Time resolved local structure measurement, applied to catalysis, reactions etc.
BL-9	SEXAFS (Scanning Extended X-Ray Absorption Fine Structure)	Bending magnet	Near neighbor information and chemical state of element in functional material
BL-11	Extreme conditions AD/ED-XRD	Bending magnet	Crystal structure of high pressure and high temperature total XRF for PDF analysis
BL-12	Angle Dispersive XRD (ADXRD)	Bending magnet	Crystal structure of bulk and thin films at high and low temperature and high pressure
BL-14	X-ray Photo-Electron Spectroscopy (XPES)	Bending magnet	Electronic structure of materials, determination of surface composition
BL-16	X-ray Fluorescence microprobe (μ XRF)	Bending magnet	Trace element analysis, chemical composition of bulk and thin film
BL-21	Protein crystallography (PX)	Bending magnet	Crystal structure of biological molecules like proteins, DNA and their complexes
BL-23	Visible diagnostic	Bending magnet	Determine the characteristics of the synchrotron beam of Indus-2
BL-24	X-ray diagnostic	Bending magnet	Determine the characteristics of the synchrotron beam of Indus-2

2. Radiation environment in Indus-2

The radiation environment in Indus-2 is dominated by bremsstrahlung radiation which is produced when electron beam interact with the accelerator components like vacuum pipes,

injection point, extraction point etc. during operation. Another source of bremsstrahlung radiation is gas bremsstrahlung, generated due to the interaction of stored electrons with residual gas molecules. Since the bremsstrahlung radiation has a broad energy spectrum from few keV to the energy of the incident electron beam (2.5 GeV). Because of the high energy, these photons develop electro-magnetic cascade in the interacting medium and as a result mixed field of electrons, positrons and photons are generated in the medium. The bremsstrahlung radiation will generate neutrons via photonuclear reactions (like giant dipole resonance, quasi-deuteron effect and photo-pion decay) with accelerator components [5]. However the cross-section for neutron production is of the order of few mbarn/nucleon and thus the contribution of neutron dose outside shielding is not significant. Due to the generation of photo-neutrons, from the structural materials, radio activity may be induced in the accelerator components. The intensity and spectral distribution of the radiations at different sections of the storage ring depend upon the beam loss scenario during various stages of operation [6-7]. The radiation shielding for the storage ring is evaluated based on the design beam loss scenario. The design beam loss scenario for Indus-2 is shown in figure A.5. Radiation source term [5] due to bremsstrahlung radiation and photo-neutrons at the reference points are calculated using the design beam loss scenario (assuming point beam loss). Based on these data, shielding thickness is evaluated to achieve regulatory limit of 1 $\mu\text{Sv/h}$ (for continuous occupancy). The calculated roof thickness is also found to be sufficient enough to reduce the neutron sky shine dose to background level.



Note: Frequency of the events are assumed to be 6 times per day and 250 days per year for all events except the upset loss during injection, where the frequency of one time a day and 250 days per year is assumed.

Figure A.5: Design beam loss scenario for Indus-2 storage ring

However if heavy beam loss takes place for long duration, then the location of beam loss may

give rise to significant induced activity. The residual activity builds with continued machine operation and reaches a saturation level depending upon its half-life. Since the beam injection is done for limited duration, the activity build-up is not much. The estimated saturation exposure rate and the dose rate from saturation activity are shown in table A.3. Low level of induced radioactivity is produced at the injection septum, where the corresponding dose rate is found to be within 1-2 $\mu\text{Sv/h}$. Measured residual activity in air and cooling water are found to be below minimum detectable activity (MDA).

Table A.3: Estimated dose rate due to induced activity in Indus-2

Material	Isotope	Half life	Radiation type & energy	*Saturation exposure rate (R-m ² /h/kW)	**Normal loss dose rate at 1m ($\mu\text{Sv/h}$)
Storage Ring					
Copper	Cu-62	9.76 min	β^+ : 2.9 MeV	6.5	1.68
	Cu-64	12.8hr	β^- : 0.6 MeV β^+ : 0.7 MeV	1.9	0.49
	Co-60	5.26 y	β^- : 0.3 MeV γ : 1.17 MeV & 1.33 MeV	0.83	0.22
Iron	Fe-55	2.6 y	e^- capture K_{α} - 5.898 keV K_{β} - 6.49 keV	9.0	2.33
Aluminum	Al-26	7.4×10^5 y	β^+ : 1.2 MeV γ : 1.8 MeV & 1.3 MeV	6.0	1.55
Injection Septum***					
Composition of Injection Septum: Vacuum Chamber -- Stainless Steel (Fe); Magnets (core material MAG36B) -- Ni (36%), Fe (64%); Coil -- Copper					
Copper	Cu-62	9.76min	β^+ : 2.9 MeV	6.5	75.42
	Cu-64	12.8 hr	β^- : 0.6 MeV β^+ : 0.7 MeV	1.9	22.1
	Co-60	5.26 y	β^- : 0.3 MeV γ : 1.17 MeV & 1.33 MeV	0.83	9.65

Iron	Fe-55	2.6 y	e ⁻ capture K _α - 5.898 keV K _β - 6.49 keV	9.0	104.71
Aluminum	Al-26	7.4 x 10 ⁵ y	β ⁺ : 1.2 MeV γ : 1.8 MeV & 1.3 MeV	6.0	69.81
Nickel	Ni-57	36 hr	β ⁺ : 0.8 MeV γ: 1.38 MeV &1.92 MeV	7.9	92.09
	Co-57	270 days	γ: 0.122 MeV & 0.136 MeV	7.5	87.26

**Obtained from saturation activity*

***During normal loss, 300 mA stored current at 2.5 GeV is assumed to be lost in 4 hours and the electrons are assumed to be lost at a single point.*

**** At the injection septum due to loss of incoming electron beam from booster synchrotron (2/3rd of 30 mA circulating current in booster synchrotron at 700 MeV)*

Because of the low beam power (~ few watt), the production of radioactive nuclides in the air and soil, as well as noxious gases due to beam losses in the storage ring are generally not considered safety issues [7-10] for synchrotron facilities. However due to high intensity and low energy synchrotron photons in beamlines, production of ozone (O₃) gas inside the experimental station of the white beamlines are found to be significantly higher than the threshold limit value of 0.1 ppm. However in monochromatic beamlines the measured ozone concentration is well below the threshold limit value.

3. Radiation safety systems in Indus-2

For ensuring radiation safety in the facility, various safety systems like personnel protection system and radiation monitoring system are implemented in the facility. Radiation safety in Indus-2 facility is ensured by engineered safety systems like shielding, ventilation, zoning, access control, search and secure interlocks, scram switches, door interlocks etc. Continuous

measurements of radiation levels are carried out by deploying radiation monitors with local and remote displays. Periodic radiation surveys are also carried out during the operation of Indus-

2. Various components of radiation safety systems for Indus-2 is shown in figure A.6

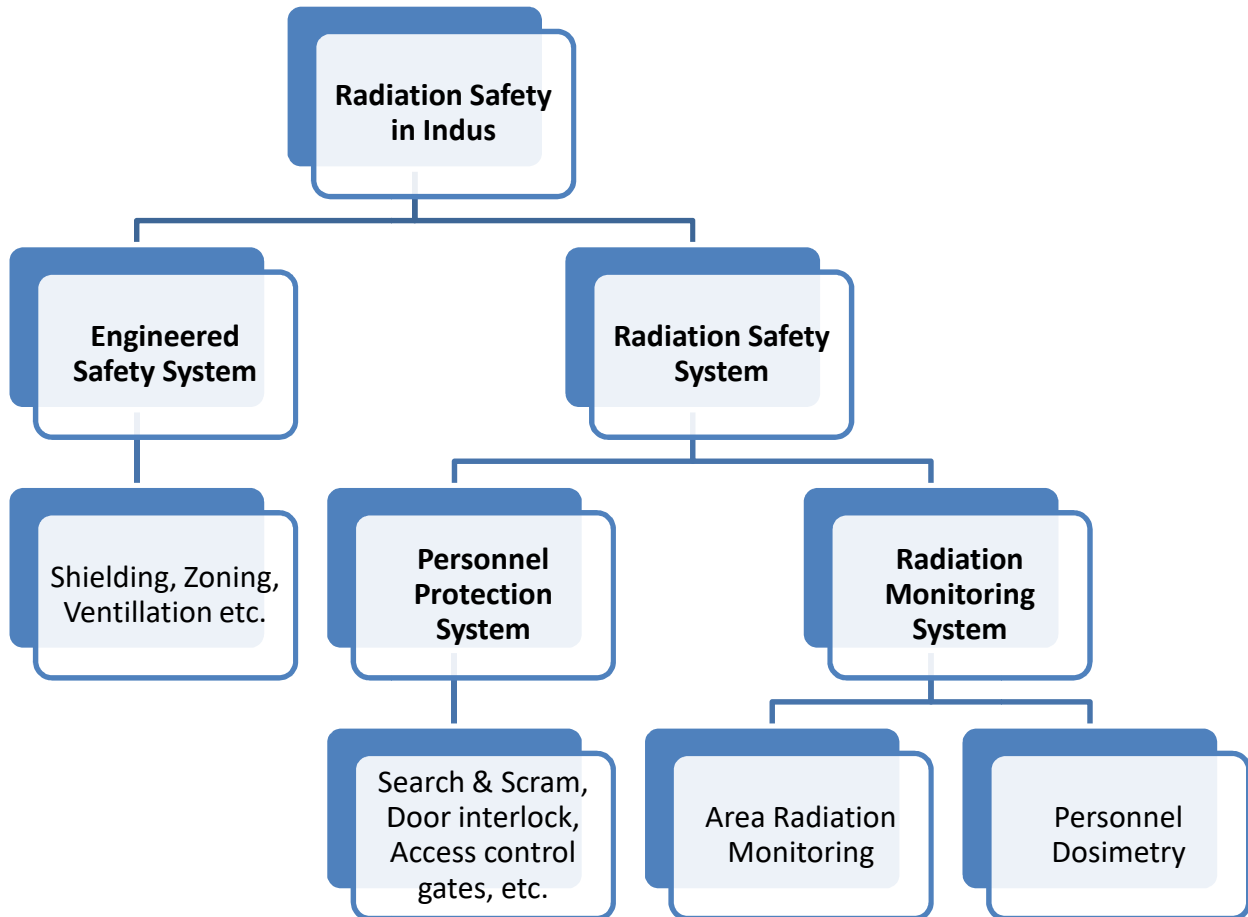


Figure A.6: Radiation safety pathway for Indus synchrotron facility

A brief description of the safety systems for Indus-2 is given below.

C.1 Zoning Philosophy

Zone-1 (Normally Accessible area):	Dose rate	< 1 $\mu\text{Sv/h}$
Zone-2 (Restricted Entry area):	Dose rate	1-10 $\mu\text{Sv/h}$ 10-100 $\mu\text{Sv/h}$ (Investigation/Action level)
Zone-3 (Prohibited area):	Dose rate	> 100 $\mu\text{Sv/h}$

If the dose rate crosses 10 $\mu\text{Sv/h}$ in the Zone-2, investigation is performed to find out the cause of

the increase in radiation level and appropriate action will be initiated to reduce it below $10 \mu\text{Sv/h}$.

C.2 Shielding

The storage ring area is shielded with 1.5 m thick ordinary concrete wall on outer side and 0.6 m thick concrete wall on inner side of the tunnel. Tunnel roof is also provided with 0.6 m thick concrete shielding. Cross-section view of the shielding for Indus-2 tunnel is shown in figure A.7. The shielding adequacy has been evaluated for design parameters (2.5 GeV, 300 mA) taking into account the normal as well as accidental beam losses as per the beam loss scenario (Refer figure-A.5). The annual dose rates at the reference points (A, B, C and D) based on the design beam loss assumptions are shown in table A.4. The calculated roof thickness is also found to be sufficient enough to reduce the neutron sky shine dose to background level. Beam line holes / gaps on the outer shield wall are plugged with appropriate shield materials to prevent any streaming of radiation to experimental hall.

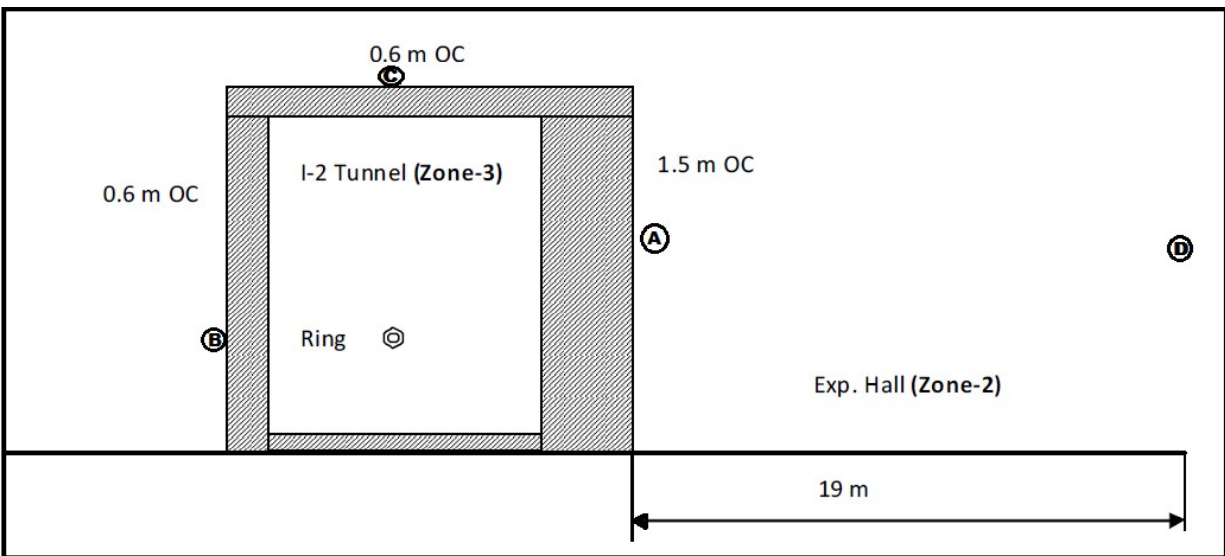


Figure A.7: Cross-section of Indus-2 shielded tunnel showing the reference points (A, B, C & D) used for shielding calculation

Table A.4: Dose per year at the reference points based on design beam loss scenario

Reference Points	Dose per year (mSv/y)	
	0 ⁰	90 ⁰
A	4.39	23.44
B	-	1349.16
C	-	344.43
D	0.93	0.86

Note: The 0⁰ and 90⁰ dose values are the dose rates outside the shield containment in the forward and lateral direction with respect to the point beam loss in the ring.

C.2 Ventilation

The saturation concentration of ozone due to a 2.5 GeV electron at 300mA is estimated to be 0.154 ppm assuming the electron beam is interacting with air to produce ozone. Therefore a ventilation rate of 1 air change per hour is maintained in the storage ring tunnel of Indus-2 to reduce the ozone concentration within 0.1 ppm. However the production of ozone gas in white beamline hutches is significantly higher than the threshold limit value. Hence as a safety measure, forced ventilation through exhaust fan is interlocked with synchrotron beam ON condition and the delay time for opening of the hutch door are provided to prevent exposure to ozone gas. 1 air change per hour has been set as the ventilation requirement in the experimental hall to avoid ozone inhalation hazard.

C.3 Personnel Protection System

RFID card based access control gates are installed at entry points to tunnel area for ensuring entry of the authorized persons only. Many Search & Scram units are placed at different locations in the ring area which forces the operation crew to search for any occupancy and

evacuate the area before the operation of the accelerator. Scram switches and pull chord system are provided to trip the accelerator by any trapped personnel. Any error in the search process will trip the system forcing the crew to search the area again. Door interlocks are also provided at the entry doors to ensure tripping of the accelerator in case of any inadvertent entry to storage ring area is attempted.

C.4 Radiation Monitoring System

Photon and neutron radiation monitors are installed in different areas in the facility for continuous monitoring of the radiation levels and the data from the monitors are displayed locally as well as made available in Indus control room.

C.5 Personnel dosimetry devices

Personal monitoring devices like Thermoluminescent Dosimeter (TLD) badges, Direct reading dosimeters (DRD) for short term users for photon and CR-39 neutron badges for neutron are provided to working personnel involved in operation and maintenance of the facility and synchrotron beamline users. The dosimetry devices are issued after attending an audio-visual training module on radiation protection, safety systems etc. and clearing a radiation protection examination.

References

1. Website: http://www.rrcat.gov.in/technology/accel/isrf_index.html.
2. Commissioning of the Indus-2 storage ring, V.C. Sahni, Asian Particle Accelerator Conf. Proc., Raja Ramanna Centre for Advanced Technology, Indore, (2007).
3. Indus Synchrotron Source: A National Facility, S. K. Deb, AIP Conf. Proc. **1447**, pp.56-59 (2012).
4. Indus-2 Synchrotron Radiation Source: current status and utilization, S. K. Deb, G. Singh

- and P. D. Gupta, Journal of Physics: Conf. Series **425**, 072009 (2013).
5. Radiological Safety aspects of the operation of electron linear accelerators, W. P. Swanson, IAEA Tech.Rep.188 (1979).
 6. Radiological considerations in the design of synchrotron radiation facilities, N.E. Ipe, SLAC-PUB 7916, January (1999).
 7. Radiation protection at synchrotron radiation facilities, J. C. Liu and V. Vylet, Radiation Protection Dosimetry **96** (4), pp. 345–357 (2001).
 8. Advanced Photon Source: Radiological Design Considerations, H. J. Moe, APS-LS-141 Revised (1989).
 9. Environmental impact from accelerator operation at SLAC, J. C. Liu, A. Fasso, S. Mao, W. R. Nelson, R. Seefred and R. Sit, Proc. 1999 Symposium on Environmental Monitoring Techniques, Kaohsiung, Taiwan & SLACPUB-8085 (1999)
 10. Radiation protection issues of bERLinPro, K. Ott and Y. Bergmann, 8th International Workshop on Radiation Safety at Synchrotron Radiation Sources (RadSynch-2015), DESY, Germany, pp. 35-40 (2015).

APPENDIX-B

Radiation quantities and units

Quantification of radiation field through the measurement of ionization produced in air by the incident radiation has been the most conventional technique. The ionization produced in air is then correlated to the dosimetry quantities. Basically there are three physical quantities used to describe radiation field kerma (K), absorbed dose (D) and exposure (X) and are defined as follows [1-4].

A. Physical quantities

1. Kerma (K)

Kerma stands for *kinetic energy released per mass* and quantifies the transfer of energy by indirectly ionizing radiation (photons and neutrons) to charged particles in the medium. Kerma is defined as the energy transferred to charged particles per unit mass in medium and is mathematically expressed as follows.

$$K(\text{Gy}) = \frac{dE_{tr}}{dm} = E\Phi \left(\frac{\mu_{tr}}{\rho} \right)_{E,Z} \quad \text{----- (B.1)}$$

Where, E_{tr} = Energy transferred to the charged particles in the finite volume, E = Energy of incident radiation, Φ = Fluence and $\left(\frac{\mu_{tr}}{\rho} \right)_{E,Z}$ = mass energy transfer coefficient, function of energy of photon (E) and atomic number (Z) of medium. Kerma is expressed in terms Gray (Gy). Due to the transfer of energy to electrons in the interacting medium, the electrons gain kinetic

energy and undergo collision loss (i.e. ionization and excitation) or radiative loss bremsstrahlung photons). The bremsstrahlung photons mostly move out of the region of interest and do not produce any appreciable measured charge. A correction term for the bremsstrahlung loss is added to the kerma and is called as collision kerma. Therefore collision kerma in air is expressed as

$$K_c = E\Phi \left(\frac{\mu_{tr}}{\rho} \right)_{E,Z} (1-g) \quad \text{----- (B.2)}$$

Here g is the bremsstrahlung correction factor or the mean correction for energy due to radiated photons.

2. Absorbed dose (D)

Absorbed dose quantifies the energy absorbed in the medium due to all kinds of radiation. Absorbed dose is defined as the energy of the incident radiation deposited per unit mass in medium and is mathematically expressed as follows.

$$D(\text{Gy}) = \frac{dE}{dm} = E\Phi \left(\frac{\mu_{en}}{\rho} \right)_{E,Z} \quad \text{----- (B.3)}$$

Where $\left(\frac{\mu_{en}}{\rho} \right)_{E,Z}$ = mass energy absorption coefficient, function of energy of photon (E) and atomic number (Z) of medium. SI unit of absorbed dose is Gray, same as that of kerma [CGS unit: rad]

$$1 \text{ Gy} = 1 \text{ J/kg} = 100 \text{ rad} \quad [1 \text{ rad} = 100 \text{ erg/gm}]$$

In simple words, it can be said that kerma quantifies the energy which is transferred to the charged particle in the medium whether it may or may not be completely absorbed in the medium, whereas absorbed dose quantifies the energy of the charged particle which is absorbed in medium.

3. Exposure (X):

Exposure quantifies ionization produced by x-ray and γ -rays in air medium and is defined as the total charge (of either sign) produced in air of unit mass when all the electrons (including positrons) liberated by photons are completely stopped in air. The use of exposure is limited to x-rays or gamma rays below 3 MeV, because of difficulty in measuring the ionization produced in air due to energetic secondary electrons.

$$X(\text{C/kg}) = \frac{dQ}{dm} \quad \text{----- (B.4)}$$

SI unit of exposure is Coulomb/kg, whereas the special unit roentgen (R) is popularly used. Roentgen (R) is defined as the amount of x-ray or gamma radiation that produces 1 esu of charge in 1 cm³ of air at STP (mass of 1 cm³ air at standard temperature of 0 °C and standard pressure of 1 atm is 0.001293 g).

$$1 \text{ R} = 2.58 \times 10^{-4} \text{ C/kg}$$

Relationship between kerma, dose and exposure

Air kerma can be quantified by measuring exposure and the relationship between the two quantities is given below.

$$K_{air} = X \left(\frac{W}{e} \right)_{air} \left(\frac{1}{1-g} \right) = \left(\frac{Q_{air}}{m_{air}} \right) \left(\frac{W}{e} \right)_{air} \left(\frac{1}{1-g} \right) \quad \text{----- (B.5)}$$

Here $\left(\frac{W}{e} \right)_{air}$ is the mean energy per charge in air and has a value of 33.97 J/C. Under charged particle equilibrium (CPE) condition, i.e. when the energy loss due to a charged particle leaving the region of interest is compensated by an identical charged particle produced outside and entering to the region of interest, the relationship between three quantities is given below.

$$D_{air} = K_{c,air} = X \left(\frac{W}{e} \right)_{air} \quad \text{----- (B.6)}$$

B. Protection quantities

Absorbed dose (D) quantifies the energy deposition in matter from ionizing radiation irrespective of the type of the medium. However in radiation protection, the energy absorption in human body from radiation and its consequences are most important. Different forms of ionizing radiation can lead to different biological effects, even for the same absorbed dose in human tissue. Similarly depending on the response of different tissues, the effect of absorbed dose also varies with different tissues in human body. Therefore protection quantities like Dose equivalent and Dose effective have been derived to quantify the radiation effects on human body and the quantities are defined as follows [1-4].

$$\text{Dose Equivalent } (D_{eq}) = \text{Absorbed Dose } (D) \times \text{Radiation Weighting Factor } (W_R)$$

$$\text{Dose Effective } (D_{eff}) = \text{Dose Equivalent } (D_{eq}) \times \text{Tissue Weighting Factor } (W_T)$$

The weighting factors, W_R and W_T have been reported and updated by International Commission on Radiological Protection (ICRP) through series of recommendation booklets. Both dose equivalent and dose effective have same unit, Sievert (Sv); 1 Sv = 100 rem [CGS unit: rem]

References

1. Introduction to Health Physics, H. Cember and T.E. Johnson, The McGraw-Hill Companies (2009).
2. Radiation Oncology Physics: A handbook for teachers and students, E. B. Podgorsak, International Atomic Energy Agency - IAEA, (2005).
3. Atoms, Radiation and Radiation Protection, J. E. Turner, Wiley-VCH Verlag GmbH & Co. KGaA (2007).
4. Introduction to Radiological Physics and Radiation Dosimetry, F. H. Attix, Wiley-VCH, Germany, (1985).